The atomic and spin-electronic structure of interfaces and extended structural defects in the Co-based full Heusler alloys

Zlatko Nedelkoski

PhD

University of York

Physics

January 2017

Abstract

The atomic and spin-electronic structure of interfaces and extended structural defects in the Co-based full Heusler alloys is studied. Interfaces between a half-metallic Heusler alloy and metal or semiconductor are fundamental and determine the performance of spintronic devices such as spin-valves or devices for spin-injection applications. It is shown that for the Co_2MnSi/Ag bulk-like terminated interfaces, the interfacial spin-polarisation significantly depends on the atomic plane termination. In addition, on the example of experimentally realised interface, part of a spin-valve, it is demonstrated that there is an additional monolayer at the interface, which as shown by the density functional theory calculations can create significantly negative local spin-polarisation, detrimental for the device performance. It is demonstrated that the interfaces between the Heusler alloy and Si, suffer from large interfacial interdiffusion which leads to a gradual decrease of magnetic moment over 2-3 nm region in which the spin-polarisation is also significantly affected. It is shown that even sharp interfaces are not desirable since they lead to reversed spin-polarisation. However, it is demonstrated that the addition of thermodynamically stable Si-Co-Si monolayer provides very high spin-polarisation across all interface layers. An ideal candidate for spin-injection applications is found to be the $Co_2FeAl_{0.5}Si_{0.5}$/Ge interface which shows very minor and atomic plane selective interdiffusion that does not affect film's half-metallic properties, absence of formation of any secondary phases and almost no interfacial strain. Based on models derived from electron microscopy observations, it is demonstrated that this interface retains very high interfacial spin-polarisation. Finally, the atomic structure of an extended structural defect observed in $Co_2FeAl_{0.5}Si_{0.5}$ thin film is revealed by electron microscopy. The performed density functional theory modelling shows that these boundaries reverse the sign of spin-polarisation, hence their presence has to be minimised in order to achieve films with better properties.

List of Contents

List of Tables

List of Figures

Acknowledgements

First of all, I am very thankful to Dr Vlado Lazarov for giving me the opportunity to work on this research, as well as for his continuous and excellent supervision. I would also like to emphasise that I am very thankful for the full scholarship, awarded to me by the Department of Physics, which made my studies here possible.

I would like to thank Prof Kohei Hamaya and Dr Shinya Yamada from Osaka University, Japan for their collaboration; their specimens were very important for this research. I would also like to thank Dr Phil Hasnip from the University of York for his support regarding the CASTEP code. I am very thankful to Dr Demie Kepaptsoglou and Prof Quentin Ramasse from the SuperSTEM Laboratory in Daresbury UK, and Dr Ana Sanchez from the University of Warwick for their collaboration on electron microscopy. Many thanks also to Dr Leonardo Lari for the training and support regarding the electron microscope in York. I would also like to thank Dr Balati Kuerbanjiang for his continuous support and collaboration, and also all my fellows PhD students from the group of Dr Vlado Lazarov. I would like to acknowledge ARCHER, the UK national high performance computing facility, which has been used continuously during this research.

Huge thanks to my family!

Declaration

I declare that the work presented in this thesis is based purely on my own research, unless otherwise stated, and has not been previously submitted for a degree in this or any other university.

List of Publications:

[1] Nedelkoski, Z., Hasnip, P. J., Sanchez, A. M., Kuerbanjiang, B., Higgins, E., Oogane, M., Hirohata, A., Bell, G. R. & Lazarov, V. K. The effect of atomic structure on interface spin-polarization of half-metallic spin valves: Co_2MnSi/Ag epitaxial interfaces. *Applied Physics Letters* **107***,* 212404 (2015).

[2] Nedelkoski, Z., Kepaptsoglou, D., Ghasemi, A., Kuerbanjiang, B., Hasnip, P. J., Yamada, S., Hamaya, K., Ramasse, Q. M., Hirohata, A. & Lazarov, V. K. Controlling the half-metallicity of Heusler/Si(1 1 1) interfaces by a monolayer of Si–Co–Si. *Journal of Physics: Condensed Matter* **28***,* 395003 (2016).

[3] Nedelkoski, Z., Kuerbanjiang, B., Glover, S. E., Sanchez, A. M., Kepaptsoglou, D., Ghasemi, A., Burrows, C. W., Yamada, S., Hamaya, K., Ramasse, Q. M., Hasnip, P. J., Hase, T., Bell, G. R., Hirohata, A. & Lazarov, V. K. Realisation of magnetically and atomically abrupt half-metal/semiconductor interface: $Co_2FeSi_{0.5}Al_{0.5}$/Ge(111). *Scientific Reports* **6***,* 37282 (2016).

[4] Nedelkoski, Z., Sanchez, A. M., Ghasemi, A., Hamaya, K., Evans, R. F. L., Bell, G. R., Hirohata, A. & Lazarov, V. K. The antiphase boundary in half-metallic Heusler alloy $Co_2Fe(Al,Si)$: atomic structure, spin polarization reversal, and domain wall effects. *Applied Physics Letters* **109***,* 222405 (2016).

[5] Kuerbanjiang, B., Nedelkoski, Z., Kepaptsoglou, D., Ghasemi, A., Glover, S. E., Yamada, S., Saerbeck, T., Ramasse, Q. M., Hasnip, P. J., Hase, T. P. A., Bell, G. R., Hamaya, K., Hirohata, A. & Lazarov, V. K. The role of chemical structure on the magnetic and electronic properties of $Co_2FeAl_{0.5}Si_{0.5}$/Si(111) interface. *Applied Physics Letters* **108***,* 172412 (2016).

1 Motivation and thesis overview

1.1 Motivation of the thesis

The field of spintronics, in which the main functionality is due to the spin of the electron, attracts significant research interest among scientists. It has been revolutionised by the discovery of the giant magnetoresistance effect, where there is a huge change in resistivity of a heterostructure upon applying external magnetic field. Since the efficiency of any spintronic device depends on the degree of current spin-polarisation, the halfmetals - materials which can in principle produce 100% spin-polarised current are of great interest.

One of the most promising materials for spintronic applications are the Co-based full Heusler alloys. Many of them have been theoretically predicted as 100% spin-polarised at the Fermi-level. The big potentials of these materials have been also experimentally confirmed; for example, by implementing them as a part of real spintronic devices showing outstandingly high magnetoresistance values [1].

Although their ideal bulk structures are predicted to have halfmetallic electronic properties, their spin-electronic structure can be drastically affected by a presence of disorder, variations from stoichiometry, strain etc. All these factors can reduce or even reverse the spin-polarisation of the half-metallic Heusler alloys, as discussed in the next chapters.

Very important for all spintronic devices are the interfaces between the halfmetallic electrodes and the neighbouring layers. At these interfaces, first of all the atomic structure may significantly differ from that in the bulk-like part, which often is the case for interfaces between a Heusler alloy and semiconductor. Also, even if the atomic structure is itself not significantly affected, i.e. the interface is abrupt, the interfacial electronic structure may not be at all desirable due to the presence of states in the band gap, which can in some cases even reverse the sign of spin-polarisation. Since the spin-polarised current of the half-metallic electrode has to be transported between the

layers independent of device geometry and application, the interfacial electronic structure drastically affects the spin-transport and can cause partial or full current depolarisation.

Although there have been studies on interfaces with half-metals, these studies have been so far mainly purely theoretical based on either ideal bulk-like terminations or assuming very simplistic models both of which often are not experimentally observed. On the other hand, in other studies, a general overview of the structure at some of these interfaces has been given, mainly without revealing their exact interfacial atomic structure.

The motivation of this thesis is to bridge these two approaches: the experiment and theory, in order to provide a detailed insight into the influence of such interfaces on the device performance. By employing atomic resolution electron microscopy imaging, the atomic structure of selected interfaces crucial for spintronics will be revealed. The constructed models will be used to perform first-principles calculations in order to determine their spin-electronic structure. Combining the experimentally derived atomic structure of the studied interfaces with first-principles modelling will give not only a complete picture of these interfaces, but also will guide future experiments in tailoring heterostructures with much better performances.

The same approach will be used to reveal the influence of extended structural defects, which have been extensively studied in other half-metallic materials, but their presence has not been so far reported in the Co-based Heusler alloys. The presence of an extended structural defect will be demonstrated in the half-metallic $Co_2Fe(Al_{0.5},Si_{0.5})$. Taking into account that structural defects can have significant influence on the thin film's properties, this is a big motivation to study its atomic and electronic structure.

1.2 Overview of the thesis

The thesis contains eight chapters. **Chapter 1** and **Chapter 2** give the motivation and a brief introduction into the subject of study. The atomic and electronic structure of the studied Co-based full Heusler alloys will be given in details. The importance of many factors that can affect their half-metallicity will be explained with particular focus on interfaces and structural defects. It will be discussed why these half-metallic materials are

crucial for spintronic applications and explained why they are an ideal solution to the well-known issue of conductivity mismatch preventing efficient spin-injection. The challenges related to the formation of secondary interfacial phases or interfacial intermixing will be addressed and correlated with the spin-electronic structure of the interfaces. In addition, the importance and influence of structural defects on the spin-electronic structure in the half-metallic Heusler alloys will be discussed.

In **Chapter 3**, the methodology used during the thesis will be discussed. This includes both the experimental and the theoretical part. The experimental part is mainly related to electron microscopy, starting from detailed description of the procedure for specimen preparation, then discussing conventional transmission electron microscopy (TEM), and finishing with the basics of the frequently used state-of-the-art high angle annular dark field (HAADF) scanning transmission electron microscopy (STEM). The second part discussed the computational methodology with focus on density functional theory which will be used to reveal the spin-electronic structure of the studied interfaces and extended structural defects.

In **Chapter 4**, first, density functional theory calculations will be performed on ideal bulk-like terminated Co_2MnSi/Ag interfaces. Then, the exact atomic structure of experimentally realised interfaces will be revealed and a presence of an additional monolayer at the interface will be demonstrated. The calculations will show that this monolayer in some cases can be very detrimental to the spin-electronic structure of these interfaces.

Chapter 5 is focussed on interfaces between a Heusler alloy and Si. It will be shown that due to the interfacial interdiffusion, the magnetic moment gradually decreases over a 2 - 3 nm region in the interface vicinity and that the spin-polarisation is also drastically affected due to the intermixing of the atomic species. In the second part of this chapter, it will be shown that even if the interdiffusion is not present, the atomically sharp interface causes spin-polarisation reversal. It will be also shown that the addition of a Si-Co-Si monolayer prevents this reversal and creates very high spin-polarisation across all interface layers. Finally, both computationally and experimentally by electron microscopy, will be shown that such $CoSi_2$ layers are thermodynamically stable to exist at the interface.

$Co_2FeAl_{0.5}Si_{0.5}$/Ge interface atomic and electronic structure will be studied in the **Chapter 6**. It will be demonstrated that this interface outperforms the interface between a Heusler alloy and Si since it does not form any secondary phases and have minor interfacial intermixing. It will be demonstrated that this minor intermixing in selective, i.e. the outdifussed Ge substitutes Fe-Si/Al in the $Co_2FeAl_{0.5}Si_{0.5}$ (CFAS) film. This minor and selective outdiffusion does not affect the interfacial spin-electronic structure, as shown by the performed calculations. It will be shown that to a good approximation this interface can be modelled with an atomically sharp termination which in turn does not show any significant loss of spin-polarisation. Hence, this heterostructure is an ideal candidate for spin-injection applications.

In **Chapter 7** it will be shown that antiphase boundaries are present in $Co_2FeAl_{0.5}Si_{0.5}$ thin films. Their exact atomic structure will be revealed by electron microscopy and by performing density functional theory calculations it will be shown that these extended structural defects can locally even reverse the sign of the spin-polarisation, hence their presence has to be minimised in order to achieve films with better properties.

In **Chapter 8** a brief summary of the results obtained in the thesis will be given and an outline of future related work will be discussed.

2 Introduction

2.1 Spintronics and its importance

Spintronics is a scientific field that studies spin-based electronics, in which the main functionality emerges from the spin degrees of freedom. The continuous advancement of the conventional electronics has enabled continuous increase of the number of transistors per unit area of an integrated circuit, and for years this dependence has followed the Moore law [2], which states that the transistor density doubles in approximately two years.

However, it is very challenging for such trend to continue unless the 'working mechanism' of the electronic devices is drastically changed. The basic constituents of the integrated circuits e.g. metal oxide semiconductor field effect transistor (MOSFET) will reach the size when further reduction will be practically impossible due to the whole spectra of effects that emerge at nano-level. For example, reducing the thickness of the insulator which is between the metallic gate and the channel, at some point will cause tunnelling of electrons through this layer, hence undesired leakage currents.

In order to overcome these inevitable challenges, fundamentally different approaches are required. Spintronics is a very promising candidate for these purposes. In contrast to the conventional electronics, here the electron spin is the one which carries the information. The spin-based electronics can therefore enable low power and high speed devices. In order to achieve such spin-based devices, several elementary functions have to be included, such as: to be able to generate spin-polarised current, to manipulate/control this spin-polarised current, and to detect it. The first model for such device was the spin field effect transistor (FET), proposed by Datta and Das [3].

The field of spintronics has been revolutionised by the discovery of the giant magnetoresistance (GMR) effect [4, 5] by the groups of A. Fert and P. Grünberg independently, and since then it attracts an enormous interest among scientists. The importance of this discovery has been recognised by the Nobel Prize in Physics, 2007. By

considering Fe/Cr superlattices, it has been demonstrated that such structures (**Figure 2.1**) show a drastic change (by about factor of two [4]) in resistance upon applying external magnetic field. The thin Cr layers antiferomagnetically couple the neighbouring Fe layers [4]. Hence, in absence of an external magnetic field, neighbouring Fe layers have opposite magnetisation directions. The measurements shown in **Figure 2.1b** have demonstrated [4] that without a magnetic field the resistance of such superlattice can be about twice higher than the resistance measured when an in-plane magnetic field is applied. The effect can be explained as following. Electrons in a given Fe layer are spin-polarised with a spin direction determined from the layer magnetisation. Without an external field, they will experience additional resistance on entering the neighbouring Fe layer since it has the opposite magnetisation direction, hence a high resistance state is observed.

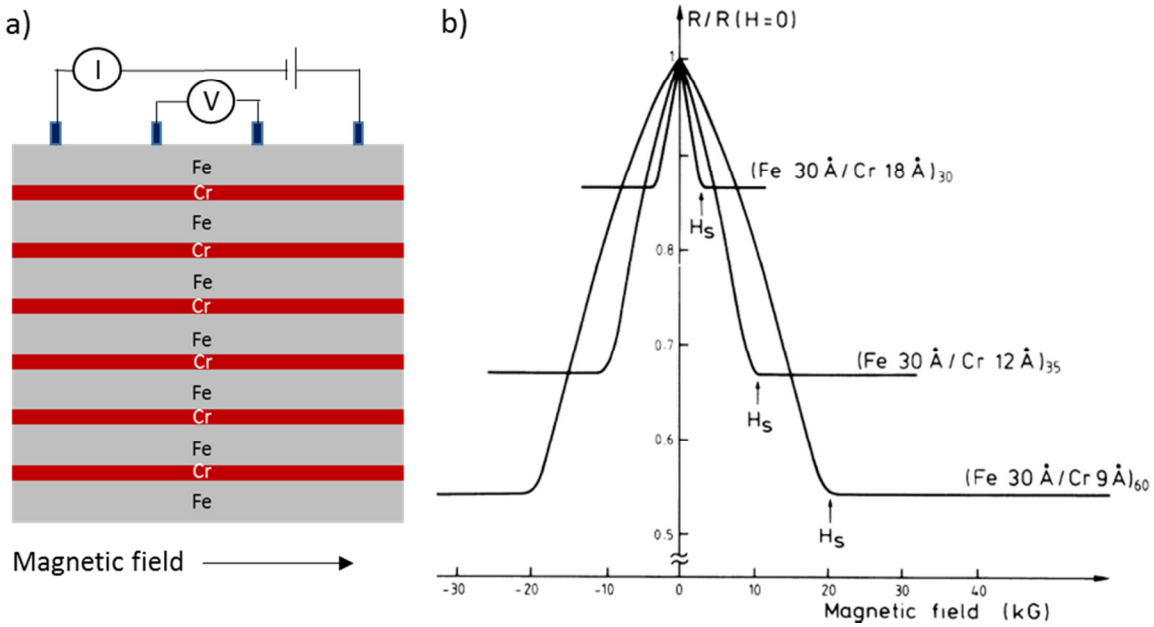

Figure 2.1 a) Schematic of a Fe/Cr superlattice used to demonstrate the GMR effect; b) Figure taken from Ref. [4] showing magnetoresistance measurements for three different samples. The three samples shown in (b) are all Fe/Cr superlattices where the thickness of each Fe and Cr layer is given in the parentheses, while the number of Fe/Cr layers in a given sample is given as a subscript. The superlattice with 60 Fe/Cr layers shows very big resistance change when the magnetic field is applied.

On the other hand, when an in-plane field is applied at given strength, this field switches the oppositely oriented magnetisation and makes Fe layers all with a same magnetisation direction. In such case, the electrons do not experience the additional resistance and travel in the same way in all Fe layers, hence a low resistance state is measured.

The huge potential of this effect was immediately obvious. With simple resistance measurements, we can very efficiently detect binary states (e.g. state up/down; equivalent to state 1/0) of magnetic field orientations. Before this discovery, the anisotropic magnetoresistance (where the resistance of a material depends on the angle between the electric current and the magnetisation direction) has been used as a magnetic field sensor in many applications including read heads in data storage technologies [6]. However, the effect is considerably smaller than the GMR. This has led to the development of GMR-based read head devices which are currently implemented in many data technologies e.g. hard disks in computers. These read heads have enabled much faster readout of information as well as significant decrease in their dimensions.

Typical heterostructures used in GMR-based devices, in addition to the superlattices originally used to demonstrate this effect, are the spin-valves and magnetic tunnelling junctions (MTJs), both schematically shown in **Figure 2.2**. Both of them show high magnetoresistance values; for example, a CoFeB/MgO/CoFeB based MTJ, reported in Ref. [7], shows magnetoresistance (MR) of even $\sim 600\%$ at room temperature and $\sim 1100\%$ at 5 K. Such MR values make these devices outstanding for many applications in magnetoelectronics.

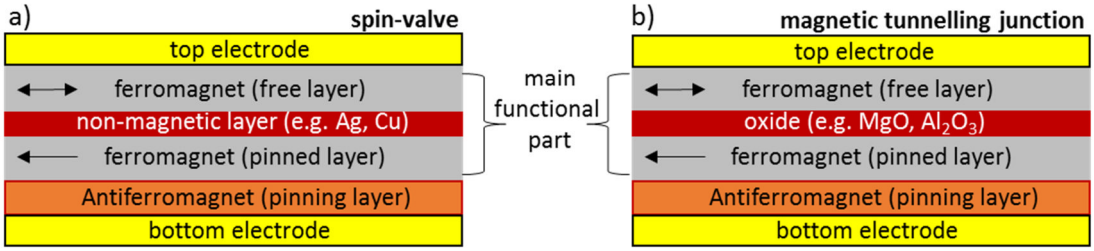

Figure 2.2 Schematic of: a) spin-valve; b) magnetic tunnelling junction [19].

In spin-valves, the functional part consists of two ferromagnetic layers separated by a non-magnetic metallic spacer (for example Ag or Cu). The purpose of the

non-magnetic layer is to separate the ferromagnetic layers and prevent ferromagnetic coupling between them, so that their magnetisations can easily transform from parallel alignment to antiparallel alignment when an external magnetic field is applied. As the **Figure 2.2a** shows, one of the ferromagnetic layers has a pinned magnetisation, i.e. regardless whether a field is applied or not, it has a magnetisation with a certain direction which can be regarded as a fixed at the fields in which the spin-valve operates. Such pinning is done through an antiferromagnetic layer (such as IrMn) [8]. Alternatively, we can use ferromagnets with drastically different coercivities; in this case the layer with high coercivity will have a fixed magnetisation in fields sufficient to change the magnetisation direction of the other electrode (i.e. the free layer). Spin-valves (SV) can operate in two geometries: current-perpendicular-to-plane (CPP) or current-in-plane (CIP). In CPP SV the current flows perpendicular to the thin films layers, while in CIP SV in-plane.

On the other hand, in magnetic tunnelling junctions, the spacer is insulating oxide (e.g. MgO, Al_2O_3). In this case, the current through the heterostructure is not diffusive as in spin-valves but tunnelling since the spacer is an insulator. Detailed treatment shows that bands matching between the electrode and barrier oxide is crucial for efficient spin dependent tunnelling and achieving very high tunnelling magnetoresistance (TMR), as demonstrated in Ref. [9] for the case of Fe/MgO/Fe based MTJ.

A very promising application of MTJs is in spin-transfer-torque magnetoresistive random access memory (STT –MRAM). A spin-polarised current which enters into a ferromagnetic layer can transfer spin-angular momentum to this layer, and for some critical current the transferred spin-torque can switch to opposite the magnetisation orientation of this ferromagnet which acts as a free layer electrode [10]. This mechanism gives the possibility to write digital information by spin current instead of using an external magnetic field, a property highly desirable for applications in novel type universal memories. STT-MRAM is a very promising candidate for this purpose. Unlike dynamical RAM (DRAM) memories which store information in capacitors experiencing low leakage currents and using constant power to refresh the bit state, taking into account the principle of work of STT-MRAM they will need power only during the writing, hence showing superior properties in terms of energy consumption and non-volatility.

2.2 Spin-polarisation and Jullière formula

For both spin-valves and MTJs, the GMR increases with the spin-polarisation of the ferromagnetic electrodes. Spin polarisation (SP) is defined (**Eq. 2.1**) as:

$$SP = \frac{n_\uparrow - n_\downarrow}{n_\uparrow + n_\downarrow} \qquad \textbf{Eq. 2.1}$$

where $n_\uparrow$ and $n_\downarrow$ are the density of states (DOS) for spin-up and spin-down electrons at the Fermi-level. The density of states at the Fermi-level is a very important quantity for materials, since it determines for example whether the studied material is an insulator/semiconductor, or metal. For some materials, such as ferromagnets (e.g. bulk Fe), the DOS for spin-up and spin-down electrons are non-equivalent, such materials are called spin-polarised materials and for them $SP \neq 0$ (**Figure 2.3**). In the limiting case, SP can be ± 1 i.e. $\pm 100\%$ which means that there is a band gap at the Fermi-level for the spin down/up electrons, respectively. Such materials are called half-metals and they are studied in this thesis.

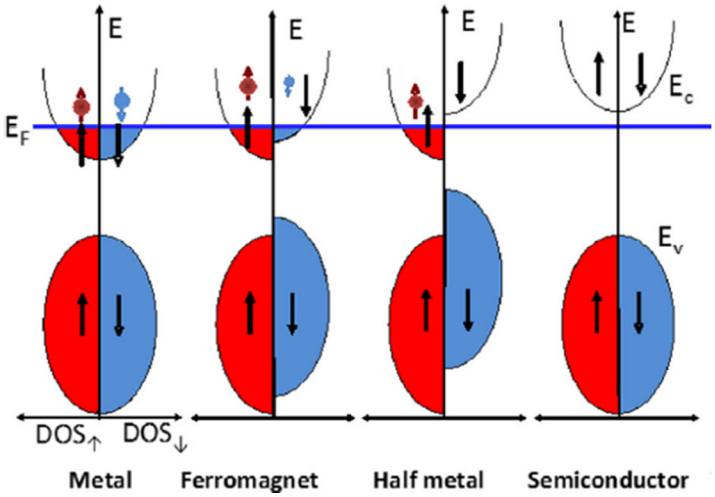

Figure 2.3 Schematic of DOS for metal, ferromagnet, half-metal and semiconductor. Figure taken from Ref. [19].

Using a simple model, Jullière [11] derived the following expressions (**Eq. 2.2**) which correlate GMR with the spin-polarisations of the two electrodes ($SP_{1,2}$):

$$\frac{R_a - R_p}{R_a} = \frac{2(SP_1)(SP_2)}{1 + (SP_1)(SP_2)}; \qquad \textbf{Eq. 2.2}$$

$$GMR = \frac{R_a - R_p}{R_p} = \frac{2(SP_1)(SP_2)}{1 - (SP_1)(SP_2)}$$

where R_a and R_p are the resistance of the GMR device in antiparallel and parallel configuration respectively. These equations show that highest GMR is realised with fully spin-polarised electrodes, as expected. If both electrodes have the same structure, by measuring GMR, the spin-polarisation can be easily calculated. This is a widely used method to indirectly estimate the spin-polarisation of ferromagnetic electrodes [1, 12].

The derivation of these expressions is relatively straightforward. We label the proportion of electrons (at the Fermi-level) with spins oriented along the magnetisation direction as a_1 and a_2 for the first and second ferromagnetic electrode respectively. First, a parallel magnetisation alignment between the two electrodes is considered. The conductivity of the whole device in this case is proportional to:

$$G_p = a_1 a_2 + (1 - a_1)(1 - a_2) \qquad \textbf{Eq. 2.3}$$

The first term gives the contribution from the electrons aligned parallel to the magnetisation. In other words from a_1 spins with this direction in the first electrode, only a fraction a_2 will manage to tunnel into the second electrode since that is the fraction of available states with spins along the same direction. The same applies for the opposite spins, a $(1 - a_2)$ fraction out of the $(1 - a_1)$ fraction in the first electrode will manage to tunnel. These two contribution give the parallel alignment conductivity coefficient G_p.

Similar considerations can be made in the case of opposite alignment. In this case the conductivity is proportional to:

$$G_a = a_1(1 - a_2) + a_2(1 - a_1) \qquad \textbf{Eq. 2.4}$$

Note that $G_p + G_a = 1$. Taking into account the definition of spin-polarisation (**Eq. 2.1**), the fractions a_i can be expressed (**Eq. 2.5**) in term of spin-polarisation:

$$a_i = (1 + SP_i)/2 \qquad \textbf{Eq. 2.5}$$

By substituting these expressions into the **Eq. 2.3** and **Eq. 2.4**, the **Eq. 2.2** can be easily obtained.

Direct measurements of spin-polarisation are very challenging and careful interpretation is required [13]. Point-contact Andreev reflection [14] and spin-resolved photoemission spectroscopy [15, 16] have been used to measure SP for several materials.

We shall note that both techniques are surface sensitive, which has to be taken into account during results interpretation. Although indirect, a very convenient method to reveal the spin-polarisation of materials is by measuring GMR, TMR of the whole device, and then computing SP using the Jullière relation (**Eq. 2.2**). Such analysis is performed quite often in literature, for example in Ref. [17] $\sim 1800\%$ TMR is observed for a $La_{2/3}Sr_{1/3}MnO_3/SrTiO_3/La_{2/3}Sr_{1/3}MnO_3$ MTJ, which is equivalent to a higher than 95% SP of the $La_{2/3}Sr_{1/3}MnO_3$ electrode. Similarly, in [18] spin-polarisation has been estimated using non-local spin-valve measurements.

2.3 Half-metals

From the above discussion it is clear that for any application in spintronics, materials that have as high as possible spin-polarisation are required. Hence, the search for half-metals, which are 100% spin-polarised materials at the Fermi-level, and revealing their atomic structure and functional properties, is of fundamental importance in spintronics.

Density of states for a half-metal are illustrated in **Figure 2.3** and compared with the DOS of metal, ferromagnet and semiconductor. In half-metals, in addition to the non-symmetrical DOS for spin up and spin down observed in ferromagnets, here there is a band gap for one of the channels. This band gap prevents any current flow for the corresponding spin channel.

Among number of predicted halfmetals, the Co-based full Heusler alloys are of special interest. They have very high Curie temperatures (~ 1000 K) - well above the room temperature, low coercivity, and are made of earth-abundant elements (e.g. Co, Fe, Si etc.). Before discussing their atomic and electronic structure as well as functional properties in details, some other known halfmetals are outlined here.

Diluted magnetic semiconductors are semiconductors which are doped with magnetic species. Some of these materials, such as Mn-doped Ge, have been predicted as half-metals [20]. Oxides such as magnetite (Fe_3O_4) or CrO_2 are also predicted theoretically and experimentally as half-metallic [14, 21]. A disadvantage of CrO_2 is that it has a very low Curie temperature (390 K). Although magnetite has a very high Curie temperature similar to that of the Co-based Heusler alloys, there are significant challenges to grow

stoichiometric thin films of magnetite without defects. There are many other forms of iron oxides such as FeO, Fe_2O_3 etc. The phase diagram for this system is very complex and pure magnetite can be grown only in a very narrow region in the phase diagram. Small deviations from ideal growth conditions always lead to variations in stoichiometry. Additional disadvantage is the presence of extended structural defects such as twin defects [22] and antiphase boundaries [23] which have rather low formation energies, hence they are abundant in thin films. In addition, it has been shown that there is an antiferromagnetic coupling at these boundaries that change the film electronic and magnetic structure. These properties make the incorporation of magnetite in spintronic devices extremely challenging.

$La_{0.7}Sr_{0.3}MnO_3$ is in the class of manganese perovskites, and it has been one of the first materials that has been experimentally demonstrated to have halfmetallic properties [24]. We note that these materials have very low Curie temperature making them not suitable for a number of applications [1]. Another class of materials that have been also predicted to be halfmetallic are pnictides such as CrAs [25] and other zinc-blende compounds of transition elements (V, Cr) with As, Sb, Te, Se [26]. The materials mentioned here are pointed out as a representative; further reviews of candidate materials and spintronics in general are given in [1, 27-29].

2.4 Heusler alloys

The first theoretical prediction of half-metallicity of a Heusler alloy was performed by de Groot et al [30]. By using first-principles calculations they showed that the half-Heusler compound NiMnSb is a 100% spin-polarised material. However, it has been demonstrated that this material suffers from Mn-segregation at surfaces/interfaces [31, 32] which in turn significantly reduce its half-metallicity. Devices based on this material have also shown very low GMR [33].

On the other hand, many full Heusler alloys have been successfully implemented in spin-valves or MTJs which show outstanding values of GMR. The very first growth/synthesis and basic characterisation studies on these materials are reported in Ref. [34, 35]. These materials have also attracted theoretical interest and many studies on electronic structure and half-metallicity have been reported [1, 36, 37]. Co-based full

Heusler alloys have been shown to be one of the most promising candidates from this group of materials. Examples of practical implementation in MTJs are given in Ref. [38] and [39] with Co_2FeAl and Co_2MnAl electrodes respectively, with Co_2MnSi electrodes in Ref. [40] and with CFAS electrodes in Ref. [41, 42] which achieve very high TMR. High MR values have been also reported in spin-valves based on Co-based full Heusler alloy electrodes [43, 44]. Significantly better spin-injection efficiency using Co-based Heusler alloys compared to conventional ferromagnetic electrodes in lateral spin-valves is shown in Ref. [45]. Taking into account these big potentials, the studied materials in this thesis are Co-based full Heusler alloys.

2.4.1 Atomic structure

In this section, the detailed atomic structure of Co-based full Heusler alloys will be explained. These materials are of the form Co_2YZ, where *Y* is *d*-block element such as Mn, Fe, while *Z* is a *p*-block element such as Si, Ge, Al etc. Their lattice is cubic, with space group 225 ($Fm\bar{3}m$). The lattice parameter for Co_2FeSi is 5.66 Å; but also the other materials belonging to this group (i.e. Co_2(Mn,Fe)(Si,Al,Ge)) have very similar lattice parameters. As can be seen from their chemical formula, they are intermetallic compounds which include Co. Their lattice can be considered as four interpenetrating face-centred cubic sublattices.

Two of these sublattices are populated by Co atoms, one by atoms of the element *Y*, and the fourth by atoms of the element *Z*. The relative shift vectors between these sublattices with respect to one of the Co-sublattices are given by (in lattice parameter units): 1st Co - (0, 0, 0); 2nd Co - (0.5, 0.5, 0.5), Y element - (0.25, 0.25, 0.25), *Z* element - (0.75, 0.75, 0.75). The two interpenetrating face-centered cubic Co-sublattices can be viewed as a simple cubic Co-sublattice, as illustrated in **Figure 2.4** for the conventional 16 atoms unit cell of Co_2FeSi. Once the atomic structure of one of these materials is known for example that of Co_2FeSi, it is straightforward to construct the structure of for example Co_2MnSi, by simply substituting all Fe atoms with Mn. Similarly, Co_2FeAl can be obtained by substituting all Si from Co_2FeSi with Al.

As discussed below, in some cases, the alloying of two Heusler alloys gives a Heusler alloy with better properties. In this case, two atomic species can occupy the same

sublattice. For example, for the case of CFAS, which is very frequently used in this thesis, the *Z* sublattice is occupied by both Si and Al with an equal concentration. The advantage of this alloy over the ternary Co_2FeSi (CFS) and Co_2FeAl (CFA) is that it has a mid-gap Fermi level [46], hence more robust properties against temperature effects or small strain fields. Another example is $Co_2(Fe,Mn)Si$ (CFMS) where Fe and Mn with an equal concentration share the Y sublattice [47].

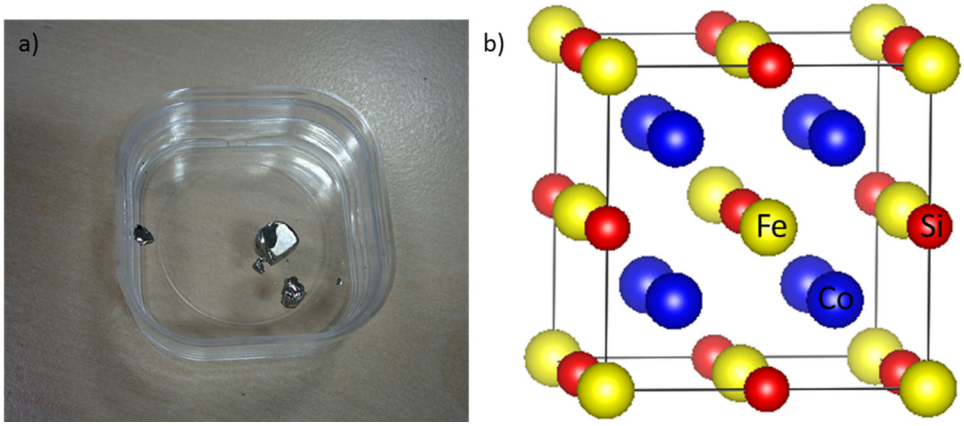

Figure 2.4 a) Bulk CFAS specimen; b) Atomic structure of the conventional 16 atoms cubic unit cell of Co_2FeSi; colour coding: Co - blue, Fe - yellow, Si - red.

It should be noted here that for ternary fully ordered Heusler alloys, the cubic cell shown in **Figure 2.4b** is not the primitive unit cell; it can be reduced to four atoms, two Co, one *Y* and one *Z*, however such cell is non-orthogonal, and not very desirable for modelling purposes.

2.4.2 Atomic plane stacking sequence along the [001] and [111] crystallographic directions

The studied Heusler alloy films in this thesis have been grown along the [111] and [001] crystallographic directions. The growth direction is directly determined from the substrate orientation and the epitaxial relationships between the film and substrate.

The atomic plane stacking sequence along both [111] and [001] directions will be illustrated here on the example of CFS. Along the [001] direction, as can be seen from the **Figure 2.5** there are alternating Co-(Fe/Si) atomic planes. Four such planes are required to

get the repeat unit (Co-Fe/Si-Co-Fe/Si) along this direction. On **Figure 2.5a** the [001] stacking is shown as seen along the [100] projection, while in **Figure 2.5b** along the $[1\bar{1}0]$ projection. Along the $[1\bar{1}0]$ projection, these materials contain atomic columns which consist of only one element. In other words, one atomic column is fully occupied by Co, other one with Si, some other with Fe. This property is particularly useful when performing *Z*-contrast (HAADF STEM) electron microscopy imaging (which is discussed in **Chapter 3**) since in many cases a straightforward compositional identification can be made based on such images. For this reason, the specimens in this thesis are prepared so that they are along such zone axis when analysed with an electron microscope.

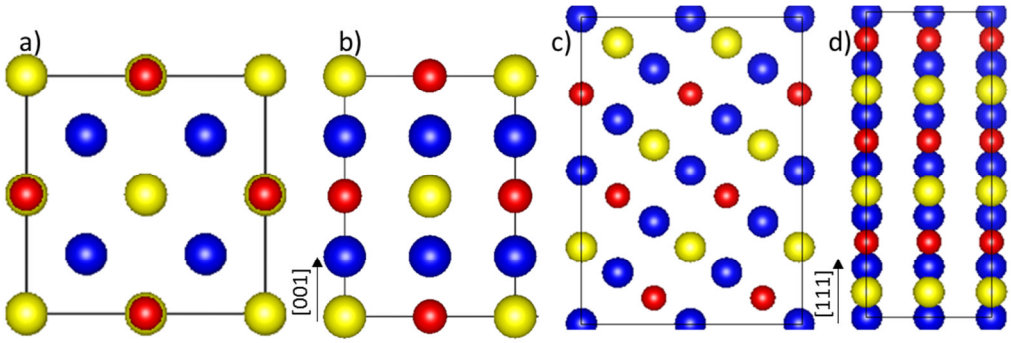

Figure 2.5 Repeat unit of CFS: a) along the [001] growth direction (the vertical direction in this figure) and [100] projection; b) along the [001] growth direction and $[1\bar{1}0]$ projection; c) along the [111] growth direction and $[1\bar{1}0]$ projection; d) along the [111] growth direction and $[11\bar{2}]$ projection. Colour coding follows the **Figure 2.4b**.

Along the [111] crystallographic directions the stacking sequence is different. It consists of …Co-Fe-Co-Si… stacking. In total twelve atomic planes are required to get a repeat unit along this direction. The lattice parameter along the [111] direction is $\sqrt{3}a$, where a is the lattice parameter of the conventional cubic cell. $[11\bar{2}]$ and $[1\bar{1}0]$ are orthogonal to the [111] crystallographic direction, and both of them are convenient for electron microscopy for the same reasons as discussed above. The atomic structure in these projections is shown in **Figure 2.5c,d**. It can be seen that along the $[11\bar{2}]$ projection, the lattice is much closer packed, hence although $[11\bar{2}]$ contains columns with single elements is less desirable than the $[1\bar{1}0]$ direction, in which the atomic columns are more separated and therefore can be better resolved by electron microscopy.

2.4.3 Origin of the band gap in the full Heusler alloys

In this section, a more detailed understanding of the minority (spin-down electrons) band gap formation will be provided. The theory of the origin of band gap in full Heusler alloys, as discussed here, has been developed by Galanakis et al. [37]. As an example, the Co_2MnZ will be analysed, however the same considerations can be easily generalised to the other Heusler alloys belonging to this class.

It has been observed that for these compounds, their magnetic moment (M) per formula unit is directly correlated (**Eq. 2.6**) with the number of valence electrons (V) via the relation:

$$M = V - 24 \qquad \textbf{Eq. 2.6}$$

First-principles calculations as well as measurements have shown that Co_2MnAl and Co_2MnGa have moment of $4\ \mu_B$, Co_2MnSi and Co_2MnGe moment of $5\ \mu_B$, and $6\ \mu_B$ per formula unit for Co_2FeSi (**Table 2.1**). All of these compounds, taking into account their number of valence electrons satisfy the rule stated above. This is so called Slater-Pauling behaviour which is also observed for the halfmetallic half-Heusler alloys, though the exact relationship contains different free term (18 instead of 24) [37].

material	*V*/form. unit	M (μ_B/ form. unit)
Co_2MnSi	29	5.0
$Co_2(Fe,Mn)Si$	29.5	5.5
$Co_2Fe(Al,Si)$	29.5	5.5
Co_2FeSi	30	6.0

Table 2.1 Number of valence electrons and magnetic moment per formula unit (computed by density functional theory calculations) for full Heusler alloys which will be most frequently used in this thesis. It can be noticed that the alloyed CFMS and CFAS also follow the Slater-Pauling behaviour, as expected.

Such behaviour suggests that the number of valence electrons in a spin-down state is fixed for all these materials within the given class (e.g. full Heusler alloys). An additional valence electron always goes to the spin-up state. If we assume that the number of valence electrons is 24 - then the magnetic moment is zero according to the **Eq. 2.6**, hence there are an equal number of spin-up and spin-down electrons. This

means that there are 12 electrons in spin-down state and this number is fixed among the considered Co-based full Heusler alloys.

If the material has for example 28 electrons, 12 spin-up electrons compensate the 12 spin-down electrons and the remaining 4 will be in a spin-up state resulting in a total magnetic moment of $4\ \mu_B$. This Slater-Pauling behaviour fits very well with the presence of a band gap for the minority (spin-down) electrons; 12 bands are fully occupied so they do not cross the Fermi-level, hence a band-gap emerges.

For Co_2MnZ there are four atoms per formula unit; two Co, one Mn and one *Z* such as Si, Al, Ge. Co and Mn are *d*-block elements while *Z* is a *p*-block element. For the element *Z* there are only *s* and *p* occupied bands. One of these is an *s*-band while three are *p*-bands. In total, these bands can accommodate 8 electrons. But the *Z* atoms may have for example 3 (e.g. when *Z* = Al) or 4 (e.g. when Z = Si, Ge) valence electrons.

By plotting the band structure it has been obtained [37] that all these four bands belonging to the *Z* element are not only below the Fermi-level but also below the *d*-bands of Mn, Co. Hence the *s*, *p* bands should be fully occupied i.e. in total 8 electrons are accommodated in them. The additional number of valence electrons required to fully fill these *s, p* bands comes from the *d*-electrons of Co and Mn.

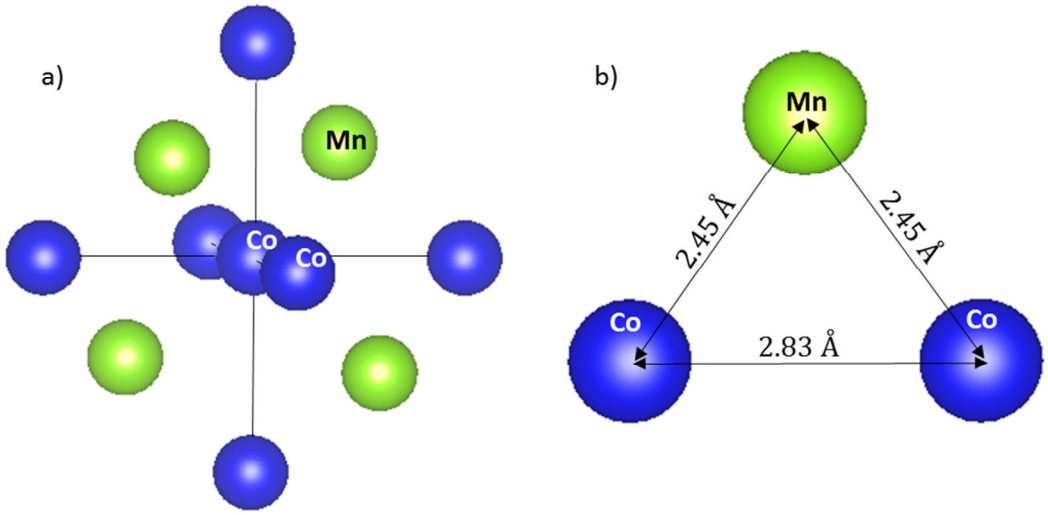

Figure 2.6 a) Visualisation of the six Co first nearest neighbours and four Mn second nearest neighbours to a Co atom in Co_2MnSi (CMS); b) Interatomic distances between nearest Co-Mn and Co-Co pairs.

In other words, when *Z* = Si, 4 electrons from Si and 4 from Co and Mn provide the 8 electrons occupying these *s, p* bands. Therefore, the number of *d*-electrons is effectively reduced ultimately affecting the magnetic moment of the compound which is determined by the number of uncompensated *d*-electrons [37]. This gives the possibility to effectively tailor their magnetic moment by choosing an appropriate valence of the *Z* element.

The *d*-bands are the ones which are closest to the Fermi-level. Due to the presence of a band gap for the minority spin, some of the spin-down bands are fully occupied by electrons while some are entirely empty. Below, we discuss how many of the *d*-bands are occupied in these materials and what determines the width of the minority band gap.

As can be concluded from **Figure 2.6** each Co atoms has 8 nearest neighbours which 4 of them are Mn and four Z element. The interatomic distance to these first nearest neighbours is 2.45 Å. The next nearest neighbours are 6 Co atoms to which the interatomic distance is 2.83 Å, hence comparable to Co-Mn distances. One atom from the pair Co-Co nearest neighbours belongs to one Co-sublattice, while the other one to the other Co sublattice. Hence, such interactions are typical for the full Heusler alloys and absent for the half-Heusler alloys for which one of the Co sublattice is empty. Although these Co-Co interactions are second nearest neighbours hence weaker than the Mn-Co interactions, they are very important in determining the width of the minority band gap, as discussed below.

The *d*-bands from one Co atom hybridise with the *d*-bands from the other Co atom (its nearest neighbour, belonging to the other Co-sublattice), and also with the *d*-bands of the nearest Mn atom [37]. Before going further and analyse this hybridisation, it should be noted that there are five types *d*-orbitals labelled as: d_{xy}, d_{xz}, d_{yz}, $d_{x^2-y^2}$, and $d_{3z^2-r^2}$; for simplicity we will label them as $d_1, d_2 \dots d_5$, respectively. The first three orbitals: d_1, d_2 and d_3 have the same symmetries, while d_4 and d_5 also have the same symmetries but different than those of the first three orbitals. The symmetry relations are important and determine the hybridisation; *d*-orbitals with same symmetries are allowed to hybridise [37], but they cannot hybridize with the *d*-orbitals with the other type symmetry.

First, the Co-Co hybridisation will be analysed. In **Figure 2.7a**, the two Co atoms from a Co-Co nearest neighbour interaction pair are shown together with their *d*-states. Due to the difference in symmetry the *d*-states slightly split in energy in two levels. One level is triple degenerate, while the other one is double degenerate. The triple degenerate *d*-states d_1, d_2 and d_3 can only hybridise with their counterparts (d_1, d_2 and d_3) from the other Co atom. These six orbitals after the hybridisation give six hybridised states; triple degenerated bonding orbital t_{2g} (the symbol reflects the symmetries of these orbitals) and triple degenerated antibonding orbital t_{1u}, which is higher in energy. On the other hand, the d_4 and d_5 orbitals from the Co-Co pair give double degenerated e_g bonding and double degenerated antibonding e_u orbital. This Co-Co hybridisation is schematically illustrated in **Figure 2.7a**. The factors in front of the orbital labels, refer to the degeneracy, for example '*2 x* e_g' means two e_g orbitals with the same energy.

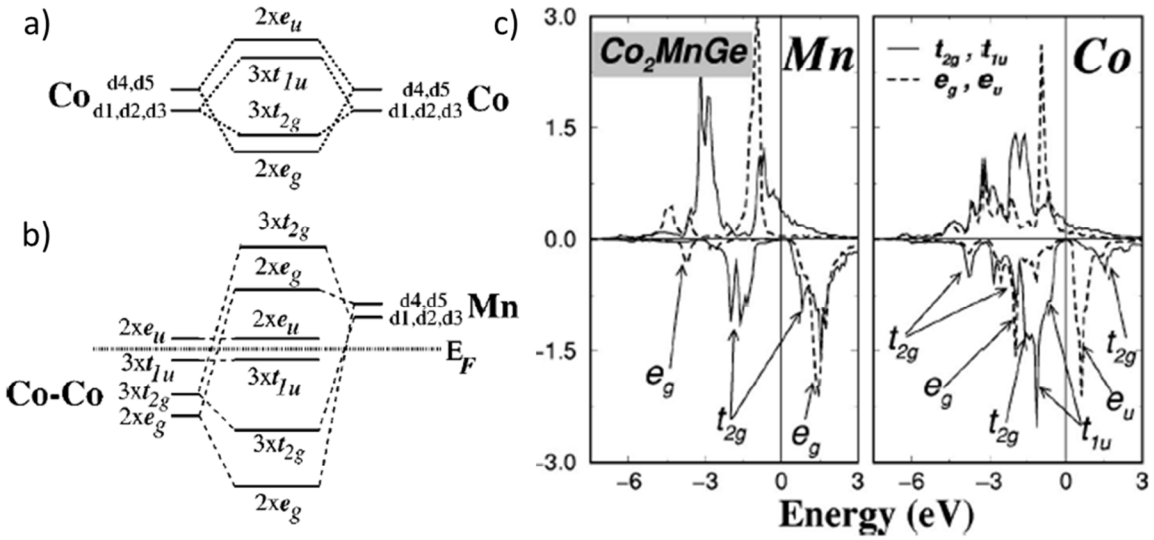

Figure 2.7 Band gap analysis on the example of Co_2MnGe. a) Schematic of Co-Co hybridisation; b) Schematic of hybridisation between the Co-Co and Mn states. The dashed line outlines the position of the Fermi-level; c) Density of states projected on e_g, e_u and t_{2g}, t_{1u} for both Mn and Co atom. The partial density of states (PDOS) plots in c) are for the Co_2MnGe Heusler alloy [37].

Now, these Co-Co orbitals hybridise with the *d*-orbitals of Mn, as illustrated in **Figure 2.7b**. The two e_g orbitals of Co-Co hybridise only with the d_4 and d_5 of Mn since they are of the same symmetry. After this hybridisation, two bonding and two

antibonding e_g states emerge. The antibonding states are well above the Fermi-level, hence unoccupied. Taking into account same symmetry arguments as above, the three t_{2g} Co-Co orbitals hybridise with the three d_1, d_2 and d_3 of Mn leading to three bonding and three antibonding t_{2g} orbitals, where the antibonding orbitals are again above the Fermi-level.

The remaining five Co-Co orbitals, two of which with e_u symmetry and three with t_{1u}, have different symmetries than those of Mn *d*-orbitals, hence a hybridisation is not possible. Therefore, 5 out of total 15 are Co-Co hybrid orbitals, while the others 10 have emerged from Co-Co-Mn hybridisation, **Figure 2.7b**.

First-principles calculations [37] have shown that the Fermi-level is positioned between the Co-Co states that do not bond with Mn, as shown in **Figure 2.7b**. In **Figure 2.7c** the projected spin-polarised density of states are shown again on the example of Co_2MnGe. First that can be noticed is that the states which have projections on the Mn orbitals lead to much wider minority band gap, compared to that of Co.

Before discussing the hybridisation, it was mentioned that Co-Co bonding is much weaker since these atoms are second nearest in comparison to Mn-Co which are nearest neighbours. Due to the weak bonding, the splitting between the Co-Co states is small, they are very close each other, and are located in between the Mn-Co hybridised orbitals. This causes the small band gap when projecting on Co, compared to Mn. As seen in **Figure 2.7c**, there are two distinctive peaks in the Co minority states near the Fermi-level, both positioned where the Mn-projected states have a band gap. These are the Co-Co hybridised orbitals; it can be seen that one peak is below the Fermi-level (these are due to the t_{1u} orbitals), while the other one above the Fermi-level (from the e_u orbitals). These Co-Co orbitals reduce the width of the band gap for the full Heusler alloys; in half-Heusler alloys such Co-Co bonding does not exist (since only one Co sublattice is occupied, the other one is empty), hence larger minority band gap is in principle to be expected.

Therefore, the analysis performed above demonstrated that for the considered full Heusler alloys, eight minority *d*-bands are populated, and seven are empty. In addition to the one *s* and three *p*-bands from the *Z*-element, that gives in total 12 fully occupied spin-down bands per formula unit.

This result is fully consistent with the Slater-Pauling behaviour which taking into account that the free term is 24, implies 12 fully occupied minority bands. By increasing the number of valence electrons, the number of populated majority *d*-states increases which in turn leads to higher magnetic moment, **Table 2.1**. In the limiting case, when all majority *d*-states would be completely filled, the magnetic moment per formula unit would reach the value of $7\,\mu_B$, since 7 minority *d*-bands will be empty and uncompensated.

2.4.4 Total density of states and the importance of alloying for the Fermi-level position

In this section, the total spin-polarised density of states is presented for bulk CFAS, the Co-based full Heusler alloy which is most frequently used in this thesis. In **Figure 2.8** the DOS are shown for the Heusler alloys CFA, CFAS and CFS. It can be noticed that all three of them are half-metallic with minority spin band gap of order of 1 eV.

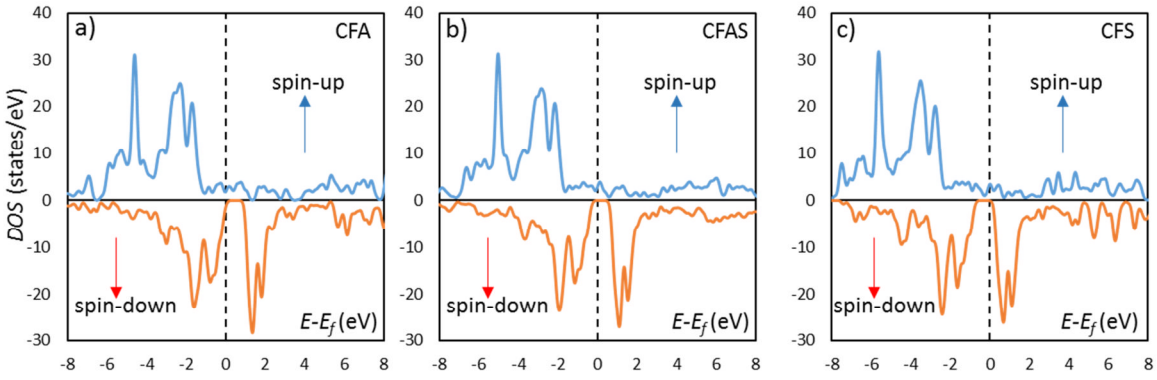

Figure 2.8 Total spin-polarised density of states for bulk: a) CFA; b) CFAS and c) CFS. Spin-up/down states are plotted in the top/bottom part of the figures, respectively. Details of these calculations are given in **Chapter 3**.

Figure 2.8 shows that both CFA and CFS have Fermi-level positioned very close to either the top of the valence band or the bottom of the conduction band, respectively. Although the spin-polarisation is still 100%, they are expected to suffer a loss in spin-polarisation as the temperature increases. In other words, any small thermal activities will effectively introduce (i.e. broaden) some density of states near the boundaries of the band-gap, hence for such Fermi-level positions that can affect the

half-metallicity. It has to be mentioned that not only temperature can affect their half-metallicity but also due to their Fermi-level position they are expected to be very sensitive, in terms of half-metallicity, to any other small variations for example structural due to strain. This has been also experimentally verified where they have been used as electrodes in MTJs reaching significantly lower TMR compared to the ones with CFAS electrodes [46, 48].

The positions of the Fermi-level in CFA and CFS (**Figure 2.8**) suggests that the alloying i.e. creating a Heusler alloy where the *Z* sublattice is populated by an equal amount of Si and Al, will position the Fermi-level close to the middle of the minority spin band-gap. The spin-polarised DOS shown in **Figure 2.8b** for bulk CFAS confirm this initial hypothesis [46].

In Ref. [46], the existence of the minority band gap in CFAS has been experimentally confirmed by measuring the differential conductance of MTJ with a CFAS electrode. Even at room temperature, the spin-polarisation has been demonstrated that is above 90%. In addition, this desirable Fermi-level position makes CFAS to have the weakest temperature dependence among the other full Heusler alloys, which is a big advantage for practical implementation in a real spintronic device. Due to the huge potentials of CFAS, it is the most frequently studied material in this thesis.

2.4.5 Factors that can affect the Heusler alloys half-metallicity: ordering, strain, point defects

The previous sections focused on the Heusler alloys structure and functional properties in the bulk. The implementation of the Heusler alloys in a real device requires thin film deposition, which in turn requires control of stoichiometry and structural/chemical ordering on an atomic level. One of the most common defects in these materials is the chemical disorder; for example Co atoms might populate some of the Fe lattice sites and vice versa.

These phenomena in turn can lead to decreased, completely destroyed or even reversed spin-polarisation. Similar behaviour can arise due to presence of strain in these structures. When these films are grown they have epitaxial relationship with the substrate/neighbouring layer. As those two lattices are lattice mismatched, there is a

strain emerging at the interface. Such strain is usually relieved away from the interface through the formation of misfit dislocations. Another very important factor is the atomic structure of the interfaces. The interfacial bonding can lead to opposite spin-states which affect the device performance, as discussed later.

In Ref. [47], the influence of atomic disorder on the half-metallicity has been studied on the example of the full Heusler alloy $Co_2Fe_xMn_{1-x}Si$. If we label the Co lattice as *X*, (Mn,Fe) as *Y* and Si as *Z*, there are XY, XZ and YZ possible atomic swaps that can occur as illustrated in the **Figure 2.9**. It has been shown that a high spin-polarisation remains preserved when there is a YZ disorder. On the other hand, disorder related to the X-sublattice can be very detrimental to the spin-polarisation, for both XY and XZ type disorder in the best case the spin-polarisation is drastically reduced, but it can be also even reversed [49].

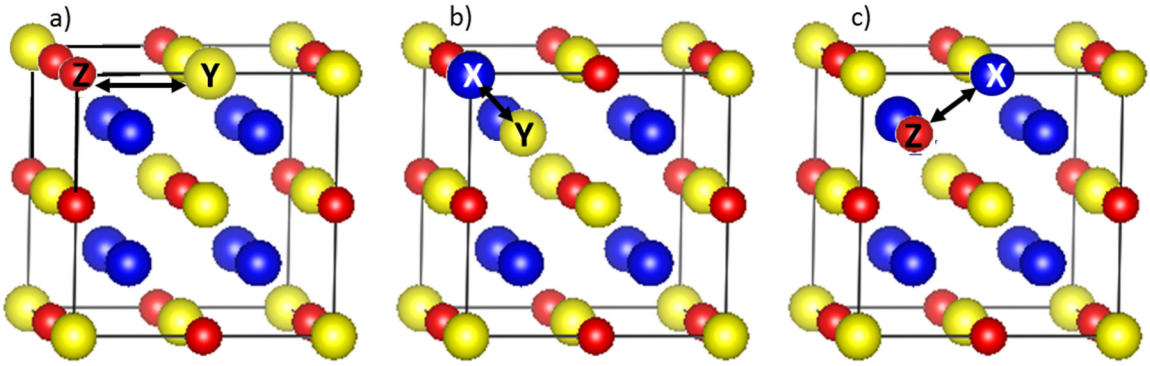

Figure 2.9 Possible atomic swaps in a Co-based full Heusler alloy: a) YZ disorder; b) YX disorder; c) XZ disorder.

However, the same calculations have shown that the Co-sublattice is much more resistant to a disorder compared to *Y* and *Z*. In other words, YZ is the dominant type disorder. These results show that the disorder can affect the half-metallicity but for relatively good films only YZ disorder can be expected (which can also be avoided by proper annealing) which in turn does not change their properties.

The lowest energy configuration for the studied full Heusler alloys is the $L2_1$, where Co atoms occupy two face-centred cubic sublattices, *Y* one, and the fourth occupied by *Z* element, as described in above sections. Very frequently however, the

grown films have *B2* ordering, where a full intermixing between the atoms on *Y* and *Z* sublattice is present. Films that have a *B2* phase can be converted to $L2_1$, by appropriate annealing at around 500 °C [50]. It has been verified experimentally that this phase has also half-metallic property [46]. Also, the half-metallicity of the *B2* phase of CFMS has been theoretically demonstrated in Ref. [51]. Furthermore, the calculations performed in **Section 5.4** on the example of CFAS also demonstrate the half-metallic character of the *B2* phase, and the unaltered magnetic moment per formula unit compared to the $L2_1$ ordering. Hence, both $L2_1$ and *B2* ordering are desirable for spintronic applications.

The influence of point defects [52, 53] as well as variations from stoichiometry [54, 55] has been also intensively studied. Regarding the strain effects, as discussed in the beginning of this section, large positive or negative strain can drastically affect the film's spin-polarisation. For example, in Ref. [56] it has been shown on the example of CFMS that under compression (negative strain) the spin-polarisation decreases and at -10% strain the material loses completely its spin-polarisation. Further compressive strain even reverses the spin-polarisation. Effects are similar for a positive strain but in this case the spin-polarisation is lost at 5% strain.

2.5 Interfaces

Spintronic devices consist of several layers of thin films. Even though the goal in most of the cases is to have structurally/chemically sharp interfaces between the layers, number of grown heterostructures have a very broad (order of nm) interfaces. For some heterostructures with special care a sharp transitions between the layers can be achieved. In these interfacial regions the behaviour can be significantly different compared to that in the bulk-like part of the layers. The atomic structure can be drastically altered which leads to different functional properties. But also, even for atomically sharp interfaces (as shown in the following chapters) the interfacial bonding can itself cause undesirable effects for the spintronic device.

For all heterostructures studied in this thesis, there is an epitaxial relationship between the Heusler film(s) and the layer(s) which are its nearest neighbours. Both the Heusler and the nearest layers are crystalline and they either have very similar lattice parameters (for example a Heusler alloy with Si, Ge) or the lattice parameters along

different directions are similar in value (for example Heusler alloy with Ag), which promotes the epitaxial crystallographic orientation between these layers.

For the case of a Heusler alloy on Si and Ge, as studied in **Chapter 5** and **Chapter 6**, both Si and Ge are [111] oriented and due to the lattice match with the Heusler alloy, the half-metallic CFAS film becomes oriented along the same [111] direction. In contrast, for the CMS/Ag interfaces presented in **Chapter 4**, there is an in-plane 45^{o} rotation between the Heusler alloy and Ag spacer. Their lattice parameters are $\sim$5.65 Å (for CMS) and $\sim$4.09 Å, respectively; the in-plane rotation will transform the Heusler lattice parameter to 5.65 Å/$\sqrt{2}$ (= 4.00 Å) and almost match with that of Ag (4.09 Å). Hence, for this heterostructure, the Ag [100] direction is parallel to the [110] of the Heusler alloy. The understanding of these epitaxial relationships is very important since many of their properties significantly depend on the orientations of the thin films.

2.5.1 Injection of a spin-polarised current across interfaces

As outlined previously, since the proposal of the spin-transistor model [3], it has been clear that both the spin-injection from a spin-polarised source into e.g. semiconductor and the spin manipulation during the transport in the semiconductor play a fundamental role for the hybrid spintronic devices. For these devices, it is crucial that the injected electrons travel long distances in the semiconductor before they are spin-depolarised. It has been already experimentally demonstrated that in semiconductors the spin diffusion length (the distance along which the electron current keeps its spin-polarisation) is very large (e.g. $\sim$4 μm for GaAs [57] and for Si it is even larger ~ 350 μm [58]).

Since the spin diffusion length is rather large, the main challenge is the injection of a spin-polarised current into the semiconductor. Conventional ferromagnetic materials such as Fe have relatively good spin-polarisation, however, devices that involved such ferromagnets as a spin source and semiconductor as a channel have not demonstrated any considerable spin-injection (at most few percent spin-polarisation of the injected current [59]).

The electric type spin-injection therefore has been a rather elusive goal. The experiments for spin-transport in semiconductors have been mainly based on an optical

spin-injection instead. In those devices, a circularly polarised laser pulse creates electron-hole pairs with preferential spin-direction, due to the circular polarisation of the incoming radiation [57]. These generated spin-polarised electrons are then traveling through the semiconductor and finally are captured by a quantum-well, where they recombine which results in emission of a polarised light. The high circular polarisation of the emitted light demonstrates that the spin generation is successful but also that the spin diffusion length in some semiconductors is relatively large.

For any large scale practical implementation, however an electrical injection of spin-polarised current is required. The very low spin injection from standard ferromagnets suggests that there has to be a fundamental issue that makes the current from spin-polarised in the ferromagnet to basically unpolarised in the semiconductor even though the length of the semiconductor is chosen smaller than the spin diffusion length. In Ref. [59] this fundamental obstacle has been addressed. It has been found that the conductivity mismatch that exists between the ferromagnet and semiconductor prevents an efficient spin-injection. In Ref. [60, 61] possible solutions to this issue are discussed.

Here, it will be briefly explained why the conductivity mismatch prevents efficient spin-injection, following the discussion in Ref. [60]. Consider an interface between a ferromagnet and semiconductor where the interface plane is the plane $z = 0$, and the current flows perpendicular to this interface plane. We also assume for simplicity that both the ferromagnet and semiconductor are semi-infinite and they terminate at the interface.

The resistivities of the spin-up and spin-down channels in the ferromagnet can be written as:

$$\rho_{\uparrow(\downarrow)} = 2[1 - (\pm\beta)]\rho_F^* \qquad \textbf{Eq. 2.7}$$

where $[1 - \beta^2]\rho_F^*$ is the total resistivity (both channels) of the ferromagnet. It is straightforward to show that β is the spin-polarisation of the ferrromagnet at the Fermi-level, since for the conductivities from **Eq. 2.7** we obtain $\sigma_{\uparrow(\downarrow)} = \sigma n_{\uparrow(\downarrow)}/(n_\uparrow + n_\downarrow)$, as expected; σ is the total conductivity of the ferromagnet. Both spin channels are treated as independent, hence the total resistance can be computed as a resistance of

two (spin-up and spin-down) resistors connected in parallel. Similarly, for the non-magnetic semiconductor:

$$\rho_{\uparrow(\downarrow)} = 2\rho_N^* \qquad \textbf{Eq. 2.8}$$

since $\beta = 0$ for the semiconductor.

At each position of this heterostructure, the following equations [60] are valid:

$$J_{\uparrow(\downarrow)} = \frac{1}{e\rho_{\uparrow(\downarrow)}}\frac{\partial \mu_{\uparrow(\downarrow)}}{\partial z} \qquad \textbf{Eq. 2.9}$$

$$J = J_\uparrow + J_\downarrow \qquad \textbf{Eq. 2.10}$$

$$\frac{\partial^2(\mu_\uparrow - \mu_\downarrow)}{\partial z^2} = \frac{(\mu_\uparrow - \mu_\downarrow)}{l_s^2} \qquad \textbf{Eq. 2.11}$$

where $J_{\uparrow(\downarrow)}$ and $\mu_{\uparrow(\downarrow)}$ are the current densities and electrochemical potentials respectively; e - the charge of electron, J is the total current, while l_s is the spin diffusion length. The **Eq. 2.11** is a diffusion equation for the difference of electrochemical potentials between the spin-up and spin-down electrons and describes the spin flipping processes which occur with a characteristic spin diffusion length l_s. For ferromagnets, this length is small e.g. 59 nm for Co [60]; for non-magnetic metals is much larger, for example for Cu is 1 μm; for some semiconductors as stated previously it can be very large.

The coupled **Eq. 2.9**, **Eq. 2.10** and **Eq. 2.11**, are relatively straightforward to be solved; the full solutions are given in Ref. [60]. Here the procedure will be briefly explained. If we consider a region far away from the interface, then the electrochemical potential should be a linear function of the distance *z*. This holds both in the ferromagnet and semiconductor. The requirement of linearity is due to the constant currents away from the interface. Also, the electrochemical potential should be the same for spin-down as it is for spin-up electrons. If this is not the case from **Eq. 2.11**, we would have spin-flips until both electrochemical potentials become equal.

On the other hand, at the interface region there should be spin-flips occurring. This is because the current from spin-polarised has to become depolarised far from the interface. How large is the region in which the depolarisation occurs, will be considered later. First, taking into account that there are spin-flips around extended interface region, we can state that there is a non-zero solution to the **Eq. 2.11**. It can be easily seen that the decaying solutions of the **Eq. 2.11** are exponentially decaying functions, with

parameters l_s which are different on both sides of the interface. Taking into account the previous discussion (on the difference in l_s), the decay is faster in the ferromagnet compared to the semiconductor.

Since all three equations are linear the full solutions for $\mu_{\uparrow(\downarrow)}$ and $J_{\uparrow(\downarrow)}$ are linear combination of the linear bulk-like terms and the exponentially decaying terms which emerge due to the spin-flipping at the interface. The unknown constants in this linear combination (the full solutions are given in Ref. [60]) can be found by using the boundary conditions discussed above (far away from the interface a recovery towards the bulk properties) as well as the continuity of both $\mu_{\uparrow(\downarrow)}$ and $J_{\uparrow(\downarrow)}$ at the interface.

Once the constants are determined, we can compute the spin-polarisation of the current at each position along the heterostructure. It is of particular interest to determine this quantity exactly at the interface plane. It can be shown [60], that the spin-polarisation at the interface is given by:

$$(SP)_I = \frac{\beta}{1 + \frac{r_N}{r_F}} \qquad \textbf{Eq. 2.12}$$

where

$$r_{F,N} = \rho^*_{F,N}\, l_s^{F,N} \qquad \textbf{Eq. 2.13}$$

is the product of the resistivity with the spin diffusion length for both ferromagnet and semiconductor/non-magnetic metal. For example, in the case of interface between Co as a ferromagnetic electrode and Cu as a non-magnetic metal the ratio $\frac{r_N}{r_F}$ is slightly bigger than one, hence the spin-polarisation of the current is reduced for more than twice at the interface plane.

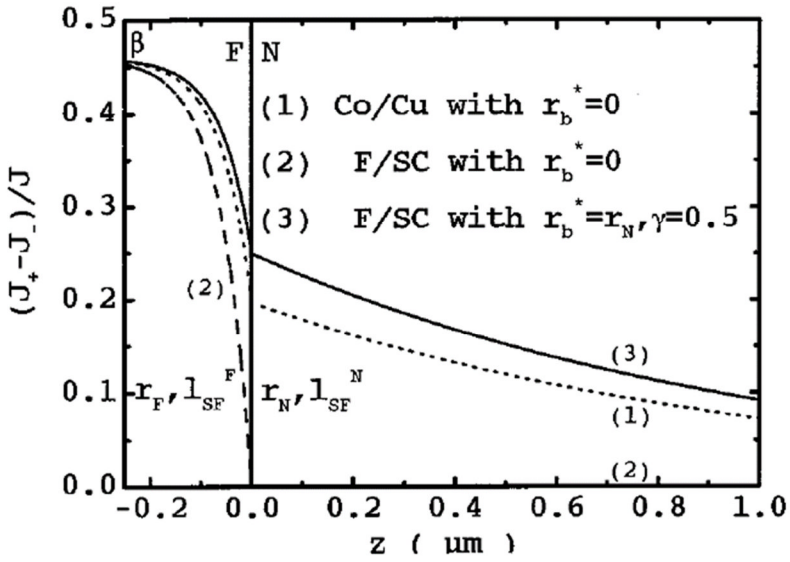

Figure 2.10 Spin-polarisation of the current is plotted as a function of the distance z. Curve (1) is for Co/Cu interface, curve (2) for Co/semiconductor (parameters of the semiconductor are given in [60]) and curve (3) is for a Co/semiconductor interface with additional interfacial resistance. Figure taken from Ref. [60].

The situation is drastically more dramatic for the case of transport across a ferromagnet/semiconductor interface where the $\frac{r_N}{r_F}$ ratio is extremely high (e.g. 10^6 for an interface between ferromagnet such as Co, and GaAs as a semiconductor). By substituting the value of this ratio in **Eq. 2.12**, we find that the current is practically completely depolarised before it enters into the semiconductor. This conductivity/resistivity mismatch is the reason that prevents a spin injection into the semiconductor.

Curve (2) in **Figure 2.10** shows the dependence of the current spin-polarisation across a ferromagnet/semiconductor interface. The complete depolarisation occurs in the ferromagnet as mentioned previously.

From **Eq. 2.9**, **Eq. 2.10** and **Eq. 2.11**, it can be easily shown that:

$$\frac{\partial}{\partial z}[J_\uparrow - J_\downarrow] = \frac{1}{2e r_{F,N}} \frac{(\mu_\uparrow - \mu_\downarrow)}{l_s^{F,N}} \qquad \textbf{Eq. 2.14}$$

which holds for both ferromagnet and semiconductor, by replacing the values of $r_{F,N}$ and $l_s^{F,N}$ for each material, respectively. Taking into account the previous discussion:

$$(\mu_\uparrow - \mu_\downarrow) = (\mu_\uparrow - \mu_\downarrow)_I \exp(\pm z/l_s^{F,N}) \qquad \textbf{Eq. 2.15}$$

$(\mu_\uparrow - \mu_\downarrow)_I$ is the difference of electrochemical potentials calculated at the interface plane. The sign $\pm$ depends on which part of the heterstructure is considered, and is to ensure a decaying electrochemical potential difference at $\mp\infty$, respectively. In the positive part of the z axis is the semiconductor, while in the negative part is the ferromagnet. Substituting the **Eq. 2.15** into **Eq. 2.14** and integrating from 0 to $+\infty$ for the semiconductor and from $-\infty$ to 0 for the ferromagnet we obtain:

$$\Delta[J_\uparrow - J_\downarrow]_{F,N} = \frac{1}{2er_{F,N}}(\mu_\uparrow - \mu_\downarrow)_I \qquad \textbf{Eq. 2.16}$$

The left part of this equation is proportional to the number of spin flips in both ferromagnet and semiconductor separately. From this equation follows that the number of spin-flips is proportional to $\frac{1}{r_{F,N}}$. Taking into account that $r_N \gg r_F$:

$$\Delta[J_\uparrow - J_\downarrow]_F \gg \Delta[J_\uparrow - J_\downarrow]_N \qquad \textbf{Eq. 2.17}$$

Hence, this expression shows that the number of spin flips in the ferromagnet is much bigger than that in the semiconductor, i.e. the current depolarisation occurs near the interface but in the ferromagnetic part, preventing any spin-injection into the semiconductor.

One way to overcome this issue is adding a thin insulating barrier which will act as an additional spin-dependent resistance [60] at the interface. Such spin-dependent resistance will create a discontinuity of the electrochemical potential difference (between spin-up and spin-down) at the interface. This in turn will make a balance between the spin flips, so that a comparable number of spin-flips occur in the semiconductor and ferromagnet. Curve (3) in **Figure 2.10** shows the current spin-polarisation dependence as a function of distance when such interface resistance is present (details of this approach are given in [60]). Such resistance can be provided for example by using a thin Al_2O_3 layer where the spin asymmetry of the interfacial resistance reaches value of 0.5 [60].

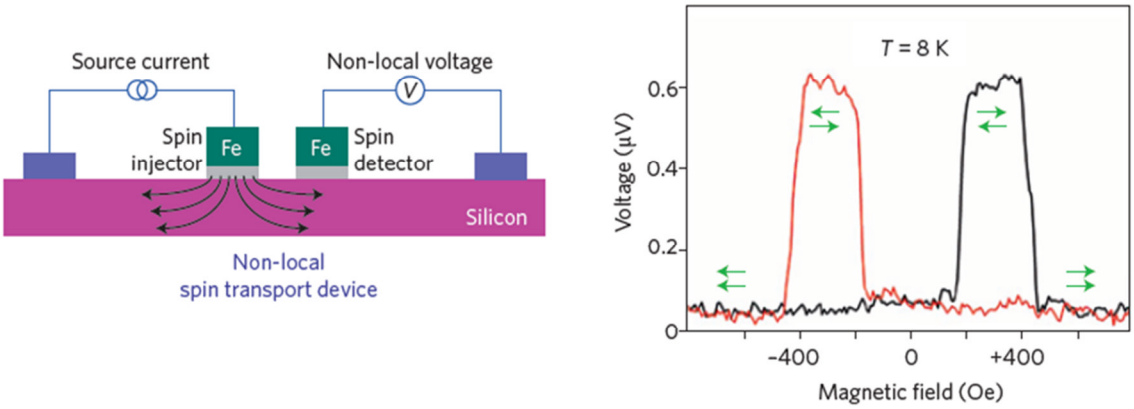

Figure 2.11 a) Hanle geometry used for measuring spin-injection from a spin-polarised electrode into semiconductor; b) Voltage measured in this setup as a function of the applied magnetic field (in-plane along the electrodes longitudinal axes). The arrows indicate the magnetisation directions of current and voltage electrodes [62].

This approach was successfully demonstrated in Ref. [63]. By using Fe as a spin-polarised electrode and Al_2O_3 thin layer as a tunnel barrier, it has been shown that spin-polarised current is injected into the Si substrate. Similar measurements were performed in Ref. [64] on the case of Fe/MgO/Si based device. The measurement setup is schematically shown in **Figure 2.11**, and has a lateral transport geometry. A constant current flows through two electrodes while the other two serve as voltage electrodes. This is so called Hanle four probe setup and is frequently used to estimate the spin-injection for these devices [62].

The electrode on the right in the voltage circuit is several spin diffusion lengths apart from the other voltage electrode so that electrons near this electrode are completely depolarised. However, they are polarised below the other voltage electrode since it is very close to the current electrode. This spin-accumulation ($\mu_\uparrow - \mu_\downarrow$) present below this electrode but absent near the other voltage electrode will cause a difference in potentials *V* between these two electrodes, proportional to the spin-accumulation.

It can be seen in **Figure 2.11** that there is a clear distinction in measured voltage between the parallel and antiparallel magnetisation orientation, which can only be possible in case of spin-polarised injected current. The detected voltage can be also

modulated by applying magnetic field perpendicular to the junction. This causes decrease of the spin-accumulation due to the spin-precession in a magnetic field [65].

Although this approach overcomes the conductivity mismatch issue, the efficiency of the injected current depends significantly on the tunnelling barrier parameters particularly its spin-tunnelling asymmetry coefficient, hence injecting completely spin-polarised current is again challenging. In addition, the device fabrication in this case is significantly more complex [66], and also such devices have higher power consumption [67].

Spin-injection has been achieved across interfaces where the conductivity mismatch is not as significant, such as from ferromagnetic semiconductor into non-magnetic semiconductor [68]. In Ref. [69], a spin-injection from magnetic semiconductor into non-magnetic semiconductor has been also demonstrated. We shall note however that although these devices are very useful conceptually, the spin-polarised sources have in these cases very low Curie temperatures.

2.5.2 Half-metals as ideal candidates for efficient spin-injection

If we consider again the **Eq. 2.12**, it can be noticed that when $\beta = 1$, i.e. half-metallic electrode, then the spin-polarisation of the current at the interface plane is 1, i.e. the injected spin-current is completely spin-polarised. This is because r_F becomes much higher than r_N as $\beta \to 1$, since $\rho_F^* \sim 1/(1-\beta^2) \to \infty$. This makes $(SP)_I \to 1$. Hence, half-metallic materials in contrast to conventional ferromagnets do not suffer from the conductivity mismatch issue. Moreover, there is no any need of introducing tunnelling insulating layer at the interface. Therefore, the half-metallic materials are very important and an ideal candidate for spintronic applications particularly for devices that involve spin-injection.

The Co-based full Heusler alloys as mentioned before due to their half-metallicity and very high Curie temperature (e.g. ~1100 K for CFS [70]), are very desirable for applications in spin-based devices.

2.5.3 The influence of interfacial atomic and electronic structure on the half-metallicity

From the previous discussion it becomes clear that the Co-based Heusler alloys have huge potentials for applications in spintronics. For any device, besides the quality of the Heusler electrodes which includes proper ordering, stoichiometry, absence of defects etc., it is crucial to retain the structural and electronic integrity at the interface vicinity. In other words, even if the Heusler electrodes are perfectly ideal and achieve 100% spin-polarisation, these spin-polarised electrons have to be transported through the interface for any functionality to be achieved. In some cases, however, the interface atomic structure is different than that of the bulk, due to presence of intermixing or formation of interfacial secondary phases.

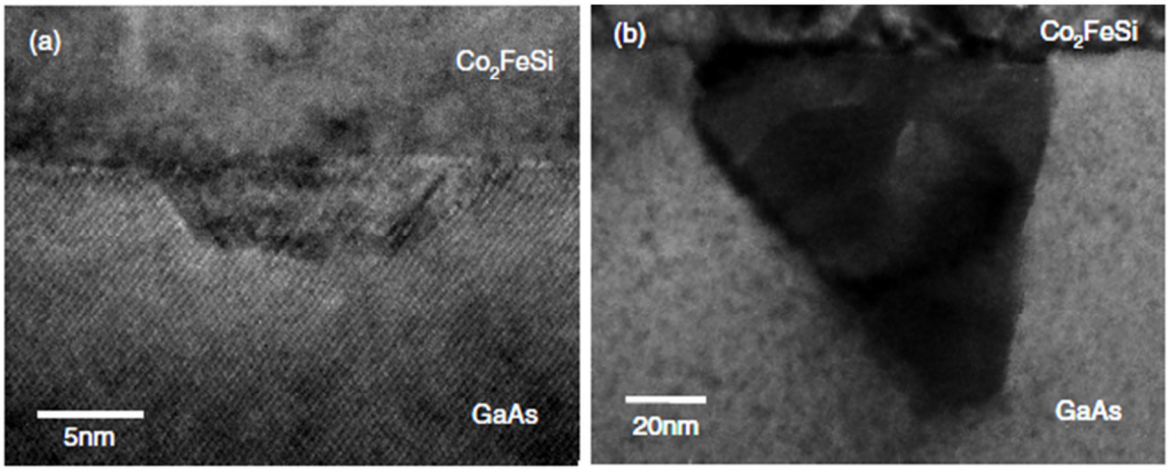

Figure 2.12 a) TEM image of a reacted area of Co_2FeSi film grown at 250 ℃ on GaAs; b) BF-TEM for growth temperature of 400 ℃ [71].

In other cases, the interfaces may be atomically sharp, but the bonding itself between the layers may significantly alter the spin-electronic structure, e.g. destroy the half-metallicity. In both cases, despite the full spin-polarisation of the electrode, the current may become drastically affected (due to the arguments discussed above), i.e. partially or fully depolarised as it flows through the interface.

There are many studies that report on the issues related to interfacial intermixing of the atomic species or even formation of secondary interfacial phases [66]. For CFS/Si(111) these challenges were addressed in Ref. [72]. It was shown that there is a

temperature dependent interfacial diffusion between the Heusler electrode and Si substrate. For the case of CFS grown on GaAs [71] the situation is even more dramatic. As seen in **Figure 2.12** there are large areas where secondary interfacial phases (in this case CoAs) are formed. Interfacial issues have been also observed for CMS/GaAs in Ref. [73, 74] and in Ref. [75] for Co_2MnGa/GaAs. Low spin-injection efficiency has also been observed when the electrode is Co_2MnGe [76] and as a possible issue the interface electronic structure has been pointed out. The study performed in Ref. [77] has showed 16% spin-injection efficiency for the hybrid device based on CFS/GaAs. In Ref. [78] although some interfacial intermixing has been observed, a promising value (about 50%) of spin-injection efficiency with CFS electrode on GaAs has been measured.

Hence, these results demonstrate that the atomic structure of the interface can be particularly important for the performance of the whole device. For some systems, the atomic structure at the interface can be completely altered preventing efficient spin-injection.

On the other hand, many other studies have focused on purely theoretical investigation of the electronic structure at interfaces with half-metal [53, 79, 80]. For example, in Ref. [81] it has been shown that the half-metallicity is lost at Co_2MnGe/GaAs interfaces. Similar studies have been performed for Co_2CrAl/InP where decrease of interfacial spin-polarisation has also been demonstrated [82]. There are also theoretical studies which show that local disorder at Co_2MnSi/Ag interfaces can significantly destroy the half-metallicity [83]. CFS/GaAs(001) interfaces including intermixing have been also shown to lose the local half-metallicity [84]. On the other hand, there are some studies which report on retaining very high spin-polarisation at some interfaces, for example in the case of (110) interfaces between a full Heusler alloy and GaAs [85]. Similarly, high spin-polarisation for some Co_2MnSi/semiconductor interfaces has been reported in Ref. [86].

As a summary, all these studies have shown that the spin-polarisation can be drastically affected at interfaces between a half-metallic full Heusler alloy and semiconductor/metal. This effect is sensitive on the exact atomic structure which is determined by the direction of growth and also by disorder/intermixing at interfaces. Majority of these studies are either for very ideal bulk-terminated interfaces or simplistic

models for interfacial disorder. Modelling based on direct observation of the atomic structure at these interfaces is still lacking.

In this thesis, a full correlation between the atomic structure, revealed by state-of-the-art electron microscopy, and spin-electronic structure, calculated by density functional theory (DFT), will be established. It will be demonstrated that such approach is crucial in order to fully address the reduction of device performance due to interface effects as well as suggest possible solutions for further improvement of their performance.

2.6 Influence from extended structural defects: antiphase boundaries

Most of this thesis will be focused on studies of the influence of interfaces (between a Co-based full Heusler alloy and metal/semiconductor) on the half-metallicity. In addition, in **Chapter 7** the presence and influence of extended structural defects in the full Heusler alloy CFAS will be studied.

Although point defects and disorder in the Co-based full Heusler alloys have been already studied, a presence of anti-phase boundaries, which are extended structural defects, has not been so far reported. Anti-phase boundaries have been however reported in other Heusler alloys. It has been shown [87] that locally they have altered magnetisation and are pinning sites for magnetic domain walls.

On the other hand, antiphase boundaries have been extensively studied in other half-metallic materials. They are very abundant in thin films magnetite (Fe_3O_4), where due to the superexchange interactions across the antiphase boundaries (APBs) they significantly alter their magnetic properties i.e. drastically increase the fields required to saturate the magnetisation [88]. Strong antiferromagnetic bonds across these APBs make these boundaries pinning sites which affect the spin-polarised transport. Due to the preference for antiferromagnetic alignment across the APB, the film's conductivity decreases compared to that of the bulk and also a MR effect is observed [89, 90]. Some of these APBs have very low formation energy [91] which explains their abundance in thin films magnetite.

In this thesis, a ¼*a*[111] APB will be studied which is observed in CFAS thin film deposited on Ge(111) substrate. In contrast to the APBs in magnetite, the APBs in Heusler

alloys are not very abundant as observed experimentally by electron microscopy and predicted theoretically by DFT calculations which show about an order of magnitude higher formation energy compared to the lowest energy APB in magnetite. In addition, it will be shown that this APB reverses the spin-polarisation locally, hence their presence is very detrimental for the thin film properties. DFT calculations will also show that the exchange interactions across the APB still favour ferromagnetic alignment, though they are significantly weakened. By using atomistic magnetic modelling, it will be shown that this weakening of the exchange constants reduces the width of the magnetic domain wall for about 20-30 nm.

3 Methodology

The results in this thesis are obtained by using both theoretical and experimental methods. In this chapter, the techniques and methodologies employed in this thesis are presented. All analysed samples have been grown and supplied by our collaborators Prof Kohei Hamaya and Dr Shinya Yamada from Osaka University, Japan and Dr. Mikihiko Oogane from Tohoku University, Japan. Molecular Beam Epitaxy (MBE) has been used to grow CFAS thin films on both Si and Ge, while sputtering for the CMS/Ag/CMS spin-valve structure grown on MgO. For more details in general about these growth methods we refer to Ref. [92, 93].

We aim to reveal their atomic structure particularly in the vicinity of the interfaces between the half-metal and metal/semiconductor as well as across the defects. In order to achieve this goal various experimental techniques have been used, mainly HAADF STEM microscopy but also the conventional TEM and selected area electron diffraction (SAED) as well as spectroscopic techniques such as energy dispersive x-ray spectroscopy (EDXS) and electron energy loss spectroscopy (EELS). Once the atomic structure is determined and realistic models are constructed based directly on these observations, DFT calculations are performed by using the plane wave pseudopotential code CASTEP. The results reveal the effects the atomic structure causes to the spin-electronic structure of these systems, which in turn determine their overall performance.

3.1 Specimen preparation for transmission electron microscopy (TEM)

In this section, the conventional method for preparing cross-sectional specimens for electron microscopy measurements is described. This procedure consists of: preparing a structure which is to be polished, followed by mechanical polishing and then finishing with ion milling until a small hole is created in the thinnest part of the specimen [94]. Only the region around the hole is thin enough and suitable for electron microscopy measurements. The rule of thumb is that the thinner the specimen is, the better it is for electron microscopy measurements.

The whole process is relatively straightforward in principle; however, it can be a very challenging one to be delivered in practice. It requires in average about 12 hours devoted work, this depends on the type of the substrate (Si/Ge require less time while oxides such as $MgO/SrTiO_3$ significantly more time), age of the polishing equipment etc. In addition to the fact that it is a lengthy process, it is also a destructive technique. From about 8 $(mm)^2$ film surface required for specimen preparation, only about several $(\mu m)^2$ can be used for performing electron microscopy; the rest of the initial material is completely useless, it is either destroyed by polishing, cutting, ion-milling etc. or remains thick (regions far away from the hole). Hence, specimen preparation requires significant and continuous attention to details at each stage, especially when the available material is very limited which can often be the case.

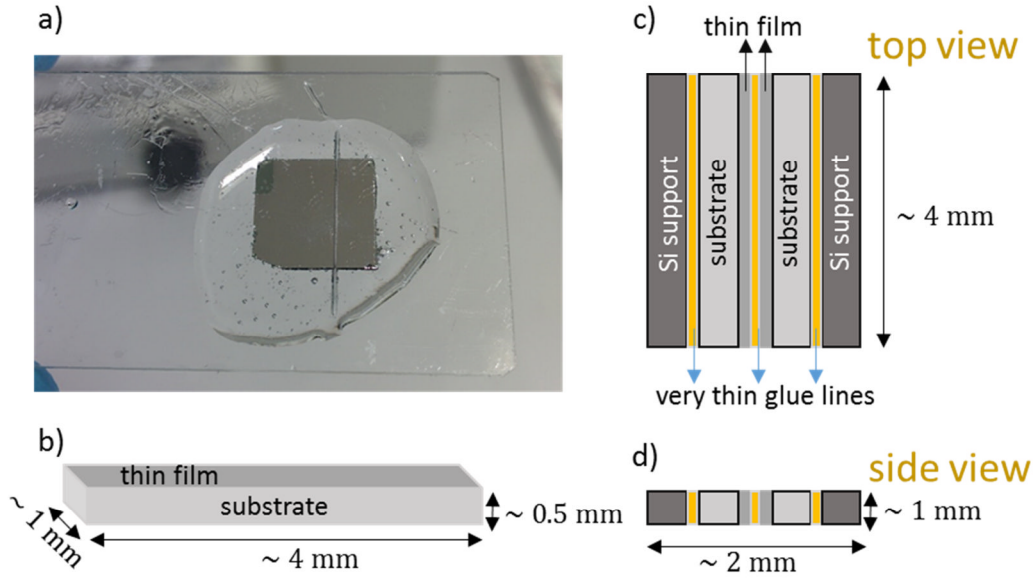

Figure 3.1 a) example of CFAS thin film deposited on a (10 mm x 10 mm x 0.5 mm) Ge substrate; the shaded area is used to mark the substrate crystallographic orientations; b) a rectangular piece with dimensions ~(4 x 1 x 0.5) mm^3 is the basic constituent of the structure shown in c) which is a schematics of the specimen ready to be mechanically polished; d) side view of the structure is c).

All specimens analysed in this thesis are either a thin film (half-metallic) or several layers of thin films deposited on a substrate which usually is with dimensions: (10 mm x 10 mm x 0.5 mm), as shown in **Figure 3.1a**. The properties of the whole structure may significantly depend on the crystallographic orientation (i.e. growth

direction) of the substrate. Also, since in electron microscope we look at the material in projection along certain crystallographic direction, we additionally need to know the in-plane orientations of the substrate.

In other words, for [111] oriented substrates (the normal of the deposited surface is along the substrate's [111] crystallographic direction), which are frequently used in this thesis, the in-plane orientations are $[1\bar{1}0]$ and $[11\bar{2}]$. If we cut the substrate parallel to the edges, then the prepared specimen will be either in $[1\bar{1}0]$ or $[11\bar{2}]$ zone axis (the viewing direction in an electron microscope). Both of them are suitable for performing electron microscopy. However for [001] oriented substrates, the in-plane directions can be [100] and [010] and both of these zone axes are not suitable for performing electron microscopy on the Heusler alloys studied in this thesis. This is because the atomic columns would contain atoms from different elements, making the analysis of their atomic structure practically impossible. Substrates directions are usually marked (**Figure 3.1a**) with shaded areas or with small cuts at the corners.

The sample preparation starts by cutting two equal pieces with dimensions (4 x 1 x 0.5) mm^3 from the sample (**Figure 3.1b**). In order to get the desired zone axis, we should take into account that these pieces will be glued in a structure which when is ready to be analysed in a microscope has substrate oriented as the edge with dimension 1 mm from the initial piece. The substrate during the cutting is glued on a glass slide (**Figure 3.1a**) using a 'crystal bond' glue which is very suitable for specimen preparation purposes as it can be melted at low temperatures (and again solidified at room temperature) or completely removed with acetone.

The cutting is done with a machine which has a thin diamond blade using very low angular velocity and very low pressure in order to reduce any damage on the specimen. Brittle substrates such as MgO easily cleave and break if we are not very careful during the cutting. After the cutting, the two pieces are unglued from the glass slide by heating. It takes only couple seconds to melt the crystal bond glue. These (substrate+film) pieces are then cleaned by leaving them for about three minutes first in acetone, then ethanol and finishing with isopropanol. For some specimens, an additional cleaning using ultrasonic bath is required.

The next step is preparing a glue which is about 1:10 mixture of hardener and resin. This gives a resultant glue mixture which can be solidified by heating at about

100 ^{o}C for 1-2 minutes. In contrast to the crystal bond, once solidified this glue mixture cannot be reversed back to liquid phase (at least not at the low temperatures used for specimen preparation). Also, once solidified, it can resist acetone, ethanol and isopropanol; hence this mixture is suitable to be used as a permanent glue into the structure which after the polishing has to be additionally heated, cleaned etc. Before using this glue, we shall always check it several times, whether we have achieved the right mixture, by pressing it hard with a wooden cocktail stick. If the cocktail stick breaks without making any damage to the solidified glue, then we know that the glue is ready to be used for gluing the cut pieces. Additional empirical indication of a right glue mixture is the dark-orange/red colour of the solidified glue. We shall always make sure that the prepared glue is of a good quality. Otherwise, if we have not properly tested it, after several hours polishing when the very thin (several microns) specimen has to be unglued from the glass slide by heating, the glue might fail and the whole structure breaks apart.

Once a right glue mixture is ready, we take the two cleaned (substrate+film) pieces and glue them together; with the film's surfaces of both pieces face-to-face. We leave these glued pieces on a hot plate for 1-2 minutes allowing the glue mixture to solidify. We need to make sure that we have pressed them together hard enough, in order to obtain as thin 'glue line' (the space between the film surfaces filled with glue) as possible. Thinner glue lines are important for two main reasons: the sample contaminates less when measured in an electron microscope, and also the ion-milling is much more effective and always gives thinner specimens.

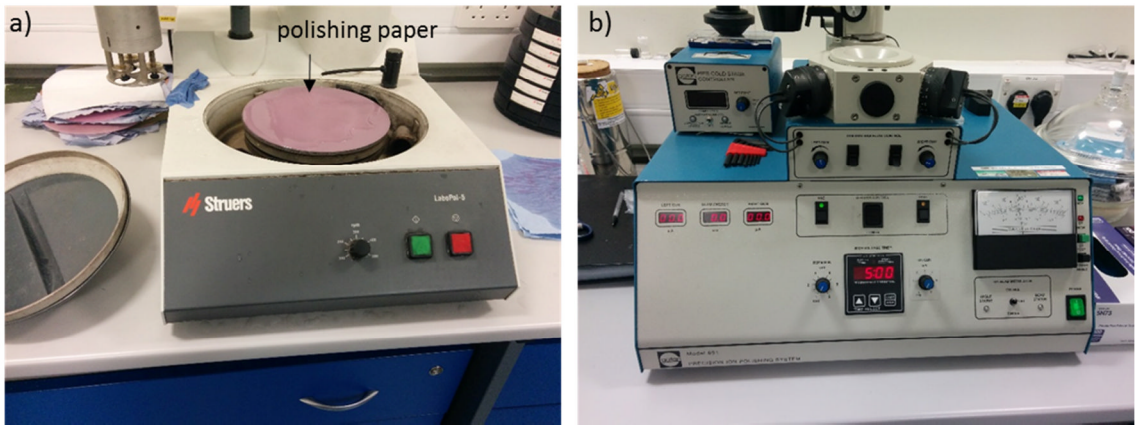

Figure 3.2 a) Polishing equipment; b) precision ion polishing system (PIPS) machine.

In order to provide an additional mechanical stability during the polishing, we glue two Si pieces which have the same size as the (substrate+film pieces), one at each side of the current structure. Besides this main purpose of the Si 'supports' they serve as a thickness guide in the final stage of the polishing. In other words, at that stage the structure becomes very thin and brittle, so it is not recommendable to measure its thickness with the conventional mechanical instrument. In such situation we can judge whether the specimen is thin enough or has to be further polished by the colour of the Si supports when we look at them using optical microscope in transmission mode. They become first reddish and when they are very thin turn to yellowish colour.

Hence, the specimen so far looks as outlined schematically in **Figure 3.1c-d**. After gluing it on a glass slide using a crystal bond (so we can easily remove it when the polishing is done) it is ready to be mechanically polished.

For polishing (**Figure 3.2**), we use four different polishing papers labelled as 1, 3, 6 and 15 μm. These values are related to the size of the particles within the paper which make the polishing possible. We use 15 μm paper for the rough polishing in the beginning while 1 μm in the final stage to make the specimen as thin as possible without breaking it. The polishing is performed manually by hand, since we have better control on the specimen compared to using a polishing machine, especially in the final stage. Constant water flow is applied during the polishing which makes the polishing paper always covered with water for cooling purposes. During the polishing, specimen thickness has to be occasionally checked. When certain thickness is reached we change the polishing paper for example from 15 μm to 6 μm. In addition to the thickness, we always have to check the quality of the sample by using optical microscope; whether the sample is broken, whether we have scratches which may further expand and damage the sample etc.

Both sides of the specimen have to be polished. We start from one side, and keep polishing until the specimen surface becomes everywhere uniformly polished, and then when the desired thickness is reached change the paper and do the same. Usually after the polishing of the first side, specimen thickness is about 500 μm. For the first side of the specimen is not much important what is the final thickness as long as is not too thick or too thin, as we have to flip it and glue a TEM grid to it. Hence, a thickness of about 0.5 mm is ideal.

Once the polishing of the first side of the specimen is finished we put the specimen on a hot plate, remove it from the glass slide and perform a cleaning. After this step, we glue (using the glue mixture) a TEM copper ring (~3 mm diameter) to the polished side of the specimen (**Figure 3.3**). This ring provides an additional and crucial mechanical support in the final stage of the polishing and also holds the specimen after the preparation is finished. Making the 'glue line' between the TEM ring and the rest of the specimen as thin and uniform as possible is very important. Almost always specimens break in the final stage of the polishing if we have not glued the TEM ring properly.

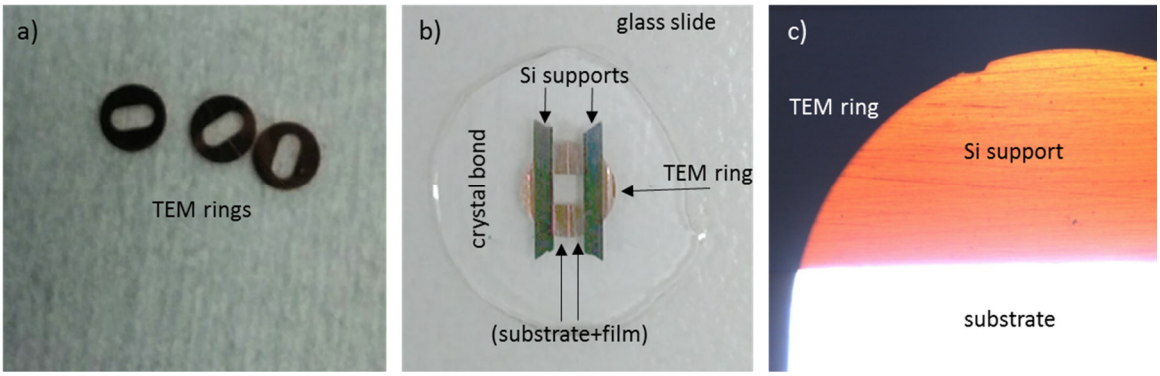

Figure 3.3 a) TEM rings; b) specimen once the TEM ring is glued; c) shows the colour of the Si supports when the specimen is very thin and ready to be ion-milled. This image is recorded by an optical microscope in transmission mode.

Once the TEM grid is glued, we flip the whole structure and glue it (using crystal bond) on the glass slide. We are now ready to polish the second side of the specimen. We start with 15 µm polishing paper and change to 6 µm when the specimen thickness is 200 µm. When the thickness becomes 130 µm we change to 3 µm polishing paper, while the final polishing step is performed with 1 µm paper for thicknesses below 100 µm. All specimen thicknesses referred above include the TEM ring (~50 µm) as well as the glue line (which is much thinner, at most few microns) between the TEM ring and the specimen.

The polishing with 1 µm paper in the final stage is the most crucial step in the specimen preparation procedure. As briefly mentioned above, in this stage the specimen is very thin and extremely sensitive. We no longer use the mechanical thickness instrument, but judge the specimen thickness by the colour of the Si supports. In the beginning of this stage they are dark (in transmission mode). When the specimen

thickness (only the specimen not including the ring) becomes several microns, the Si supports transmit light and we see them as reddish/yellowish in transmission (**Figure 3.3c**). When we notice yellowish colour we stop polishing.

Once the polishing is done we cut the material outside the copper ring by using a sharp tip cutting pen. We then heat the glass slide and remove the specimen which is now only within the copper ring. We perform again cleaning with acetone, ethanol and isopropanol to remove completely any crystal bond leftovers and the specimen is ready to be ion-milled using PIPS machine.

The PIPS machine sputters material from the sample by using two focused Ar-beams; the Ar atoms can be accelerated up to 6 keV. For the specimens prepared in this thesis we use a value of $\sim$3.5 keV. Schematic of the ion-milling is shown in **Figure 3.4a**. The Ar-beams are hitting the specimen under $\sim 6^{o}$ angle (the PIPS machine can be operated at angles up to 10^{o}) while the sample is rotating around a vertical axis with angular speed of 3 rpm (revolution per minute). The beams are hitting the centre of the specimen and at some point they will drill a small hole. The whole idea of the ion-milling is to create a very small hole so that obviously in the vicinity of that hole we would have an area with a gradually decreasing thickness. The hole has to be small; otherwise, if we keep ion-milling we would lose the thinnest and best region of our specimen. Hence, it is important to periodically check the condition of the specimen using an optical microscope.

At the beginning of this process we run the machine for $\sim$15 minutes and then check the glue-line by using an optical microscope. After couple such iterations (normally for nicely polished specimens on Si substrate the whole process takes about an hour; when the substrate is MgO it takes about 2-3 hours) we start seeing the formation of a thickness valley around the glue line. When we notice such features, we still keep running the ion-milling but we reduce the milling time for the next iteration.

At some point, the central region of the valley will start showing thickness fringes (**Figure 3.4c**) which indicates that the region has become very thin. When such fringes emerge we shall reduce the milling time for the next iteration to at most 5 minutes. The hole is just about to appear at this stage and milling for more time might lead to 'over-pipsed' sample i.e. creation of a very big hole and useless specimen. When we notice a small dark hole in the optical microscope (in reflection mode) surrounded by

fringes we know that the hole has appeared and we stop the milling process. We shall only clean the specimen using the standard procedure described above and the specimen is ready to be put in an electron microscope.

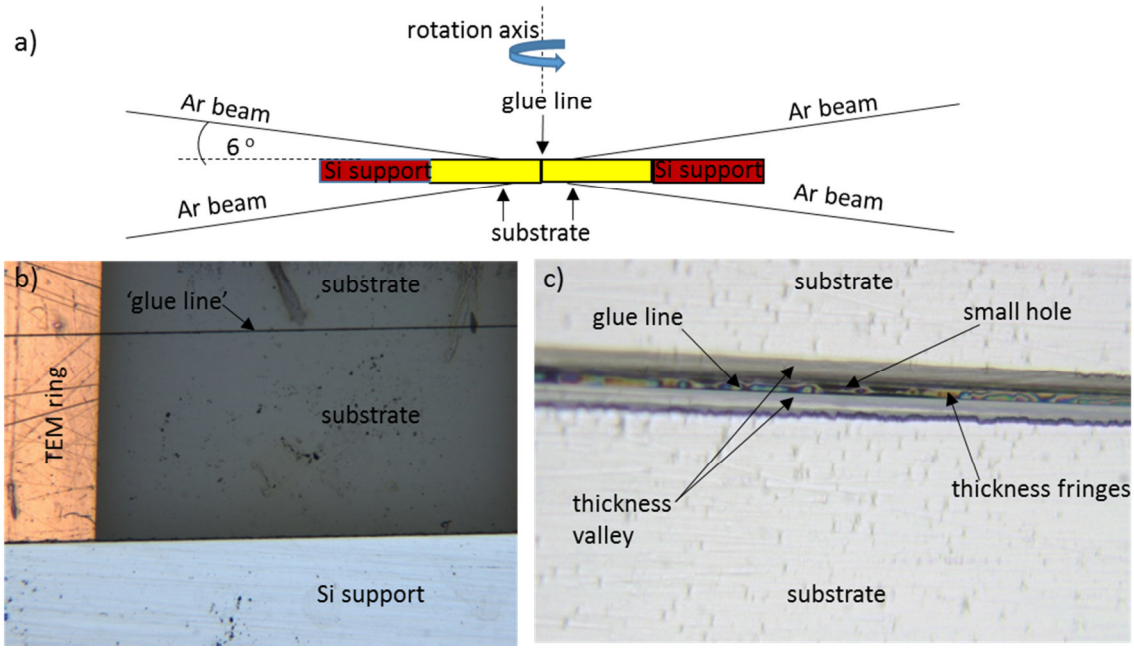

Figure 3.4 a) Schematic of the milling process; b) the specimen looked at in optical microscope (using reflection mode) during the final stage of polishing; c) shape of the glue line after the ion-milling is finished; we can see the formation of a small hole surrounded by thickness fringes.

Finally, it is worth to mention that TEM specimens can also be prepared by using Focused Ion Beam (FIB) machine. An advantage of the FIB method is that it requires very small amount of material and also it is an automatic procedure, but disadvantage is that it is a very expensive technique. Also, the quality of a sample nicely prepared by the conventional procedure described in this section quite often is much better (i.e. thinner and cleaner specimens) compared to the ones prepared by FIB.

3.2 Electron microscopy

Electron microscopy is a very powerful and widely used technique for materials characterisation at atomic/nanoscale. The development of electron microscopes has been inspired by the need to improve the resolution that can be achieved by using a

conventional optical (light) microscope. Couple years after the discovery of the wave properties (proposed by de Broglie) of particles including electrons and the experimental confirmation of this principle by the groups of Davison and Germer as well as Thomson and Reid, the idea of an electron lens has been developed and implemented in the first electron microscope designed by Knoll and Ruska (1932) [95].

There are two main reasons for using electrons, the first is obviously they can have very small wavelength but in addition, an equally important factor is that they can be easily and efficiently controlled/manipulated by lenses which is crucial for achieving high resolution in a microscope. This is the case because they are charged particles in contrast to for example small wavelength X-rays which in principle should enable very high resolution, but the issue in this case is that due to their charge neutrality building efficient lenses for them is very challenging. They also practically do not refract in glass, which in turn is the main working mechanism of the visible light lenses.

The equation which enables to compute the electron wavelength can be straightforwardly derived by using the de Broglie formula (**Eq. 3.1**), which gives the relationship between the momentum (p) and wavelength (λ):

$$\lambda = \frac{h}{p} \qquad \textbf{Eq. 3.1}$$

(where h is the Planck's constant), combined with the relativistic equation that correlates the particle momentum with its energy. Taking into account that the kinetic energy which the electron has obtained when it leaves the electron gun (operating at voltage V) is equal to eV, the following expression, (**Eq. 3.2**) for the wavelength of electron accelerated in potential difference V , is obtained:

$$\lambda = \frac{h}{\left(2m_0 eV\left(1 + \frac{eV}{2m_0 c^2}\right)\right)^{1/2}} \qquad \textbf{Eq. 3.2}$$

where m_0 and e are the mass and charge of the electron respectively while c is the speed of light.

Since the image in an electron microscope is formed by the transmitted (through the sample) electrons, very thin specimens (~50 nm) are required, which can sometimes be challenging to achieve especially when atomic resolution imaging or spectroscopy is needed. An additional important factor which has to be taken into account when analysing specimens by electron microscopy is the possible 'beam damage' that can affect

the specimen. Due to the very high energy of the incoming electrons, some specimens e.g. biological specimens can be partially or fully destroyed. However, the specimens analysed in this work are resistant to the beam and a careful specimen preparation enables both successful imaging and spectroscopy.

An electron microscope is a very expensive and complex machine. In order to record atomic resolution images, obviously we need a very sophisticated machine which includes many functional parts. In a simplified picture, we can regard the microscope as a machine that: *i)* generates high energy electrons (usually 100-200 keV), *ii)* have a complex system of electron lenses which focus the electron beam on the specimen, *iii)* after the electrons have interacted and transmitted through the specimen they are collected and manipulated again by lenses until a magnified image is obtained on the viewing screen. The electrons in these microscopes are equivalent to the light in optical microscopes. They are generated and accelerated by the electron gun (which is the source of high energy/small wavelength electrons), deflected/focused along the microscope column using magnetic lenses and detected either by charge-coupled-device (CCD) cameras or directly on a fluorescent viewing screen. One of the most crucial parts of an electron microscope are its lenses.

3.2.1 Lenses in an electron microscope and their imperfections

In contrast to conventional optical lenses (**Figure 3.5a**), where the light is focused due to refractions at the lens, in an electron (magnetic) lens, the focusing is achieved by using strong magnetic fields generated by the electric current that flows in the Cu – coils (**Figure 3.5b**). The mechanism responsible for deflection of the electrons as they travel through such lens is the Lorenz force. Due to the presence of both parallel and normal component of the electron's velocity, the electron travels along a spiral path within the lens. These spiral trajectories are the reason that causes the images recorded with electron microscopes to rotate in-plane when we change magnification during the measurements.

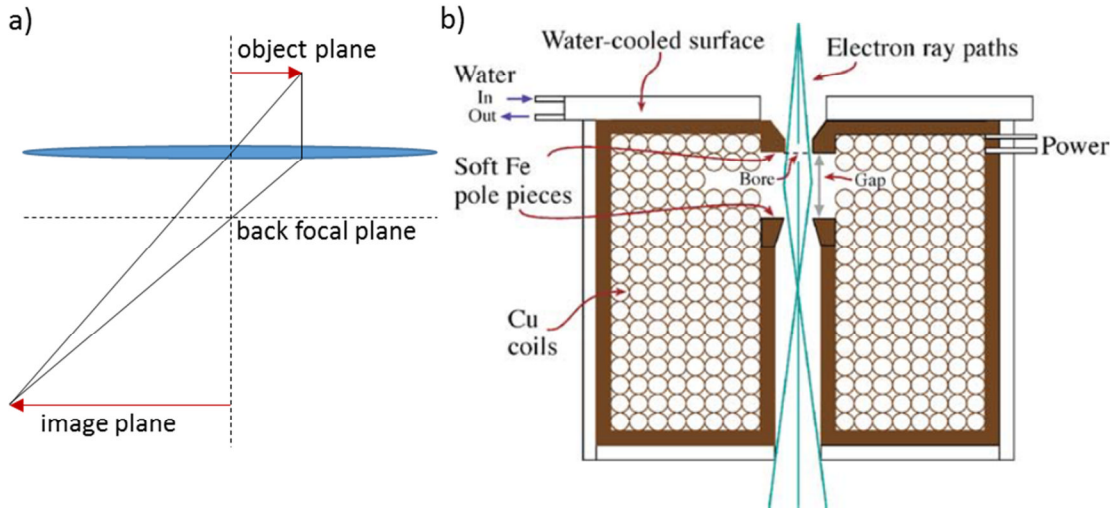

Figure 3.5 Schematic of a) conventional optical lens and the image formation mechanism; b) cross-section of a magnetic lens [95].

Although the magnetic fields within the lens provide a controllable mechanism to modify the trajectories of the electrons, the electromagnetic lenses are much more imperfect compared to optical lenses. The reason are obviously the challenges to create a desired magnetic field within the lens so that the lens acts in the same way for all electrons e.g. paraxial and off-axis, the challenges to create ideally cylindrically symmetric fields etc. The minimisation of these imperfections can drastically improve microscope resolution. Spherical aberrations, chromatic aberrations and astigmatism are the most significant factors related to the lenses that ultimately affect the ability to achieve even higher resolutions [95].

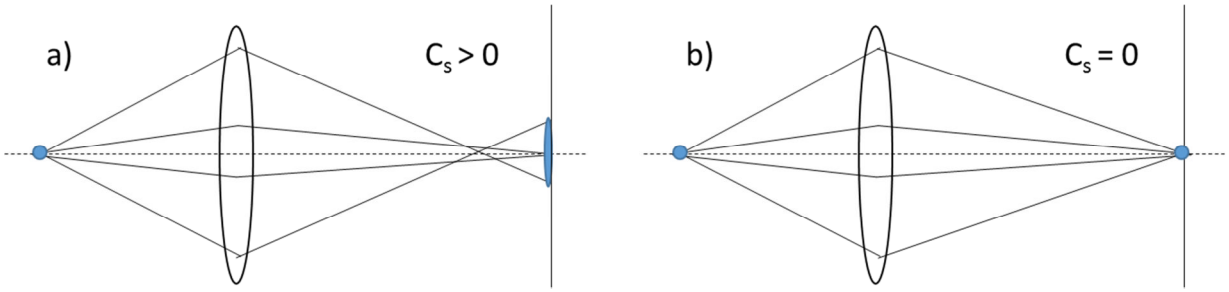

Figure 3.6 Imaging a point object with electromagnetic lens which has a) $C_s > 0$; b) $C_s = 0$. The lens in (a) generates blurred disk at the imaging plane, which is due to the difference in focus between the paraxial and off-axis 'rays'.

Spherical aberrations are caused by the inability of the electromagnetic lens to act in the same way for the off-axis electrons as it does for the paraxial electrons [95]. In other words electrons that are coming at the lens 'far away' from the optical axis will be focused at a different distance from the lens compared to the paraxial electrons. When we image a point object, some electrons travel near the optical axis but some are at larger angles, hence the image created by such lens is not a point but a blurred disk (**Figure 3.6**).

Therefore, spherical aberrations decrease the microscope resolution. Many microscopes today have C_s correctors (C_s is the spherical aberrations coefficient); these are complex systems of lenses (quadrupole, hexapoles, octapoles) in which the currents are interdependent and controlled automatically by computer. The correctors are designed to modify the electron beam so that any electron whether it travels under paraxial condition or far away from the optical axis it will be focused in the same point. Microscopes with C_s correctors have significantly improved spatial resolution, some of them reaching values even below 1 Å.

Another type aberration is the chromatic aberration which is caused by the difference in wavelength of the electrons. Such difference appears due to the energy spread of the electrons coming out of the electron gun. The electrons with lower energy will be deflected more i.e. they will have shorter focal length which taking into account the same arguments as above, will create blurred disk at the imaging plane rather than a point. The modern microscopes however, have quite good electron sources (based on field emission i.e. cold field emissions gun) which can achieve electron beam with energy spread of ~0.3 eV. Further improvement nowadays is achieved by using monochromators which can provide an electron beam with energy spread of ~0.15 meV. Besides the energy dispersion due to the source, an additional contribution can arise due to the energy losses after the electrons have interacted with the specimen. The solution to this issue is to apply energy filtering which is practically implemented in energy filtered (EF)TEM.

In addition, astigmatism is another imperfection which worsens the microscope's spatial resolution. This effect arises due to inhomogeneities of the magnetic field around the microscope optical axis. Main contribution is within the lens, but some might appear also due to charged contaminations when the microscope apertures are not perfectly

clean [95]. These magnetic field non-uniformities can be corrected with stigmators, which are octapoles generating small compensating magnetic fields.

3.2.2 Imaging and diffraction modes in conventional TEM

In this section, it will be explained how the whole system of lenses can be easily transferred from one to another setup giving several imaging/diffraction modes, all providing some particular information about the specimen structure.

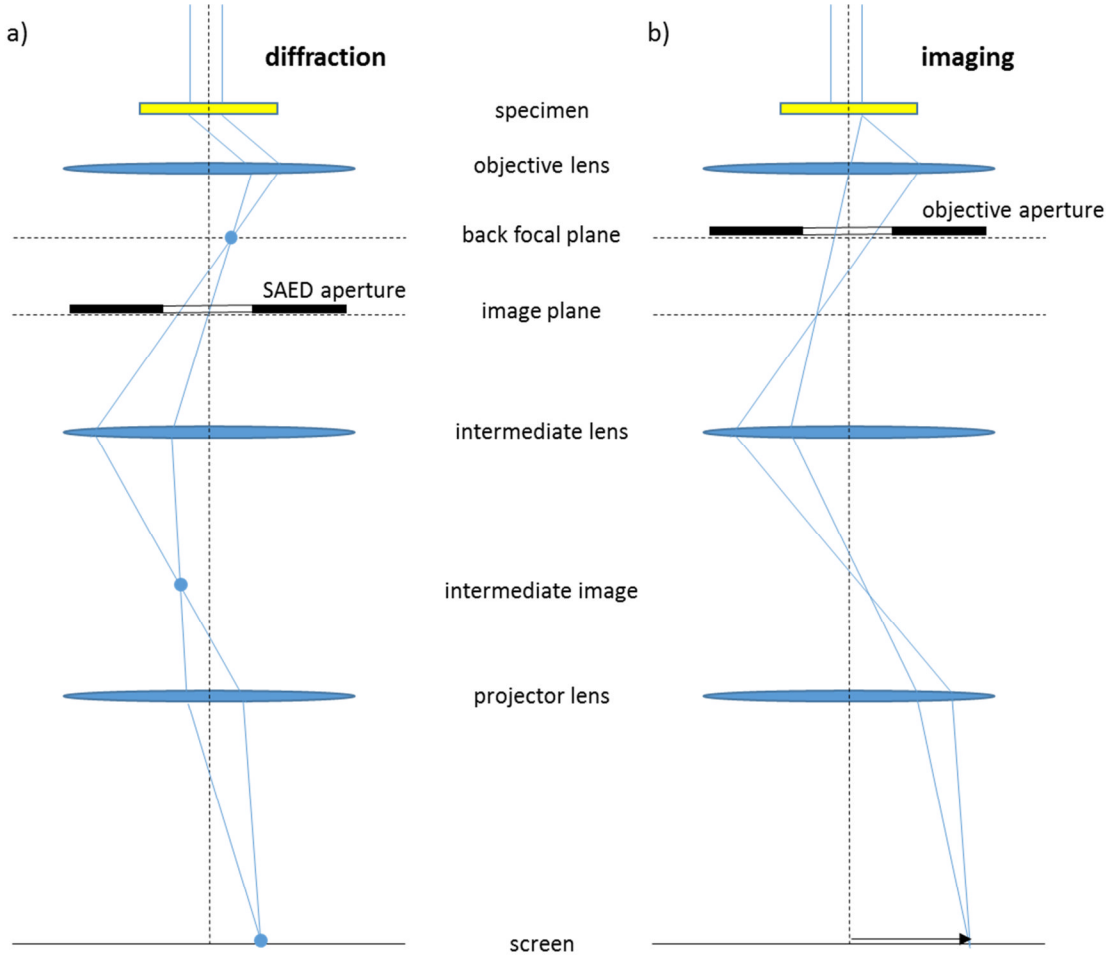

Figure 3.7 Schematic of a) diffraction, b) imaging mode in conventional TEM [95]. By changing the lenses strength and using apertures we are able to easily transfer between diffraction and imaging mode. Note that the schematic is simplified and illustrates the basic principles of work. The practical implementation involves many more lenses.

The system of lenses between the electron gun and the specimen is called illumination system. As the name suggests, the functionality of these lenses is to collect the electrons coming out of the source and 'focus' them on the specimen either as a

parallel beam (required for example for collecting diffraction patterns) or convergent beam (as it is the case in STEM mode).

Next, the imaging system in conventional TEM will be considered. Once we have illuminated the specimen and the electrons have interacted with the specimen, another complex system of lenses is used to record either an image or a selected area electron diffraction (SAED) pattern. Although the real implementation is more complex and involves more lenses, in the **Figure 3.7** a simplified schematic of the microscope operation in imaging and diffraction mode is given. In simple approximation, the system of lenses below the specimen consists of objective, intermediate and projector lens. Below the objective lens two optical planes are of particular interest, the back focal plane and the image plane both belonging to the objective lens. After the electrons have interacted with the specimen, its bottom (exit) surface acts as an object for the objective lens. The objective lens creates an image of this object in its imaging plane, while in the back focal plane a diffraction pattern is formed.

In the diffraction mode (**Figure 3.7a**), the strength of the intermediate lens is chosen so that it takes the back focal plane (of the objective lens) as its object, while in the imaging mode (**Figure 3.7b**) the image plane (of the objective lens) acts as an object for the intermediate lens [95]. First let consider the diffraction mode. As described above, in the back focal plane of the objective lens we have the diffraction pattern of the illuminated area of the specimen which for crystalline specimens is a pattern of very bright diffraction spots, which arise as a result of scattering from the corresponding sets of atomic planes. If we consider one such reflection (the blue point in **Figure 3.7a**), then this point is imaged by the intermediate lens into a point at the image plane of the intermediate lens where we form an intermediate image. This image is then magnified by the projector lens and focused on the screen. Hence this setup gives a magnified image of the back focal plane of the objective lens i.e. a diffraction pattern. In many cases, it is proving very useful to get a so called selected area diffraction pattern, i.e. the diffraction pattern that comes from specific region of the specimen. In order to achieve this, we insert a SAED aperture in the image plane (objective lens), as shown in **Figure 3.7a**. Since in this plane an image of the specimen is formed, by moving the aperture we can choose only the area which we are interested in. Hence by using an aperture any contribution from the rest of the specimen will be avoided in the resulting SAED pattern.

In the imaging mode, (**Figure 3.7b**) the intermediate lens strength is chosen so that it takes the image plane (of the objective lens) as its object, and then this image is further magnified by the projector lens [95]. We can operate in this mode without the SAED and objective apertures, however sometimes it is very useful to insert the objective aperture. This aperture is at the back focal plane of the objective lens and has the purpose to select the desired area of the diffraction pattern. If we put the aperture at the centre it will transmit only the central spot from the diffraction pattern and the final image on the screen in such case is called a bright field (BF) image. We can also choose another i.e. non-central diffraction spot, in which case we form so called dark field (DF) image [95]. This is illustrated in the **Figure 3.8**; by choosing the central reflection with the objective aperture we get a BF image, while if we shift the aperture so that it transmits the [h_1, k_1, l_1] diffraction spot we get the corresponding DF image. BF and DF TEM images give very useful information about the specimen structure, since the contrast in these images depends on the scattering properties of given specimen area; these are diffraction contrast imaging modes. For example, if we have a polycrystalline specimen and perform a DF imaging we will see very bright the grains which are oriented in a way to satisfy the Bragg condition to produce the diffraction spot chosen for the DF imaging.

We can also operate in another imaging mode, so-called high resolution transmission electron microscopy (HRTEM). In this case, we do not use a particular diffraction spot(s) from the back focal plane, but remove the objective aperture so that the whole diffraction pattern is transmitted. In this mode, we get much more information about the specimen since we have allowed all diffraction spots to participate in the resultant image on the screen. Each of this diffraction spots give useful information about the corresponding atomic planes. Hence, for the HRTEM imaging the final image is actually a complicated interference pattern [95]. This imaging mode can give us some useful information about the specimen e.g. lattice fringes, but each such image has to be carefully interpreted. The HRTEM contrast for crystals is a periodic pattern however the atomic columns cannot be straightforwardly determined from such patterns since the contrast depends on the imaging conditions and specimen thickness.

In other words, if we want to extract useful information from such images, developing atomistic models and performing image simulations on such models are required. Most of the electron microscopy images in this thesis are HAADF STEM images,

which allow us to extract much more reliable information from the specimen, as the contrast in these images is more straightforward to be interpreted [95, 96]. TEM imaging in this thesis is used to obtain overall information such as film thickness, but not for analysis of the specimen structure at the atomic level, where the HAADF STEM imaging is more suitable.

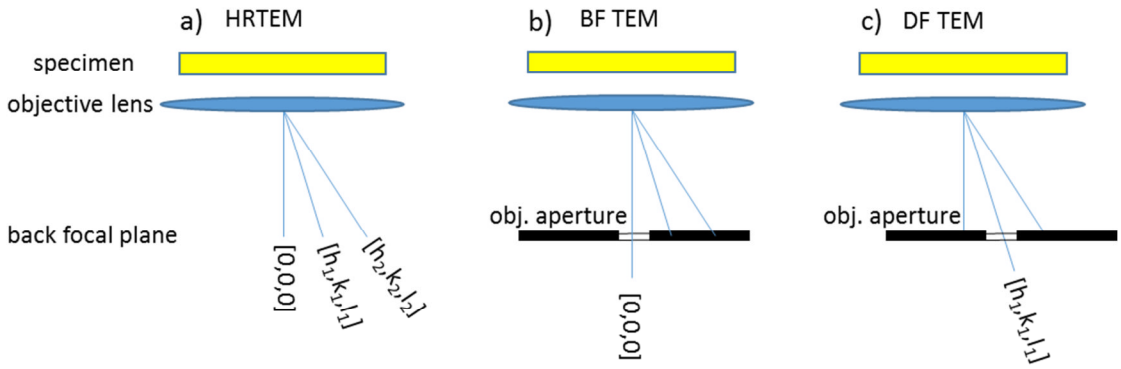

Figure 3.8 Schematic of a) HRTEM; b) BF; c) DF TEM imaging. It is shown how by using the objective aperture we can switch between these three complementary imaging modes. Note that [*h*, *k*, *l*] are the Miller indices for the corresponding atomic planes.

Note that the electron microscopes design is now advanced so that the switching between imaging (BF, DF, HRTEM) and diffraction modes is simple and takes just couple seconds.

3.2.3 Scanning Transmission Electron Microscopy (STEM)

The STEM technique is very frequently used in this thesis to extract information about the atomic structure of the film, interfaces or defects. This microscopy technique is widely used in material sciences since it can provide us with sub-angstrom resolution information about the specimen [21, 96], which makes this method very attractive. Obviously, achieving such high-resolution is not a trivial problem. We need to successfully implement two challenges, the first is finding an appropriate method, and the second is to reach the level in technology when the instrument design is so advanced so that such practical implementation can be achieved. The HAADF STEM imaging is one of the outstanding achievements of physics in general, both conceptually and practically. Taking into account that a STEM microscope is a complex system of macroscopic objects, the

careful design has enabled outstanding stability in order atomic resolution imaging to be possible.

As the name suggests, the STEM mode operates by scanning/rastering a sub-angstrom probe across the specimen surface [96]. The lenses above the specimen which include the condenser and objective lens have the purpose to create a convergent beam which is focused to a sub-angstrom region called the 'probe' [96, 97]. The specimen is positioned along the optical axis so that its position matches with the position where the beam converges and the probe is formed. Hence, in contrast to the conventional TEM imaging, in the STEM imaging we have point-like illumination. By having a point-like illumination we are able to obtain local information of the specimen structure on angstrom scale. In STEM the probe is scanned across the specimen, stopping at each point for a certain time (microseconds), in order to obtain information for an extended region. Hence, pixel-by-pixel we generate information for certain specific area of interest. In order to perform the required scanning, we need to be able to shift the probe across the specimen surface. This positioning of the probe is done by using system of scanning coils (**Figure 3.9a**) which create controlled magnetic fields required to deflect the probe from the central to a desired (*x*, *y*) position [96].

The scanning makes the STEM images to be serial mode images i.e. obtained pixel-by-pixel compared to the parallel mode TEM images where the whole image is generated at once. There are enormous advantages of the STEM mode. We obtain a pixel-by-pixel information about the specimen, and in this way a resultant image which not only that contains more information but is also much more straightforward for interpretation (if the collection angles of the scattered electrons are large) [96, 98]. The images are formed by a sub-angstrom probe (in recent microscopes) and the underlying mechanism for the image formation in STEM is the scattering of electrons from the specimen/atomic columns [98].

Imaging in STEM can be performed by using different modes. It is crucial for the STEM imaging, to be able to get a proper probe; all important probe forming lenses are above the specimen plane. Below the specimen, in contrast to TEM mode, here we do not use lenses to magnify/construct an image. This is another fundamental difference compared to TEM. We only need detectors to record either a BF STEM or HAADF STEM image [95, 96].

The scattering of electrons at the specimen, produces electrons which are travelling under different angles, some of them at very low angles but some of them at 'very high' angles. Obviously, we can form two types of images depending which electrons we have chosen to work with. The low angle electrons (up to several mrad) form so called BF STEM images while the electrons scattered at high angles form HAADF STEM images [96]. There are also middle-angle-annular-dark-field (MAADF) STEM images where the detector is also annular but collects the electrons scattered under medium range angles, although these are less frequently used for analysis. The geometry of the BF STEM and HAADF STEM detectors is illustrated in the **Figure 3.9b**. The HAADF detector is of annular type i.e. it has a hole at the centre and it is sensitive only at certain high angle range typically in the interval (70 - 200 mrad).

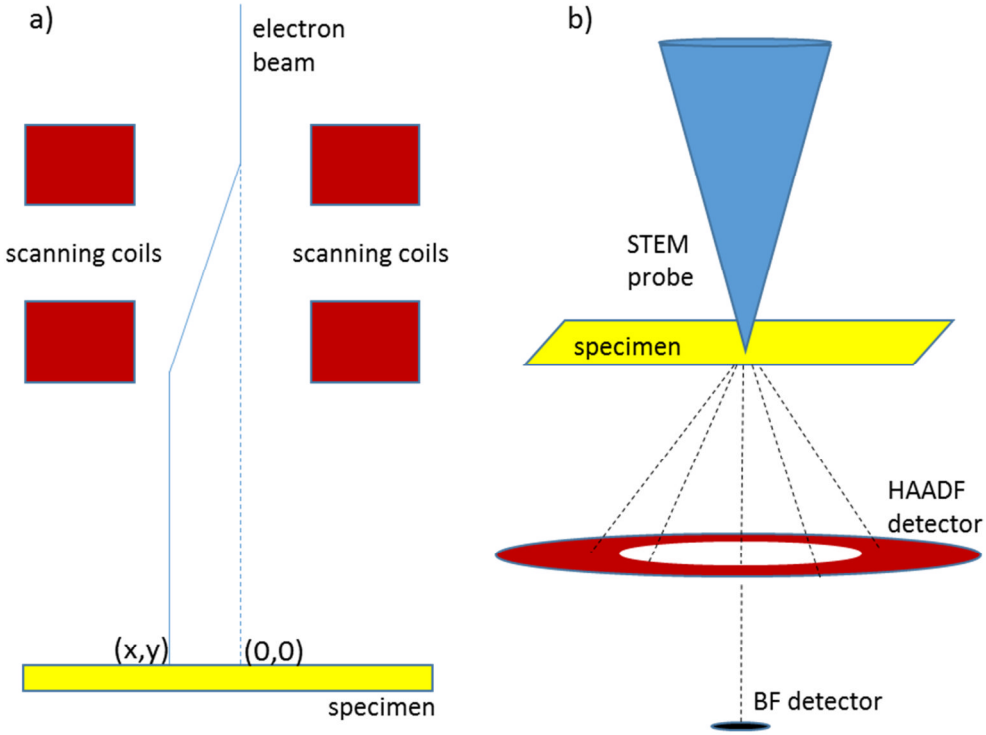

Figure 3.9 STEM imaging. a) Schematic of the scanning mechanism. The scanning coils generate magnetic fields required to obtain the desired shift (*x*,*y*); b) Schematic of the geometry of imaging detectors. The electrons are scattered from the specimen's atomic columns; the ones travelling under high angle are collected by the annular type HAADF while the low angle electrons are transmitted through the hole of the HAADF detector and collected by the BF detector.

The electrons travelling under low angles go through the centre of the HAADF detector and are detected by the BF detector. The images obtained in BF STEM mode are again challenging for interpretation as these images are still phase contrast images. Annular BF STEM (where the electrons traveling under very small angles with respect to the optical axis are not included) has been used to image light elements [99, 100]. On the other hand, the high angle electrons are incoherent making the resulting signal more straightforward to be interpreted [98]. A bright pixel in HAADF images corresponds to scattering centre, the more intensity is collected at given pixel the heavier are the elements along that atomic column. This straightforward correlation between the atomic number and the intensity in the HAADF images is the reason why this imaging mode is widely used in the scientific community, and quite frequently throughout this thesis. Before explaining the HAADF STEM imaging mode, we should mention another important fundamental difference between the STEM and TEM, which is the image magnification mechanism.

In a TEM we magnify the images produced by the electrons at the specimen exit surface in a way similar to that in conventional optical microscope, i.e. by carefully setting the focal lengths of the system of lenses so that the final image dimensions are much bigger that those of the object [95]. In STEM imaging, taking into account that there are no lenses below the specimen, the concept of magnification has to be carefully explained. In this case, the image dimensions are defined by the so called scanning window, which is the region of the specimen surface being scanned by the beam [96].

The microscope is programmed so that this window is sampled equidistantly in both dimensions and at each ‘pixel’ of this area the beam scans for a very short time interval. If we work at very high magnification the distance between these pixels is very small (in many modern STEM this is much smaller than the interatomic distances). On the other hand, in the case of low magnification these pixels are far away, making impossible for example to reveal the specimen atomic structure. Therefore, the magnification in STEM images is directly determined by the dimensions of the scanning window [96].

The probe is fundamentally important for the STEM imaging mode, for example, its size determines the image resolution, while its shape is directly related to the quality of the probe forming lenses and determines the quality of the final image [96]. Since the probe is an image of the electron source (the active part of the gun), first of all we need

sources that are point-like i.e. produce highest brightness (current density per solid angle) possible. In other words, with smaller source active area we get smaller probe size. In addition, by simple optical considerations, it can be shown that the probe diameter can be controlled by the convergence semi-angle of the beam below the objective lens [97]. With bigger convergence semi-angles we can get smaller probes. However, the aberrations at the objective lens start to dominate and set a limit on the probe size [97].

Hence, in order to further reduce the probe size, a reduction of the spherical aberration coefficient is required. In the modern dedicated STEM instruments such correction is performed with C_s correctors which are complex systems of lenses modifying the beam before it enters the objective lens [101]. Manufacturing an ideal electromagnetic lens which does not create aberrations is proving very challenging. As mentioned before, the off-axis rays are deflected more which makes them focus closer to the lens than the paraxial rays. What the C_s corrector does is that it diverges the off axis rays so that this additional angle would compensate for the over-deflection caused by the objective lens [101]. Such correctors have enabled sub-angstrom probe size, which in turn leads to a very high spatial resolution of the final STEM image.

Finally, a simplistic schematic of the functional parts of a dedicated STEM microscope is shown the **Figure 3.10**. We shall note that in many modern dedicated STEM microscopes the whole column is reversed so that the gun is at the bottom and the detectors are at the top (**Figure 3.10**). It is designed this way, since the gun is the heaviest part and provides better mechanical stability of the whole system when is installed at the bottom part of the microscope.

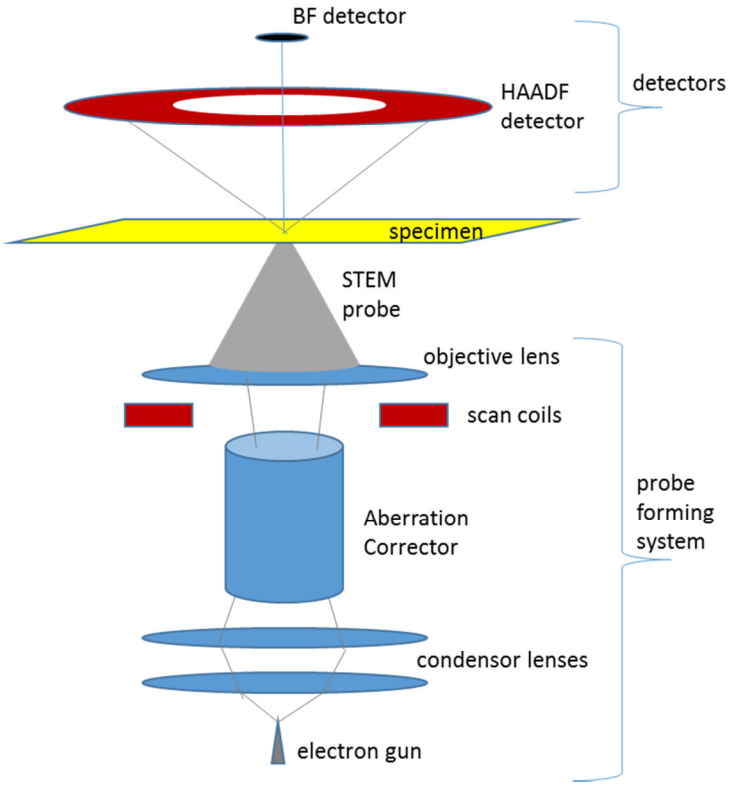

Figure 3.10 Simplified schematic of a dedicated STEM microscope [102].

3.2.4 High Angle Annular Dark Field (HAADF) STEM

In contrast to the coherent HRTEM, the HAADF STEM images are formed by incoherent electrons since they are scattered under very high angle. These high angle electrons have experienced Rutherford scattering (proportional to the atomic number (Z) as $\sim Z^2$) at the specimen, which occurs when the electron travels very close to the positively charged core of given atom [96]. Hence, an image recorded in this mode is not a phase contrast/interference image. Due to the incoherency, the intensity recorded by the annular HAADF detector can be represented as a sum of all scattering intensities coming from the specimen's 'scattering centres' which have interacted with the probe [97]. This allows the atoms from the specimen to be treated mainly as independent scattering centres and certainly enables more straightforward interpretation of the resultant images [97].

Taking into account the size of the probe for modern dedicated STEM microscopes (for example ~0.9 Å for the Nion UltraSTEM 100 microscope at SuperSTEM, Daresbury, UK), when we operate at very high magnification, the probe can visit several pixels all

positioned in-between two neighbouring atomic columns. For specimens with small thickness along the zone axis, and in the case of low-index zone axes, these conditions make the signals coming from two neighbouring atomic columns practically independent. Hence, atomic columns that contain elements with higher atomic number Z appear brighter in the image compared to lower Z elements, as the intensity is $\sim Z^2$ due to the Rutherford alike scattering [97]. Also, an atomic column will appear brighter even if it has the same Z as some other column which contain less number of atoms in that projection.

These properties can be very useful for compositional identification of the atomic columns when the specimen is imaged along appropriate zone axis. For example, some half-metallic materials such as magnetite have neighbouring columns which contain only Fe but different number of Fe atoms in different atomic columns [21, 23]. In such case, we will observe brighter/darker contrast in the resulting HAADF image, which can be used to judge whether the desired atomic ordering is achieved. On the other hand, for some other materials, such as the Heusler alloys analysed in this thesis, neighbouring atomic columns can have the same number of atoms, but in column '1', there are only atoms from the element Z_1, while in column '2', only atoms from the element Z_2 [50]. In such case, taking into account the Z^2 contrast dependence, we can perform chemical identification, and in some case straightforwardly reveal the atomic structure of the specimen. These properties of the HAADF STEM imaging illustrate its usefulness as well as potentials and explain the wide applicability of this technique in physical sciences. Moreover, this imaging can be performed simultaneously with EELS and EDXS so that with one acquisition we get both structural and chemical information of the specimen [21, 103, 104].

As discussed above, advantages of this imaging mode are enormous. We should be aware however, that due to the extremely small probe size, some specimens may suffer a damage when exposed with the beam [95]. The samples analysed in this thesis are in general resistant to beam exposure. Also, the strong probe may easily attract any contaminations present at the specimen surface, and very quickly make the imaging impossible. In addition, thickness here plays a very important role; in general thinner specimens are required compared to those for HRTEM imaging. Hence, with the HAADF STEM imaging we can obtain very useful insights at the atomic level however, we should be aware that we face some challenges which can be to a good extent avoided for

very well-prepared specimens. We shall also be aware that this technique is not that sensitive for low *Z* elements, due to the Z^2 contrast dependence.

During practical operation, there is always a possibility that the probe's axis is slightly misaligned with respect to an atomic column or slightly off from ideal convergent beam etc. All these effects would effectively reduce the spatial resolution of the acquired HAADF STEM image. However, such small effects are to some extent compensated by the phenomenon called channelling, which plays a very important role for the HAADF STEM images quality [97]. The physics behind this phenomenon is that the atomic columns are positively charged and attract the negatively charged electrons from the probe more compared to the interstitial region. Hence, the atomic columns can be regarded as a channel which the probe electrons tend to follow as they travel through the specimen, hence reducing the beam broadening i.e. improving the spatial resolution [97]. Some details about the channelling are presented in the following paragraph.

We label the potential energy (with respect to vacuum) of the probe electron as U_0 when this electron is in the interstitial region, then along the atomic columns this energy is $U_0 + U$, where *U* is the potential energy difference between the atomic columns and interstitial region. Taking into account that the total energy of the electron is conserved when the electron from vacuum enters into the specimen, due to the presence of lower potential energy along the atomic columns, its kinetic energy is increased in this region. That means that the module of the wave vector is bigger in the atomic columns compared to the interstitial region; which implies that the wavelength is smaller. This difference in electron wavelengths between atomic columns and interstitial region will cause total reflection of the electron which travels under angle smaller than the critical angle (φ). The corresponding geometry is illustrated in **Figure 3.11**. It can be easily shown [97] that the critical angle can be estimated using the relationship:

$$\varphi = \frac{\sqrt{-\frac{2mU}{\hbar^2}}}{\sqrt{\frac{2m(E-U_0)}{\hbar^2}}} \approx \sqrt{-\frac{U}{E}} \qquad \textbf{Eq. 3.3}$$

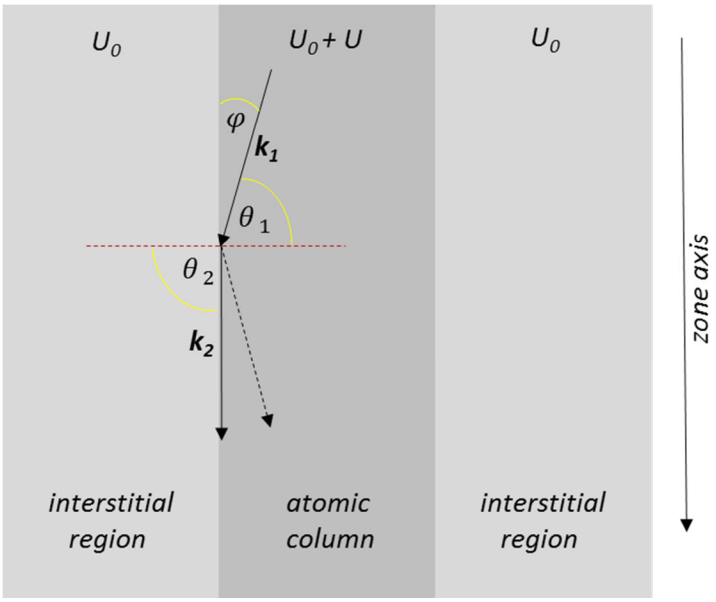

Figure 3.11 An electron with wave vector $\boldsymbol{k_1}$ travels under critical angle φ with respect to the hypothetical interface between an atomic column and interstitial region. For this angle and any other smaller, the electron will be reflected from the interface (dashed vector) and the column in such case acts as an optical fibre channelling the electrons through the sample [97]. The potential energies (with respect to the vacuum) of the probe's electron are labelled with $U_0 + U$ and U_0 for the atomic column and interstitial region respectively.

where E is the electron total energy equal to eV (100 or 200 keV for the microscopes used in this thesis). Typical values for this angle are several miliradians. The numerator and denominator of the first ratio in **Eq. 3.3** are the components (i.e. normal and parallel component with respect to the atomic column/interstitial region interface) of the wave vector $\boldsymbol{k_1}$. These expressions for the components can be derived using the relationship between kinetic energy and wave-vector as well as the fact that the tangential component of the wave-vector is not modified when crossing the interface. Taking into account these considerations, simple calculations lead to the **Eq. 3.3**.

These results mean that the imaging is to some extent resistant to small deviations of the incident angle up to the critical angle. Electrons coming to the specimen under smaller angle will travel all the way down the column similarly as the light in optical fibre, hence improving the spatial resolution of the HAADF image [97].

Another important factor worth to be mentioned is the tunnelling of electrons between neighbouring atomic columns. It was shown above that the electron which travels along the atomic column is effectively confined in that region due to the channelling effects. It experiences an energy barrier at the interstitial region, but next to it there is another atomic column which is another potential well. From quantum mechanics is known that as long as the distance between such two atomic columns is small there is a considerable probability for the electron to tunnel from the initial atomic column to the neighbouring one. The process is probabilistic, hence the likeliness of realisation increases with the specimen thickness along the beam direction [97]. As a result, for very thick specimens the intensity coming from given atomic column contains some contributions from its neighbours. This phenomenon is one additional reason why the HAADF STEM imaging requires very thin specimens.

3.3 Software for analysis of microscopy images and visualisation of atomistic models

Digital Micrograph is a software which communicates between user and microscope. Besides this primary function required during the measurements, this software has implemented many post-processing tools and is widely used in the microscopy community and in this thesis. Digital Micrograph is used in this thesis for several elementary purposes such as image rotation, measuring distances, plotting intensity profiles but also for some more specific tasks such as calculations of Fourier transform of images, Bragg filtering, image alignment etc. Many additional tools can be found in [105].

Several HAADF STEM images presented in this thesis are constructed by series of images. In order to improve the quality of the image, often, instead of acquiring a single image, quick acquisition of several (~ 30) images is performed. This procedure reduces the exposure on the specimen. The specimen can also drift during this acquisition; hence the collected series of images has to be aligned. In this thesis, such acquisitions were performed and the alignment done in Digital Micrograph which already has a spatial drift correction script [106] that, based on statistical correlations, aligns the images. This algorithm takes a reference image and calculates the amount of shift along (*x, y*) for each image of the series, with respect to the reference. After this step, a final image is

constructed as an average of the drift-corrected images from the series. Digital Micrograph will be also used to plot the element specific maps using the EELS measurements. Some images were also analysed with ImageJ [107], which is freely available software for image processing in general.

Very useful tool for material scientists are also the software packages which can help us to create and visualise atomistic models such as VESTA [108], JEMS [109], CrystalKit [110] etc. Majority of the atomistic models presented in this thesis are visualised in VESTA. We also often need information about material structures. There are many databases available online such as ICSD which is freely available [111].

3.4 Simulations of microscopy images

Image simulations are required for some systems in order to check the validity of the proposed model. Due to the interference origin of the HRTEM, these images usually require performing image simulations which should explain the observed phase contrast and ultimately reveal the underlying atomic structure of the specimen. Although the contrast is much more straightforward to be interpreted, HAADF STEM image simulations are also in some cases required. In the **Section 5.4**, HAADF STEM image simulations are performed in order to demonstrate the contrast differences between *B2* and $L2_1$ ordering of the Co-based Heusler alloy CFAS [112].

The method which majority of computer codes for simulating images have implemented is called multislice approach [113]. The idea is to divide the specimen along the beam direction in many slices ideally each of them containing one atomic plane. Let us assume that one such slice is illuminated with a plane wave electron function. As the electron travels, the phase of this plane wave changes as $2\pi z/\lambda$. Since in the specimen an electron experiences additional energy (potential energy), this modifies its kinetic energy i.e. momentum which ultimately affects the electron wavelength. This change of wavelength in turn causes additional phase difference. Simple calculations show [113] that this additional phase difference can be written as $\sigma V_p z$, where $\sigma = 2\pi me\lambda/h^2$ is so called interaction parameter (m - the electron relativistic mass, h - Planck constant), V_p is the electrostatic potential in the specimen, z is the travelled distance. As a result, the exit wave function is a product of the incident wave function multiplied by the so called specimen transmission function $t(\boldsymbol{x})$:

$$t(\boldsymbol{x}) = \exp[i\sigma v_z(\boldsymbol{x})]\,;$$
$$v_z(\boldsymbol{x}) \equiv v_z(x,y) = \int V_p\,(\mathrm{x,y,z})\mathrm{d}z \qquad \textbf{Eq. 3.4}$$

with a phase which depends on the projected potential $v_z(x,y)$. These arguments are valid only for a very thin slice; the method itself is called weak-phase object approximation, and is the starting point for multi-slice calculations. The electrostatic potential is the sum of the potentials of the atoms in the considered slice, which are already computed and tabulated for each element. Hence, the specimen transmission function can be determined as a function of the position (*x, y*). Calculations show that the transmission function is strongly localised to the nuclei of the atoms within the slice.

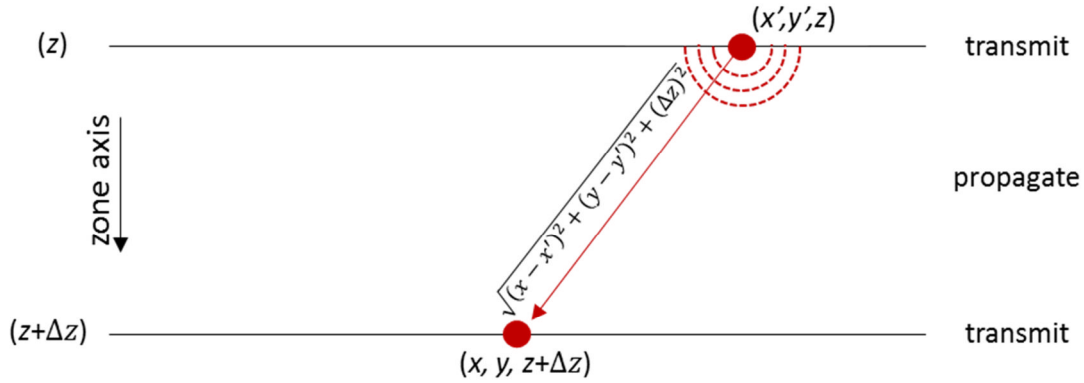

Figure 3.12 Schematic of the multislice approach. The wave-function at point $(x, y, z + \Delta z)$ is a sum of all spherical waves originating from (x', y', z) where $z = const.$ is the position of the previous slice. The amplitude of each such secondary spherical wave is proportional to the transmission function.

Using the result that the transmission function is localised to the slice, in order to compute the electron's wave function that is incident on the next slice, the multislice method does the following [113]. First, it takes the wave function incident on the i^{th} slice (with coordinate *z,* as shown in **Figure 3.12**), and calculates the transmitted wave function through this slice (i.e. the incident wave function is multiplied by the specimen transmission function). Then using the Huygens principles, the wave function incident on the next slice (with coordinate $z + \Delta z$) can be determined as a sum of all spherical secondary waves originating from the previous slice (after they have been transmitted through that slice i.e. multiplied by the specimen transmission function). This can be written [113] mathematically as:

$$\Psi_{i+1}(x, y, z + \Delta z) = p(x, y, z) * [t(x, y, z)\Psi_i(x, y, z)] \qquad \textbf{Eq. 3.5}$$

where $p(x, y, z)$ is so called propagator function and '$*$' stands for a convolution over the in-plane coordinates (x, y). The propagator is directly related to a spherical wave originating from the previous slice. Applying such procedure *N* times, where *N* is the total number of slices, the wave function at the specimen exit surface can be easily obtained. It should be mentioned that the practical implementation of these algorithms is often much easier in Fourier space; the convolution becomes a simple multiplication. Taking the Fourier transform of the exit wave function we obtain the wavefunction at the position of the objective lens aperture (diffraction plane).

All this discussion applies if the lenses are ideal however, as discussed previously, imperfections (such as spherical aberration) are often present. The lenses introduce additional phase difference (described by the so called transfer function of the lens) to the incoming ray, and this is dependent on the angle under which they enter the lens. Hence, for each ***k*** vector the lens transfer function give the additional phase difference. Taking this into account, we need to multiply the Fourier transform of the electron exit wave function by the transfer function of the lens [113]. By doing so, we obtain the final image in Fourier space; remains only to inverse-transform this function to get the final image observed at the imaging plane.

For HAADF STEM simulations there are differences; the objective lens in this case focuses the beam into a probe before it enters the specimen. Hence instead of a plain wave we shall work with a probe incident wave function which is ultimately determined by the microscope parameters, such as objective lens convergence angle, aberrations etc. Also, after the multislice calculations have been performed we take as a signal only the electrons scattered under high angles as defined by the HAADF detector. This means using the Fourier transform of the exit wave function, we first calculate the intensity (the modulus squared) and then integrate it in diffraction space over the area defined by the detector geometry (collection angles range) [113].

The programs for HAADF STEM simulations such as QSTEM [114] used in this thesis, also implement algorithms to deal with temperature effects i.e. to include the thermal diffuse scattering (TDS) [113, 115]. These codes create small displacements of the atoms from their original positions according to the thermal distribution function. Several

such configurations are generated and for each of them an image is simulated then the final image is the average of each of these constituents.

3.5 Spectroscopic techniques: Energy Dispersive X-ray Spectroscopy (EDXS) and Electron Energy Loss Spectroscopy (EELS)

Additional benefit of the STEM microscopy, besides the ability to give atomic resolution structural information, is that it can be easily coupled i.e. simultaneously performed with spectroscopy measurements [96]. In other words, the extremely small STEM probe size enables to reveal the local chemistry either by detecting the generated X-rays (EDXS) or by analysing the energy losses of the transmitted electrons (EELS) [95]. These two techniques will be employed in **Chapter 6** where it will be revealed what is the spatial distribution of the outdiffused Ge into the CFAS film. In this section, both EELS and EDXS STEM are briefly introduced.

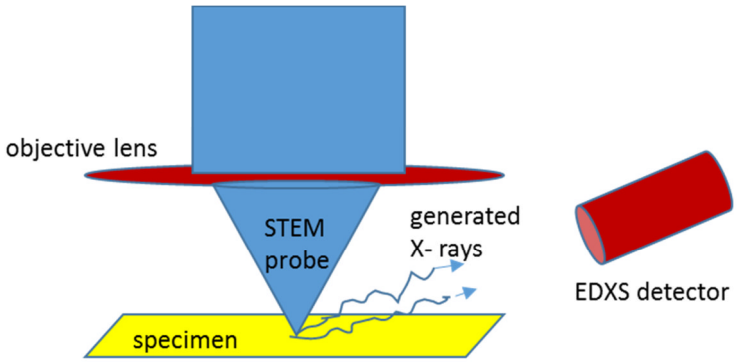

Figure 3.13 Schematic of the EDXS geometry in a STEM microscope.

EDXS is based on the analysis of the X-rays generated by the high energy convergent electron beam incident on the specimen, as shown schematically in the **Figure 3.13**. These X-rays are collected by the EDXS detector which can vary in design; Si drift detector was used in our measurements. The principle of work of these semiconductor based detectors is that the incoming high energy X-ray is absorbed and the energy is transferred to an electron which is in turn transferred from the valence band into the conduction band and accordingly a hole in the valence band is created. Due to the much higher energy of the X-rays ($\sim$keV) compared to the energy required to create electron-hole pair ($\sim$eV) one incoming X-ray typically generates thousands such pairs [95]. This charge is collected on the detector electrodes and transformed into a

voltage as a representative signal. Obviously, the detected voltage is proportional to the energy of the X-ray, which is the basic mechanism utilised to produce the spectra of the generated X-ray radiation [95]. Taking into account the mechanism of work of the detector, it is very important such detectors to be able to process the X-ray signal in a very short time interval. In other words, the detectors implemented in modern microscopes have high efficiency which means they can process completely one X-ray, before the next one enters the detector.

By scanning the probe across the desired area of the specimen, at each position, an X-ray spectrum is collected; all these spectra are unified in a so called spectrum image. Such images give the X-ray energy distribution at each beam position. This energy distribution in turn is directly related to the local chemistry [96]. Besides the continuous braking X-ray radiation, each of these spectra contains characteristic X-ray peaks [96]; these emerge due to the electron transitions from one to another energy level within given atom releasing the energy in a form of X-ray. These transitions occur as the high energy electron ejects a core electron from given atom, and the vacant state is occupied by other electron from some upper energy state. These peaks are characteristic for each element; hence chemical identification can be performed [95]. The recent developments in this field particularly the fact that the detectors are significantly improved, makes EDXS vary desirable technique which is already reaching the ability of atomic resolution [104].

Another useful technique is EELS which can achieve even better spatial resolution, and can give much more insights regarding specimen chemical composition and bonding environment [95]. In contrast to EDXS, here the energy losses of the transmitted electrons are used to form the energy spectrum which is again directly related to the local chemistry of the specimen. While traveling through the specimen the electron can experience scattering events or transmit without being affected. The electrons which have not lost energy form the most intense contribution of the whole energy spectra. This peak is huge compared to the others present in the collected spectra and is called zero-loss peak. Although the zero-loss peak is not of crucial importance when doing EELS, it can be used to determine the specimen thickness. Each material has a typical scattering length which measures the average distance between two scattering events. Thicker specimens will increase the number of scattering events all of which reduce the intensity of the zero loss peak, hence providing a method for thickness determination [95].

In the so called low loss region (energy losses below ~50 eV) most emphasised is the plasmon peak. It emerges as a result of energy lost which is transferred to excite a plasmon (collective oscillatory mode for the weakly bounded electrons). These peaks are characteristic for different materials giving an opportunity to identify the compound by comparing with standards available in literature. More importantly, in the low loss region there are other features which give an opportunity to determine finer details such as interband transitions, band gaps etc. [95].

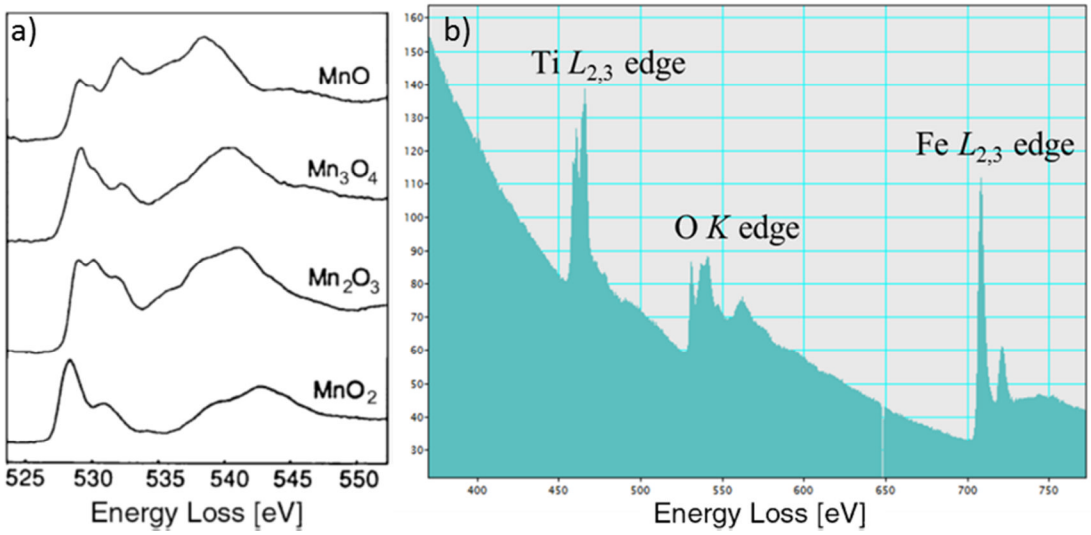

Figure 3.14 a) Oxygen *K*-edge for several Mn oxides, showing that the shape of the edge is different in each oxide which can be utilised to distinguish them [97]; b) EELS spectra collected at $Fe_3O_4/SrTiO_3$ interface showing the characteristic edges for Ti, O and Fe and the power-law decaying background [21].

For chemical identification more important is the so called core-loss region, which shows characteristic features for each element, in addition to the power law decaying background. These features emerge due to energy losses of the incoming electron; the energy lost is transferred to 'ionise' the atom by ejecting an electron from the core shells. Here, in contrast to EDXS, we detect the primary process i.e. the energy loss; in EDXS we detect the secondary process, i.e. the atom goes back to the ground state either by emitting X-ray or Auger electron. The ratio between emitted X-rays and scattering events is not always close to one, particularly for the light chemical elements, in which case EELS is much more efficient technique. An example of EELS spectra is shown in the **Figure 3.14**.

Similar as in EDXS, these characteristic edges can be used to perform chemical identification [21, 116, 117]. In this work, EELS was used in addition to EDXS to confirm the HAADF conclusions about the spatial distribution of Ge into a CFAS thin film. Co and Fe $L_{2,3}$ edges appear at ~ 790 eV and 710 eV respectively, while the Ge $L_{2,3}$ at ~ 1200 eV, hence making possible to easily distinguish their signal without any post-processing which is often required for elements which give core-edges very close in energy e.g. those of Si and Al.

There are variants of the instrumentation which measures the electron losses and record the EELS spectra. Modern dedicated STEM microscopes (as the one used in this thesis) have so called post-column EELS detector. The acquisition can be made simultaneously with HAADF STEM imaging. While the electrons scattered at high angles are detected by the HAADF detector, majority of the electrons (including both those who suffered or not energy losses) travel under very small angle and go through the hole of the HAADF detector. They are then directed to a spectrometer (system of magnetic lenses) which can spatially separate them into different channels according to their energy, and using electronics produce a digital signal shown on screen. This EELS setup is very convenient since it does not affect the imaging mode. Taking into account that EELS spectra is formed by the transmitted electrons very high spatial resolution can be achieved. In Ref. [21] for example is demonstrated that EELS achieves atomic resolution and in combination with HAADF STEM gives unprecedented insight into the atomic structure of magnetite.

Finally, we would like to note that EELS can provide more insightful analysis and better spatial resolution compared to EDXS, however much thinner specimens are required for such analysis [95].

3.6 First-principles calculations

The previous sections showed that the electron microscopy and spectroscopy can provide us with detailed information of the atomic structure of materials. Although the atomic structure is of particular importance, its knowledge has to be always accompanied with appropriate modelling i.e. what such particular structure brings as (un)desired property. In order to obtain such further insights into the considered heterostructures,

first-principles calculations are employed to reveal how the atomic structure of the considered half-metallic materials affects their spin-electronic structure particularly in the vicinity of interfaces and structural defects. By using this approach, it is possible to make a full correlation between the atomic structure of these systems and their functional properties which is the ultimate goal for successful implementation of these materials in real spintronic devices.

The most widely used approach to model electronic properties of materials at atomic level is density functional theory calculations. Many DFT computing codes are nowadays available; in this thesis the CASTEP code [118] will be used. CASTEP is a plane-wave, pseudopotential parallel code capable to perform variety of calculations including total energy calculations, constrained or unconstrained geometry optimisation, band-structure calculations, generate pseudopotentials, molecular dynamics calculations etc. Due to its parallelisation/optimisation it can perform first-principles calculations on systems with large number of atoms very efficiently. Below, the DFT basics will be summarised with focus on the calculations involved in this thesis.

3.6.1 Density functional theory (DFT) – general concepts

The discovery of the wave nature of particles and the formulation of the quantum mechanics has enabled a big progress in the understanding of the nature at/below the nanoscale. Although it is in the foundation of the quantum mechanics, the approach which involves solving Schrödinger equation becomes increasingly inefficient as the number of electrons in the system increases. The next huge step forward into the field was the formulation of the DFT by Hohenberg and Kohn [119]. The underlying principles of this theory are that: the external potential which in turn determines the total energy of the system is a unique functional of the electron density; the electron density which minimises this total energy functional describes the ground state of the system. This general concept is in fact a reformulation of the quantum mechanics from Schrodinger equations approach into electron density approach. It is exact in principle; however, the difficulty here is that the DFT does not specify the exact form of the total energy functional (i.e. the exchange-correlation contribution to this functional). The total energy functional (**Eq. 3.6**) can be written [120] as:

$$E[\rho] = T[\rho] + \int \rho(\boldsymbol{r}) v_{ext}(\boldsymbol{r}) \mathrm{d}^3\boldsymbol{r} + E_H[\rho] + E_{xc}[\rho] \qquad \textbf{Eq. 3.6}$$

where the terms are the kinetic energy, energy due to the external field (all external potentials including the electron-nuclei interactions), the Hartree term (Coulomb interactions between electrons), and the exchange-correlation term (which does not have a classical equivalent), respectively. The exchange functional is not explicitly known, although there are expressions which can very accurately describe this contribution for many systems. The total energy functional assumes an equivalent set of totally independent 'electrons' which do not interact each other, but only with an effective field (in which they also contribute). Taking this into account the electron density (**Eq. 3.7**) has the form [120] :

$$\rho(\boldsymbol{r}) = \sum_{i=1}^{N} |\Phi_i(\boldsymbol{r})|^2 \qquad \textbf{Eq. 3.7}$$

where $\Phi_i(\boldsymbol{r})$ are the wave functions occupied by the system of *N* independent 'electrons'. On the other hand, the first and third term in **Eq. 3.6** are given [120] as:

$$T[\rho] = \sum_{i=1}^{N} \int {\Phi^*}_i(\boldsymbol{r}) \left(-\frac{\hbar^2}{2m} \Delta \right) \Phi_i(\boldsymbol{r}) \mathrm{d}^3\boldsymbol{r}$$
$$E_H[\rho] = \frac{1}{2} \frac{e^2}{4\pi\varepsilon_0} \int \mathrm{d}^3\boldsymbol{r}' \int \mathrm{d}^3\boldsymbol{r} \frac{\rho(\boldsymbol{r})\rho(\boldsymbol{r}')}{|\boldsymbol{r} - \boldsymbol{r}'|} \qquad \textbf{Eq. 3.8}$$

Using **Eq. 3.6**, **Eq. 3.7** and **Eq. 3.8**, by employing calculus of variations one can show [120] that the solution of the following equations (**Eq. 3.9**) (called Kohn-Sham equations [121]) minimises the total energy functional i.e. determines the ground state of the system:

$$\left(-\frac{\hbar^2}{2m} \Delta + v_{eff} \right) \Phi_i = \varepsilon_i \Phi_i \quad ;$$
$$v_{eff} = v_{ext} + \frac{e}{4\pi\varepsilon_0} \int \mathrm{d}^3\boldsymbol{r}' \frac{\rho(\boldsymbol{r}')}{|\boldsymbol{r} - \boldsymbol{r}'|} + \frac{\delta E_{xc}[\rho]}{\delta\rho} \qquad \textbf{Eq. 3.9}$$

Hence the problem is now transformed to solving a system of differential equations describing *N* particles experiencing an effective potential (v_{eff}) (determined self-consistently).

The first approximation that has to be made in this Kohn-Sham approach is to propose a functional that will describe the exchange-correlation energy. That is not a trivial problem and it does not yet exist an exact functional, but several approximations

are developed in literature. The most widely used approaches to this problem are the local density approximation (LDA) [122] and generalised gradient approximation (GGA) [123]. The LDA approach assumes that the local contribution to the exchange-correlation functional is equal to that of the uniform electron gas with same local electron density [120]. In other words, the exchange-correlation energy can be written (**Eq. 3.10**) as:

$$E^{LDA}{}_{xc}[\rho] = \int \rho(\boldsymbol{r})\varepsilon_{xc}^{\mathrm{unif}}[\rho_{\uparrow}(\boldsymbol{r}), \rho_{\downarrow}(\boldsymbol{r})]\mathrm{d}^3\boldsymbol{r} \qquad \textbf{Eq. 3.10}$$

where $\varepsilon_{xc}^{\mathrm{unif}}$ is the exchange correlation energy per particle for uniform electron gas [124]. This approximation prefers smoothly varying electron density. The functional produces satisfactory results for many systems however improvements are required [120]. Another approach is GGA which goes beyond and assumes that the exchange-correlation functional is not only dependent on the local electron density but also on its gradient, with the aim to correct for the in-homogeneities of the electron density, which are emphasised for example at chemical bonds. Hence [120],

$$E^{GGA}{}_{xc}[\rho] = \int f[\rho_{\uparrow}(\boldsymbol{r}), \rho_{\downarrow}(\boldsymbol{r}), \nabla\rho_{\uparrow}(\boldsymbol{r}), \nabla\rho_{\downarrow}(\boldsymbol{r})]\mathrm{d}^3\boldsymbol{r} \qquad \textbf{Eq. 3.11}$$

There are many proposals for the function *f* (**Eq. 3.11**) [120]; the most widely used is the PBE (Perdew–Burke–Ernzerhof) [123] functional which was also employed in all DFT calculations performed in this thesis.

There is another approximation which is employed in majority of density functional codes. Such codes effectively model only the valence electrons, while the core electrons together with the nuclei are neglected and replaced with pseudopotentials [120, 125]. In other words, core electrons are assumed to not in any way be affected by the valence electrons and together with the nuclei generate an effective potential which is then experienced by the valence electrons.

The potential in close proximity of atoms cores is very strong which makes the wavefunctions have lot of nodes (highly oscillatory functions) in these regions, which is not desirable when the wavefunctions are represented as a linear combination of plane waves. However, a majority of the properties depends basically on the electron wavefunctions outside the atomic cores, not within them. In order to avoid the highly oscillatory behaviour of the wavefunctions in the core region, the pseudopotential approach is used; the core electrons and nuclei are replaced with softer effective potential. Such pseudopotentials are required to reproduce the same valence

wavefunctions outside the atoms cores (defined by cut-off radius) as those calculated from all-electron calculations [125].

An additional requirement on the pseudopotentials is that they should be transferable. In other words, although they are generated in an 'atomic' environment, they need to reproduce the accurate valence wavefunctions (outside the core region) in other (i.e. in solids) environments as well [126]. Therefore, this pseudopotential approach has many benefits; it reduces the number of electrons quite significantly which in turn greatly reduces the cost of the computations and replaces the rapidly changing wavefunctions at the core region with smoother ones which also improves the efficiency/speed of the calculations. More details on the pseudopotential approach in general and practical construction of pseudopotentials are available in Ref. [126-130]. In CASTEP there are implemented algorithms which can generate on-the-fly pseudopotentials for each chemical element, but there are also libraries with already computed pseudopotentials.

Now, once the potential experienced by the valence electrons is known, the Kohn-Sham equations can be solved. For crystals, taking into account the Bloch theorem [120], the wavefunctions from (**Eq. 3.9**) can be expanded (**Eq. 3.12**) as:

$$\Phi_i(\boldsymbol{r}) = \sum_{\boldsymbol{G}} c_{i,\boldsymbol{G}} e^{\mathrm{i}(\boldsymbol{G}+\boldsymbol{k})\boldsymbol{r}} \qquad \textbf{Eq. 3.12}$$

where the sum is over the ***G*** vectors of the inverse lattice, ***k*** is a wave vector with values determined from the boundary conditions of the whole system. For systems with large dimensions ***k*** is a 'continuous' variable, with N_{tot} (the number of unit cells in the systems) possible values. This plane wave expansion is particularly convenient mathematically compared to working with some other basis sets. By inserting **Eq. 3.12** into the Kohn-Sham equations (**Eq. 3.9**), the eigenstates and energy eigenvalues can be determined.

We shall note that the coefficients of the plane-wave expansion (**Eq. 3.12**) rapidly decrease as ***G*** increases, meaning that accurate description can be made even if the sum is truncated up to the plane wave with kinetic energy E_c, which is called cut-off energy [126]. Hence, in any numerical computations the expansion is not to infinity, but up to a certain cut-off energy. This cut-off energy depends on the material which is being studied; for the Co-based Heusler alloys studied in this thesis the cut-off energy is 500-600 eV, as

demonstrated in **Figure 3.15**. Materials with more delocalised wavefunctions can be described using lower cut-off, while ones with strong bonding need larger cut-off energy.

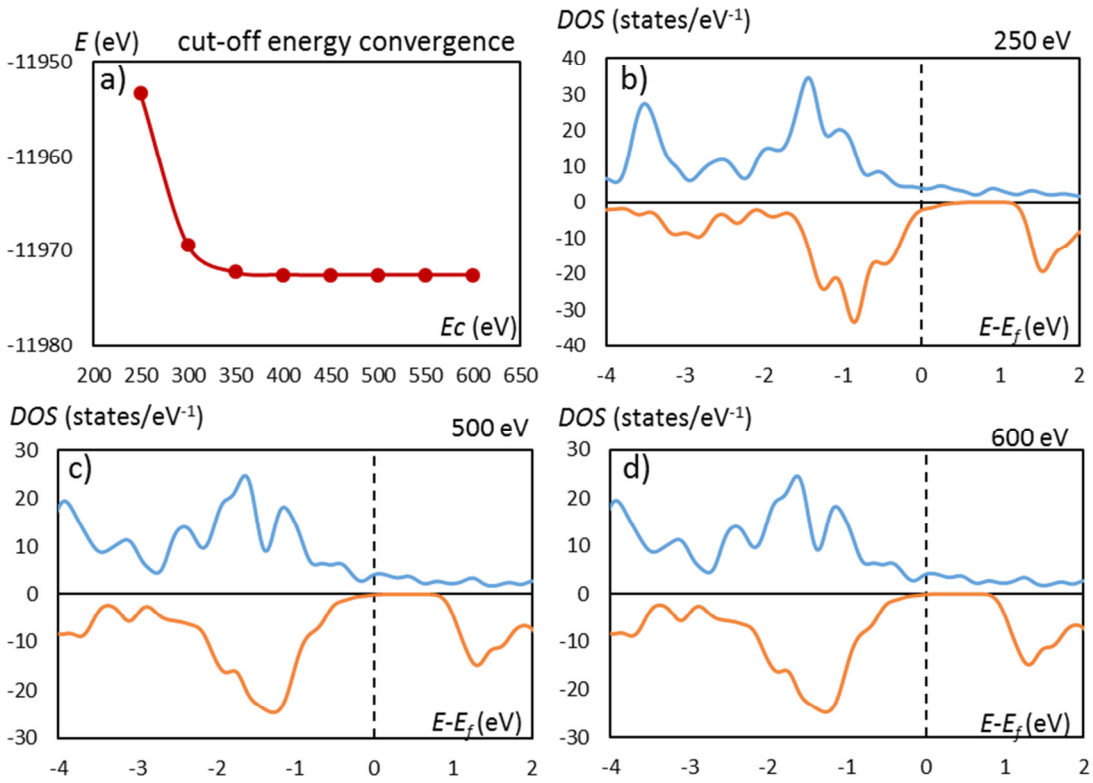

Figure 3.15 Convergence test for the cut-off energy on the example of CMS. a) Total energy is plotted as a function of the cut-off energy; it shows that the cut-off energy region of (500-600) eV provides well-converged total energy. DOS plots for cut-off energy of b) 250 eV; c) 500 eV; d) 600 eV. The almost identical plots in (c) and (d) further confirm the validity of the chosen cut-off energy.

It is also worth mentioning that many subroutines during the computations are performed in Fourier space due to the convenient form of the basis set, which in turn significantly improves the efficiency of the calculations. Since the Kohn-Sham equations contain potentials which themselves depend on the wavefunctions (indirectly through the electron density), the procedure for finding the solutions of these equations is self-consistent and many iterative steps are performed until a convergence is achieved [126].

This procedure [126] is schematically illustrated in **Figure 3.16**. First, the crystal pseudopotential is calculated knowing the atomic numbers and their positions

(contributions from all atoms pseudopotentials are added up). The cut-off energy is chosen and the wavefunctions are expanded as a series of plane waves truncated at the cut-off energy. Then, some initial trial electron density is chosen (arbitrary, but reasonable). With this density the Hartree and exchange-correlation potentials are calculated. Once this is done, the Kohn-Sham equations are solved, for example by matrix diagonalisation. This gives us the wavefunctions which can be used to compute the electron density. This (output) electron density is compared with the initial (input) electron density; if these differ within predefined allowed error, then the solution is accepted and other properties such as total energy are computed. If they differ more, the output density is used as an input for the new iteration and so on, until the convergence is achieved. Note that many codes use linear combination of the input and output density as an input for the new iteration, which achieves faster convergence [120, 126].

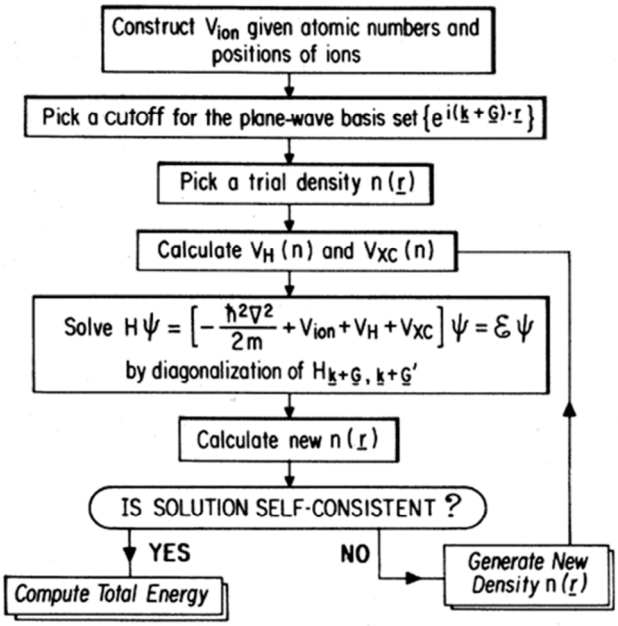

Figure 3.16 Schematic of the computational procedure to calculate the total energy of given material. Figure taken from Ref. [126].

3.6.2 Brillouin zone sampling

By solving the equations for a given ***k*** vector, the energy levels can be determined. As discussed above ***k*** is quasi-continuous variable, hence 'full characterisation' should involve performing calculations for the huge amount of possible ***k*** points in the first Brillouin zone. Certainly, such calculations for each ***k***-point are neither practically possible

nor particularly required. Instead, the Brillouin zone is usually sampled with a ***k***-points grid, and calculations are performed only at the sites of such grid. Such sampling facilitates the calculations, yet provides desired accuracy to compute many materials properties [120]. There are many properties/parameters of materials, which are defined as an integral of a function over the whole Brillouin zone. The simplest such example is the electron density [120]. Not only the electron density, but also the total energy and many other properties, are defined as integrals of the form [120]:

$$f = \int_{BZ} f_{\boldsymbol{k}} \mathrm{d}^3 \boldsymbol{k} \qquad \textbf{Eq. 3.13}$$

We shall note here that the integrand is a periodic function, i.e. invariant to shifts which are integer number of ***G*** vectors. The main idea of introducing ***k***-points grids is to be able to accurately compute such integrals by sampling the Brillouin zone with carefully selected grids. In some very special cases computing $f_{\boldsymbol{k}}$ only at one 'special' ***k***-point gives us the value of the integral as discussed in Ref. [131], or at several special points weighted appropriately [132]. While these methods require analysis of the crystal and its symmetries in order to be able to identify which ***k*** points are special, there is a general scheme introduced by Monkhorst and Pack [133] which works for any crystal. The proposed grid is equally spaced and defined by:

$$\boldsymbol{k}_{n_1,n_2,n_3} = \sum_{i=1}^{3} \frac{2n_i - N_i - 1}{2N_i} \boldsymbol{G}_i \qquad \textbf{Eq. 3.14}$$

where $n_i = 1,2,\ldots,N_i$; and N_i are integers; they are parameters that characterise the density of the Monkhorst-Pack grid. These parameters also determine how many Fourier components should have the function f so that the averaging over the Monkhorst-Pack grid leads to the exact value (the one computed using the integral over the whole Brillouin zone) [120]. Exact integration up to certain Fourier component is the reason why such specific expression for the grid has been chosen. Denser grids produce more accurate results but decrease the speed of the calculations. Hence a trade-off between these two parameters is required. Standard convergence tests are usually applied to find out how dense our grid is required to be. It is worth noting that majority of first-principles codes have algorithms which can find the symmetries of the studied system, i.e. identify the equivalent ***k***-points. This procedure significantly reduces the number of ***k***-points

which are actually used during the calculations [120]. For example, (5 x 5 x 5) grids when symmetries are present can be reduced to only few non-equivalent ***k***-points.

In this thesis, grids with ***k***-points spacing of (0.03 - 0.04) 2π $Å^{-1}$ have been used; which together with the (500 – 600 eV) cut-off energy produce well converged results. Taking into account the symmetries in the Co-based Heusler alloys, the calculations involved in this thesis usually include about ten ***k***-points (e.g. 8, 12, 16 or similar). Majority of the calculations have been performed on the national supercomputer ARCHER, using parallel computing environment. CASTEP tends to be most efficient when the number of cores used is a multiple of the number of ***k***-points, so that each core calculates integer number of ***k***-points, in the same time other cores calculate another set of ***k***-points, and then the results are unified.

3.6.3 Band structure, Density of States (DOS), Partial Density of States (PDOS)

By plotting the energy levels for 'all' ***k*** vectors in the Brillouin zone, so called band structure is produced. 'Bands' are usually plotted in 2D by projecting the band structure along certain desired paths in the ***k***-space. Lines (i.e. bands) with very complex shapes are obtained; by following some band (say the i^{th} energy band) we actually move along the i^{th} energy level states of all ***k***-values along the chosen path. By analysing the band structure for given material, we can tell for example whether the valence electrons can be modelled by using the free electron approximations (which is the case for mainly parabolic bands), or they are more localised (which is the case for more flat bands).

By counting all states in infinitesimally small energy interval around energy *E*, the density of states can be calculated. DOS are extensively used throughout this thesis. In general, very useful information can be obtained by analysing the density of states. Their behaviour is crucial in particular at the Fermi-level. In other words, no states around the Fermi-level is a characteristic for semiconductors/insulators, while states at the Fermi-level are present in the case of metals. In half-metals for one spin-channel there are states, but for the other one there is a band gap. Hence, plotting spin-polarised DOS is of prime importance for the analysis of half-metallic materials. The spin-polarised DOS (number of states, per unit energy and per unit volume) can be calculated by the following expression [120]:

$$\rho^{\uparrow,\downarrow}(E) = \frac{1}{(2\pi)^3}\int_{B.Z.} \delta\left(\varepsilon_{i,\boldsymbol{k}}^{\uparrow,\downarrow} - E\right)\mathrm{d}^3\boldsymbol{k} \qquad \textbf{Eq. 3.15}$$

where $\varepsilon_{i,\boldsymbol{k}}^{\uparrow,\downarrow}$ is the i^{th} spin-up/down($\uparrow,\downarrow$) energy level at given wave-vector $\boldsymbol{k}$; δ stands for the Dirac delta function.

As discussed above, it is impossible to compute $\varepsilon_{i,\boldsymbol{k}}^{\uparrow,\downarrow}$ for all possible $\boldsymbol{k}$, so they are computed at the sites of the Monkhorst-Pack grid. In order to get the real band dispersion, and not delta-like features (which arise artificially from the discretisation) a smearing i.e. Gaussian broadening is applied which in fact does the following transformation [134]:

$$\delta\left(\varepsilon_{i,\boldsymbol{k}}^{\uparrow,\downarrow} - E\right) \rightarrow \frac{1}{\sqrt{2\pi\omega^2}}\exp\left(-\frac{\left(\varepsilon_{i,\boldsymbol{k}}^{\uparrow,\downarrow} - E\right)^2}{2\omega^2}\right) \qquad \textbf{Eq. 3.16}$$

where ω is called fixed-broadening (smearing) parameter. Hence, the smearing actually transforms from Gaussian with zero to Gaussian with variance equal to ω^2. Obviously, extremely small smearing parameter would introduce undesirable delta features, but also extremely large smearing parameter would introduce states where there are no states for example, hence a mid-range smearing needs to be chosen. This fixed smearing scheme is implemented in OPTADOS [135], a code which can calculate and plot DOS, PDOS, and many other functionalities. The OPTADOS code is linked with CASTEP; i.e. the already computed wavefunctions and energy levels from CASTEP are used as inputs in OPTADOS. OPTADOS has been used in this thesis for all DOS/PDOS plots.

So far, the so called total DOS were discussed. This quantity includes all contributions from all the species in the unit cell. Such analysis is appropriate for bulk systems. For supercells which contain for example two interfaced materials the total DOS usually do not provide any valuable information. What is required in such cases is to 'project' the density of states, i.e. to expand them onto contributions from e.g. atoms, regions, orbitals and so on. These requirements have led to the development of codes (such as OPTADOS used in this thesis) which can calculate projected (partial) density of states. Such calculations in fact involve expansion of the wavefunctions into a new basis set which is a linear combination of atomic orbitals. Hence, for example, if the density of states which emerge due to a given atom are required, from the expansion only the terms which contain the atomic orbitals belonging to that atom are kept. This idea is generalised so that PDOS can be calculated not only atom-by-atom but also layer-by-layer (which is

often much more useful), or projected by specific orbitals etc., by constructing the corresponding projector operators [134, 136].

In this thesis, taking into account that interfaces and defects are studied, PDOS are extensively used. Layer-by-layer PDOS will be plotted to explore how these interfaces and defects affect the half-metallicity.

3.6.4 Hubbard-U term

The approximations that are made during DFT calculations sometimes can cause difficulties in getting more accurate values for some quantities in some materials. For example, conventional DFT calculations predict that a class of strongly correlated materials called Mott-insulators should be conductive, but they are in fact insulators at low temperatures. These issues emerge due to the very strong exchange-correlation effects present at these materials caused by the strongly localised '*d', 'f'* orbitals [125].

The strong on-site repulsive interactions between, for example, the localised *d*-electrons are more properly modelled by inclusion of the so called Hubbard-U term [125, 137]. This idea originates back from the Hubbard model [138] which explains the presence of band gap in the Mott-insulator [139]. The Hubbard model is based on the tight-binding approximation where the electrons are basically occupying orbitals of given atom and electron hopping between atoms/orbitals can explain the conductivity. In addition to the 'hopping' part of the Hamiltonian, the model has so called '*U*' part which adds an additional energy *U* for electrons located at the same site (atom), which effectively reduces the hopping mechanism. As this term gets bigger, the transfer of electrons from one atom to another becomes less likely; i.e. band gap emerges/increases.

The successfulness of these ideas in treating strongly correlated materials has been the motivation to add to the DFT Hamiltonian such term in order to improve the contributions from the localised electron-electron interactions. Such algorithms are already embedded in CASTEP and have been employed in this thesis.

It has been shown that for the Co-based Heusler alloys adding the Hubbard-U leads to more accurate band-gaps [47]. Ab-initio computation of the Hubbard-U parameter is not straightforward and there is no general scheme since these contributions are also correlated with the quality of the exchange-correlation functionals used during the calculations. Usually, this term is determined empirically, i.e. a *U*

parameter should be found so that it recovers some expected features for given material, such as the band gap. For the *d*-states in Co-based Heusler alloys this term is (2-3) eV and it has also been demonstrated that the results are not very sensitive to the precise value of *U* [47]. For the calculations involved in this thesis a value of 2.1 eV for '*U*' has been used [47, 140] for all *d*-elements (Co, Fe and Mn) which are present in the studied Heusler materials.

3.6.5 Geometry optimisation

Often, for example for supercells which contain interfaces between two materials, defects or even bulk materials, we do not know the exact positions of the atoms neither the precise value of the supercell lattice parameters. In other words, for example, if an interface is studied then we know to a good approximation the positions of the atoms far away from the interface since they behave as the bulk. However, in close proximity of interfaces or defects, the bonding environment (distances between atoms, angles, etc.) is altered.

Hence, prior to doing fine calculations and obtain the electronic structure, the coordinates of all atoms need to be optimised. In the optimum position, forces on all ions as well as stresses on the supercell vanish. In order to find the optimised positions many DFT codes including CASTEP have implemented already developed geometry optimisation algorithms. For example, CASTEP implements the Broyden-Fletcher Goldfarb-Shanno (BFGS) algorithm [141]. Geometry optimisation algorithms are iterative, so that at each step they compute forces and displace the system to a new lower energy state.

The optimisation in general can be classified as unconstrained (where atoms are allowed to occupy any position) or constrained where some of the atoms positions are fixed or they depend on the other atoms positions through some constraints. Both methods are available in CASTEP and they are used for the calculations presented in this thesis. For example, for interfaces between two materials related with an epitaxial relationship and small lattice mismatch, the in-plane (interface plane) lattice parameters are usually fixed to some mid-value (with respect to the bulk lattice parameters of the two materials) since even if these parameters are optimised there will be a strain in both materials which is in reality quite often relieved through the formation of for instance misfit dislocations.

We shall also mention that the geometry optimisation is not a trivial task and still there is an ongoing research for construction of optimisers which would find the ground state in less iterative steps. The geometry optimisation part of the calculations is almost always by far the longest compared to for example the time required to compute spin-electronic structure using known atomic positions. Even on supercomputers such as ARCHER with many cores running in parallel it took days for some of the supercells studied in this thesis. Hence construction of clever initial configuration particularly at the interface region can significantly reduce the time needed for computations. The convergence criteria in CASTEP can be set as required by the user; for all calculations in this thesis the default values have been used [141]; hence the force on each atom is converged to less than 0.05 eV/Å.

3.7 Atomistic magnetic simulations

In **Chapter 7** where an APB structural defect present in CFAS thin film will be analysed, in addition to the DFT calculations, we perform atomistic magnetic simulations to reveal how this defect influences the magnetic domain wall width. DFT calculations are first-principles method and they are very convenient and efficient as long as the analysed system does not contain large number of atoms. As the number of atoms increases such calculations are computationally very expensive, and cannot be effectively used to simulate properties on a macroscale. Macroscale calculations include for example simulations of hysteresis loops in magnetic materials [142]. In such cases, usually a two-stage approach is employed. First, some local characteristics/parameters are computed by first-principles calculations, and then these are used as input parameters for a large-scale code.

Many magnetic properties are dependent on the exchange interactions in a magnetic material. In other words, neighbouring atoms may prefer ferromagnetic or antiferromagnetic alignment of their magnetic moments. An exchange interaction constant is defined as the energy required to switch the magnetic moment in opposite direction. Exchange interactions have been already computed from first-principles for some simple systems i.e. bulk half-metallic materials such as magnetite [143] and CMS [144]. Once the exchange interactions are known, we can use them as already known

input parameters to perform 'classical' macro-scale calculations in order to estimate many useful magnetic properties [142].

By employing such an approach, in **Chapter 7** atomistic magnetic calculations using the VAMPIRE code [142] are performed. First, we calculated the average exchange interactions at the APB defect and then using the VAMPIRE code, the magnetic domain wall width for bulk and APB models was computed. The VAMPIRE code is a parallel code, which can run very big supercells in an efficient way.

The code requires as input the magnetic moments of all atomic sites (which were calculated by DFT) as well as the exchange constants ($J_{i,j}$) between pairs of atoms. The Hamiltonian of the system contains the exchange term, but also can include anisotropies and the interaction with an external magnetic field (Zeeman term):

$$H = H_{exchange} + H_{anisothropy} + H_{ext.\ field} \qquad \textbf{Eq. 3.17}$$

with

$$H_{exchange} = -\sum_{i \neq j} J_{i,j} \boldsymbol{S}_i \boldsymbol{S}_j \qquad \textbf{Eq. 3.18}$$

where $\boldsymbol{S}_i$ is the magnetic moment direction for a given site. Knowing the explicit form of the Hamiltonian, by using the Landau-Lifshitz-Gilbert equation [142], the dynamic of each magnetic moment can be numerically simulated. By allowing the system to relax, after enough simulation steps the system converges in the lowest energy configuration, which was used to estimate the domain wall width; it will be shown (**Chapter 7**) that the domain wall width in presence of APB defects is reduced by 20-30 nm compared to the one for bulk Heusler alloy.

4 Correlation between the atomic and spin-electronic structure of Co_2MnSi/Ag interfaces

4.1 Introduction

In this chapter, the atomic and electronic structure of the interface between the full Heusler alloy CMS electrodes and Ag as a spacer will be studied. This interface is a functional part of a grown spin-valve structure. The discussion will be limited to the (001) interfaces between CMS and Ag. In the beginning, the properties of ideal i.e. bulk-terminated interfaces will be explored.

Two possible ideal bulk-like termination of the (001)-oriented Co_2MnSi electrode can be identified, these are Co-Co/Ag and Mn-Si/Ag. In other words, along the [001] direction the CMS electrode can terminate on either a Co-Co or Mn-Si atomic plane. By performing DFT calculations it will be shown that these two interfaces have significantly different interfacial spin-polarisation, which in principle gives an opportunity to tailor the spin-valve overall performance.

While the interface with Mn-Si/Ag termination shows greatly reduced but still a spin-polarisation with the same sign as the bulk-like Co_2MnSi part, the spin-polarisation of the Co-Co/Ag interface has reversed sign. In addition to Co_2MnSi electrodes, the case of Co_2FeSi electrodes will be also considered, and it will be demonstrated that the Co-Co/Ag interface is again worse in terms of spin-polarisation compared to the one at the Fe-Si/Ag interface.

The majority of the studies reported so far, have focused either on the experimental performance of spintronic devices [145-150] or on purely theoretical studies of the role of interfaces on the local spin-electronic structure [53, 83, 151], as discussed before. Here, these two approaches are combined. It will be shown that a correlation between the experimentally determined atomic structure and theoretical modelling based on the revealed atomic structure, is necessary and crucial for performing

studies which will explain the measurements but also guide how to improve the performance of the spintronic devices.

Hence, in addition to studying ideal bulk-like terminated interfaces, we go beyond and explore the real atomic structure at these interfaces, which are part of a spin-valve device. By employing the state-of-the-art aberration-corrected atomic resolution HAADF STEM microscopy we reveal the exact interface atomic structure. It will be demonstrated that the atomic structure is different from a bulk-like terminated interface yet the interface is atomically abrupt.

A presence of an additional interfacial monolayer is detected between the Co_2MnSi electrode and Ag spacer. By analysing the structure of both interfaces, i.e. between the top-electrode/spacer and between bottom-electrode/spacer, it will be shown that this layer is present at both interfaces suggesting that its formation is thermodynamically favourable. Then interfacial models will be built based on the HAADF STEM observations and by using DFT calculations it will be analysed how this additional layer affects the interface performance.

It will be calculated that this layer can bring reversed spin-polarisation with significant negative values, hence causing spin-scattering processes at the interface. Therefore, even though the bulk-like Co_2MnSi electrodes are perfect with a $L2_1$ ordering, a significant decrease of the magnetoresistance can be expected, due to the presence of this layer. Finally, it will be shown that the intermixing at this interface is very minor and that any minor intermixing will not further deteriorate the device performance.

The results obtained during this study are published in Ref. [50] .

4.2 Methods and details of the DFT calculations

In order to provide an insight into the interface electronic properties, DFT calculations using the CASTEP code [118] will be performed. An illustration of CASTEP input files is provided in the **Appendix 1**. The modelling of the interfaces between the Heusler electrode and Ag spacer requires the construction of supercells. All constructed supercells in this work have two identical interfaces per supercell and are fully repetitive along the three orthogonal directions. Each supercell consists of three Ag unit cells and three Heusler unit cells along the [001] direction.

During the geometry optimisation, the two lateral (in-plane with respect to the interface) lattice parameters were fixed to a value of 4.02 Å, while both the third lattice parameter and the fractional coordinates of all atoms were fully geometrically optimised, as described in the methods chapter. The value of 4.02 Å is in between the lattice parameter of Ag and $a/\sqrt{2}$ where a is the lattice parameter of the Co_2MnSi Heusler electrode. Hence both the Heusler alloy and Ag spacer are only slightly strained $(\sim 1\%)$. In reality, neither the spacer nor the electrode is strained since the strain is relieved through the formation of misfit dislocations at the interface [56].

For all calculations, the PBE+U exchange-correlation functional was used with the Hubbard-U term set to 2.1 eV for the *d*-block elements Co, Mn and Fe. The plane wave cut-off energy was set to 600 eV. The Brillouin zone is sampled using Monkhorst-Pack grid with *k*-points sampling spacing of $0.035 \cdot 2\pi$ Å^{-1}, which corresponds to 8x8x1 grid size. After the first step of the calculations i.e. the geometry optimisation task, the resulting optimised structures were used to calculate layer-by-layer PDOS. The PDOS were computed and analysed by using the OPTADOS program with *'fixed broadening'* scheme, where the *'fixed broadening'* parameter was set to 0.1 eV.

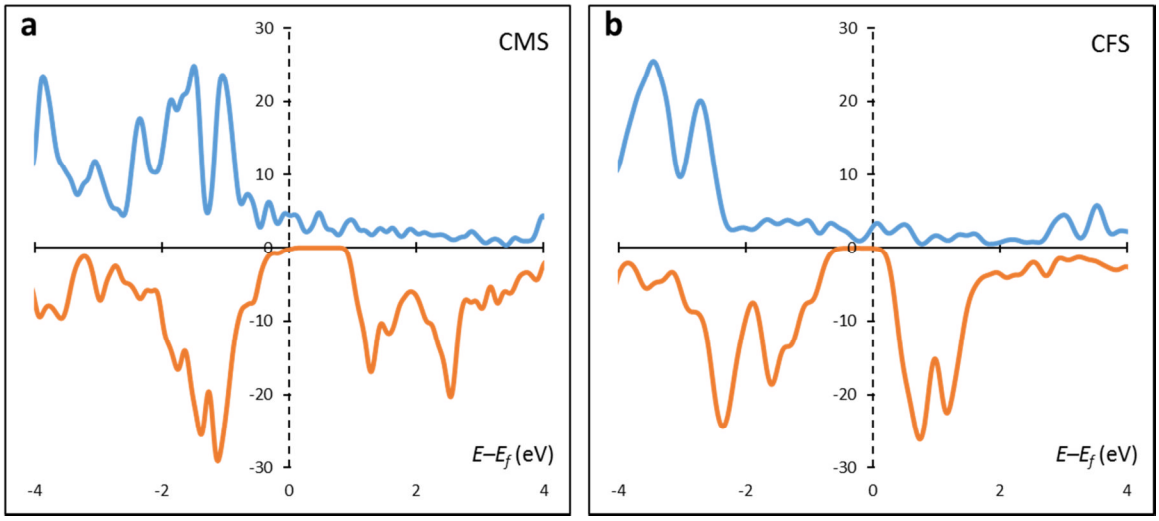

Figure 4.1 Spin-polarised DOS for bulk: a) Co_2MnSi and b) Co_2FeSi. The states from spin-up electrons are presented with blue solid line (shown in the upper half of the figures), while red solid line (shown in the lower half of the figures) is for the states from spin-down electrons. Vertical axes (DOS) are in units of states/eV per unit cell.

Spin-polarised DOS calculations for bulk CMS and CFS using their conventional 16 atoms cubic cells are shown in **Figure 4.1**. These calculations are performed with the parameters and conditions discussed above. The half-metallic character is observed in both presented spin-polarised DOS; this is a necessary quality check for the validity of the chosen parameters, which are then used to model the influence of the interfaces between the Heusler electrode and the Ag spacer.

4.3 DFT study of ideal bulk-like terminated Co_2MnSi/Ag interfaces

We start with presenting the electronic properties of bulk-like terminated CMS/Ag interfaces. The lattice parameters of the conventional cubic CMS (5.66 Å) and Ag (4.09 Å) unit cells are different; however they are related via $\sqrt{2}$ relationship, which gives only 2% lattice mismatch. Hence, in order to achieve epitaxy between these two structures a rotation (of either CMS or Ag) of 45^0 around the [001] direction is required. This means that the crystallographic orientations between the electrode and spacer are given by the following relationships: CMS(001)||Ag(001) and CMS[110]||Ag[100]. The interfaces considered in this work are parallel to the (001) planes of CMS (or equivalently to the (001) planes of Ag).

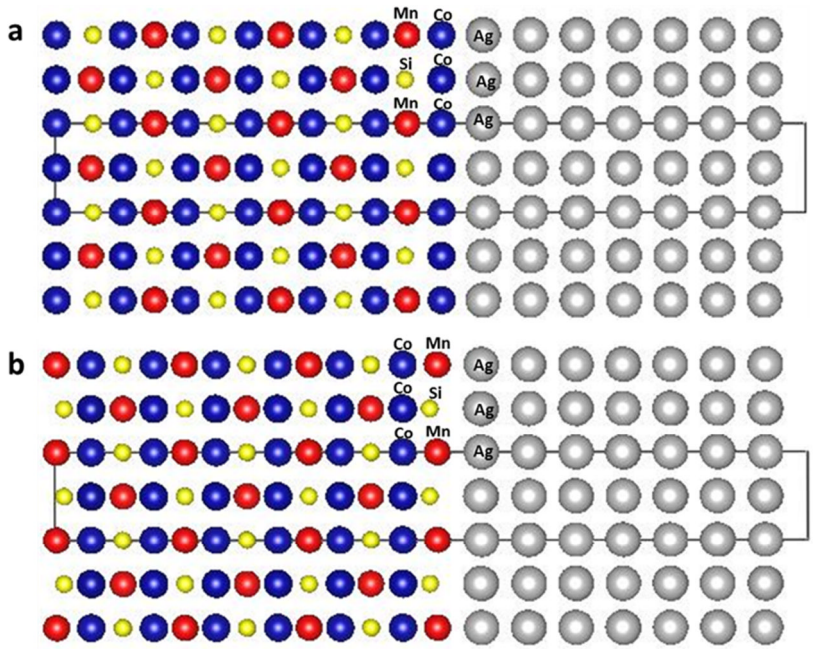

Figure 4.2 Structural models of the ideal bulk-like terminated CMS/Ag interfaces: a) with Co-Co terminated CMS, b) with Mn-Si terminated CMS. The black rectangles outline the supercell size.

It is worth noting that along the considered [001] direction, the atomic planes stacking sequence of CMS consists of alternating Co-Co and Mn-Si planes. There are two Co atoms within the unit cell in a Co-Co plane, while one Mn and one Si for the Mn-Si atomic plane. This means that the interface for the case of bulk-like termination can be created by joining either a Co-Co or Mn-Si with a Ag plane.

Hence, the CMS electrode can terminate on either Co-Co or Mn-Si plane leading to two possible bulk-like terminated interfaces. For simplicity in notation, the interface where the CMS part terminates on a Co-Co plane will be referred to as Co/Ag interface, while the interface where the CMS part terminates on Mn-Si plane will be referred to as Mn-Si/Ag interface. In **Figure 4.2** the structural models for both interface terminations are shown after the performed geometry optimisation.

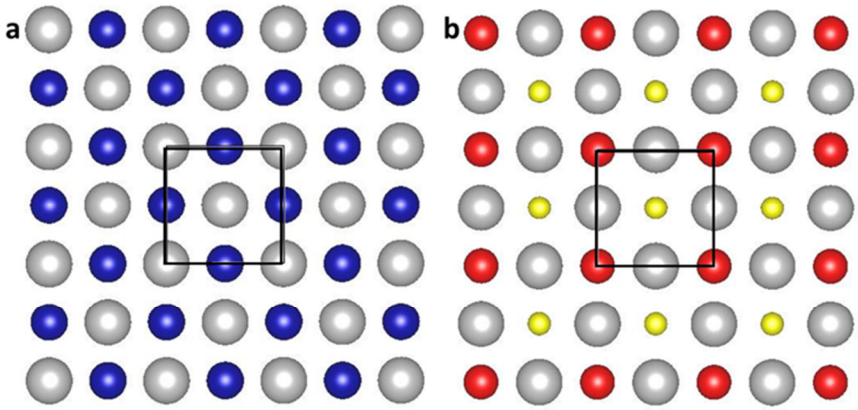

Figure 4.3 A top-view of the interface atomic planes (nearest planes from both CMS and Ag part of the supercell), viewed along the [001] direction, for: a) Co/Ag and b) Mn-Si/Ag interface. The rectangles represent the repeat unit. Colour coding is the same as in the **Figure 4.2**.

Before we proceed to a discussion of the results, it should be mentioned that another important factor which was taken into account while building the models is the relative in-plane positioning between the CMS and Ag interface planes. There are certainly an infinite number of mathematically possible relative in-plane shifts between the CMS and Ag lattice, however from symmetry principles one can easily conclude that, for an example, for the Co/Ag interface, Co atoms can sit on top of Ag atoms or in the centres of the Ag lattice, as illustrated in **Figure 4.3**. The same applies to the Mn-Si/Ag interface. The lower energy position was checked by performing energy calculations for

the two different cases. As expected, the results showed that the centred position has lower energy compared to the case when atoms sit on top.

The observations and analysis of the optimised coordinates shows that for the Co/Ag interface, the nearest Co-layer to the interface shows 13% out-of-plane relaxation (relative to its bulk-like position) towards the Ag spacer. In contrast to the Co/Ag interface, when the interface is terminated on a Mn-Si atomic plane, it can be seen that the distance Si-Ag (projected) is significantly different compared to that between Mn and Ag (projected). In this case, the atomic relaxed coordinates show that Si is 18% further from Ag compared to Mn. This significant difference, suggests that the bulk-like Mn-Si termination is likely to transform into other more energetically favourable termination.

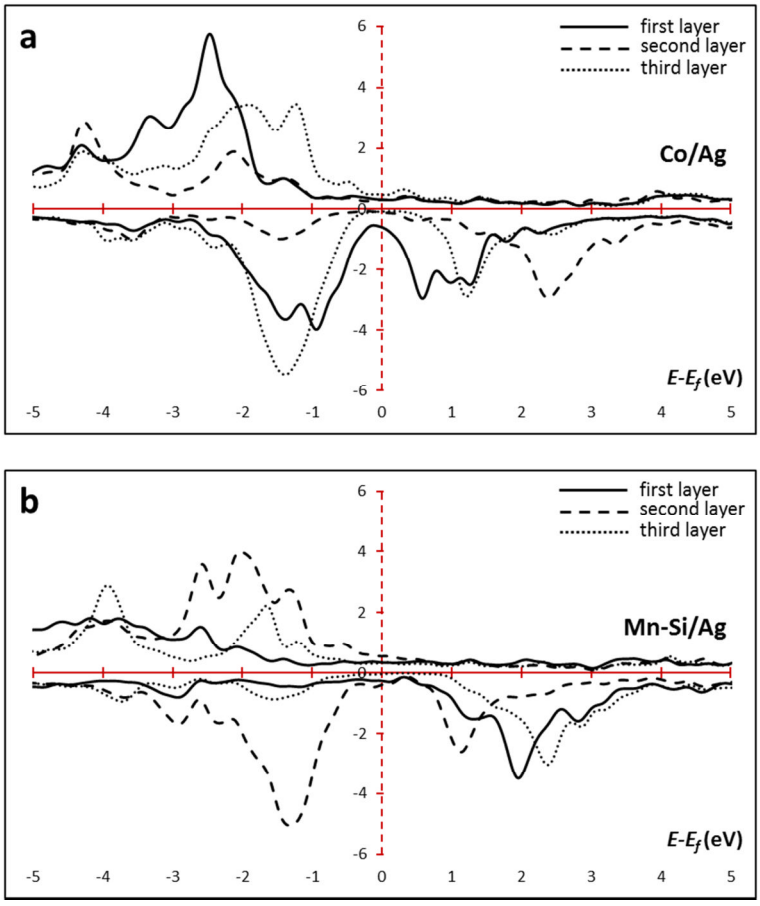

Figure 4.4 Spin-polarised PDOS (electrons/eV) for the first three atomic layers of the CMS electrode in the case of: a) Co/Ag and b) Mn-Si/Ag interface. Solid, dashed and dotted lines represent the PDOS for the first, second and third CMS atomic layer respectively.

Layer-by-layer PDOS for both interfaces are shown in **Figure 4.4**. These results were used to calculate the spin-polarisation (SP) at the Fermi-level for both Co/Ag and Mn-Si/Ag interfaces. The presented plots are the spin-polarised PDOS from the first three atomic planes of the CMS electrode. In both models, the SP at the interface is significantly different compared to the bulk-like region (which is 100% positively spin-polarised) of the CMS electrode. The SP value of the first layer is: -31% and +14% for the Co/Ag and Mn-Si/Ag models, respectively. These results show that the Co/Ag interfacial SP becomes inverted i.e. negative SP, while at the Mn-Si/Ag interface the SP is positive, however it is significantly reduced. By following the layer-by-layer SP from the interface towards the bulk-like part, it can be noticed that for both interfaces the SP fully recovers after the first 3-4 atomic planes.

4.4 Comparison with the ideal bulk-like terminated Co_2FeSi/Ag interfaces

It is interesting to note that the trend observed for ideal bulk-like terminated CMS/Ag interfaces does not change when Mn is fully substituted by Fe. The SP value in this case i.e. for CFS/Ag interfaces, for the first atomic layer is as following: -50% and -39% for Co-Co/Ag and Fe-Si/Ag terminations, respectively.

The layer-by-layer PDOS for both models are shown in **Figure 4.5**. Note that for these CFS/Ag bulk-like terminated interfaces, independent of the interface atomic plane termination, the SP of the interface layer is inverted. However, the recovery towards positive 100% SP occurs within 3-4 atomic planes, similarly to the case of CMS/Ag interfaces. Hence, these results show that in both cases, i.e. for CFS and CMS electrodes, the bulk-like Co-Co termination is undesirable since it brings inverted SP at the interface.

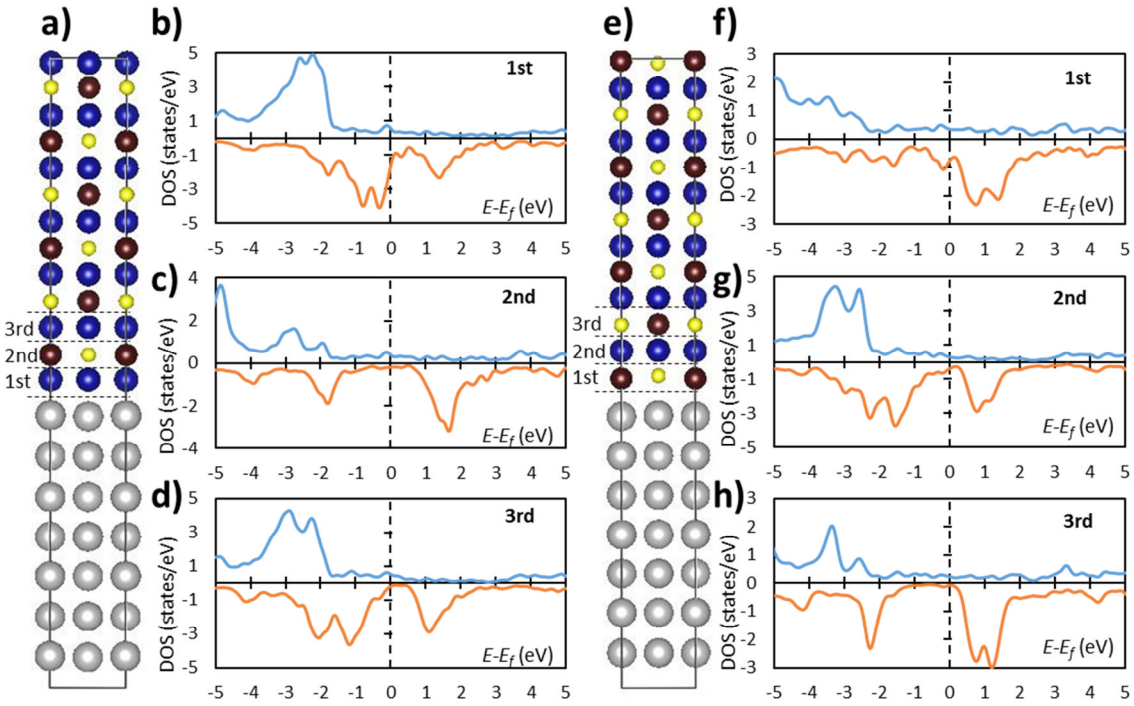

Figure 4.5 a) Structural model of the Co-Co terminated model for the case of a CFS electrode, where the PDOS for the first three atomic layers of CFS are presented in: b), c) and d) respectively. e) Structural model of the Fe-Si terminated model for the case of a CFS electrode, where the PDOS for the first three atomic layers of CFS are presented in: f), g) and h) respectively. Colour coding of the structural models is as follows: Ag - grey, Co - blue, Fe - brown and Si - yellow.

4.5 The structure and growth methods for the spin-valve device

The spin-valve heterostructure used in this thesis was grown by Dr. Mikihiko Oogane at Tohoku University, Japan, on MgO(001) oriented substrate. This spin-valve device has the following layers:

MgO(substrate)/Cr(40 nm)/Ag(50 nm)/CMS(20 nm - bottom electrode)/Ag (5 nm - spacer)/CMS (5 nm - top electrode)/Ru(10 nm - capping layer).

Both Co_2MnSi electrodes have been deposited by sputtering technique using a Co–Mn–Si (Co: 43.7%, Mn: 27.95%, Si: 28.35%; all given as an atomic-%) alloyed target which gives stoichiometric Co_2MnSi composition. After the deposition of both bottom and top CMS electrodes, the structure has been annealed at 500 ^{o}C and 350 ^{o}C respectively in

the sputtering chamber in order to improve the ordering. Overview electron microscopy images of the spin-valve device are presented in the **Figure 4.6**.

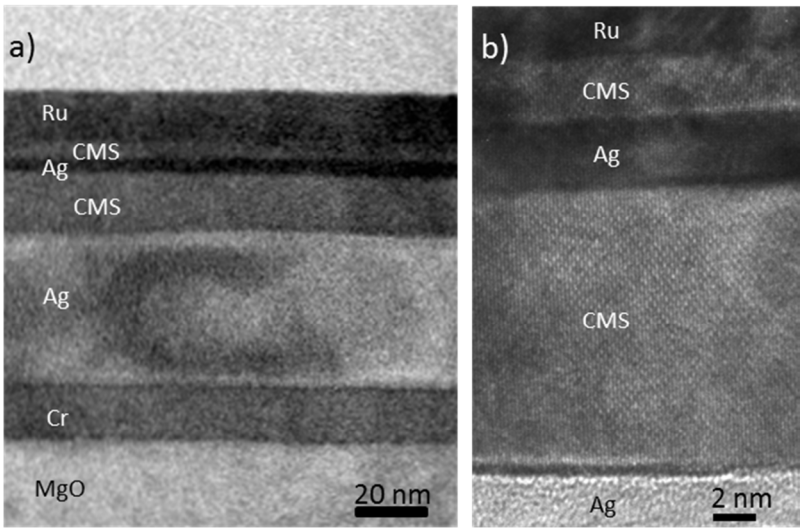

Figure 4.6 a) BF-STEM; b) HRTEM overview images of the spin-valve. The layers which are part of the device are labelled.

4.6 HAADF STEM and DFT study of experimentally realised Co_2MnSi/Ag interface

Cross-sectional specimens were prepared by the conventional methods described in **Chapter 3** i.e. thinning by mechanical polishing and finishing with low energy (3.5 kV) Ar-ion milling. The atomic level HAADF STEM microscopy measurements were performed using an aberration-corrected JEOL ARM microscope operating at 200 kV (at the University of Warwick), and JEOL 2200-FS microscope operating at 200 kV (at JEOL Nanocentre at York).

Figure 4.7 shows overview images of the functional part of the studied spin-valve structure, showing the overall ordering of the CMS electrodes and the abruptness of the interfaces with the Ag spacer.

Since the contrast of the HAADF STEM images depends on the atomic number (Z) as $\sim Z^2$, this enables to distinguish uniquely chemical elements. The microscopy here is performed along the $[1\bar{1}0]$ crystallographic direction of the CMS electrodes. In this direction, as discussed in **Section 2.4.2**, along the atomic columns different elements are

distributed, i.e. Co, Mn, Si are all in different atomic columns, hence they can be easily identified.

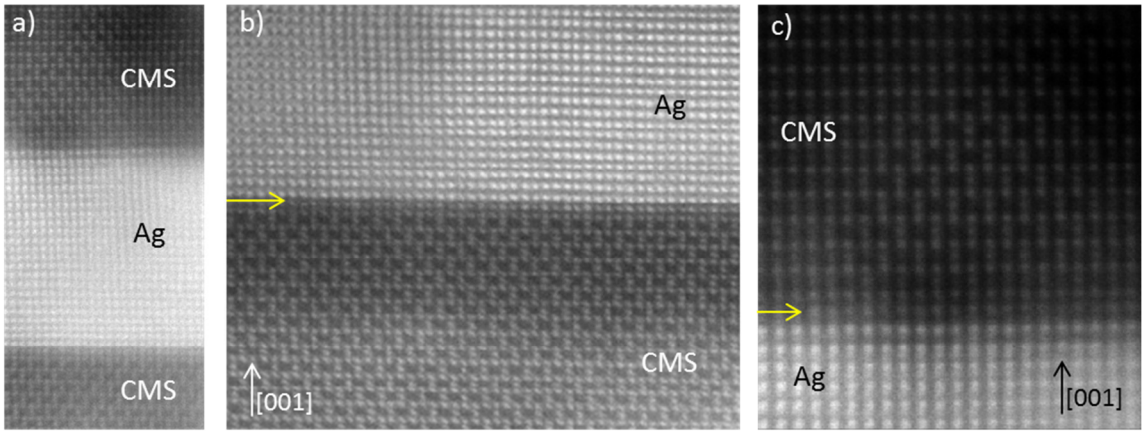

Figure 4.7 HAADF STEM overview images of a) the functional part of the spin-valve CMS (top electrode) / Ag (spacer) / CMS (bottom electrode); b) magnified view of the CMS(bottom electrode)/Ag(spacer) interface; c) magnified view of the CMS(top electrode)/Ag(spacer) interface. All images are taken along the [1-10] crystallographic direction. The yellow arrows are to outline the existence of an additional layer at the both interfaces, between the CMS electrodes and Ag spacer.

It can be noticed that both electrodes have very good structural ordering. The bottom electrode shows an ideal $L2_1$ ordering while the top electrode shows mainly $L2_1$ but regions with *B2* ordering are also present. The reason for this is the difference in annealing temperatures for the top and bottom electrodes. The top electrode has been annealed at lower temperature (350 ^{o}C) which resulted in partial $L2_1$ ordering with inclusions of *B2* ordering. The bottom electrode has been annealed at 500 ^{o}C which results in an ordered $L2_1$ structure. Lower annealing temperature for the top electrode is required in order to keep the structural integrity of the CMS/Ag interfaces after the deposition of the thin Ag metallic spacer.

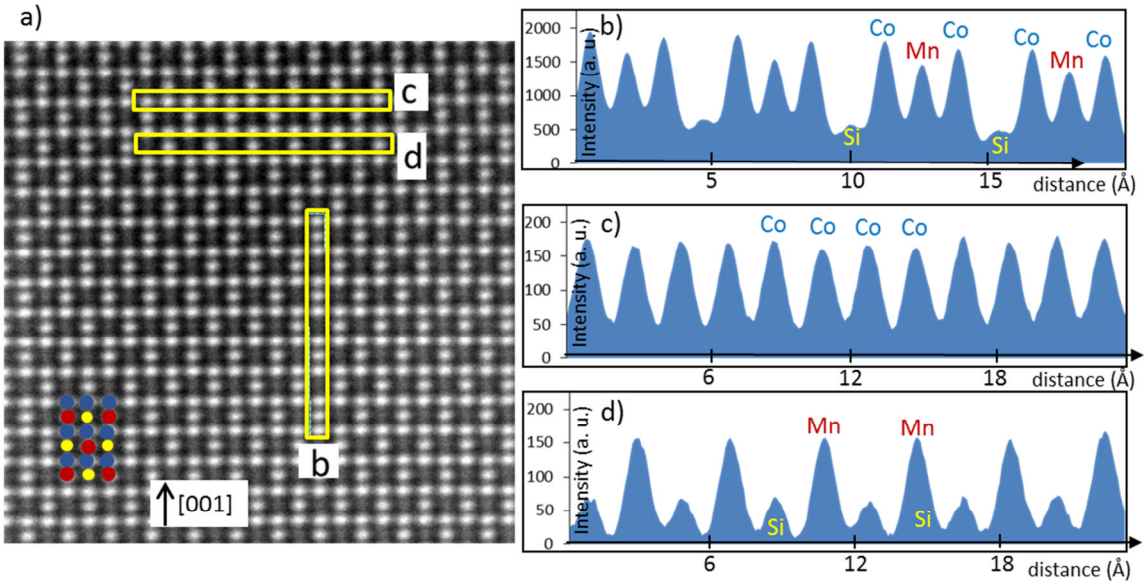

Figure 4.8 a) HAADF STEM image of the bulk-like part of the bottom CMS electrode showing perfect $L2_1$ ordering. The intensity profiles shown in b), c) and d) are taken along the yellow rectangles (averaged along the smaller dimension) labelled in (a) with the corresponding letter. The colour coding of the overlaid structural model is as following: Co – blue, Mn – red, Si – yellow.

Figure 4.8a is an atomic resolution HAADF STEM image of the bulk-like part of the bottom CMS electrode. This image shows the characteristic atomic planes stacking sequence along the [001] direction which consists of alternating Co-Co and Mn-Si planes. The intensity profile given in **Figure 4.8b** demonstrates that even though Co and Mn have very similar atomic number, the distinctive Co-Mn-Co pattern can be distinguished. However, due to the intensity variations coming from the background or thickness effect it can be very challenging only from the absolute intensities to conclude if an atomic column is Co or Mn. This is particularly the case at the interface regions as shown in the discussion below. **Figure 4.8c,d** show both uniform distribution of intensity coming from the Co atomic columns at a (001) Co-Co atomic plane as well as alternating low-high intensity pattern along the Mn-Si (001) plane which is a characteristic for the $L2_1$ ordering.

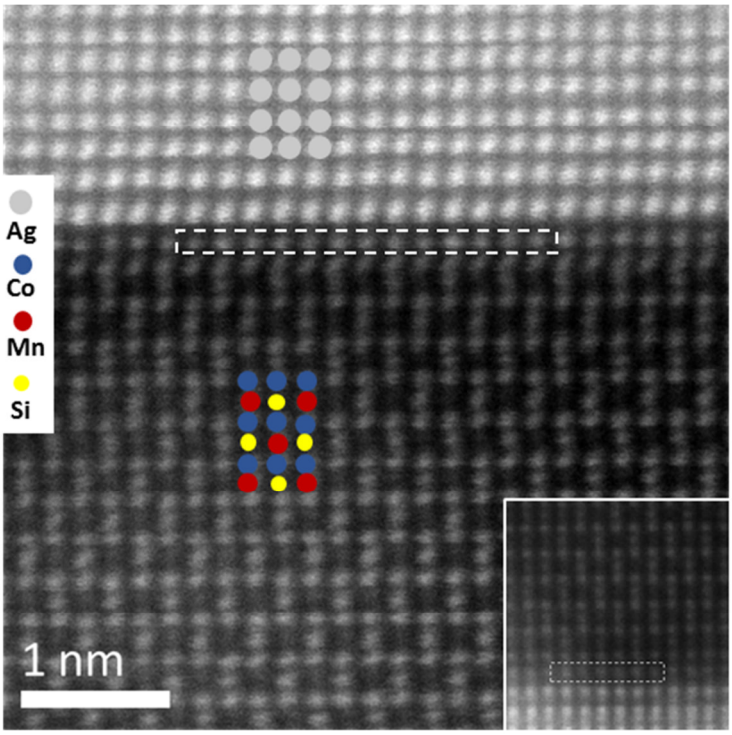

Figure 4.9 HAADF STEM images of the CMS (bottom electrode)/Ag and CMS (top electrode)/Ag (given as inset) interface, with overlaid structural models. Dashed rectangles indicate the extra layer present at both interfaces.

Knowing the atomic structure of the bulk-like part of the CMS electrodes, next we focus on the atomic structure in the interface vicinity. Once the atomic structure at the interface is determined, that will allow us to construct realistic models and by DFT calculate how the spin-polarisation changes towards the interface.

Atomic resolution HAADF STEM images of both CMS (top electrode, shown as an inset)/Ag and Ag/CMS (bottom electrode) interfaces are presented in **Figure 4.9.** If we follow the bulk-like atomic layer-by-layer stacking sequence, the second nearest layer to the interface can be identified as a Co layer. The additional layer above the Co layer (for the bottom electrode), following the bulk-like atomic stacking is expected to be a Mn-Si atomic plane. However, the intensity contrast of the HAADF STEM image clearly shows that Mn-Si atomic plane as an interface termination is not present. Hence, the interface is not determined by a bulk-like termination. It can be noticed that exactly the same atomic plane stacking is observed for both interfaces, top and bottom. This phenomenon indicates that the formation of this structurally non-bulk layer (additional atomic plane) is

energetically favourable over the bulk-like terminations considered in the beginning of this chapter for the ideal interfaces.

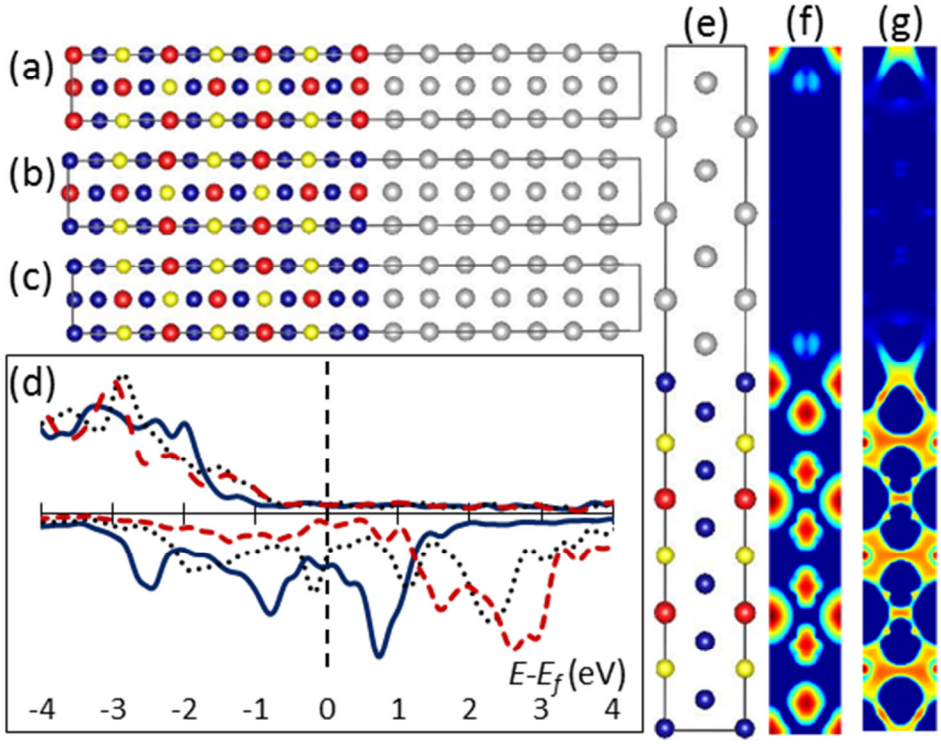

Figure 4.10 Structural models for a) Mn-Mn/Ag, b) Mn-Co/Ag c) Co-Co/Ag interface. d) Spin-polarised PDOS (electrons/eV) for the first (i.e. the non-bulk-like) atomic interface layer shown with: blue solid curve for Co-Co/Ag, black dotted curve for Mn-Co/Ag and red dashed for Mn-Mn/Ag. e) (100) atomic plane viewed along the (100) direction for the Co-Co/Ag supercell, with the net spin f) up, g) down density plots for this atomic plane; red colour represents maximum while blue minimum density.

As discussed above, for the Mn-Si/Ag interface there is a large relaxation (at the interface) of the Si atoms geometrical positions towards the bulk CMS part. This phenomenon suggests that there will be a driving force to substitute Si at the interface plane with other element, explaining the formation of the observed structurally non-bulk-like layer. Hence, the formation of this additional interface layer can be correlated with the buckled structure at the ideal Mn-Si/Ag interface.

Comparing the atomic column intensities of the interface layer with the bulk-like Mn and Co atomic columns (**Figure 4.9**), indicates that this additional layer could be

either single Mn or Co, or mixed Co-Mn atomic plane. Due to the very bright contrast from Ag and very dark from Si, these two elements can be excluded as possible to form this layer.

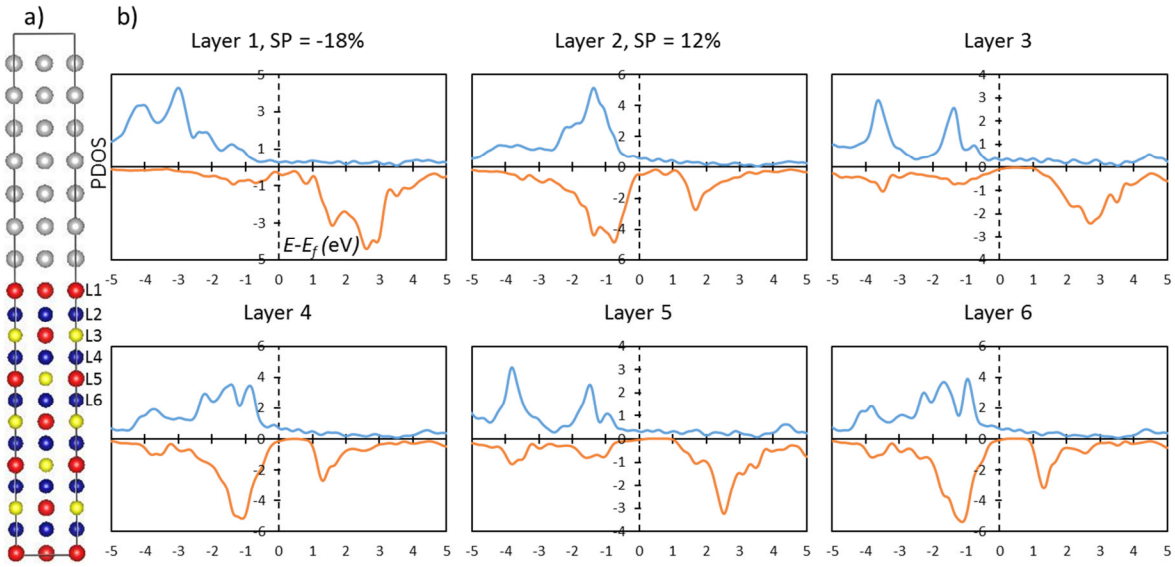

Figure 4.11 a) Structural model and b) layer-by-layer PDOS for the Mn-Mn/Ag interface model. The spin-polarisation at the Fermi-level is given for the first two layers. The labels L1-L6 in (a) stand for Layer 1 – Layer 6, respectively. Colour coding follows previous figures.

Due to the very similar atomic number of Mn and Co, they cannot be uniquely distinguished from the HAADF STEM images, at the interface region. Therefore, in order to provide insight into the influence of this additional non-bulk layer on the interface spin-electronic properties, three representative interface models are built. These correspond to an additional layer of: a) Mn, b) Mn-Co and c) Co (referred to as Mn-Mn/Ag, Mn-Co/Ag and Co-Co/Ag, respectively). All these models are shown in the **Figure 4.10** after the performed geometry optimisation.

Figure 4.10d shows the PDOS of the additional interface layer for all three models. The calculated SP values are -7%, -68% and -73% for Mn, Mn-Co and Co extra layer, respectively. It can be noticed that the SP has reversed sign for all three models and has increasing trend with the increase of concentration of Co.

These results clearly show that the formation of the additional structurally non-bulk layer can significantly modify the SP at the interface, by changing its sign as well as the magnitude, as strikingly observed for the Co terminated interfaces. This result is somehow expected because the Co-Co/Ag model has two monolayers of Co at the interface, hence Co bulk-like electronic structure at the interface can be expected. Note that the bulk Co is strongly negatively spin polarised (-71%).

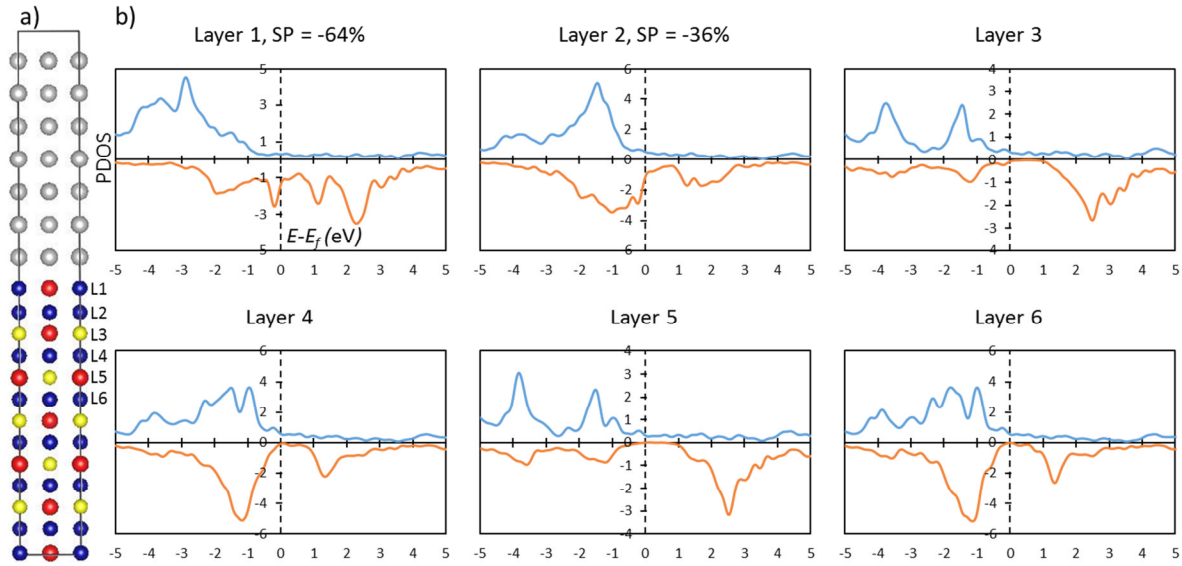

Figure 4.12 a) Structural model and b) layer-by-layer PDOS for the Co-Mn/Ag interface model. The spin-polarisation at the Fermi-level is given for the first two layers. The labels L1-L6 in (a) stand for Layer 1 - Layer 6, respectively. Colour coding follows previous figures.

In **Figure 4.10f,g**, the net spin density (up/down) at (100) plane (**Figure 4.10e**) for the Co-Co/Ag model, are plotted. It can be seen that the net spin-up density does not significantly change at the interface compared to the bulk one. On the other hand, there is localisation of spin-down density around the Co layer. Due to the existence of this almost inversely spin polarised layer, the interface can act as an additional scattering centre for the positively spin-polarised current of the CMS electrode.

For completeness, layer-by-layer PDOS for all three considered structural models are presented in **Figure 4.11**, **Figure 4.12** and **Figure 4.13**. The first interface layer in all models is labelled as 'Layer 1', and PDOS for the next five atomic planes are also calculated and plotted. Since there is a recovery of the spin-polarisation towards the bulk

value after about two atomic planes, the spin-polarisation values only for the first two layers are shown in the figures. The other atomic planes give bulk-like spin-polarisations.

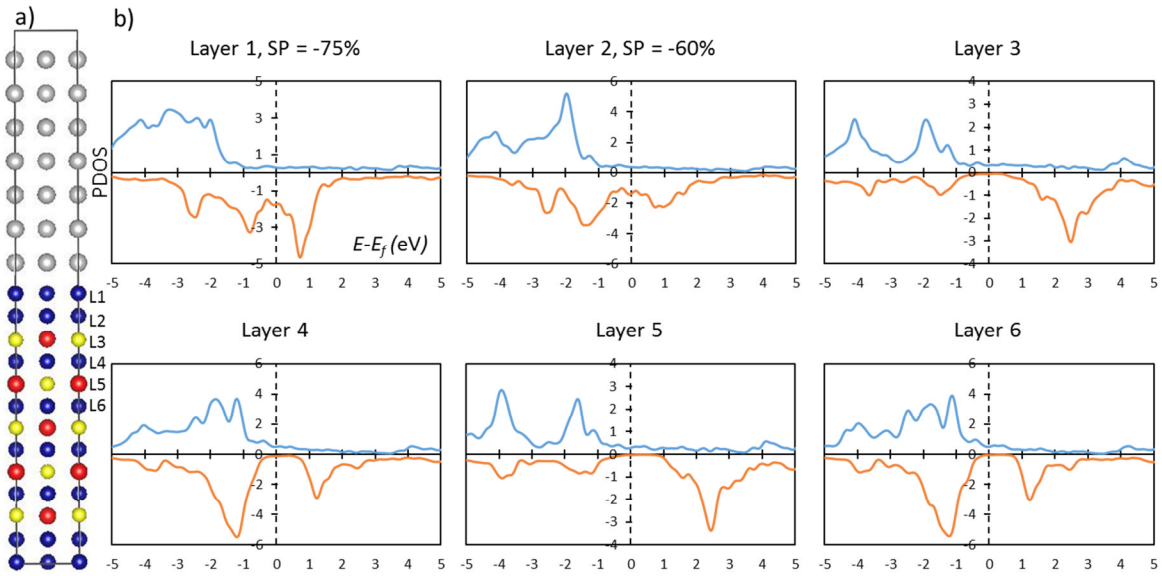

Figure 4.13 a) Structural model and b) layer-by-layer PDOS for the Co-Co/Ag interface model. The spin-polarisation at the Fermi-level is given for the first two layers. The labels L1-L6 in (a) stand for Layer 1 - Layer 6, respectively. Colour coding follows previous figures.

4.7 The influence of minor Ag out-diffusion into the Co_2MnSi electrode

Finally, the role of outdiffusion of Ag into the CMS electrodes on the SP of the interface will be addressed. Due to the very high atomic number of Ag compared to Co and Mn, significant inter-mixing at the interface would be easily distinguishable in the HAADF STEM images. Detailed analysis of the interface images shows that only very small amount of Ag outdiffuses and almost exclusively to the first interface layer of CMS. An example of an interface region where clearly a presence of Ag is observed is shown in the **Figure 4.14**.

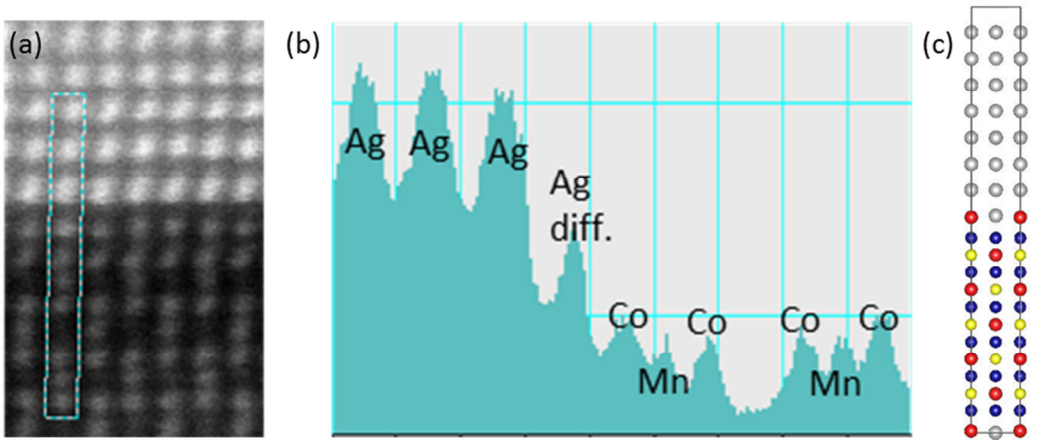

Figure 4.14 Diffusion of Ag into the first CMS layer. a) HAADF STEM image at the CMS/Ag interface. b) Vertical intensity profile of the dashed area in (a) showing small diffusion of Ag in the first CMS layer. c) Mn-Ag/Ag structural model used to estimate the influence of the Ag out-diffusion. The Co-Ag/Ag model is constructed in the same way, the only difference is that the Mn from the first interface atomic plane is replaced with Co.

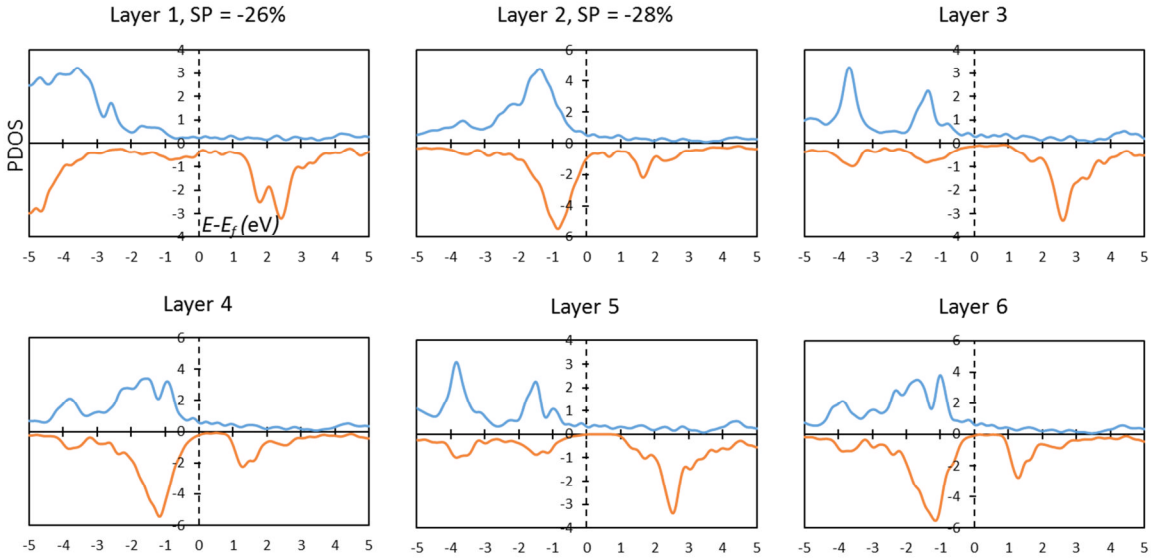

Figure 4.15 Layer-by-layer PDOS for the Mn-Ag/Ag structural model. The spin-polarisation at the Fermi-level is given for the first two layers.

In order to understand the effect of Ag diffusion on the interface electronic structure, we create two interface models that incorporate Ag within the first interface layer corresponding to a diffusion of Ag into the Mn-Mn/Ag or Co-Co/Ag interface layer.

These will be labelled as Mn-Ag/Ag and Co-Ag/Ag, respectively. The atomic structure after the geometry optimisation for the Mn-Ag/Ag interface model is shown in **Figure 4.14c**.

The spin-polarised layer-by-layer PDOS for the interface layers for both Mn-Ag/Ag and Co-Ag/Ag models are shown in **Figure 4.15** and **Figure 4.16**, respectively. The results show that the trend of the spin-polarisation is not considerably affected when Ag atoms out-diffuse into the first interface layer. In other words, Mn-Ag/Ag shows similar spin-polarisation at the Fermi-level to that of Mn-Mn/Ag interface model, while Co-Ag/Ag similar to that of the Co-Co/Ag interface model.

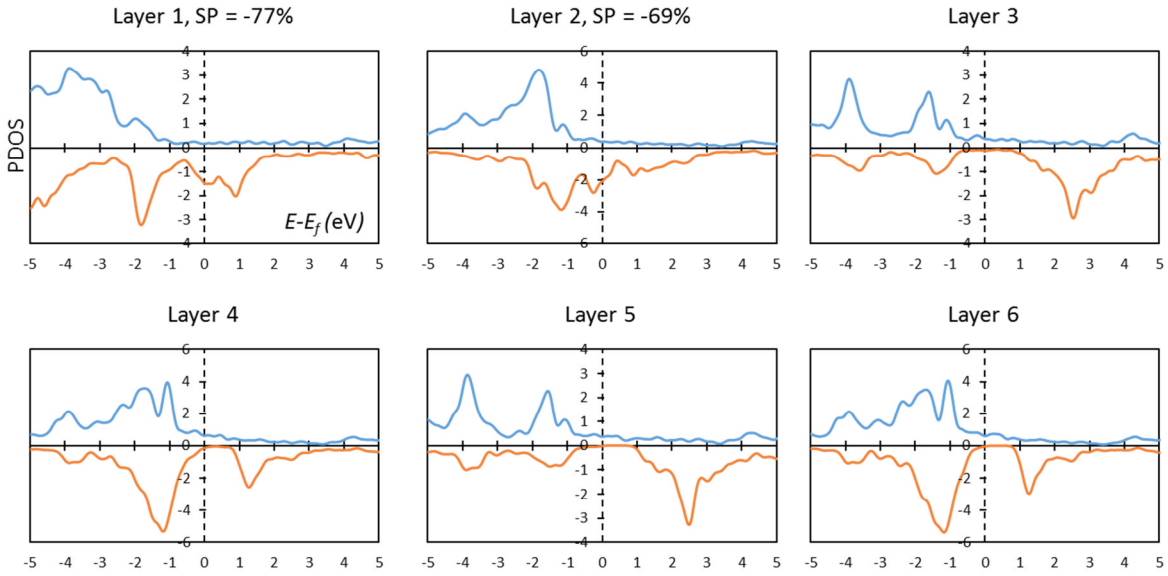

Figure 4.16 Layer-by-layer PDOS for the Co-Ag/Ag structural model. The spin-polarisation at the Fermi-level is given for the first two layers.

It should be also noted that the modelled out-diffusion is quite high (50%) as the first interface plane contains two atoms in the considered supercell, one of which is Ag. Note that the experimental images show very low out-diffusion. In order to model such low out-diffusion it is required to create a very big supercell which in turns requires huge amount of computer time. However, this is not required since even for large out-diffusion of Ag, the spin-electronic structure at the Fermi-level is not significantly affected. These findings show that as long as the presence of Ag is within the interfacial layer, which was experimentally showed to be the case, the properties of the interface are not significantly affected.

4.8 Conclusions

In summary, by density functional theory calculations bulk-like terminated CMS/Ag interfaces were studied and it was shown that the interface spin-polarisation of these interfaces strongly depends of the interface atomic structure. The bulk-like Co/Ag termination creates negatively spin-polarised interface. In contrast to the Co/Ag terminated interface, the ideal bulk-like Mn-Si/Ag interface keeps the character of the SP of the CMS electrode, but with significantly reduced value of 14%.

Atomic level structural analysis of sputtered CMS/Ag/CMS layers, part of a spin-valve, shows that the CMS/Ag interface is terminated with an additional structurally non-bulk-like Co/Mn layer, observed for both CMS(top)/Ag and Ag/CMS(bottom) interfaces. Independently of its chemical nature, this additional interface layer reverses the spin polarisation, with the highest negative SP value calculated for the Co-Co/Ag interface. This study showed that although the electrodes are ideally ordered and the interface is abrupt, significant decrease of the performance can be expected due to the formation of the additional layer.

Finally, the DFT calculations for models describing Ag out-diffusion into the first interface layer: Mn-Ag/Ag and Co-Ag/Ag showed that Ag presence within the first interfacial layer of CMS does not significantly affect the spin-electronic structure.

We can conclude that the interfacial spin-polarisation which in turn determines the performance of the CMS based spin-valve heterostructures, is strongly correlated with the interface atomic structure. This property can be potentially exploited to engineer a heterostructured spin-valves showing better performance.

5 Correlation between the atomic and spin-electronic structure of Heusler alloy/Si(111) interfaces

5.1 Introduction

In this chapter, the atomic and electronic structure of Heusler alloy/Si(111) interfaces is studied. The detailed knowledge of the atomic structure of these interfaces is very important for the integration of Co-based half-metallic materials with the current large scale integrated circuits technologies i.e. for the development of Si-based spintronic devices. In contrast to the interfaces with metals as discussed previously, half-metal/semiconductor interfaces can suffer from the formation of secondary interfacial phases which are detrimental for the spin-electronic structure in the interface vicinity and ultimately determine the spin-injection efficiency into Si.

Here, the atomic structure at the interface with Si(111) is studied on the example of the CFAS Heusler alloy. First, by combining EELS and HAADF STEM imaging, it is determined how the chemical composition changes as we approach the interface. The results show that even though the growth has been performed at room temperature there is an intermixing of the atomic species in the interface vicinity.

Although EELS shows an interdiffusion at the interface, HAADF STEM images will demonstrate that the underlying Heusler structural lattice does not change even at the interface, which is due to the substitutional nature of the interdifussion. This will be used to construct atomistic models of the interface atomic structure and estimate the local magnetic moment as well as spin-polarisation. DFT calculations will show that the changes in local chemical structure bring gradual decrease of the magnetisation over $\sim$3 nm thick region at the interface.

The second part of this chapter is a theoretical study on how using indirectly the out-diffusion one can improve the spin-electronic structure at the interface. Taking into account the substitutional nature of the diffusion, the nominal terminating plane of the

CFAS film is determined, i.e. the atomic plane stacking sequence in the interface vicinity. In case of minimised out-diffusion of Si into the CFAS film, such sharp interface model is becoming representative model of the interface.

Hence, it will be studied how the interface would behave in terms of its spin-electronic structure, in case the growth method is further optimised and gives even narrower region of out-diffusion. It will be shown that although such an interface would be experimentally very challenging to realise, it is not even the desirable one. In other words, in the limit of a sharp interface between Si and CFAS, there are interface states which reverse the spin-polarisation at the interface, making this atomic structure undesirable for applications.

An interfacial atomic structure that gives very high spin-polarisation across all interface layers is proposed. By adding a monolayer of $CoSi_2$, it is shown that such structure will significantly improve the interfacial properties, and also such layer is thermodynamically stable to exist at the interface. This will be further confirmed by direct observations of such layers at the interface by employing HAADF STEM. Finally, it will be demonstrated that the monolayer not only would improve the spin-electronic structure across the interface but also pin the Fermi-level near the conduction band edge, both desirable for efficient spin-injection into the Si substrate.

The results obtained during this study are published in Ref. [152] and Ref. [112].

5.2 Growth and microscopy methods

The CFAS/Si heterostructure has been grown by Dr Shinya Yamada at Osaka University, Japan. A 25 nm-thick CFAS film has been prepared by co-deposition of Co, Fe, Si and Al using molecular beam epitaxy, on a cleaned 10 x 10 mm^2 Si (111) substrate at room temperature [153, 154].

Cross-sectional TEM samples were prepared by the conventional methods that include mechanical thinning and finishing with Ar ion-milling. TEM imaging and SAED were performed using JEOL 2011 microscope operating at 200 kV. Atomic level imaging and EELS were performed on a Nion UltraSTEM 100 microscope at SuperSTEM Laboratory, Daresbury UK with the help from Dr Demie Kepaptsoglou. The microscope was operated

at 100 kV, with a convergence angle of 30 mrad; the inner detector angle for HAADF STEM imaging and the EELS collection angle were 76 mrad and 31 mrad, respectively.

5.3 Low magnification imaging and selected area electron diffraction

We start with an overview TEM imaging of the sample as shown in **Figure 5.1**. The low magnification image presented in **Figure 5.1a** shows that the grown CFAS film has a uniform thickness of 25 nm and that it forms an abrupt (structurally) interface with the Si substrate. The film/substrate interface abruptness is also observed at the high magnification TEM image presented in **Figure 5.1b**, which additionally shows the atomic planes contrast fringes.

Next, a SAED pattern is recorded in order to reveal the crystallinity of the film and the epitaxial relationships with the substrate. The SAED pattern is presented in the **Figure 5.2a**, recorded from a region which covers Si substrate and CFAS film. This figure demonstrates a single crystal nature of the CFAS film and the epitaxy with the substrate.

Taking into account the relatively small lattice mismatch between CFAS and Si of ~4%, in case of a simple cube-on-cube epitaxy we would expect observation of two very similar i.e. almost overlapping diffraction patterns in the recorded SAED pattern. However, the recorded SAED shows a specific epitaxial relationship between the CFAS and Si, which is not the standard 'cube-on-cube' epitaxy.

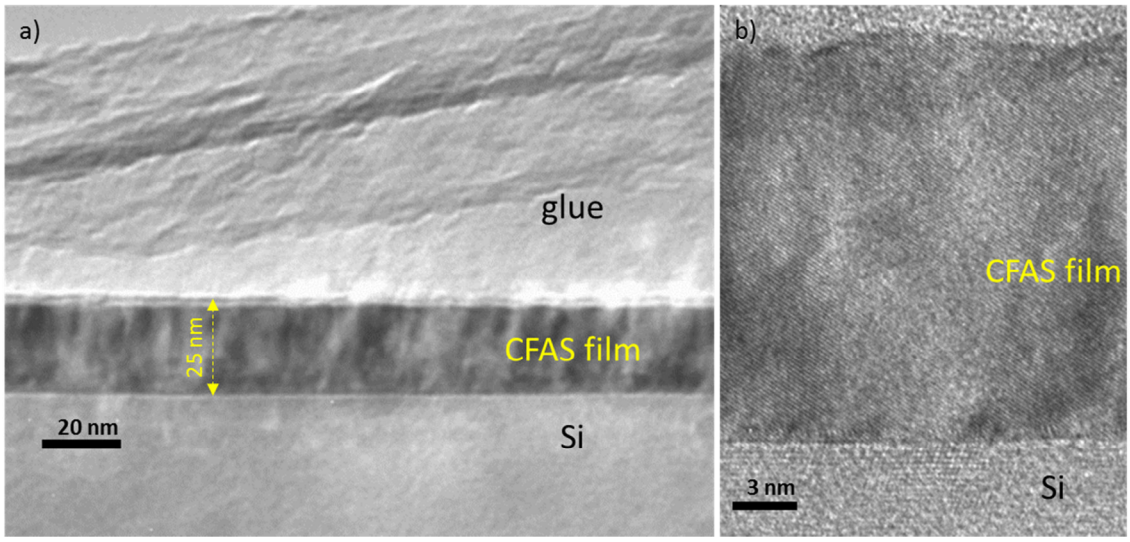

Figure 5.1 a) Low magnification and b) high magnification TEM image showing that the film is uniform and that the interface with the substrate is structurally abrupt.

In order to determine the exact epitaxial relationship SAED simulations are performed using the CrystalKit software package [110]. The case of simple epitaxy is shown in **Figure 5.2b**. By twinning the film with respect to the substrate i.e. when these are related by the following relationships: Si$(1\bar{1}0)$ ||CFAS$(\bar{1}10)$ and Si(111)||CFAS(111), we get the SAED pattern shown in **Figure 5.2c.** This pattern is exactly what is observed experimentally, i.e. the comparison between the experimental diffraction pattern and the simulated SAED in **Figure 5.2c** demonstrates that the film/substrate epitaxy is determined by a twinned epitaxial relationship.

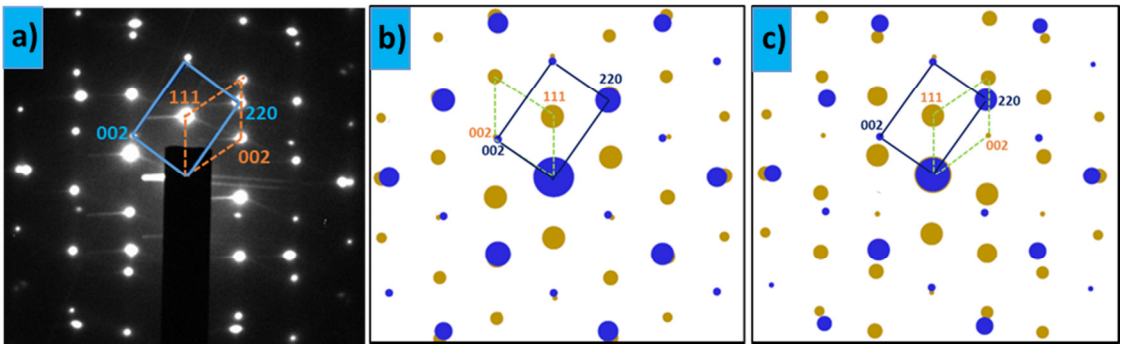

Figure 5.2 a) SAED pattern recorded along the $[1\bar{1}0]$ zone axis from an area that includes both film and substrate. The unit cell of the diffraction pattern is labelled with blue solid for the film and orange dashed rectangle for the Si substrate. b) and c) are simulated SAED patterns along the: b) $[1\bar{1}0]$ viewing direction for both CFAS and Si; c) $[1\bar{1}0]$ viewing direction for CFAS and $[\bar{1}10]$ viewing direction for Si.

5.4 HAADF STEM analysis of the $Co_2FeAl_{0.5}Si_{0.5}$ (CFAS) film atomic structure and ordering

Next, we shall focus on the atomic structure of the grown film. In **Figure 5.3** a sub-Å resolution HAADF STEM image from the bulk-like part of the CFAS film, recorded along the $[1\bar{1}0]$ crystallographic direction, is presented. As discussed before, this zone axis allows us to determine the atomic ordering of the film. For a *B2* ordered film, we would observe alternating high-low atomic columns intensity contrast along the [001] direction, while for $L2_1$ ordering additional intensity variations would appear along a (001) Fe-Si/Al atomic plane due to the significant difference between the atomic number of Fe and Si/Al.

Using the QSTEM software package (an example of QSTEM input file is given in **Appendix 2**), HAADF STEM image simulations are performed for the two structural phases of CFAS. The result for $L2_1$ ordering is presented in **Figure 5.3b** and in **Figure 5.3c** for a *B2* ordered CFAS. For the $L2_1$ structural ordering, both Co and Fe can be easily distinguished from the Al/Si sites. The image simulation for a *B*2 ordered CFAS (**Figure 5.3c**) shows the same atomic column intensities along a Fe-Al/Si plane due to the full intermixing. By comparing the intensity profiles along the [001] crystallographic direction between the simulated images and the recorded HAADF STEM image, it can be concluded that the film has predominantly *B*2 ordering.

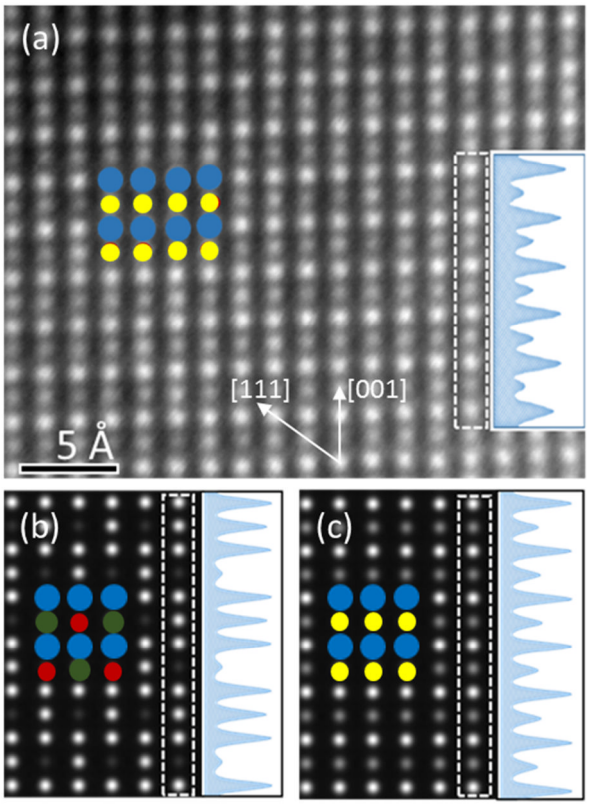

Figure 5.3 a) HAADF STEM image (recorded along the $[1\bar{1}0]$ zone axis) from the CFAS bulk-like part showing its structural ordering. This image is rotated by $\sim 54°$ in order to get [001] along the vertical direction. Simulated HAADF STEM images for CFAS with: b) $L2_1$ and c) *B2* ordering. Insets in (a), (b) and (c) are vertical intensity profiles (averaged along the horizontal dimension of the rectangles) from the areas outlined with the dashed rectangles. By comparing the intensity profile in (a) with those in (b) and (c) we can easily conclude that the film has predominately *B2* ordering. The colour coding of the overlaid structural models: Co - blue; Si/Al - red; Fe – dark green; Fe-Si/Al - yellow.

Hence, the film has a *B2* ordering, and this structural phase, as discussed previously, has very similar properties compared to the ones of $L2_1$. In order to further illustrate this point, DFT calculations are performed and presented in **Figure 5.4**. This figure shows the spin-polarised DOS for both structural phases. Even though there are a small number of states in the vicinity of the Fermi-level for the minority spins, the *B2* ordering still keeps very high spin-polarisation. In addition, these calculations also show that the value of the magnetic moment remains the same in both structural phases and equal to 5.5 μ_B/formula unit.

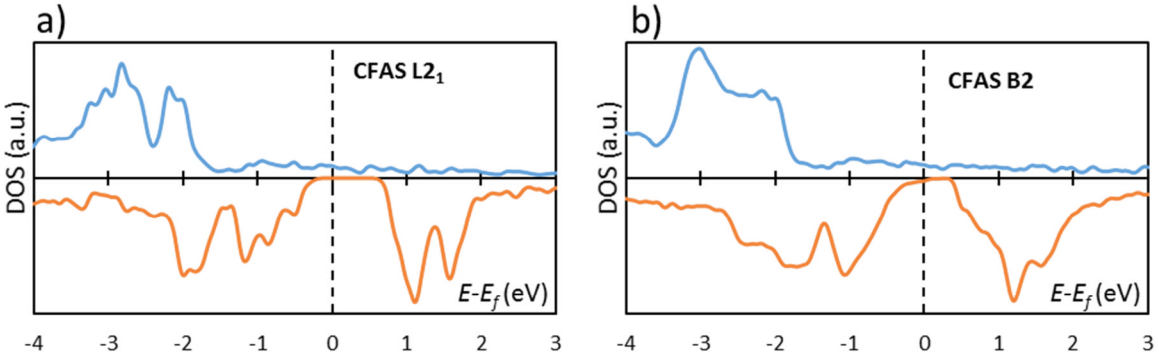

Figure 5.4 Spin-polarised DOS for: a) $L2_1$ and b) *B2* - ordered CFAS. The DOS from spin-up electrons are presented in the top part, while for spin-down in the bottom part of the plots.

5.5 HAADF STEM and EELS at the interface

Once the atomic structure of the film away from the interface is determined, we next proceed to reveal if and how the CFAS atomic structure changes when we approach the interface. **Figure 5.5** is a HAADF STEM image of the interfacial region. It can be clearly seen that the underlying face centered cubic lattice is unaltered even at the interface, however significant changes of the intensity are observed which suggests to possible intermixing between the atomic species. In order to reveal the intermixing, EELS measurements were performed. The measurements presented in the **Figure 5.6** were performed at SuperSTEM, Daresbury, UK by Dr Demie Kepaptsoglou.

Figure 5.6a shows an overview HAADF STEM image, while in **Figure 5.6b-e** the EELS maps generated using the Fe $L_{2,3}$, Co $L_{2,3}$, Si *K* and Al *K* EELS edges are shown. These

maps show that due to intermixing between the atomic species, the chemical composition does not abruptly change when we move from the film into the substrate; a 2 – 3 nm diffusion region emerges. The profiles in **Figure 5.6f** show that there is a gradual decrease of the Fe signal over ~3 nm, while the Co atoms are slightly less affected by the diffusion process; Co signal shows a shoulder at the interface. In other words, Co/Fe composition ratio increases as we approach the interface.

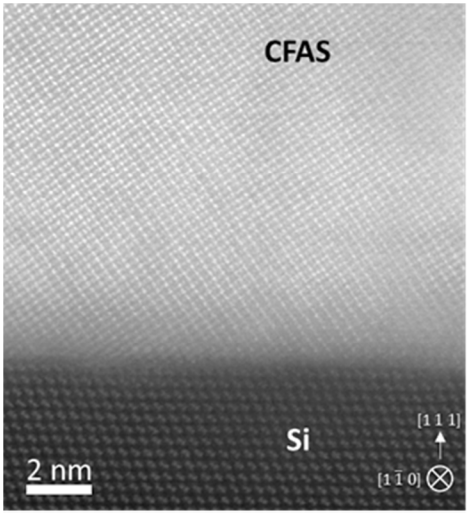

Figure 5.5 Atomic resolution HAADF STEM image of the interface recorded along the [1-10] zone axis.

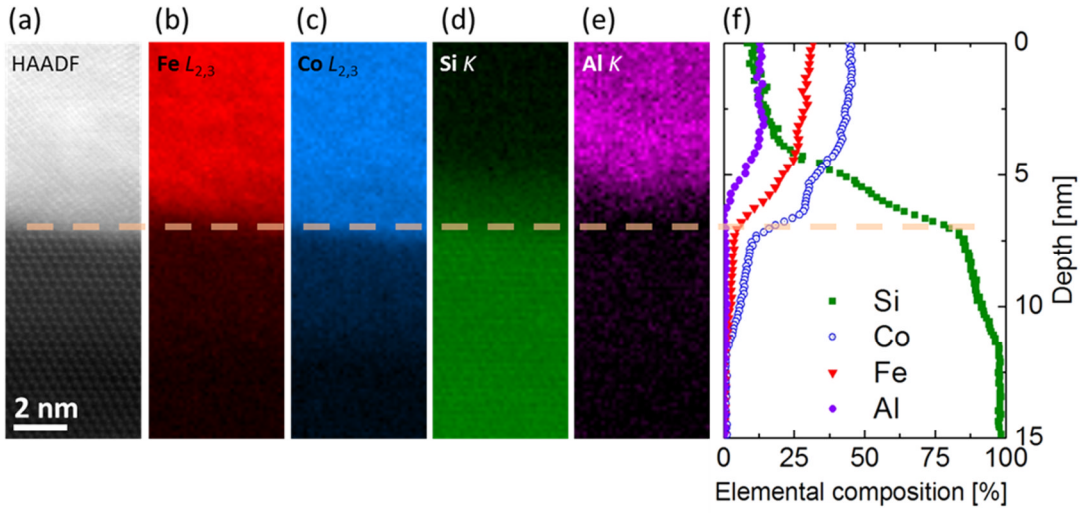

Figure 5.6 EELS analysis of the CFAS/Si interface [112]. a) HAADF STEM image recorded simultaneously with the EELS. Spatially resolved EELS intensity of b) Fe $L_{2,3}$; c) Co $L_{2,3}$; d) Si K and e) Al K edge signal; f) Intensity profiles across the interface for each of the atomic species. The dashed line is a guide for the eye.

5.6 DFT study on the origin of the interfacial phases and their influence on the magnetic moment and spin-electronic structure

The results from the previous section showed that the outdiffused Si is more likely to substitute Fe than Co. In order to explain this phenomenon, starting from the conventional Co_2FeSi 16 atoms cubic unit cell, we create two configurations. In the first, one Si replaces one Fe atom (i.e. $Co_8Fe_3Si_5$), while in the second one, Si replaces a Co atom ($Co_7Fe_4Si_5$).

Total energy calculations show that the formation energy of the $Co_7Fe_4Si_5$ is -0.14 eV/atom, while for $Co_8Fe_3Si_5$ is -0.25 eV/atom. The lower formation energy when Si replaces Fe, indicates that it is more likely the out-diffused Si to substitute Fe than Co, fully consistent with the observations.

For simplicity, and taking into account the similarities between CFS and CFAS, Al was omitted in these calculations; also the EELS profiles show very high Si/Al composition ratio in the interface vicinity, hence this approximation is valid at the interface. These results that Si is predominantly substituting Fe are not surprising because these two elements are very likely to intermix even in the bulk-like CFAS region, resulting in a *B2* ordering.

Label	C_{Fe}(%)	C_{Co}(%)	M	SP(%)	Label	C_{Fe}(%)	C_{Co}(%)	M	SP(%)
CFS	1	1	24	100	c5	0	0.875	4.6	4
c1	0.75	1	20	100	c6	0	0.75	2.7	-17
c2	0.5	1	16	89	c7	0	0.625	1.7	-75
c3	0.25	1	11.6	41	c8	0	0.5	0	0
c4	0	1	7	-22					

Table 5.1 Influence of structural disorder on the magnetic moment [M (μ_B/unit cell)] and spin-polarisation at the Fermi-level. The CFS conventional 16 atoms cubic unit cell is chosen as a reference. C_{Fe} and C_{Co} refer to the concentration (i.e. number of Fe/Co atoms in a considered configuration divided by number of Fe/Co atoms in the CFS bulk unit cell) of Fe and Co, respectively.

The calculations were performed using the CASTEP code with Hubbard-U term set to 2.1 eV for both Co and Fe; plane wave cut-off energy of 600 eV; and Monkhorst-Pack

grid with *k*-points sampling spacing of 0.03·2π $Å^{-1}$. For all considered configurations, the lattice parameters and atoms fractional coordinates were fully geometrically optimised.

Next, it is studied how the atomic structure at the interface affects the magnetic and electronic properties of the CFAS. Taking into account that the CFAS type lattice is unaltered despite the interdiffusion, several atomistic configurations are built all with a Heusler lattice but different chemical composition, **Table 5.1**.

For each of these interfacial phases, constructed using the knowledge of the chemical composition at the interface which was obtained from the EELS measurements, DFT calculations are performed to compute their magnetic moment and spin-polarisation at the Fermi-level. Al is again omitted in this analysis since as discussed above its presence in the interface region is very low, compared to Si.

The first four configurations labelled as *c1*, *c2*, *c3* and *c4* (**Table 5.1**) are constructed by gradually replacing the Fe atoms from the CFS conventional cubic unit cell with Si atoms. This is consistent with the EELS elemental profiles which showed that the outdiffused Si is much more likely to replace Fe atoms. The results show that the magnetic moment gradually decreases from 24 μ_B/unit cell in CFS to 7.0 μ_B/unit cell for the configuration *c4*. As shown in the **Table 5.1**, the spin-polarisation also suffers significantly by this out-diffusion.

Not only Fe but also the Co signal decreases up to a shoulder value where the signal is about half of that in the bulk-like CFAS region. Such phase which is characterised by half of the CFS's Co species being populated, is the $CoSi_2$ structure, which exists as a stable bulk phase, it is not spin polarised and has no magnetic moment. In one of the next sections it will be demonstrated that the formation of such a phase is energetically favourable at the interface.

The next four configurations are constructed according to the discussion in the previous paragraph, i.e. the concentration of Co is gradually decreased until we reach the $CoSi_2$ structure. This series of configurations further decreases the magnetic moment reaching zero for the *c8* configuration. These conclusions obtained by the DFT modelling that the magnetic moment gradually decreases across the interface have been also experimentally confirmed (work in preparation) by polarised neutron reflectivity (PNR) measurements [112]. The spin-polarisation of these phases is even worse and it is often

reversed, as shown in the **Table 5.1**. Spin-polarised DOS for all considered configurations are presented in **Figure 5.7**.

To summarise, these calculations show that the increased Si incorporation in the film leads to a gradual decrease of magnetic moment as well as significant reduction of spin-polarisation in the vicinity of the interface. Therefore, besides the structural integrity of the CFAS/Si interface, the interfacial intermixing has to be fully addressed in order to make use of the CFAS film's half-metallicity.

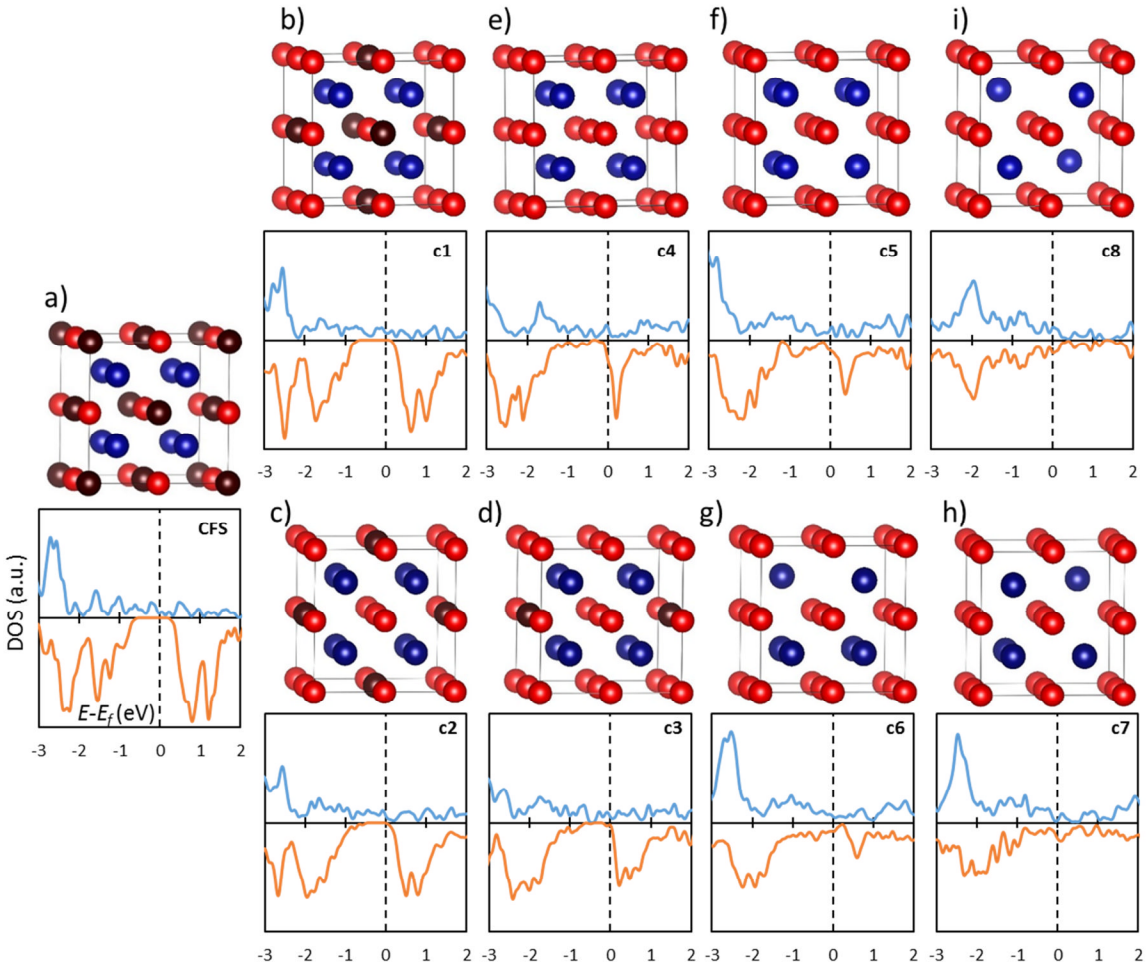

Figure 5.7 Structural models and spin-polarised DOS for: a) bulk CFS; b) - i) *c1-c8* configurations. Colour coding: Co - blue; Fe - brown; Si - red.

5.7 The spin-electronic structure of atomically abrupt Heusler alloy/Si(111) interfaces

So far we studied the correlation between the atomic and electronic structure of the experimentally realised CFAS/Si heterostructure. This growth method has given an interface which is rich in Si, and creates a $2-3$ nm region with significantly reduced spin-polarisation and gradually decreasing magnetic moment. Even though this growth method has provided a relatively narrow interdiffusion region, further optimisation is certainly required in order to create atomically sharp CFAS/Si interfaces.

However, as discussed before, even atomically abrupt interfaces sometimes do not lead to an interfacial electronic structure desirable for spintronic devices. Therefore, it is important to study the interface atomic structure's influence on the SP and consequently determine interface atomic configurations which retain a high SP. In this section, the electronic structure of an atomically sharp CFS(111)/Si(111) interface will be studied. By employing DFT calculations, it will be shown that this interface gives reversed interfacial SP. This SP reversal will be demonstrated that is present also for CFAS and CMS films.

First, the atomically sharp CFS/Si(111) interface is considered. Both the CFS film and Si substrate, are oriented along the [111] crystallographic direction. In addition to the shared [111] direction, the following epitaxial crystallographic relationships are satisfied: CFS$(1\bar{1}0)$ ||Si$(\bar{1}10)$ and CFS$(11\bar{2})$ ||Si$(11\bar{2})$. A twinned epitaxial relationship is chosen since it corresponds to the experimental observations, i.e. the results from the SAED analysis. We shall mention that such twinning is also observed at CFAS/Ge(111) interfaces studied in the next chapter. Moreover, it will be demonstrated, by creating two models: twinned and non-twinned, that there is a relatively big energy difference between these two interface models, which is why we consistently observe twinned CFAS/Si(Ge) interfaces.

In contrast to the CMS/Ag interfaces, the lattice matching (only small lattice mismatch) between the Heusler alloy and Si, allows construction of a supercell model with in-plane lattice parameters equal as the Si (111) and CFS (111) in-plane lattice parameters. DFT calculations are performed using a periodically repeating supercell consisting of six Si and eight CFS unit cells along the [111] direction. The CFS lattice can be

regarded as two superimposed zinc-blende (GaAs type) sublattices, Co-Si and Co-Fe, shifted by half of the [111] diagonal of the conventional cubic unit cell.

This together with the epitaxy with respect to the Si substrate, gives a shared Si (111) interface plane between the film and substrate. Hence, the interface plane in our model is the shared Si (111) plane from the Co-Si zinc-blende sublattice. The validity of such interface termination is confirmed below by the HAADF STEM image from the interface region. Recalling that CFS along [111] crystallographic direction consists of … Co|Fe|Co|Si … atomic plane stacking sequence, the atomic plane stacking in the CFS/Si(111) interface vicinity is …Co|Fe|Co|Si|Si|Si... , as shown in **Figure 5.8** after performed DFT geometry optimisation.

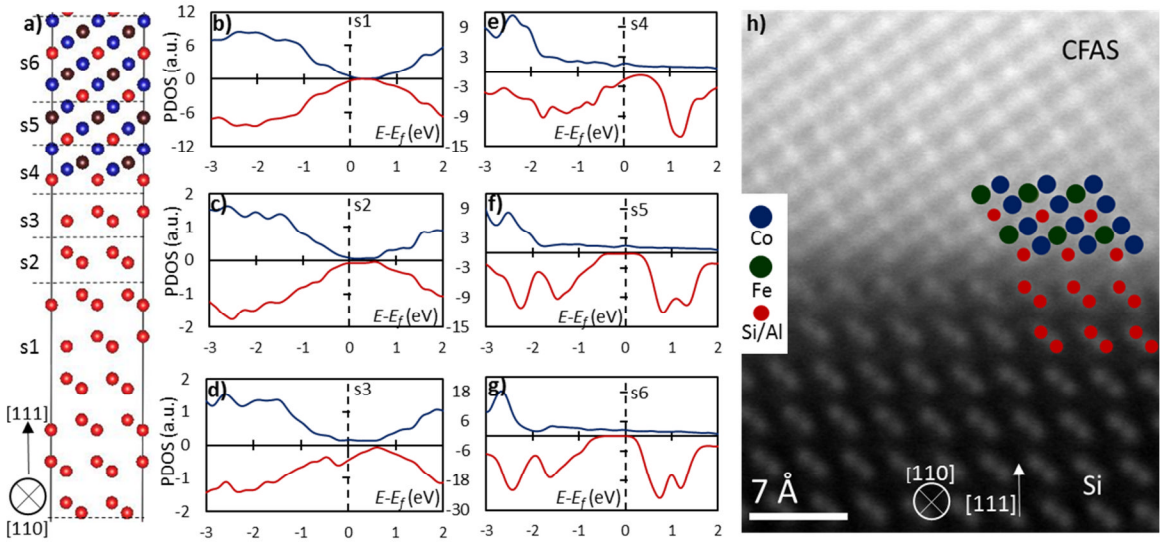

Figure 5.8 a) Structural model of the abrupt CFS/Si interface viewed along the [110] crystallographic direction. Colour coding: red - Si, blue - Co, brown - Fe; b) - g) Spin-polarised PDOS for the regions outlined in (a) and labelled as (*s1*) - (*s6*). Spin-up states are plotted in the top part while spin-down in the bottom part of the plots; h) Atomic resolution HAADF STEM of the CFAS/Si interface imaged along the [110] zone axis, with overlaid structural model.

During the optimisation, the supercell's in-plane (interface plane) lattice parameters were fixed to a value in-between the CFS and Si lattice parameters but closer to the CFS one, in order to minimise the effects of artificial strain on the CFS electronic structure. The perpendicular lattice parameters as well as the fractional coordinates for

all atoms were fully geometry optimised. Cut-off energy was set to 600 eV, while the *k*-point sampling spacing was $0.03 \cdot 2\pi$ Å^{-1}.

Figure 5.8h is an atomically resolved HAADF STEM image that shows the atomic structure of the CFAS/Si(111) interface. The EELS measurements discussed above have shown that Al is supressed from the interface region, hence it is to be expected that CFS/Si(111) interface would show the same interface structure. Even though a sizeable intermixing of the atomic species across the interface is observed, it is possible to reveal the atomic plane stacking sequence at the interface. Analysis of the atomic stacking sequence from the experimental image clearly shows that the interface is determined by the shared Si(111) atomic plane. This allows us to create a model of an atomically sharp CFS/Si(111) interface, and calculate its spin-electronic structure.

The analysis of the atomic positions after the DFT geometry optimisation shows that the first two Co atomic planes (region *s4* in **Figure 5.8a**) at the interface retain their bulk-like positions, while the nearest Fe plane to the substrate shows ~33% relaxation (towards the substrate) compared to its bulk-like position. This relaxation suggests to strong interactions between Fe and Si atoms in the interface region.

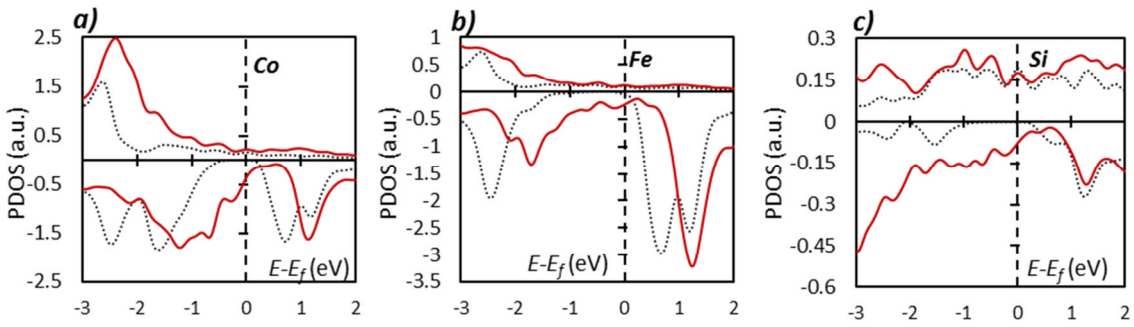

Figure 5.9 PDOS by atomic species for the sharp CFS/Si(111) interface model, calculated for: a) Co; b) Fe and c) Si interfacial atoms (region s4 in **Figure 5.8a**) (shown with red solid curves) and compared with PDOS for the corresponding atom in the bulk-like CFS environment (black dotted curves).

In **Figure 5.9**, the DOS are projected by atomic species, and shown for the Co, Fe and Si atoms at the interface compared to those in the bulk-like environment, i.e. away from the interface region. The interface states reflect the interactions between the

atomic species at the interface region; significant presence of states can be seen for Fe and Si which is expected taking into account their relaxed geometric positions at the interface.

Next, we proceed to the analysis of the layer-by-layer PDOS for the sharp CFS/Si(111) interface model. Spin-polarised PDOS for the layers in the interface vicinity are shown in **Figure 5.8b-g.** Since the model is along the [111] crystallographic direction, where 12 atomic planes of CFS are required to get a unit cell, for simplicity we divide the interface into six regions, labelled as *s1-s6* (**Figure 5.8a**) for which spin-polarised PDOS will be computed. Starting from the bulk-like CFS region we can see that its bulk-like electronic structure extends up to the first third of the CFS unit cell i.e. regions labelled as *s5* and *s6* are essentially not affected by the interface.

However, significant changes emerge into the regions *s3* and *s4* due to the interfacial interactions. Using these PDOS curves, the SP values for *s3* and *s4* regions are calculated and they are: -45% and +6%, respectively. This means that the first third of the CFS unit cell (region *s4*) is basically non-polarised, while the first dumbbell layer from the Si substrate (region *s3*) has induced spin-polarisation with the opposite sign to that of bulk CFS, due to the specific bonding with the film.

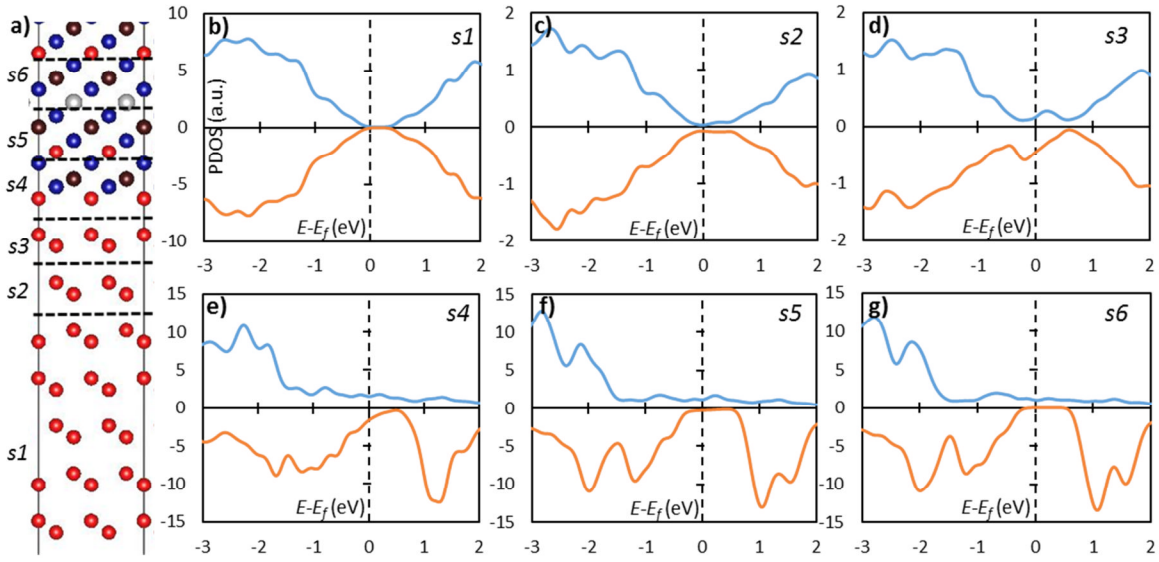

Figure 5.10 DFT study of an atomically sharp CFAS/Si interface. a) Structural model shown along the [110] viewing direction. Colour coding: red - Si, white - Al, blue - Co, brown – Fe; b) - g) Spin-polarised PDOS for the regions outlined in (a) and labelled as (*s1*) - (*s6*).

These states coming from the spin-down electrons are localised to the interfacial Si (*s3* region) and CFS (*s4* region) layers (**Figure 5.8d,e**). Therefore, although the experimentally realised interface has disadvantages due to the intermixing, even if the outdiffusion is completely absent, such interface will not be desirable since it has a reversed SP.

The results from these DFT calculations show that the magnetic moment is also changing near the interface; for the interfacial Fe (region *s4*) is reduced to 3.2 μ_B from the bulk value of 3.3 μ_B; while for Co the magnetic moment decreases from 1.3 μ_B in the bulk to 1.0 μ_B at the interface, gradually over three Co (111) atomic planes.

The reversal of the SP observed at the atomically sharp CFS/Si(111) interface is also present at CFAS/Si (**Figure 5.10**) and CMS/Si (**Figure 5.11**) interfaces. This shows that the observed effect is independent of the exact chemical nature of the Co_2(Fe,Mn)(Al,Si) electrode.

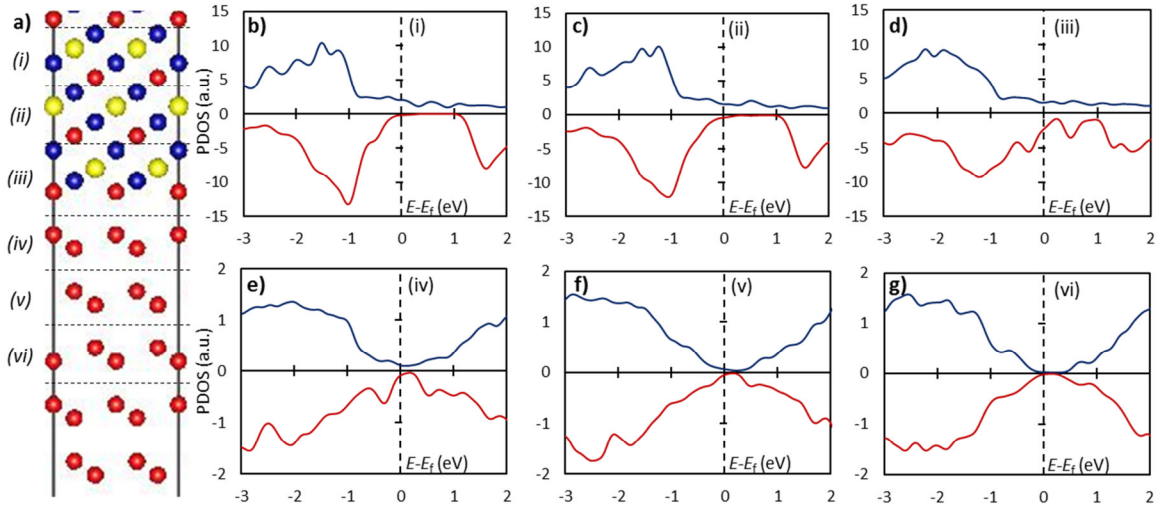

Figure 5.11 DFT study of an atomically sharp CMS/Si interface. a) Structural model shown along the [110] viewing direction. Colour coding: red - Si, blue - Co, yellow – Mn; b) - g) Spin-polarised PDOS for the regions outlined in (a) and labelled as (*i)* - (*vi*).

5.8 Thermodynamically stable structures at the Co_2FeSi/Si(111) interface

From the discussion above, it is clear that further tailoring of the interfacial atomic structure is required in order to avoid the detrimental SP reversal. One way to achieve this aim is to modify the interface atomic structure by adding additional layers between the film and substrate which would be thermodynamically stable to exist as such at the interface. Such layers would be required to have a similar lattice to that of the film and substrate and also would be ideal if they have similar chemical composition with them. An addition of layers from the experimentally observed interfacial silicide phases would satisfy both requirements, i.e. it is expected these to be stable and fit with the film and substrate lattices.

The exact atomic structure at the interface depends strongly on the kinetic effects during the growth, however we can estimate which silicide structure is most energetically favourable to exist at the interface. From the family of all Co and Fe silicides, $CoSi_2$ and Fe_3Si are of particular interest due to their crystal lattice match to that of CFS. The $CoSi_2$ silicide can be obtained starting from the CFS structure, if we remove one of the two Co sublattices and replace the Fe sublattice by Si. Similarly, by replacing the two Co sublattices in CFS with Fe, the Fe_3Si silicide is obtained. A visualisation of these structures is shown in the **Figure 5.12**.

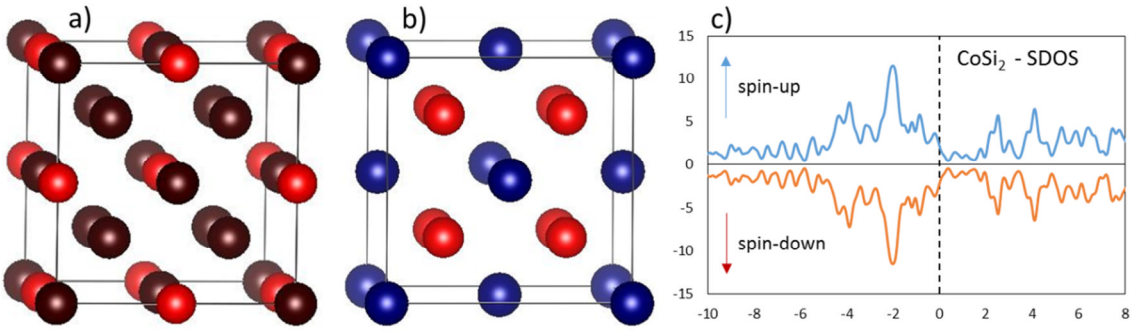

Figure 5.12 Visualisation of the crystal structures of: a) Fe_3Si; b) $CoSi_2$. Colour coding: Fe - brown, Si - red, Co – blue; c) Spin-polarised DOS for bulk $CoSi_2$.

DFT calculations on the following bulk structures: Co_2FeSi, Si, Fe_3Si and $CoSi_2$ give: (in units: eV/formula unit): -2767.75; -162.70; -2450.37; -1247.50, respectively, for their

total energies. If we add up the energies of 3 Co_2FeSi + 10 Si and compare with the energy of 6 $CoSi_2$ + Fe_3Si, we get an energy difference of 5.1 eV in favour of silicide's formation. Although this is an estimate which ignores the interface contributions, these results are in agreement with the observations that at the CFS/Si interface formation of interfacial silicides phases is more favourable compared to preserving atomically abrupt interface.

Additional calculations show that the formation energy of $CoSi_2$ is -0.37 eV/atom, while for Fe_3Si is -0.35 eV/atom, which means that amongst the silicide phases which share similar lattice structure with that of the film and substrate, $CoSi_2$ is the most likely phase to be formed. These formation energies of $CoSi_2$ and Fe_3Si were obtained by calculating the total energies of bulk Co, Fe, Si, Fe_3Si, and $CoSi_2$ per formula unit, followed by comparison of: *i*) the energies of Co + 2 Si with $CoSi_2$ to get the formation energy of $CoSi_2$; and *ii*) comparing 3 Fe + Si with Fe_3Si to get the formation energy of Fe_3Si.

In addition to this formation energy analysis suggesting a likely formation of $CoSi_2$ phase at the interface, the relative chemical composition between the film and substrate would also favour $CoSi_2$ compared to Fe_3Si. In other words, the Co composition would gradually increase from zero in Si, one sublattice in $CoSi_2$, to two sublattices in Co_2FeSi, in contrast to the Fe_3Si stoichiometry which would require a peak of the Fe concentration within several atomic planes at the interface. These conclusions for the stability of $CoSi_2$ as an interfacial phase were further confirmed by experimental verification of a formation of $CoSi_2$ nano-islands with thicknesses of 1 - 2 monolayers at the CFAS/Si interface, as shown in **Figure 5.13**. It is also worth noting that the stability of the interface between $CoSi_2$ and Si has been already experimentally verified by the growth of thick $CoSi_2$ films on Si [155].

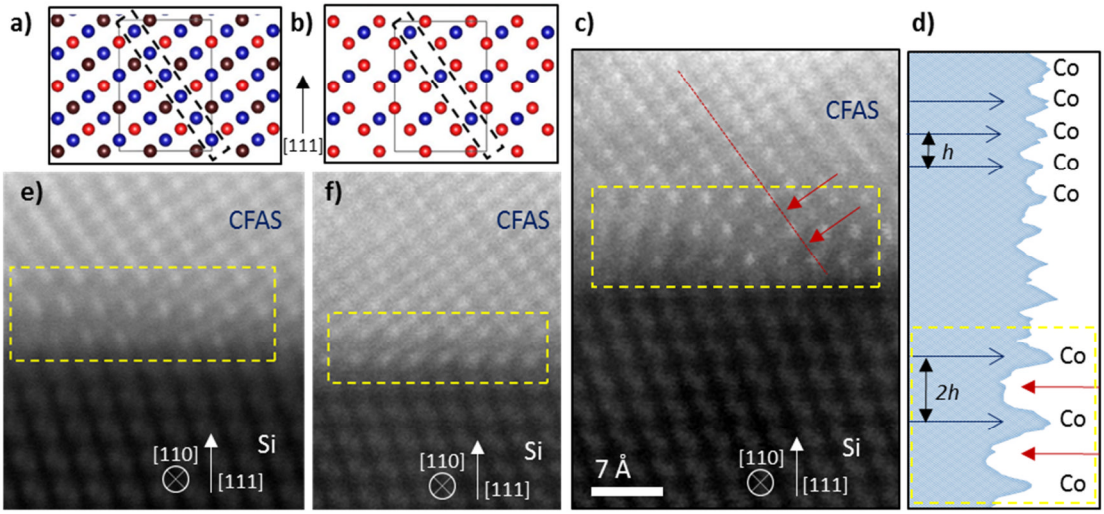

Figure 5.13 Structural models for bulk: a) CFS; b) $CoSi_2$ (in [110] projection) along the [111] direction. Dashed rectangles correspond to the red dotted line in (c) and outline that every second CFS's Co (111) plane is not present in the $CoSi_2$ structure; c) HAADF STEM image of the CFAS/Si interface showing the presence of $CoSi_2$ nano-islands, outlined by the yellow dashed rectangle; d) Intensity profile along the red line in (c) demonstrating the absence (in the region outlined by the yellow rectangle) of every second CFS's Co atomic column, as expected for a $CoSi_2$ structure. Blue arrows outline the Co atomic columns positions, while red the positions of the missing Co atomic columns. This profile shows the '*h*' and '2*h*' periodicity of Co atomic columns in the Heusler film and $CoSi_2$, respectively; e) and f) more HAADF STEM images of the CFAS/Si interface showing $CoSi_2$ nano-islands with thicknesses of 1 - 2 layers, outlined by the yellow dashed rectangles.

5.9 Improvement of the spin-electronic structure by adding a Si-Co-Si monolayer

The formation of $CoSi_2$ layers at the interface motivates to investigate the effects of such layers on the interfacial SP. Along the [111] direction, the $CoSi_2$ unit cell contains three Si-Co-Si monolayers (**Figure 5.13b**). The atomic stacking of this characteristic Si-Co-Si monolayer is similar to Co-Fe-Co-Si layers in CFS with Fe planes replaced by Si and every second Co plane vacated (**Figure 5.13a,b**).

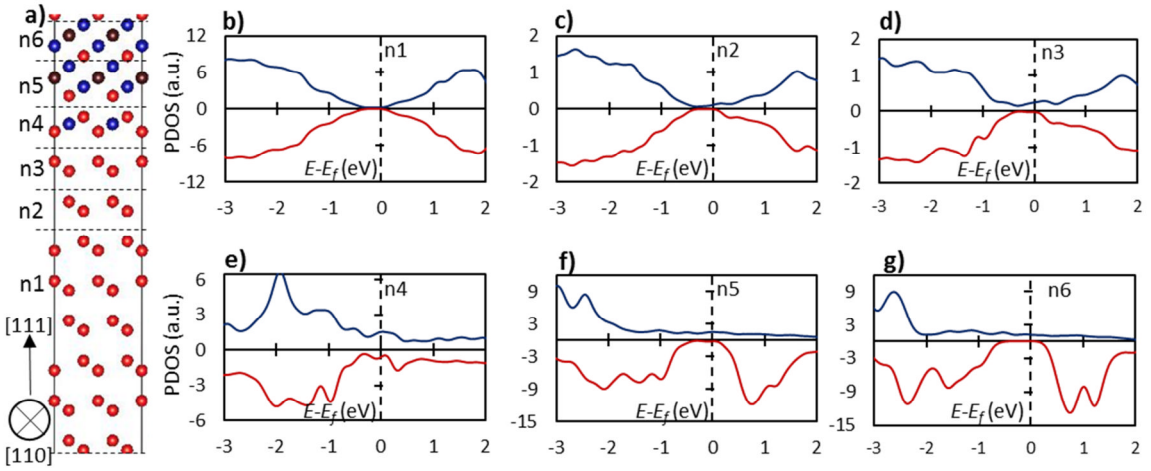

Figure 5.14 a) Structural model of the CFS/Si-Co-Si/Si interface shown along the [110] viewing direction. Region 'n4' represents the Si-Co-Si monolayer. Colour coding: red - Si, blue - Co, brown - Fe. b) - g) Spin-polarised PDOS for the regions outlined in (a) and labelled as (*n1*) - (*n6*).

First we consider an interface model with a single Si-Co-Si monolayer between Si and CFS, presented in **Figure 5.14**. This figure shows that the addition of a Si-Co-Si monolayer has a profound effect on the SP across the interface, with the most striking feature being the recovery of the positive SP in all interface layers. In contrast to the abrupt interface, the first interface layers of the CFS (region *n5*) show only a slight reduction of SP while the Si-Co-Si monolayer has an induced positive spin-polarisation (~45%). Note that the first two Si interfacial bilayers (*n*3 and *n*2 regions) also have a small positive spin density of states, which makes them positively spin-polarised at the Fermi-level (~75%).

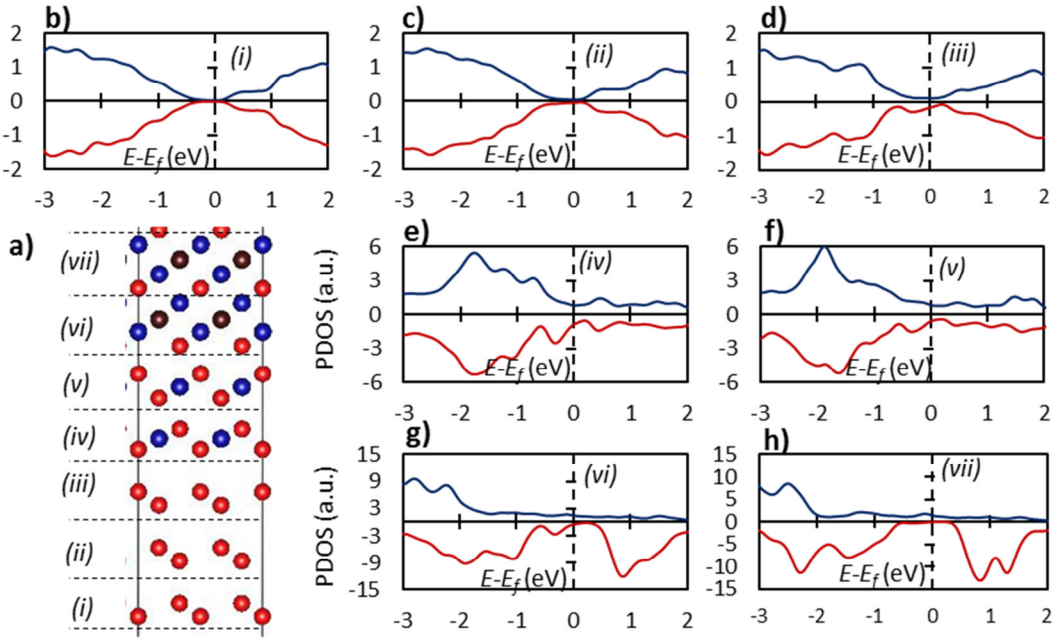

Figure 5.15 DFT study of a CFS/SiCoSi-SiCoSi/Si interface, i.e. with two Si-Co-Si monolayers (regions (iv) and (v)). a) Structural model shown along the [110] projection. Colour coding follows previous figures. b) - g) Spin-polarised PDOS for the regions outlined in (a).

Hence, in contrast to the abrupt CFS/Si, the insertion of a Si-Co-Si monolayer fully recovers the positive SP of CFS in the interface region. The inclusion of a Si-Co-Si monolayer is also affecting the recovery of the bulk magnetic moment. While the sharp interface requires several CFS's Co(111) atomic planes to recover the bulk magnetic moment of 1.3 μ_B on the Co sites, the magnetic moment on Co atoms when the Si-Co-Si layer is introduced, immediately reaches the bulk value except for the Co atoms in the first interface plane, where it has the value of 1.0 μ_B. This together with the significantly improved SP, demonstrates a significant impact of the Si-Co-Si monolayer, which essentially provides an electronically and magnetically sharper interface in comparison to the structurally sharp CFS/Si interface.

In addition to the model with a single Si-Co-Si monolayer, calculations for a double monolayer are performed and shown in **Figure 5.15**. The results show that the SP values for the regions (iii), (iv), (v) and (vi) are: -17%, -3%, +17% and +44%, respectively, which demonstrates that the interfacial Si bilayer (region (*iii*)) as well as interfacial CFS layers (region (vi)) still have much better SP compared to those at the abrupt interface.

However, as the number of Si-Co-Si monolayers increases, these monolayers would gradually recover their bulk-like metallic structure which is non-magnetic and has no spin-polarisation.

Hence, any practical implementation would require tailored growth of the naturally occurring $CoSi_2$ in order to achieve continuous coverage with a single monolayer.

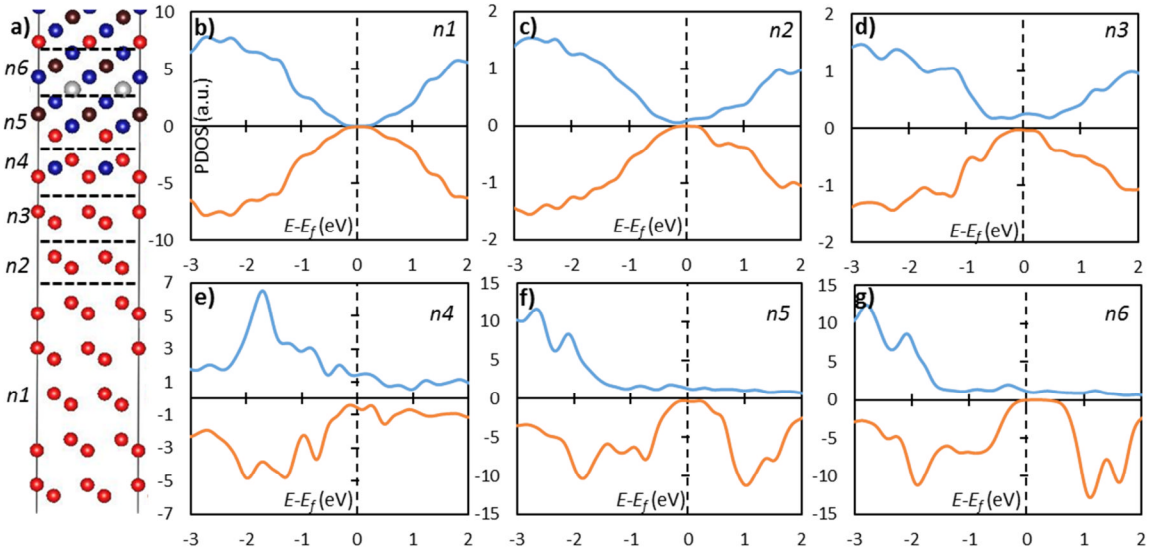

Figure 5.16 DFT study of a CFAS/Si-Co-Si/Si interface; Si-Co-Si monolayer is in the region 'n4'. a) Structural model shown along the [110] projection. Colour coding: red - Si, white - Al, blue - Co, brown – Fe; b) - g) Spin-polarised PDOS for the regions outlined in (a).

Calculations are also performed for CFAS and CMS electrodes. The results (**Figure 5.16** and **Figure 5.17**) demonstrate continuously high positive SP confirming that the beneficial effect of the Si-Co-Si monolayer holds also for CFAS and CMS electrodes.

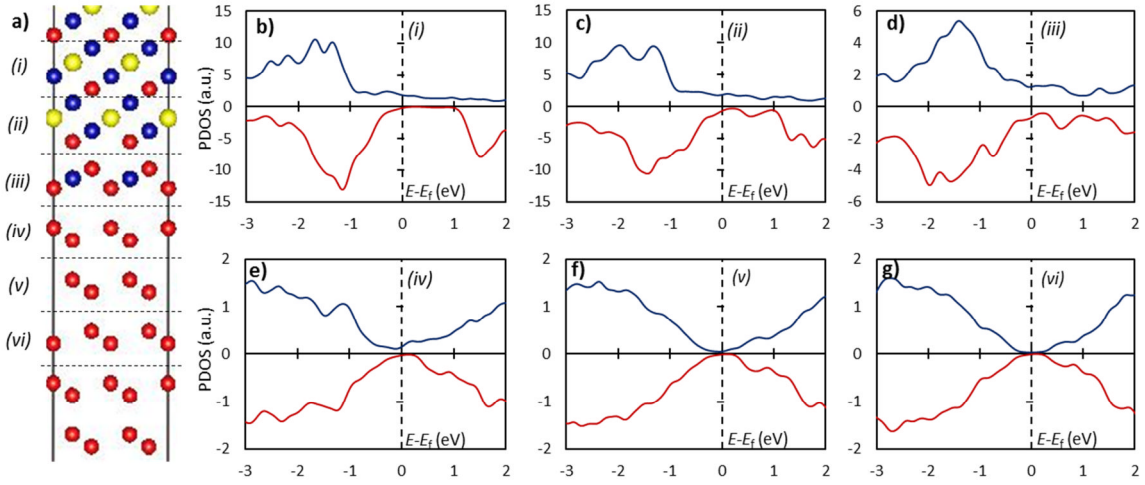

Figure 5.17 DFT study of a CMS/Si-Co-Si/Si interface; Si-Co-Si monolayer is in region (iii). a) Structural model shown along the [110] projection. Colour coding: red - Si, blue - Co, yellow – Mn; b) - g) Spin-polarised PDOS for the regions outlined in (a).

5.10 Band offsets

In addition to the importance of the interfacial SP, another factor which contributes to the spin injection efficiency is the position of the Fermi-level with respect to the semiconductor conduction band edge. The spin transport from the conduction band of CFS to the conduction band of Si will be more efficient if the difference between these two characteristic energies is smaller.

Figure 5.18 shows the averaged potentials for both interface models: abrupt CFS/Si and CFS/Si-Co-Si/Si. The plotted potential is a sum of the local part of the pseudo potential, Hartree term and exchange term. These potentials were averaged in-plane (i.e. planes parallel to the interface plane) followed by double averaging along *z* over the unit cells of Si and CFS, and plotted along the direction normal to the interface plane.

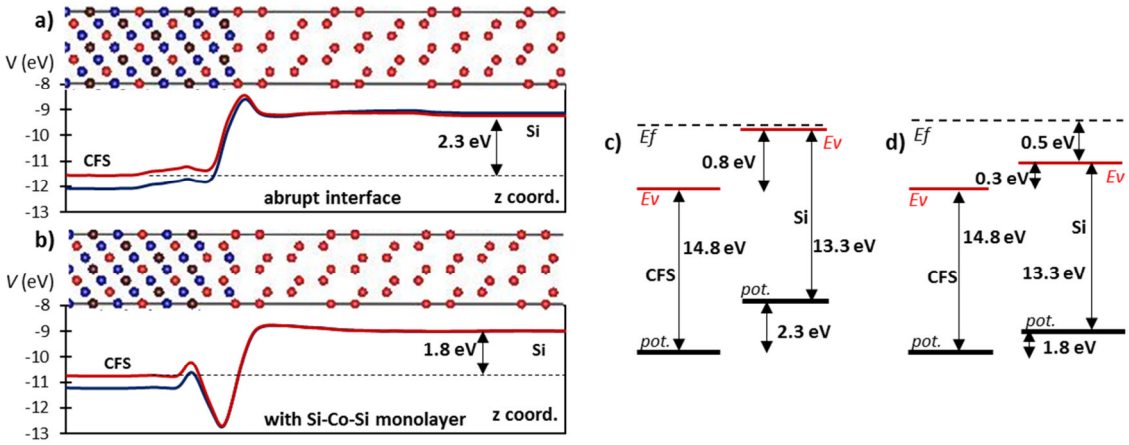

Figure 5.18 Average potentials across the: a) abrupt CFS/Si and b) CFS/Si-Co-Si/Si interface models; blue curve - average potential for spin-up, red for spin-down electrons. Band alignment schematic for the: c) abrupt CFS/Si and d) CFS/Si-Co-Si/Si interface. Solid black and solid red line stand for the average potentials and valence band edges for the minority spins, respectively. The Fermi-level is outlined by the dashed black line. Note that in (c) the energy difference between E_f and E_v is less than 0.1 eV.

Valence band edges are calculated separately for bulk Si and CFS with respect to their averaged potential, and then offset for the calculated potential difference across the interface [156]. The results (**Figure 5.18a,b**) show that the potential difference for the majority (respectively minority) electrons between the film and substrate is 2.8 eV (respectively 2.3 eV) for the abrupt CFS/Si interface, while for CFS/Si-Co-Si/Si they are 2.3 eV (respectively 1.8 eV).

Therefore, the presence of a Si-Co-Si monolayer lowers the average potential difference between the film and substrate by 0.5 eV. By using the calculated potential difference, the band alignment for the two interface models is plotted in **Figure 5.18c,d**. This figure shows that for the sharp interface model the Fermi-level is positioned just next to the valence band for Si (<0.1 eV energy difference). However, the energy shift of the bands by 0.5 eV when the Si-Co-Si monolayer is included, positions the Fermi-level in the substrate band gap, far away from its valence band edge. This decreases the energy difference required to be overcome in order to transfer the carriers from the film into the substrate, hence improving the spin injection efficiency.

5.11 Conclusion

In this chapter it was shown that in the experimentally realised CFAS/Si(111) interface there is a 2 - 3 nm intermixing region, in which the magnetic moment and spin-polarisation gradually decrease. Hence, an improvement of the growth is required in order to be able to utilise the half-metallic properties of the electrode. By DFT calculations however, it was demonstrated that even the sharp (i.e. atomically sharp with an ideal bulk-like termination) Co_2(Fe,Mn)(Si,Al)/Si(111) interfaces are not desirable for spintronic applications since they bring reversed SP in the interface vicinity.

An alternative atomic interface structure was proposed which is favourable energetically and fully removes the SP-reversal. It was shown that the addition of a Si-Co-Si monolayer recovers the positive spin-polarisation of the Heusler/Si interface and creates more desirable interface due to the much higher spin-polarisation and preserved magnetic moment, which is the ultimate goal for efficient spin injection into Si; even though such an interface is not atomically sharp due to the presence of an additional Si-Co-Si monolayer. Moreover, it was demonstrated that such monolayer shifts the Fermi-level from the valence band edge (abrupt interface case) towards the conduction band edge of Si. The significantly improved spin-polarisation and smaller energy difference between the conduction band edge of Si and Heusler film, make this interface highly desirable for device applications.

6 $Co_2FeAl_{0.5}Si_{0.5}$/Ge(111) as an ideal candidate for efficient half-metal/semiconductor interface

6.1 Introduction

Creating atomically abrupt interfaces between Heusler alloys and semiconductors which provide high interfacial spin-polarisation is essential for the development of spintronic devices. However, as discussed previously, this can be a rather challenging task.

Important parameters which determine the quality of these interfaces are the lattice matching between the film and substrate as well as the chemical stability in terms of minimal intermixing in the interface region and absence of formation of any interfacial secondary phases. Hence it is important to find a system which will satisfy these requirements and in addition have a particular atomic interfacial structure which does not decrease/reverse the local spin-polarisation.

In this chapter, on the example of the CFAS/Ge(111) interface, it is demonstrated that almost atomically sharp half-metal/semiconductor interfaces are achievable. It will be shown that this heterostructure does not form any interfacial secondary phases and provides fully coherent interface due to the excellent lattice match between CFAS and Ge.

By using electron microscopy, the exact atomic structure at the interface will be determined and used to construct a realistic interface model. DFT calculations will demonstrate that this interface preserves high spin-polarisation and also retains the CFAS magnetic moment up to the interface with the semiconductor.

Finally, by employing atomic resolution chemical mapping it will be demonstrated that the intermixing between the atomic species at the interface is minor and limited to a very narrow ~ 1 nm region at the interface. Moreover, these spectroscopic EELS/EDXS measurements show that the minor Ge outdiffusion into the film is selective i.e. Ge outdiffuses along the Fe-Si/Al atomic planes of the film. Further DFT calculations show that this atomic plane selective diffusion neither affects the structural integrity nor the spin-electronic structure of the interface.

The results obtained during this study are published in Ref. [157].

6.2 Overview images of the heterostructure and epitaxial relationships

The CFAS/Ge(111) specimen was grown by Dr Shinya Yamada at Osaka University, Japan, employing the same growth methods as described in the previous chapter for the CFAS/Si(111) interface. Cross-sectional transmission electron microscopy samples were prepared by FIB (performed by Mr Arsham Ghasemi). SAED patterns and HRTEM images were recorded using a JEOL-2011 TEM microscope and aberration-corrected JEOL JEM-2200FS microscope both operating at 200 keV.

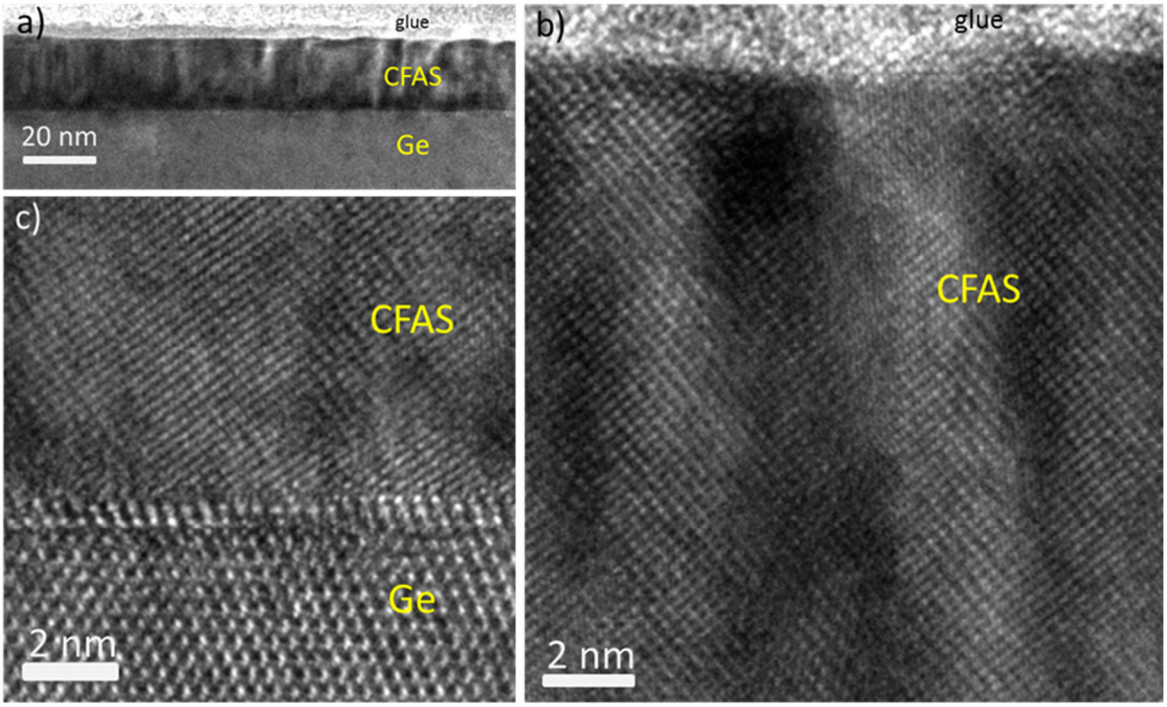

Figure 6.1 High resolution TEM microscopy on the CFAS/Ge(111) heterostructure. a) Low magnification image showing a uniform CFAS film with a thickness of ~18 nm and abrupt interface with the substrate. HRTEM images from: b) the top region of the CFAS film and c) the interface region.

Figure 6.1 shows HRTEM images of the CFAS/Ge(111) heterostructure. It can be seen that the film is uniform with a thickness of ~18 nm. Although further advanced electron microscopy imaging is required in order to make conclusions about the ordering of the CFAS film, these HRTEM images show a sharp interface between the film and

substrate as well as a uniform intensity pattern throughout the film characteristic for Heusler type lattice.

In **Figure 6.2a**, a SAED pattern is shown from an area that includes both film and substrate. This figure demonstrates the single crystal structure of the CFAS film and the epitaxial relationship with the substrate. Taking into account the excellent lattice parameter matching between CFAS and Ge (only 0.2% mismatch), in a case of a simple epitaxy one would expect an overlap of the film's and substrate's diffraction reflections, as shown in **Figure 6.2c**.

However, the diffraction pattern reveals that the epitaxy with the substrate is different. There is a twinned epitaxy determined by the following epitaxial relationships: CFAS(111)||Ge(111) and CFAS$(1\bar{1}0)$ ||Ge$(\bar{1}10)$. The simulated diffraction pattern shown in the **Figure 6.2b** calculated assuming a twinned epitaxial relationship shows an excellent correspondence with the experimental diffraction pattern.

Hence, the twinning phenomenon is also observed for the CFAS/Ge(111) interface in addition to the CFAS/Si(111) case discussed in the previous chapter. Later in this chapter, by DFT calculations it will be shown that the twinned interface is much lower in energy compared to the interface with a simple epitaxy, hence it is not surprising why such twinning phenomenon is consistently observed at these interfaces.

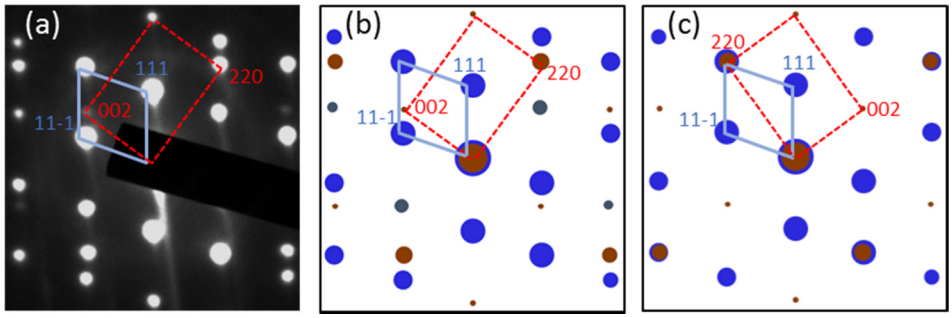

Figure 6.2 a) SAED pattern from an area that includes both film and substrate, showing the single crystal nature of the grown film and the epitaxial relationship with the substrate; b) Simulated SAED diffraction pattern assuming twinned epitaxy with respect to the substrate which shows excellent agreement with the observations. c) Simulated SAED diffraction pattern assuming simple epitaxy with respect to the substrate. Colour coding: red – film, blue - substrate. The reflections shown in grey colour appear due to double diffraction in the substrate.

6.3 Structural ordering of the CFAS film

In this section, the atomic ordering of the CFAS film is revealed by using atomic resolution HAADF STEM imaging performed along the [1-10] crystallographic direction as shown in **Figure 6.3a,b**. As discussed in the previous chapters, performing HAADF microscopy along the $[1\bar{1}0]$ crystallographic direction is beneficial since the atomic species are in separate atomic columns, which makes the chemical identification in the bulk-like region of the film relatively straightforward.

In other words, for a *B2*-ordered film one expects alternating high (Co planes) - low (Fe-Si/Al planes) intensity contrast for the atomic columns along the [001] crystallographic direction. Such intensity profile is presented in **Figure 6.3d** from which it can be easily concluded that the film has a *B2* ordering.

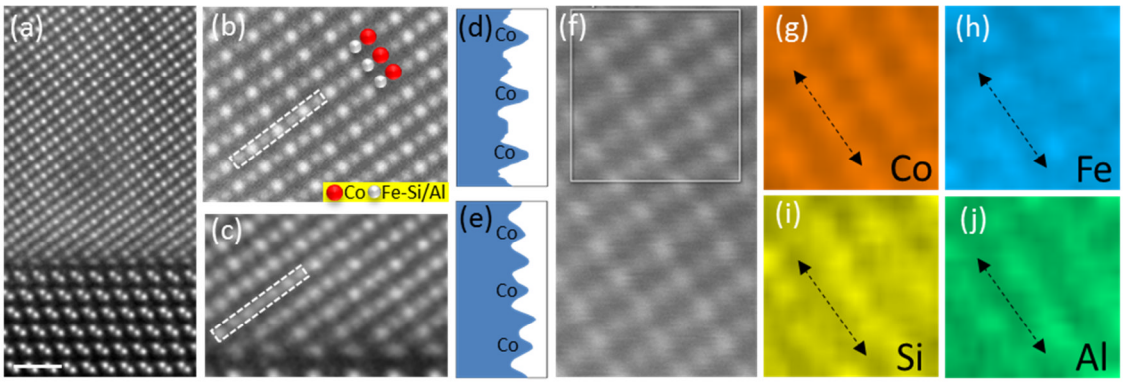

Figure 6.3 a) Overview HAADF STEM image along the $[1\bar{1}0]$ zone axis, showing the abruptness of the CFAS/Ge interface at atomic level. The white scale-bar corresponds to 0.7 nm; b) HAADF STEM image from the bulk-like film region showing the distinctive Co-(Fe-Si/Al) atomic planes repeat pattern along the [001] crystallographic direction characteristic for *B2* ordered CFAS. The line profile along the white dashed rectangle is given in (d); c) HAADF STEM image from the interface region showing that the distinctive Co-(Fe-Si/Al) atomic planes repeat pattern is lost due to out-diffused Ge atoms from the substrate; with the corresponding line profile shown in (e). These STEM images are obtained by registration of a stack of images recorded in quick succession which gives precision in the image; g) - j) K_α edge EDXS maps for: Co, Fe, Si and Al, respectively, from the area outlined in (f) located in the bulk-like region of the film. The dashed arrows are along a Co(001) plane, shown as a guide to the eye.

The film's *B2* ordering extends up to the interface with the substrate except for ∼1 nm region in the vicinity of the interface, as shown in **Figure 6.3c.** The distinctive pattern characteristic for *B2* ordering observed away from the interface is lost in this region. These structural changes are clearly seen in the intensity profile taken along the [001] direction from a region in the vicinity of the interface, as shown in **Figure 6.3e**.

This profile shows an increase in intensity of the columns identified as Fe-Si/Al in the bulk-like part of the film. Such intensity increase on these atomic columns can appear if Ge atoms (brighter than all other CFAS's atomic species in HAADF STEM images) diffuse into the CFAS film. This initial conclusion will be confirmed later in this chapter by performing EDXS analysis at the interface region.

Next, in **Figure 6.3g-j** EDXS maps are shown from the bulk-like region of the CFAS film, which are constructed using the K_α edges for each element. The clear separation between Co and Fe-Si/Al atomic planes is confirmed by these maps in addition to the observations of the HAADF STEM images, as discussed above.

These STEM and EDXS measurements were performed on an ARM200F microscope at the University of Warwick with help from Dr Ana Sanchez. The microscope was operated at 200 kV and has JEOL annular field detector in the range 70 - 280 mrad.

6.4 Analysis of the atomic structure at the interface

Next, in order to reveal the exact interfacial atomic structure, a chemical analysis is performed by using atomic resolution EDXS simultaneously with STEM imaging. EDXS line profiles are presented in **Figure 6.4,** which show that the region of outdiffusion/intermixing for this interface is very narrow (∼1 nm).

These intensity profiles are recorded using the K_α edges for each of the atomic species of CFAS and Ge. The **Figure 6.4** clearly shows a sharp decrease of the Co signal, compared to the more gradual decrease of that of Fe, Si and Al. In addition, the Ge signal gradually decreases across the interface, due to the small outdiffusion of Ge into the CFAS film over a ∼1 nm region, which is fully consistent with the initial conclusions from above based on the STEM imaging observations. In order to reveal the spatial distribution of the outdiffused Ge into the film and confirm the initial conclusions that Ge atoms outdiffuse in the Fe-Si/Al atomic planes, an EDXS chemical mapping is performed.

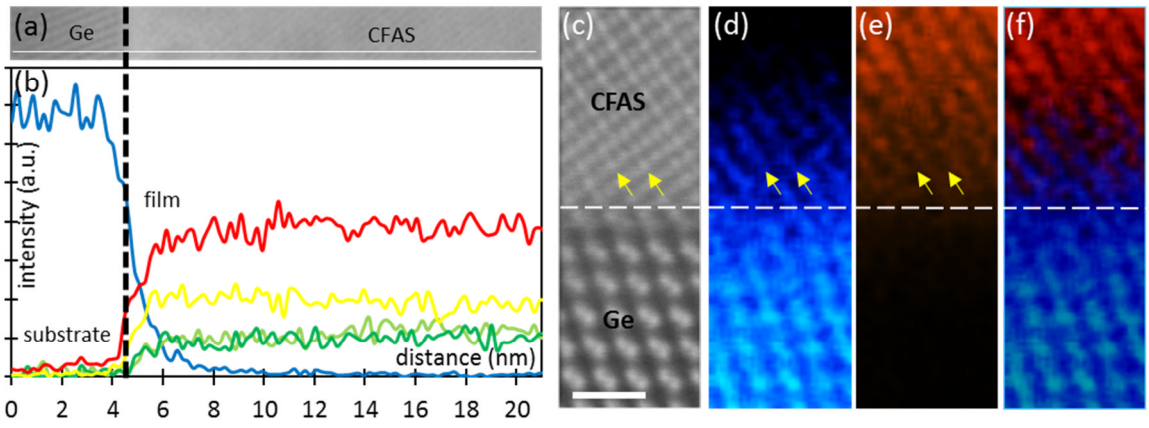

Figure 6.4 EDXS analysis at the CFAS/Ge(111) interface. b) Intensity signal from the K_α edge of Ge - blue curve, Co - red, Fe - yellow, Si - dark green, Al - light green; all simultaneously recorded during an EDXS linescan along the white line in (a); c) HAADF STEM image at the interface acquired simultaneously with the EDXS K_α edge maps. The scale-bar corresponds to 0.7 nm; d) Ge K_α edge map showing the selective outdifussion of Ge across the reference interface plane (white dashed line); e) Co K_α edge map showing the abrupt decrease of the Co signal across the interface. Yellow arrows are inserted as a guide to the eye; f) Ge and Co overlaid map clearly showing the out-diffused Ge atoms in the Fe-Si/Al atomic planes.

Figure 6.4c is a HAADF STEM image in the vicinity of the CFAS/Ge interface acquired simultaneously with the EDXS maps shown in **Figure 6.4d-f** and serves as a reference image for the EDXS maps. **Figure 6.4d** is the EDXS map formed from the Ge K_α edge, while the Co K_α edge map is shown in the **Figure 6.4e**. Above the reference interface plane which is labelled with a dashed white line as a guide to the eye, there is a decaying Ge intensity signal which confirms the presence of Ge out-diffusion into the CFAS film over a ~1 nm region.

This map reveals the spatial distribution of the Ge outdiffusion; it shows that the out-diffusion is constrained along the (001) Fe-Si/Al planes. On the other hand, the Co K_α edge map shown in the **Figure 6.4e** confirms that Co remains on its original lattice i.e. the increased intensity of the Fe-Si/Al planes in the HAADF STEM images cannot be attributed to a Co-related disorder. The described phenomenon of selective diffusion is

clearly summarised in the map presented as **Figure 6.4f** which is constructed by overlaying the Co and Ge elemental maps.

The specific localisation of Ge and Co was also confirmed by acquiring atomically-resolved EELS maps, as shown in the **Figure 6.5**. This measurement was performed at SuperSTEM Laboratory, Daresbury UK, with help from Dr Demie Kepaptsoglou. The same microscope conditions as for the CFAS/Si(111) interface were used.

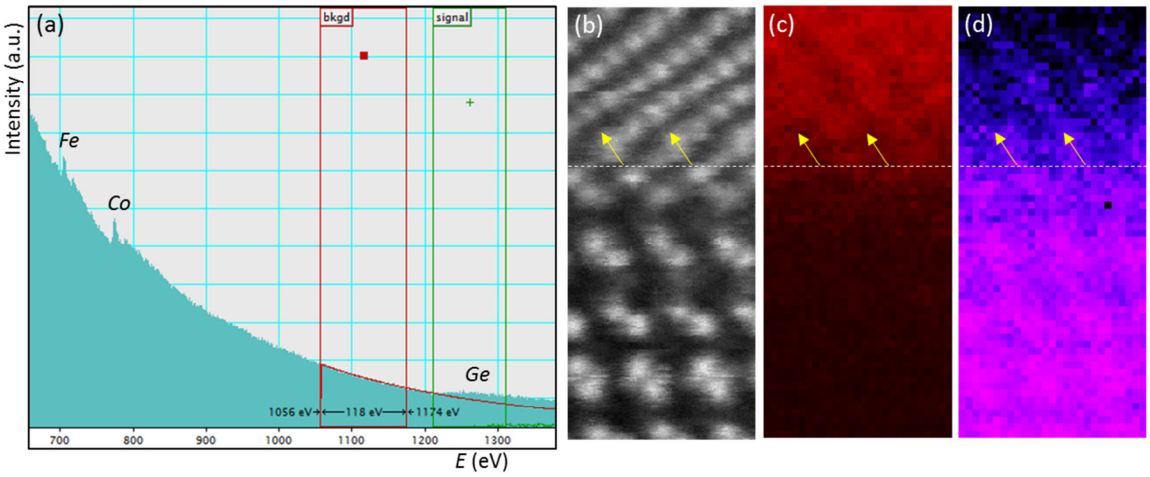

Figure 6.5 a) EELS spectrum from the region shown in (b). $L_{2,3}$ EELS edges (labelled in (a)) were used to construct the maps in (c) and (d). Using an energy window before each edge a power-law curve (coloured in red in (a)) which models the background is fitted; b) HAADF STEM image acquired simultaneously with the EELS maps; c) Co $L_{2,3}$ edge map showing the abrupt decrease of the Co signal across the interface; d) Ge $L_{2,3}$ edge map showing the selective out-diffusion of Ge across the reference interface plane (white dashed line). Yellow arrows are inserted as a guide to the eye.

6.5 The origin of the selective out-diffusion and its influence on the half-metallicity

It should be emphasised that Co_2FeGe exists as a bulk full Heusler alloy and has a lattice parameter very similar to the one of $Co_2Fe(Si,Al)$ (only ~0.9% mismatch). Hence, it is not surprising, taking into account the similarities between Co_2FeGe and CFAS structures, that substitution of Si/Al by Ge atoms from the substrate can emerge in a narrow interfacial region.

Due to the *B2* ordering of the film which makes the $L2_1$'s Fe and Si/Al sites undistinguishable, once Ge is incorporated in the CFAS lattice it remains localised on the Fe-Si/Al planes. Next, total energy DFT calculations are performed to compute the substitutional energies for Ge-Fe as well as Ge-Co swaps. The results show that swapping Ge with Fe costs 0.5 eV, while a Ge-Co swap requires an energy of 2.5 eV. This result shows that there is a very high energy barrier for Ge to move on the Co-sublattice explaining why a selective diffusion is observed.

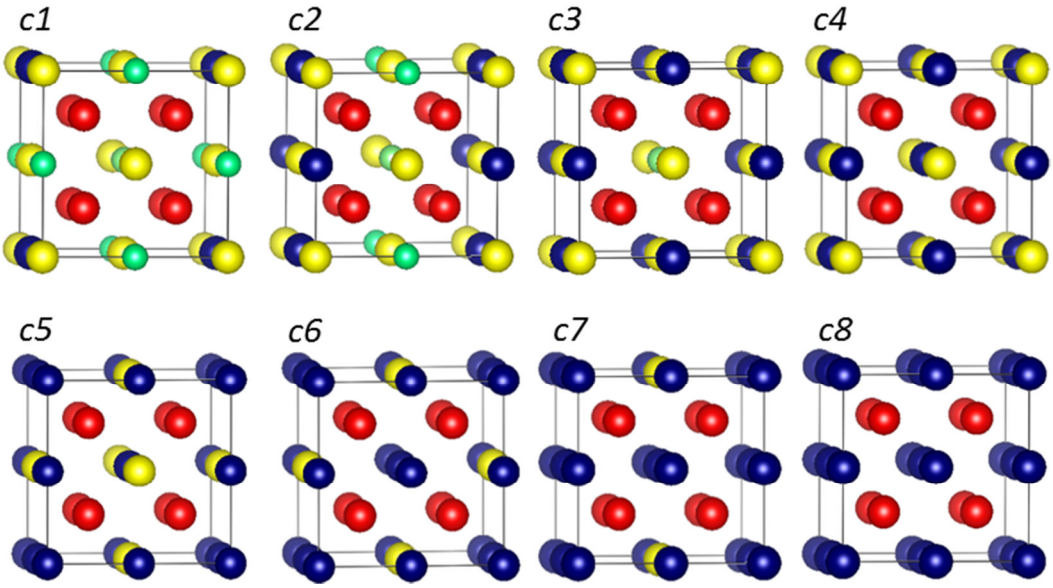

Figure 6.6 Structural models for the configurations *c1-c8.* Colour coding: Ge – blue, Co – red, Fe – yellow, Si – dark green, Al - light green.

Next, the influence of the out-diffused Ge on the interfacial spin-electronic structure is studied. DFT calculations are performed on selected configurations (**Figure 6.6**) constructed when Ge atoms substitute Fe and Si/Al in the bulk CFAS unit cell, as shown in the **Table 6.1**. The results show that even a rather large concentration of Ge into the CFAS unit cell does not significantly affect its spin-polarisation, while the magnetic moment is only slightly changing.

label	n(Fe)	n(Si/Al)	n(Ge)	M	SP	label	n(Fe)	n(Si/Al)	n(Ge)	M	SP
CFAS	4	4	0	22	100	c5	3	0	5	20	100
c1	4	3	1	22	100	c6	2	0	6	15.8	69
c2	4	2	2	23	100	c7	1	0	7	11.2	88
c3	4	1	3	24	100	c8	0	0	8	7	24
c4	4	0	4	24	100						

Table 6.1 Magnetic moment [M (μ_B/unit cell)] and spin-polarisation [SP (%)] of configurations *c1-c8* obtained when Ge atoms gradually substitute the Fe-Al/Si atoms in the bulk CFAS unit cell. 'n' stands for the number of atoms per unit cell for each of the atomic species.

In the limiting case when all Fe-Si/Al sites are populated by Ge, which is the 'c8' configuration in **Table 6.1**, the spin-polarisation and magnetic moment are significantly reduced. However, such an environment is hugely rich with Ge and do not correspond to the real chemical structure obtained using the EDXS measurements, which showed considerable presence of Fe in the interface region compared to zero in the case of 'c8' configuration. Hence, at the observed small incorporation of Ge into the film, there are practically no any detrimental effects on the spin-electronic structure.

It should be mentioned that in contrast to the observed Ge in Fe-Si/Al columns which keeps very high spin-polarisation, Ge - Co substitutions would drastically affect the electronic structure; disorder related to the Co-sublattice can locally even reverse the sign of the spin-polarisation as shown in Ref. [49]. However, as discussed above, the energy required for this disorder is rather large, hence such disorder is neither expected nor observed in the chemical mapping analysis.

In the previous chapter, it was predicted by DFT and demonstrated experimentally that at the CFAS/Si(111) interface secondary phases i.e. Fe and Co silicides do form. This is not the case for the CFAS/Ge(111) heterostructure, which in turn as shown above is very stable without any formation of secondary phases. In addition to the absence of strain between Ge and CFAS which can affect the interfacial atomic structure, Ge is also much heavier element hence it is likely to diffuse in a much narrower region compared to Si.

Furthermore, there are no Co-Ge compounds with a structural lattice which can match that of the Heusler alloy. Hence, it would cost much more energy for such phase to be accommodated at the interface compared to the, for an example, $CoSi_2$ phase observed at the CFAS/Si heterostructure, which in turn has a compatible lattice structure to both Si and CFAS. On the other hand, from the Fe-Ge compounds, Fe_3Ge has Heusler-like lattice, however as discussed in the previous chapter the presence of such phase at the interface would mean a peak in Fe concentration in a very narrow interfacial region which is thermodynamically less likely to happen.

Similarly as for the CFAS/Si(111) interface, DFT calculations were performed in order to provide an additional argument for the structural stability of this interface. The formation energies of bulk Co_2FeGe + bulk Ge are compared with the formation energies of Fe_3Ge + Co_2Ge, which are representatives of stable Ge compounds with Fe and Co.

The energy difference between 3 Co_2FeGe + Ge and Fe_3Ge + 3 Co_2Ge (secondary-phases) is 0.12 eV/atom, which indicates that a formation of secondary Ge-Co/Fe phases at the interface is not likely. It is worth noting that these calculations ignore the additional energy required to incorporate the Co_2Ge structure at the interface due to the different type of lattice; this additional factor makes the formation of secondary phases even less likely. These results are different from the results obtained for the CFAS/Si interface, where it was demonstrated that the energy difference between (3 Co_2FeSi + 10 Si) and (Fe_3Si + 6 $CoSi_2$) is -0.23 eV/atom, i.e. there is a thermodynamic drive to form silicides at the interface between Si and CFAS.

6.6 Atomistic model of the CFAS/Ge interfacial structure and spin-polarised partial density of states

As discussed in previous chapters ideally we need interfaces which retain very high spin-polarisation. However, it was demonstrated on the example of CMS/Ag and CFAS/Si that the interfacial spin-polarisation can drastically differ compared to the one in the bulk-like part of the material. It can be significantly reduced or even reversed which leads to spin-scattering phenomena detrimental to the spin-injection efficiency into the semiconducting substrate. In this section, by using HAADF STEM microscopy, the

interfacial atomic structure will be revealed and atomistic model of the interface will be constructed which will be later used to perform DFT calculations.

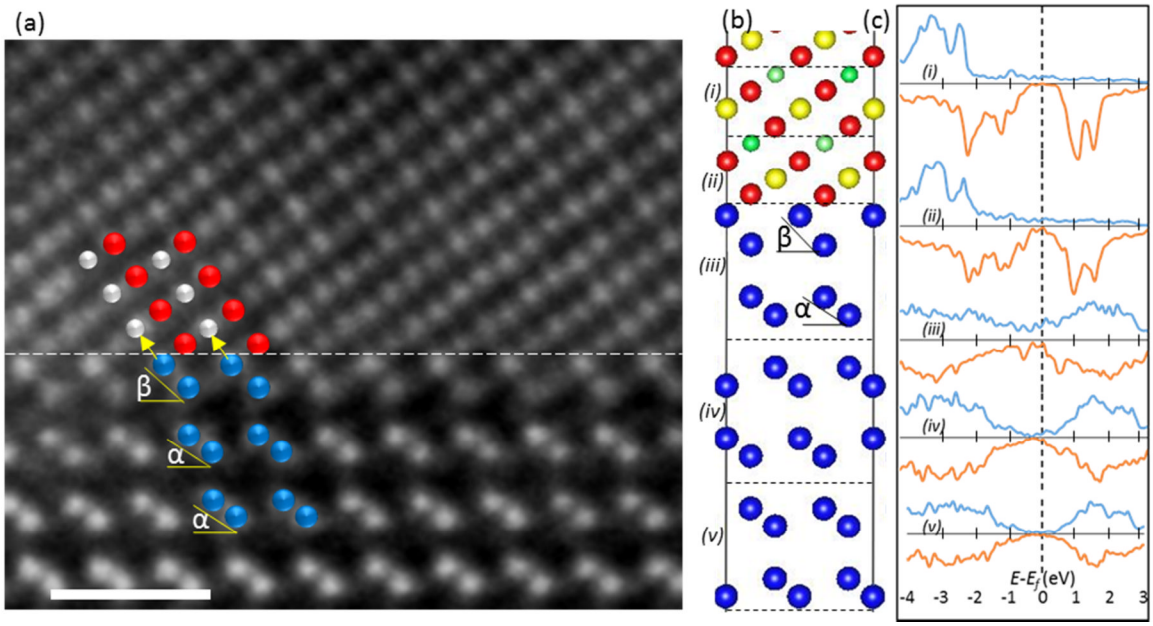

Figure 6.7 a) HAADF STEM image of the interface showing that the CFAS film terminates on a Co(111) atomic plane. This image is obtained by registration of a stack of images, recorded at SuperSTEM. The white scale-bar corresponds to 0.7 nm. The tilt angle of the Ge dumbbells from α = 37° in the bulk-like region increases to β = 51° for the interfacial Ge bilayer; b) Structural model of the CFAS/Ge interface viewed along the $[1\bar{1}0]$ crystallographic direction; c) Spin-polarised PDOS for the regions labelled as (i) - (v) in (b). Colour coding: Ge - blue; Co - red; Si/Al - green, Fe - yellow, Fe-Si/Al - grey (columns present in *B2* phase).

In **Figure 6.7a** an atomic resolution HAADF STEM image of the interface is shown. The dashed white line is a guide to the eye and outlines a reference interface plane which separates the film from the substrate. Starting from the bulk-like CFAS region (above the reference interface plane) when approaching the substrate, the atomic plane stacking sequence: …-Co-(Fe-Si/Al)-Co-(Fe-Si/Al)-… characteristic for bulk *B2* ordered CFAS is observed. It can be noticed that the nearest (111) atomic plane to the substrate is a Co (111) plane. Hence, the CFAS film terminates on this plane.

The bilayer below the reference interface plane is a Ge dumbbell layer. It can be observed that due to the interface bonding the dumbbells of the Ge interface bilayer are

tilted by an additional angle of (β-α)∼15°, as illustrated in the **Figure 6.7a**. Note that the bulk Ge dumbbells in $[1\bar{1}0]$ projection are under an angle of α = 37° with respect to the $[11\bar{2}]$ direction.

In the previous sections, it was shown that there is a small outdiffusion of Ge into the film along specific atomic planes. However, it was also demonstrated that this process does not affect the Heusler-fcc structure of the film neither does it change its electronic structure. Using the atomic plane stacking sequence at the interface obtained from the HAADF microscopy, we build an interface model neglecting the presence of small intermixing. Taking into account the above discussion, such model is well representative for the atomic/electronic structure of the CFAS/Ge interface.

The interface model is shown in **Figure 6.7b** after the performed DFT geometry optimisation. For clarity, the interface is divided into five regions labelled as (*i*) - (*v*) and for each of them spin-polarised PDOS are computed and presented in **Figure 6.7c**. In the regions away from the interface i.e. layer (*i*) and layer (*v*) the bulk-like features of the CFAS and Ge, respectively, are recovered.

The interfacial CFAS region (*ii*) shows that near the Fermi-level there is a small number of spin-down interfacial states; however, this does not significantly affect the spin-polarisation at the Fermi-level which is still very high. Similarly, due to the interface bonding a small number of states emerge into layer (*iii*); yet this layer is significantly positively spin-polarised. In other words, this sharp interface preserves the very high spin-polarisation of the CFAS in the interface vicinity, a property that is highly desirable for spintronic applications.

Finally, we demonstrate that the sharp atomic interface model reproduces the distances and angles of the interfacial Ge dumbbell bilayer with respect to the interfacial Co layer from the CFAS film. **Figure 6.7b** shows the relaxed coordinates of the atomic layers in the interface region. As in the experiment, the interface Ge bilayer shows the same tilting angle in comparison to the angle in the bulk Ge dumbbells, hence confirming that the effect of the small interdiffusion on the interfacial structure is negligible.

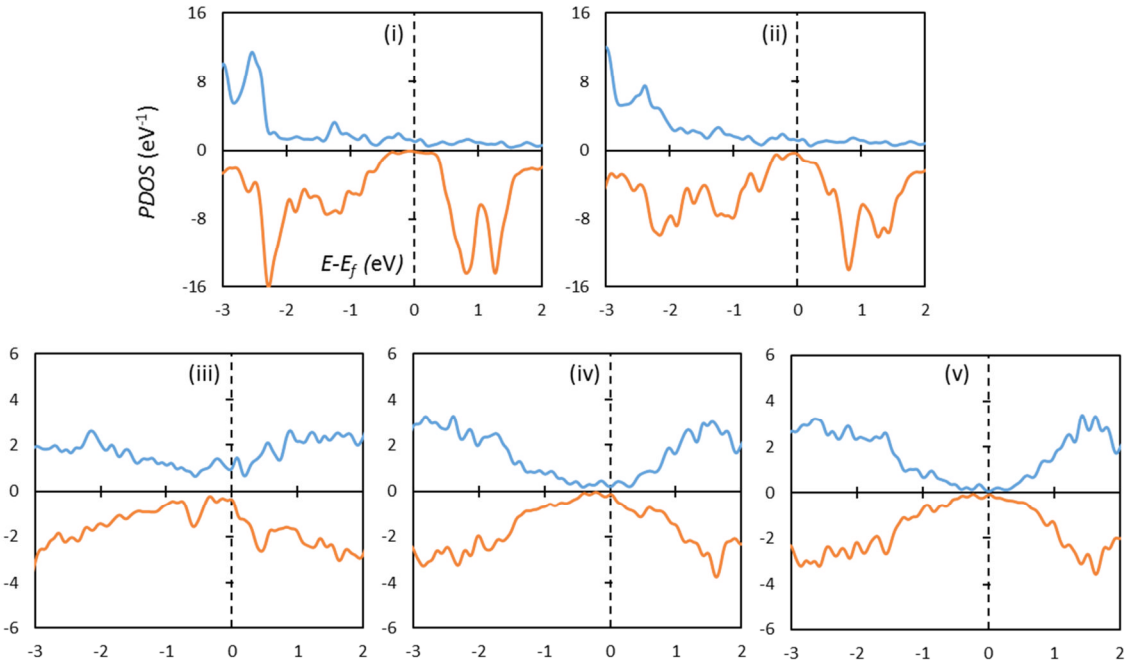

Figure 6.8 Spin-polarised PDOS of Co_2FeGe/Ge(111) interface. Regions labelled as (i) - (v) are chosen exactly in the same way as in **Figure 6.7b**; the only difference is that all Al/Si sites in the supercell are fully substituted with Ge.

The DFT calculations were performed with the CASTEP code using a periodically repeating supercell which contains two equivalent interfaces. The supercell is large enough (28 Ge and 13 CFAS atomic planes along the [111] direction) so that the CFAS and Ge bulk-like electronic structure is recovered in the regions away from the interfaces. Similar as in the previous chapters, the following parameters were used: Hubbard-U term of 2.1 eV for both *d*-block elements Co and Fe; plane wave cut-off energy of 600 eV; *k*-point sampling spacing of $0.03 \cdot 2\pi$ Å^{-1}. All atomic coordinates as well as the perpendicular (with respect to the interface plane) lattice parameter were geometry optimised. PDOS were calculated with the OPTADOS code using the fixed Gaussian broadening scheme.

In Ref. [157], PNR measurements have been performed for this heterostructure and the results show an abrupt decrease of the magnetic moment at the interface, hence confirming the validity of the constructed interface model.

It was shown above that the small Ge outdiffusion does not have any significant effect on the electronic structure. The analysis was performed on bulk-structures. For

completeness, and in order to provide an additional quality check, here are also shown (**Figure 6.8**) the PDOS across a Co_2FeGe/Ge(111) interface, where all Si/Al atoms are substituted with Ge. The results show again a presence of very high spin-polarisation in all interfacial regions, i.e. the same behaviour as for the model of abrupt CFAS/Ge heterostructure.

6.7 DFT study of a CFAS/Ge model with a simple epitaxial relationship

The atomistic model for the interface studied in the previous section was constructed taking into account the twinning phenomenon. Since twinning at these interfaces is consistently observed, we should expect the twinned structure to be lower in energy compared to the non-twinned one. In this section, for completeness, a computational study is performed for a model with a simple epitaxial relationship between the film and substrate, i.e. non twinned CFAS/Ge interface.

The results presented in the **Figure 6.9**, show that this interface completely destroys the local spin-polarisation. In other words, the spin-polarisation values for the interfacial regions (ii) and (iii) are -12% and +2%, respectively. The buckled atomic positions in the interface vicinity are an initial indication that this interface atomic structure is very likely high in energy (i.e. metastable). This indication is confirmed by total energy calculations for both type interfaces: twinned and non-twinned.

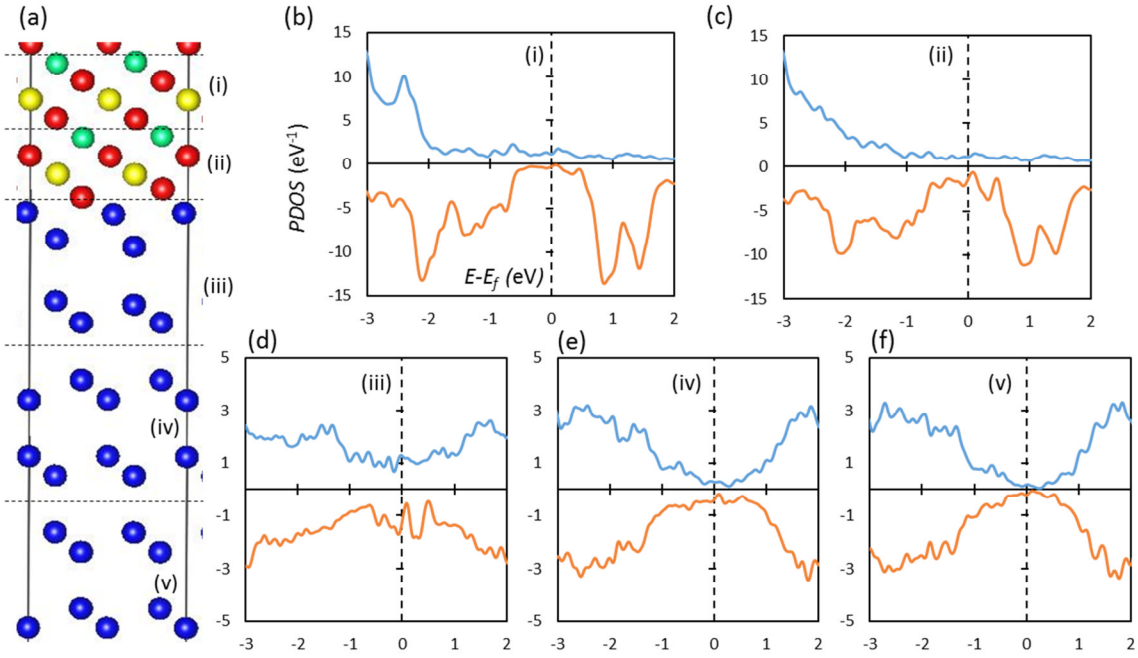

Figure 6.9 DFT study of a non-twinned CFAS/Ge(111) interface. a) Structural model viewed along the $[1\bar{1}0]$ crystallographic direction; b) Spin-polarised PDOS for the regions labelled as (i) - (v) in (b). Colour coding is the same as in **Figure 6.7**.

Taking into account that the twinned and non-twinned supercell models have the same number of atoms we can easily compute the energy difference which arises due to the interfacial twining. By using the total energies for the twinned and non-twinned supercell models, an energy difference of 0.3 J/m^2 is obtained in favour of formation of a twinned interface, which agrees with the observations.

It should be emphasised that these results demonstrate that it is always beneficial to create atomistic models directly from observations; although the atomic plane stacking sequence is identical for the twinned and non-twinned interface, they significantly differ in their spin-electronic structure.

6.8 Conclusion

In this chapter, it was shown that a CFAS film forms an abrupt interface with the Ge(111) substrate. By combining atomic resolution imaging and spectroscopy, it was demonstrated that there is a minor out-diffusion of Ge, limited to a very narrow 1 nm interfacial region. By performing EDXS chemical mapping, the spatial distribution of the

diffusion was revealed, i.e. it was shown that the Ge atoms outdiffuse into the Fe-Si/Al atomic planes of the CFAS film. In addition, DFT studies showed that due to this selective behaviour, the outdiffusion does not affect the film's structure and properties.

By using the information obtained from electron microscopy a realistic interface model was constructed and used to compute the PDOS across the interface layers. The calculations showed that this particular interface structure preserves very high spin-polarisation. This study demonstrates that the half-metallic Heusler alloy CFAS can form atomically and magnetically sharp interfaces with Ge which preserve high interfacial spin-polarisation. Therefore, this heterostructure outperforms the CFAS/Si(111) heterostructure and provides a model of ferromagnet/semiconductor interface which is highly desirable for spintronic applications as well as fundamental spin injection studies.

7 The atomic structure of an antiphase boundary in $Co_2Fe(Al_{0.5},Si_{0.5})$ and its influence on the electronic and magnetic properties

7.1 Introduction

So far, the atomic and electronic structure of interfaces between a full Heusler alloy and metal or semiconductor was studied. As mentioned in the introduction, the influence on the half-metallicity from several factors including ordering, point defects, strain, variations from stoichiometry etc. has been extensively studied. Many of these factors have been shown to drastically affect the film's half-metallic properties. While extended structural defects have been studied in detail in other half-metallic materials such as magnetite [91], their presence has not so far been reported in the Co-based full Heusler alloy. The understanding of their atomic structure and how they influence the film's properties is crucial for guiding the development of devices with better properties.

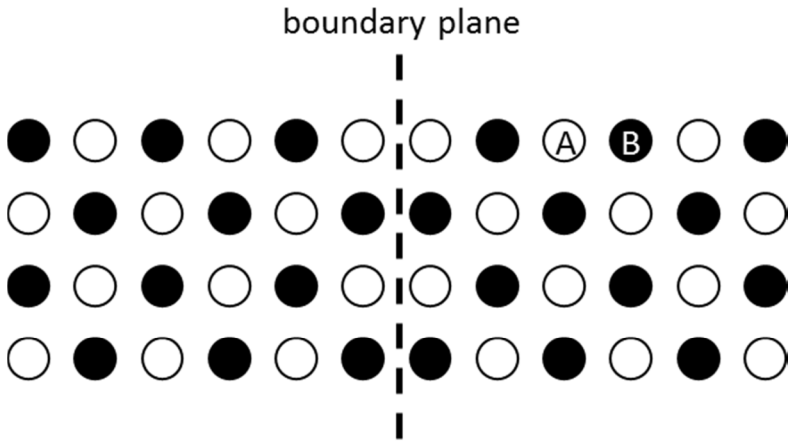

Figure 7.1 Schematics of an APB defect in a lattice with two elements A and B. The boundary plane is outlined with the dashed line.

In this chapter, the presence of antiphase boundaries (APBs), which are extended structural defects (**Figure 7.1**), in thin films of CFAS will be demonstrated. By employing aberration-corrected HAADF STEM imaging, their exact atomic structure will be revealed.

We find that the observed APB can be described with the shift vector ¼*a*[111], where *a* is the CFAS lattice parameter. Based on these atomic resolution images, an atomistic model of the APB is created and used to perform both DFT and atomistic magnetic calculations.

The results from the DFT calculations show that these structural defects do not affect the preference for ferromagnetic (FM) ordering. In other words, the grains across the boundary are still ferromagnetically coupled. However, even though the interactions across the APB keep the FM preference, it will be shown that their strength is significantly reduced which in turns leads to slightly shorter magnetic domain wall width compared to that in the bulk, as computed by the atomistic magnetic calculations.

In addition, by computing the layer-by-layer spin-polarised PDOS across this APB, it will be demonstrated that the local spin-polarisation is reversed i.e. electronic states that are negatively spin-polarised emerge at the Fermi-level and determine the electronic properties of the boundary. Finally, the low presence of these extended structural defects will be correlated with their relatively high formation energy. In other words, by DFT calculations it will be shown that the formation energy of the experimentally observed APB is 0.9 J/m^2, which is almost an order of magnitude higher compared to that of the APB in Fe_3O_4 [91].

The results obtained during this study are published in Ref. [158].

7.2 Methods

The APB analysed in this chapter was observed in the CFAS film grown on Ge, i.e. the same specimen from the **Chapter 6**. Hence, both growth and microscopy methods are the same and details can be found in the **Chapter 6**.

DFT calculations were performed with the CASTEP code using periodically repeating supercells which contain two equivalent APBs. The PBE+U exchange-correlation functional was used, where the Hubbard-U term was set to 2.1 eV for all *d*-block elements: Co, Fe and Mn. The plane wave cut-off energy was set to 600 eV, while the Brillouin zone was sampled using a Monkhorst-Pack grid with a *k*-point sampling spacing of $0.03 \cdot 2\pi$ $Å^{-1}$. The atomic coordinates were fully geometry optimised. Spin-polarised PDOS were calculated with the OPTADOS code using fixed Gaussian broadening scheme.

Atomistic spin dynamics simulations were performed using the VAMPIRE code [142] with Heisenberg exchange and uniaxial anisotropy energy. The uniaxial anisotropy constant is set to 20 kJ/m^3 [159], while the uniaxial anisotropy axis is set along the [11-2] crystallographic direction of CFAS, as discussed in Ref. [160]. The values of the exchange interaction constants in the bulk, are taken from ab-initio calculations performed in Ref. [144]. These are Mn-Co(0.43) = 2.80 mRy; Co-Co(0.50) = 0.75 mRy; Mn-Mn(0.70) = 0.35 mRy; Co-Co(0.86) = 0.30 mRy. Here, the values in parenthesis are the distances between the pair of interacting atoms given in lattice constant units, while Ry stands for Rydberg (1 Ry = 13.6 eV). These four nearest neighbour interactions are the strongest; the others are becoming very low as the interatomic distance increases. Since their contribution is very small, they are omitted in the performed magnetic calculations, for simplicity. The constructed supercells for the atomistic magnetic simulations have dimensions of ~16 nm x 16 nm x 280 nm. More details regarding some of the scripts used during this study and input files are provided in **Appendix 3**.

7.3 Atomic structure of the antiphase boundary

Figure 7.2a shows an atomic resolution HAADF STEM image of the film region that contains the structural defect. The defect is in the middle of this image and the boundary plane is labelled with the white dashed line. On either side of the boundary plane, left or right, this HAADF STEM imaging shows a distinctive bright-dark contrast for the atomic planes along the [001] direction.

The bright contrast from this pattern corresponds to Co atomic columns, while the darker to Fe-Si/Al atomic columns. This is expected for a *B2* ordered film, as discussed in the previous chapters. In other words, for a *B2* ordering, we would expect the following atomic plane stacking sequence … Co-(Fe-Si/Al)-Co-(Fe-Si/Al)… along the [111] crystallographic direction, which is exactly as observed in **Figure 7.2a**.

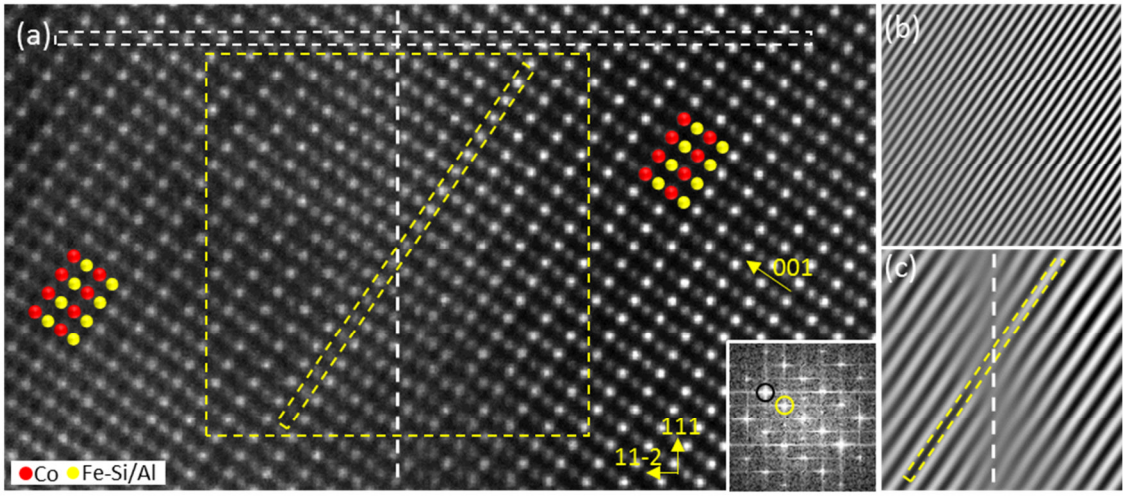

Figure 7.2 a) An atomic resolution HAADF STEM image at the APB defect performed along the $[1\bar{1}0]$ zone axis. The defect plane is labelled with dashed white line. The dashed white rectangle is along a (111) plane, while dashed yellow rectangle along a (001) atomic plane. The colour coding of the overlaid structural model is shown in the legend. A fast Fourier transform of the area within the yellow dashed square, is shown as an inset and used to construct the filtered images in (b) using the spot marked with a black circle and (c) using the spot marked with a yellow circle; both of them are [001] type diffraction spots.

As it can be seen from this figure, the distinctive atomic column stacking pattern, characteristic for the bulk-like part of the film, is disrupted at the boundary plane. This can be easily noticed by following the atomic columns of the (001) plane outlined by the yellow dashed rectangle.

In other words, by considering these (001) atomic planes, across the boundary it can be observed that the positions of Co atomic columns switch to Fe-(Si/Al) atomic columns. The same observations apply for the (111) atomic planes, i.e. by following the atomic plane outlined by the white dashed rectangle, the Fe-(Si/Al) atomic columns are switched to Co columns across the APB.

This discontinuity of Co and Fe-Si/Al columns, occurring at the APB, is further demonstrated by the Fourier filtered images shown in **Figure 7.2b,c**. It can be noticed from **Figure 7.2c** that the atomic planes shift along the [111] crystallographic direction. In other words, from **Figure 7.2c** can be seen that, left of the defect the dashed rectangle is

between the filtered planes, while on the right of the defect boundary plane the yellow dashed rectangle includes the plane.

Since this filtered image gives every second (001) atomic plane, the observed shift correlates well with the fact that Co atomic columns switch to Fe-Si/Al and vice versa across the APB. On the other hand, structurally, ignoring the chemistry, the (001) atomic planes are continuous across the APB as observed in **Figure 7.2b**. The same holds for the (111) atomic planes.

By observing the atomic column stacking in **Figure 7.2a**, we can notice that if we start from an arbitrary atomic column, we need to move three (111) atomic planes in vertical direction (i.e. [111] direction) to get to another atomic column. If the starting atomic column is Co, then the first column that we meet along the vertical direction would be Fe-Si/Al; or alternatively starting from Fe-Si/Al the first one would be Co.

Such shift of three atomic planes along the [111] crystallographic direction occurs at the APB, and this results in switching of Co with Fe-Si/Al atomic columns and vice versa. As discussed in **Section 2.4.2**, along the [111] crystallographic direction there are 12 in total atomic planes per repeat unit, hence the observed APB can be described with a shift vector of ¼*a*[111], where *a* is the lattice constant of CFAS.

7.4 Spin-polarisation in the boundary vicinity

In this section, the influence of the APB on the local SP will be discussed. **Figure 7.3a** shows the atomistic model constructed based on the atomic resolution HAADF STEM imaging (**Figure 7.2a**). This model consists of two bulk-like CFAS regions shifted relative each to other by the APB vector ¼*a*[111], i.e. a shift of three (111) atomic planes along the [111] crystallographic direction. For simplicity, only the region in the APB vicinity is shown in this figure, the supercell however is larger and contains another equivalent APB at the end.

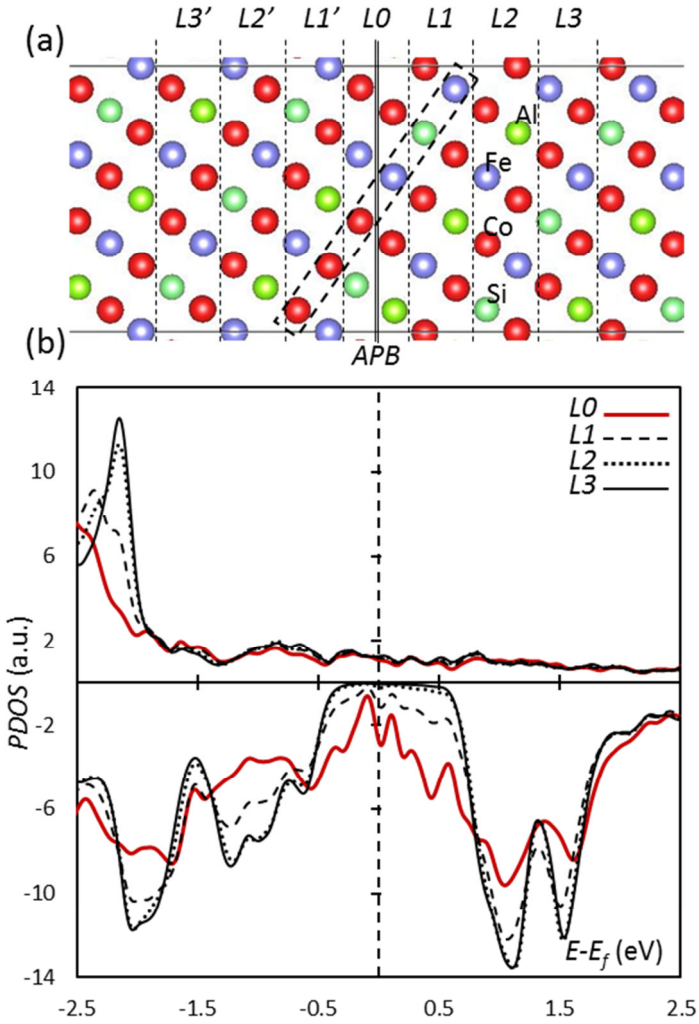

Figure 7.3 a) Structural model of the APB viewed along the $[1\bar{1}0]$ projection. The vertical direction corresponds to [111]; (001) plane is along the black dashed rectangle. The boundary plane is labelled with the double solid line, while the dashed lines are used to separate the supercell into seven blocks. These are used to compute and plot the spin-polarised PDOS shown in (b) where spin-up states are shown in the top part and spin-down in the bottom part of the plot.

In order to compute and plot the spin-polarised PDOS, the region shown in this figure is divided into seven blocks labelled as *L3', L2', L1', L0, L1, L2, L3,* as illustrated in **Figure 7.3a**. The corresponding spin-polarised PDOS at the boundary (region *L0*) and for the next three neighbouring bilayers (*L1, L2* and *L3*) are shown in **Figure 7.3b**. Due to the symmetries present in the supercell, the spin-polarised PDOS from the regions *L1', L2'*

and *L3'* do not differ from those of *L1, L2* and *L3,* hence only the PDOS for the region right of the boundary plane are shown in the figure.

The first that can be noticed is that the effect of the APB on the SP is localised to the first two-three bilayers. At the APB (layer *L0),* there are significant number of spin-down states which make this region inversely spin-polarised (compared to the bulk-like part of the electrode) with spin-polarisation value of -44%.

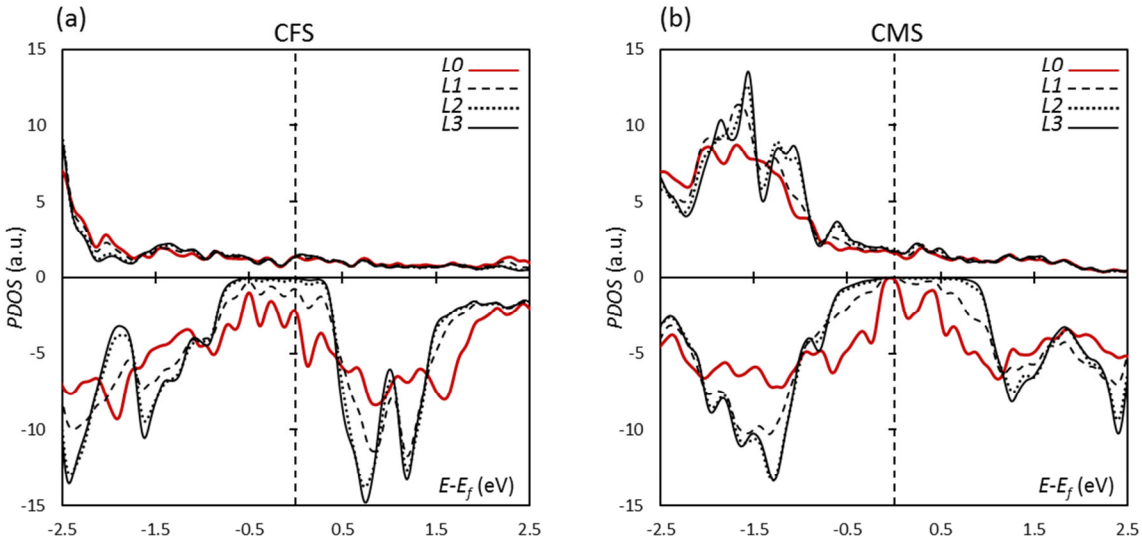

Figure 7.4 Spin-polarised PDOS across the APB in a) CFS and b) CMS. Both, labels and colour coding follows from **Figure 7.3**.

Away from the structural defect, the spin-polarisation recovers gradually towards the bulk value. The first bilayer *L1* has spin-polarisation of +4%, i.e. practically depolarised, while from the bilayers *L2, L3* onwards the properties become bulk-like. It should be noted that the layers *L2* and *L3* already show proper band gap $\sim$1 eV for the minority (spin down) electrons, as expected for bulk CFAS.

The experiment and modelling so far were performed on APBs in CFAS. However, for completeness and in order to find out whether the spin-polarisation reversal is dependent on the exact chemical composition of the Co-based full Heusler alloy, APBs in both CMS and CFS are considered. The results from the corresponding DFT calculations are shown in the **Figure 7.4**. As seen in this figure, the effect of the APB is considerable in both cases.

For the case of APB in CFS, the situation is very similar to that of APB in CFAS, as expected, i.e. the spin-polarisation at the Fermi-level becomes reversed. On the other hand, in CMS the spin-polarisation remains with a positive sign at the Fermi-level, however the band gap becomes hugely reduced.

All these calculations performed for three different Co-based full Heusler alloys show that the APBs in these materials can be very detrimental for the spin-electronic structure of the electrode. In other words, the transport of a spin-polarised current may become drastically affected, in particular for spintronic devices operating in planar geometry, where the APBs will act as extended regions for spin-scattering events.

7.5 Strength of exchange interactions at the antiphase boundary

In this section, the strength of the exchange interactions across the APB is studied. The exchange constants are proportional to the energy required to transform the ferromagnetic alignment into antiferromagnetic, and in Co-based full Heusler alloys these interactions are between two atoms.

In order to illustrate this concept, we can consider the Heusler alloy CMS. The exchange interactions are between the magnetic species, i.e. they can be Co-Co, Mn-Co and Mn-Mn. All these interactions have a characteristic value of the exchange interaction constant and determine the magnetic behaviour of these materials, their Curie temperature, coercivity etc.

Material	E_{bulk}^{AFM} - E_{bulk}^{FM} (J/m^2)	E_{APB}^{AFM} - E_{APB}^{FM} (J/m^2)	E_{form} (J/m^2)
CFAS	0.73	0.49	0.90
CFS	0.62	0.30	0.92
CMS	0.53	0.18	1.14

Table 7.1. Energy differences for CFAS, CFS and CMS models. E_{form} stands for the APB formation energies, E_{bulk}^{AFM} - E_{bulk}^{FM} is the energy difference between the AFM and FM bulk models; while E_{APB}^{AFM} - E_{APB}^{FM} is the same quantity but for APB supercell models.

First-principles calculations of exchange constants is not a trivial problem. It has been done so far only for simplistic systems, including the bulk CMS [144]. In this study, the bulk values for the exchange interactions computed in Ref. [144] will be used. By using these bulk values and performing further DFT calculations for the energy differences between the antiferromagnetic and ferromagnetic states in presence of APB, the strength of the exchange interactions at the APB defect will be calculated.

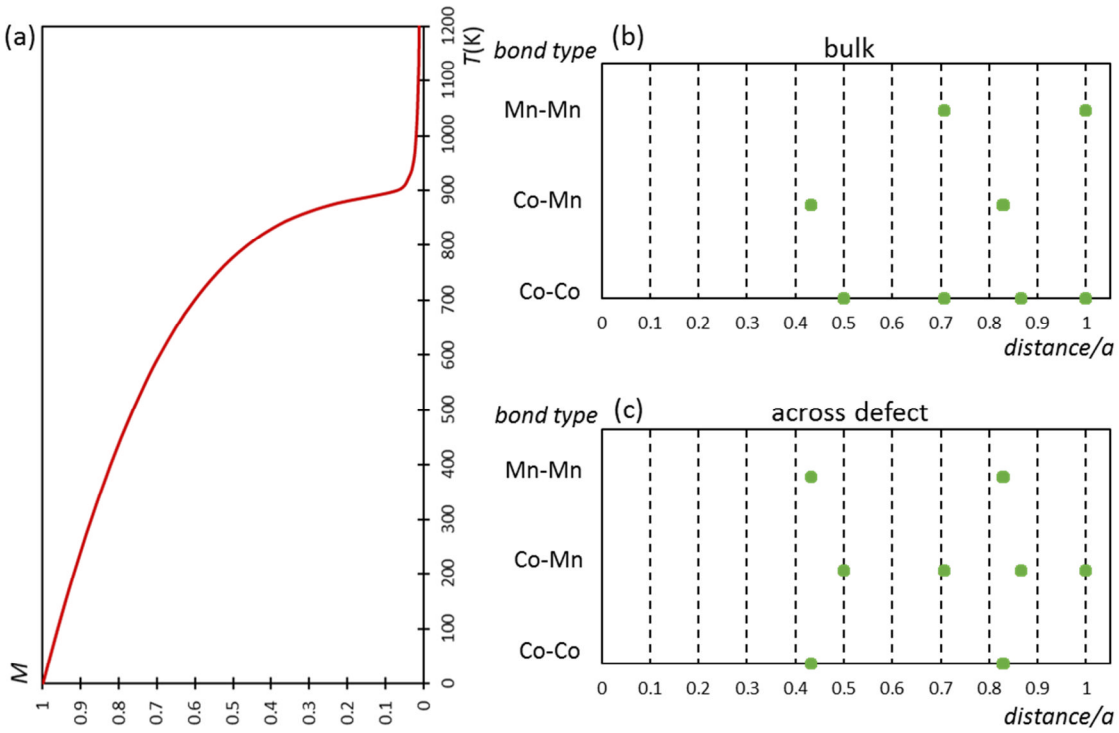

Figure 7.5 a) Curie temperature simulation showing the dependence of the normalised magnetisation as a function of temperature. This simulation was performed on a bulk CMS using a supercell with dimensions 8 x 8 x 8 nm. Analysis of the bonds for a) bulk CMS, b) across APB in CMS. The bond distribution is shown as a function of the interatomic distance given in lattice constant (labelled with *'a'*) units.

First, the following calculations are performed. Four supercells with the same size and number of atoms, equal to those of the supercell which was used for PDOS calculations, are created. The first two are bulk CFAS supercells; one of them has all of the magnetic moments aligned along the same direction, while the other one is divided into two halves having an opposite magnetic moment alignment. Total energy DFT calculations are performed for all four supercells.

As expected, the antiferromagnetically coupled supercell has higher total energy by 0.73 J/m^2 with respect to the ferromagnetically aligned supercell. The same two sets calculations performed on a supercell with an APB defect in the middle, separating the two halves, show that the ferromagnetic alignment between the two halves is still favoured, but with smaller energy difference between the antiferromagnetic and ferromagnetic configuration. The energy difference in this case is 0.49 J/m^2.

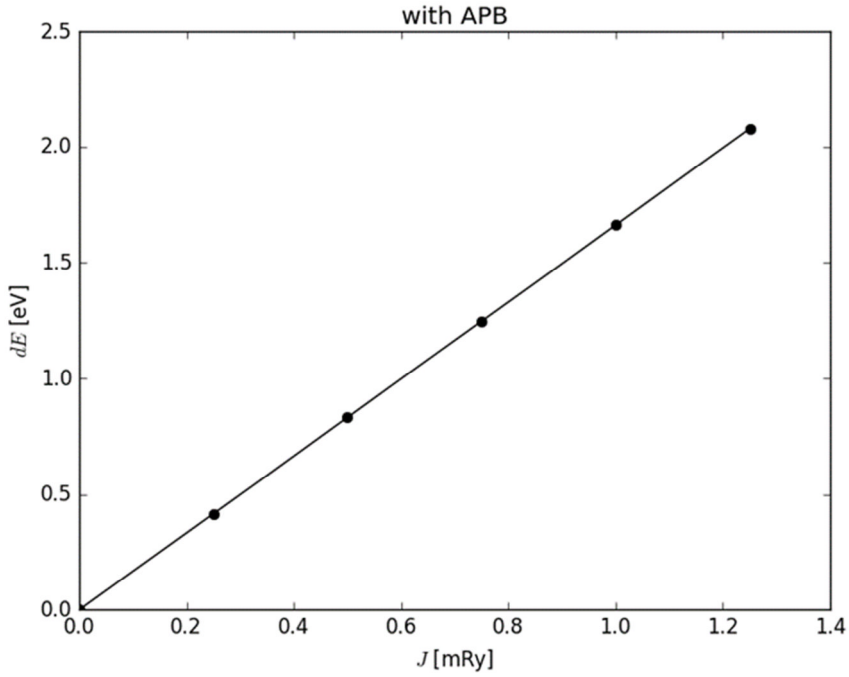

Figure 7.6 The energy difference between AFM and FM configuration for the APB supercell model as a function of the exchange constant *J*.

The results from these calculations demonstrate that the exchange interactions are significantly weakened across the APB defect. **Table 7.1** shows the total energy differences between antiferromagnetic (AFM) and FM configurations for the considered supercells.

For completeness, the same analysis is performed for APBs in CFS and CMS. As can be seen from the **Table 7.1**, the reduction of exchange interactions strength across the APB is most pronounced for the case of CMS. For this Heusler alloy, the strength of ferromagnetic coupling between the grains across the APB is reduced by a factor of ~3, compared to the bulk.

The weakened exchange interactions across the APB can affect the width of the magnetic domain wall in Heusler alloys films. One can estimate this effect once the average exchange constants across the APB are known.

Exchange interactions are strongly localised and decay very fast as the inter-atomic distance increases, as shown for the bulk CMS in Ref. [144]. In **Figure 7.5b,c** an overview of the bond types across the APB defect as a function of the inter-atomic distance is presented. Curie temperature atomistic magnetic simulation performed for the bulk CMS using the known bulk exchange interactions, shows that a good value of the Curie temperature (slightly above 900 K) is obtained (the measured one is 985 K) even by taking into account only the first four shortest interactions, as demonstrated in **Figure 7.5a**.

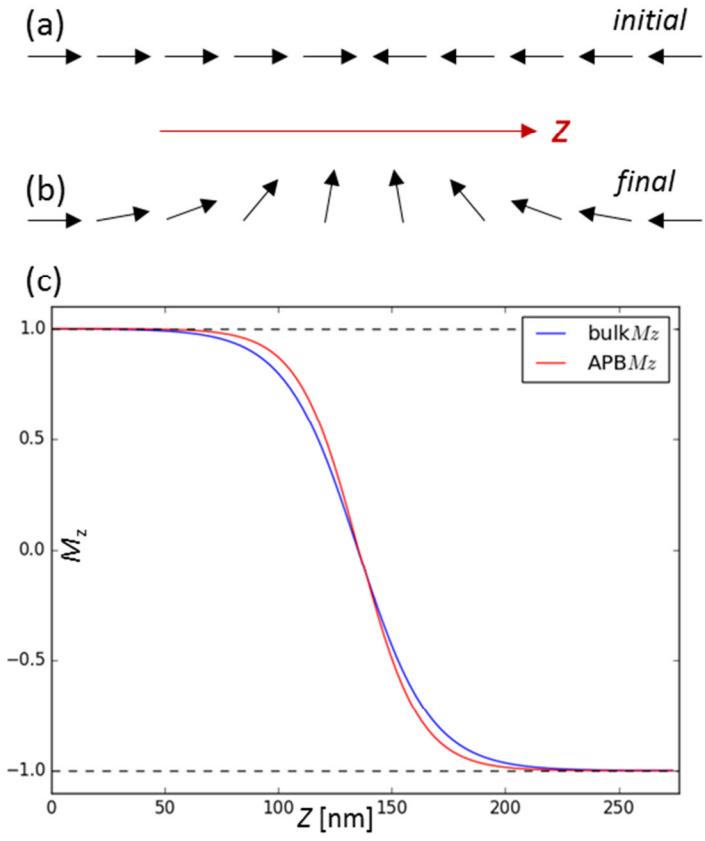

Figure 7.7 Schematics of a) initial b) final magnetic configuration used to calculate the width of the magnetic domain wall for both bulk and APB models as shown in c) where the relative magnetisation is plotted as a function of the distance along the longest dimension of the supercell.

Next, in order to obtain an estimate value of the shortest (and strongest) range exchange interactions across the APB, the following method is used. To the shortest three interactions an equal value of average *J*, which is to be determined, is assigned.

By varying this *J* value in a given range, for each value of *J* the energy difference between the antiferromagnetic and ferromagnetic state is calculated and the results are plotted in **Figure 7.6**. This energy difference was computed using the Heisenberg term of the Hamiltonian in the VAMPIRE code (**Section 3.7**). Since from the previously performed DFT calculations we already know that the energy difference between AFM and FM configuration is 0.9 eV, using the curve in **Figure 7.6**, it can be seen that to this energy difference value corresponds *J* = 0.6 mRy.

By using the obtained *J* value, magnetic atomistic simulations are performed. These magnetic domain wall calculations presented in **Figure 7.7** show that there is a slight change of the width of the magnetic domain wall in a presence of an APB.

These calculations are performed using the VAMPIRE code on large supercells (size details are given in **Section 7.2**). The magnetic moments are initially set in opposite directions at each half of the large supercell model (the APB is in the middle of the supercell). The whole system is then allowed to relax until a convergence is obtained. The converged configurations from these calculations are shown in the **Figure 7.7**.

Figure 7.7 shows that the effect of the APB is small but noticeable. The relative magnetisation (M_z), where *z* is the longest axis of the supercell, in the presence of APB decreases slightly faster in comparison to the bulk case. The domain wall width for the bulk (all parameters used during the simulations are given in **Section 7.2**) is ∼150 nm. The presence of the APB reduces the domain wall width by about ~25 nm, as a result of the weakened exchange interactions.

These results demonstrate that the APB's influence on the overall magnetic properties of Co-based full Heusler alloys is not as dramatic as in materials systems with super-exchange interactions, for an example in magnetite, where the nature of the bonding changes from ferromagnetic in the bulk to strong antiferromagnetic at the APB.

7.6 Formation energy and likely origin of antiphase boundary formation

In this section, the formation energies of the ¼*a*[111] APBs in CFAS, CMS and CFS are computed by comparing the total energies of APB and bulk supercells. For the case of CFAS, the APB formation energy is computed to be 0.9 J/m^2. As shown in the **Table 7.1**, the formation energy values are very similar in the case of APB in CFS or CMS, where we obtain 0.92 J/m^2 and 1.14 J/m^2, respectively. All these values are order of magnitude higher compared to the formation energy of the APB present in magnetite [91]. These relatively high formation energies explain the low APB presence in Co-based Heusler alloy thin films.

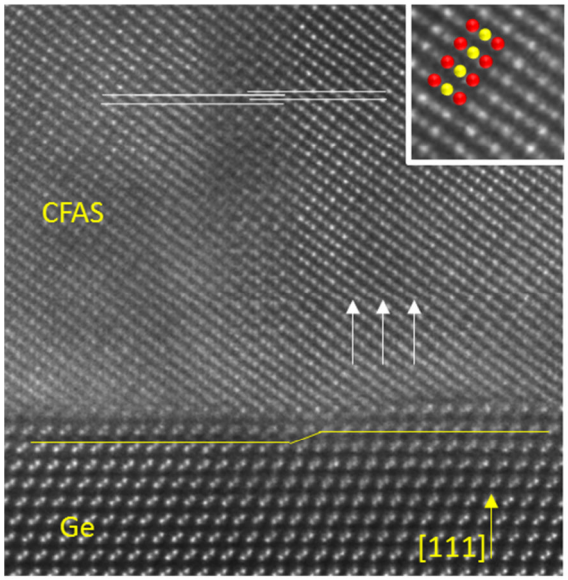

Figure 7.8 Low magnification HAADF STEM image at the APB (outlined by the white interpenetrating lines) vicinity. The step at the Ge surface is outlined by the yellow line. The inset is magnified view of the CFAS bulk-like part shown for better visualisation of the crystallographic directions.

Finally, it should be mentioned that the observed APB is located just above a step in the Ge surface, as shown in the **Figure 7.8**. The close proximity of the step in the substrate surface and the APB in the film, suggests that Ge(111) surface steps can act as nucleation centres for APB formation. This could be used as a mechanism to control their abundance in the thin films.

7.7 Conclusion

It this chapter it was demonstrated that APBs can form in Co-based full Heusler alloys thin films. By performing DFT calculations, it was shown that these extended structural defects lead to a significant density of states in the minority spin band gap which for the case of CFAS reverse the local spin-polarisation. In addition, these calculations also showed that the ferromagnetic alignment still remains favoured when an APB is introduced, however the exchange interactions across the defect are significantly weakened.

Moreover, by performing atomistic magnetic simulations, it was shown that this weakening of the exchange interactions across the APB causes a slight reduction of the magnetic domain wall width compared to that of the bulk. This study has demonstrated that the APBs have considerable effects on the spin-electronic structure. Although their presence is low in the analysed thin films of CFAS, it has to be further minimised, possibly by avoiding steps in the Ge surface, in order to fully exploit the half-metallic character of the electrode in particular for planar type spintronic devices.

8 Conclusion

In this work it was shown that by combining state-of-the-art electron microscopy imaging with first-principles calculations a full correlation between the atomic and spin-electronic structure of interfaces and extended structural defects in the Co-based full Heusler alloys can be established. The electron microscopy imaging demonstrated that their atomic structure can drastically differ from that in the bulk-like part of the thin film which often may be very detrimental for the overall device performance.

It was shown that for Co_2MnSi/Ag the interface atomic structure is not an ideal bulk-like terminated; a presence of an additional monolayer was demonstrated. This additional monolayer as shown by the density functional theory calculations can create huge negative spin-polarisation which will significantly affect the spin-polarised transport across this interface.

The interface between the Heusler alloy and Si which is quite important for spin-injection applications, was demonstrated that can suffer from considerable interfacial intermixing which has significant impact on both spin-polarisation and magnetic moment. It was also shown that the corresponding abrupt interface, in case the interdiffusion can be completely avoided, will not give a desirable interfacial spin-electronic structure. The reversal of the local spin-polarisation in the case of a sharp interface can be fully avoided and very high spin-polarisation across all interface layers can be obtained, by adding a monolayer of Si-Co-Si which is thermodynamically stable to exist at the interface.

The interface between $Co_2FeAl_{0.5}Si_{0.5}$ and Ge, which have almost the same lattice parameter, does not suffer from these challenges, i.e. it does not form any secondary interfacial phases and also has a very minor and atomic planes selective Ge outdiffusion into the film. By first-principles calculations it was shown that this minor Ge outdiffusion does not affect the structural integrity and spin-electronic structure of the interface. It was demonstrated that this interface is characterised with very high interfacial spin-polarisation, hence it is an ideal candidate for spin-injection applications.

It was also demonstrated that extended structural defects are present in the Co-based full Heusler alloys. Their exact atomic structure was revealed by employing electron microscopy. The density functional theory calculations showed that these structural defects can lead even to a reversal of the sign of local spin-polarisation. Although it was shown that their formation energy is significantly higher compared to the low energy structural defects in other halfmetals such as magnetite, the presence of these defects has to be further minimised in order to fully exploit the huge potentials of the Heusler alloys.

There are many possibilities for further research into this subject. Certainly, there are plenty of potential interfaces that can be also studied by the same approach presented here which will potentially reveal all the interfaces with big potentials. Since it was shown that the spin-polarisation can significantly depend on the exact atomic interfacial structure, it is worth to also further study the possibility of controlled growth of interfaces with desired atomic structure. Another potential study is to explore the possibility to control the structural defects density by controlling the steps of the substrate surface. Finally, from more fundamental point of view, the twinning phenomenon observed at many of these interfaces is worth to be studied in details.

Appendix

Appendix 1

Here the '.cell' CASTEP file for the bulk CMS is given:

```
%block lattice_abc
5.65 5.65 5.65
90 90 90
%endblock lattice_abc

%block positions_frac
Co 0.250  0.250  0.250
Co 0.250  0.750  0.750
Co 0.750  0.250  0.750
Co 0.750  0.750  0.250
Co 0.250  0.750  0.250
Co 0.250  0.250  0.750
Co 0.750  0.750  0.750
Co 0.750  0.250  0.250
Mn 0.000  0.000  0.000
Mn 0.000  0.500  0.500
Mn 0.500  0.000  0.500
Mn 0.500  0.500  0.000
Si 0.500  0.500  0.500
Si 0.500  0.000  0.000
Si 0.000  0.500  0.000
Si 0.000  0.000  0.500
%endblock positions_frac

%block hubbard_u
Co d: 2.1
Mn d: 2.1
%endblock hubbard_u

symmetry_generate
snap_to_symmetry
kpoint_mp_spacing 0.03

%block cell_constraints
1 1 1
0 0 0
%endblock cell_constraints
```

The main section of the '.param' CASTEP file for the same system is given here:

```
task : geometryoptimisation
PDOS_CALCULATE_WEIGHTS : true
write_cell_structure : true
spin_polarised : true
cut_off_energy : 600 eV
xc_functional : pbe
spin : +20
max_scf_cycles : 100
```

Appendix 2

An example of a QSTEM input file is given below (only the most important part is shown here):

```
mode: STEM
filename: CFAS_L21.cfg
resolutionX:  0.050000
resolutionY:  0.050000
NCELLX: 8
NCELLY: 25
NCELLZ: 8
v0: 200.000000  % beam energy
tds: yes % include thermal diffuse scattering
temperature: 300.000000      % temperature in Kelvin
slice-thickness: 2.005000  % slice thckness in A
slices: 50                   % number of different slices per slab
center slices: yes     % center slices
slices between outputs: 10  % give intermediate results after every 10 slices
periodicXY: no           % not periodic in x- and y-direction
periodicZ: no            % not periodic in z-direction

scan_x_start:  5.000000  % X position of top left corner of scan window
scan_x_stop:   25.000000       % X position of bottom right corner of scan window
scan_x_pixels: 200     % number of pixels in X-direction
scan_y_start:  5.000000
scan_y_stop:   25.000000
scan_y_pixels: 200
detector: 85.000000 170.000000 detector1 0.000000 0.000000

% STEM probe parameters
nx: 400          % array size used for probe
ny: 400    % ny = nx, if not specified
Cs: 0.0011000            % Spherical abberation in mm
C5: 1.756000             % C_5 abberation in mm
Cc: 1.600000      % Chromatic abberation in mm
```

dV/V: 0.000001 % energy spread in eV (FWHM)
alpha: 24.000000 % Illumination angle in mrad
defocus: 0.000000
astigmatism: 0.000000
astigmatism angle: 0.000000

Appendix 3

In this appendix several selected scripts used during the APB study, all written in Python, will be provided. For clarity, only the main functional part of the scripts will be shown.

a) Plotting energy difference between antiferromagnetic and ferromagnetic state as a function of the exchange constant *J.*

This script (only the main part of it is shown here) takes a supercell that contains APB as an input. The reading part is not shown here, however the atom positions and labels are contained into the variable 'matr'. The first column contains the name of the elements, while the next three their fractional coordinates. This supercell has size (a,b,c) and contains 96 atoms; it is the same supercell used to simulate the PDOS with DFT calculations. The script uses cutoff distance 'rc=1' in lattice constant units. Hence, any interaction between two atoms which are more than a lattice constant apart is not taken into account, since it is of negligible strength. More details of the script are shown in parenthesis/quotations within the code given below.

```
a=3.9926
b=27.6523
c=9.76878
lat_const=a*2**(0.5)
inv_lat=1/lat_const
rc=1.0

(''Here the main exchange interaction constants for the bulk are defined.'')
MnCo5 = 2.80*10**(-3)*2.1798741*10**(-18)
CoCo5 = 0.75*10**(-3)*2.1798741*10**(-18)
MnMn7 = 0.35*10**(-3)*2.1798741*10**(-18)
CoCo8 = 0.30*10**(-3)*2.1798741*10**(-18)

(''The part below creates repeats of the starting supercell, so that the starting supercell is then surrounded by equivalent neighbours in each direction.'')
```

```
dt = np.dtype((np.float64))
f=np.array([0,0,0,0,0,0,0,0,0,0],dtype=dt)
for ix in range(-1,2):
   for iy in range(-1,2):
      for iz in range(-1,2):
         f_index=0
         for j in range(0,96):
            if matr[j,0]=='Co':
               number=0
            elif matr[j,0]=='Mn':
               number=1
            else:
               continue
```

(‘’Depending on the atom’s position, i.e. left or right with respect to the defect, different values for ‘orientation1’ (which gives the moment direction in FM configuration) and ‘orientation2’ (which gives the moment direction in AFM configuration) are allocated.’’)

```
            orientation1 = 1
            orientation2 = 1
            if matr[j, 2] >= 0.5:
               orientation1 = 1
               orientation2 = -1

            p1 = np.array([number, matr[j, 1] + ix, matr[j, 2] + iy, matr[j, 3] + iz, ix, iy, iz,
f_index,
                     orientation1, orientation2])
            f = np.vstack((f,p1))
            f_index=f_index+1
```

(‘’The expanded supercell which has 27 times more atoms than the starting supercell is then stored in the variable ‘f’.’’)

(‘’In the code below, the exchange constant *J* is increasing from 0 with a step ‘delta_J’ and later on for each step the energy difference between AFM and FM state is computed.’’)

```
table=np.array([0,0])
mRy=10**(-3)*2.1798741*10**(-18)
delta_J=0.25*mRy
for mm in range(0, 6):
   energy_diff = 0
```

(''From here starts the part which finds all the interactions within the cutoff radius, and if such interaction has a *J* value which is not negligible, the interaction is added to the list of all interactions.'')

```
   for i in range (1,f.__len__()):
      tem=f[i,:]
      if (tem[4]*tem[4]+tem[5]*tem[5]+tem[6]*tem[6])==0:
         for j in range(1,f.__len__()):
            tem1=f[j,:]
            distance=inv_lat*(a*a*(tem[1]-tem1[1])**2+b*b*(tem[2]-
tem1[2])**2+c*c*(tem[3]-tem1[3])**2)**(0.5)
            if (distance<rc) and (distance>0.0):
               dx = tem[4] - tem1[4]
               dy = tem[5] - tem1[5]
               dz = tem[6] - tem1[6]
               ch=0
               if (distance > 0.4) and (distance < 0.55):
                  if (tem[0]+tem1[0])<=2:
                     J = mm * delta_J
                     ch = 1
               if (distance>0.42) and (distance<0.44) and ((tem[0]+tem1[0])==1):
                  J=MnCo5
               elif (distance>0.48) and (distance<0.51) and ((tem[0]+tem1[0])==0):
                  J=CoCo5
               elif (distance>0.65) and (distance<0.75) and ((tem[0]+tem1[0])==2):
                  J=MnMn7
               elif (distance>0.84) and (distance<0.9) and ((tem[0]+tem1[0])==0):
                  J=CoCo8
               else:
                  if ch==0:
                     continue
               factor = 0.5
               if (dx**2+dy**2+dz**2)!=0:
                  factor = 1
```

(''For each contributing interaction, the energy difference '*dE*' between AFM and FM state is calculated by multiplying *J* with the product of magnetic moment orientation for each atom of the pair, and then taking difference between AFM and FM state. This contribution is then added to the 'energy_diff' which contains the total energy difference from all interactions.'')

```
               dE = factor*J*(tem[8]*tem1[8]-tem[9]*tem1[9])
               energy_diff = energy_diff + dE
```

```
    energy_diff = energy_diff/(1.6*10**(-19))
    table=np.vstack((table,np.array([mm*delta_J/mRy,energy_diff])))

(''The part below plots the results.'')

plt.plot(table[1:,0],table[1:,1],'k-o')
plt.ylabel(r'$dE$ [eV]')
plt.xlabel(r'$J$ [mRy]')
plt.title('with APB')
plt.show()
```

b) Generator of large supercell

This script (only the main part is shown) takes as an input a Heusler cell (in suitable coordinates so that [111] direction is along 'c' axis), with a size (a,b,c) and 96 atoms, the same as the ones used for the PDOS plots, and expands it along the 'b' direction ny = 100 times. The fractional coordinates of the initial (a,b,c) cell are stored in 'matr' where the first column stores the name of each atom, while the next three their fractional coordinates. If the 'b' fractional coordinate for given atom in the final expanded cell is greater than 0.5 then a shift along 'c' by 0.25 is performed. This shift is to create an APB in the middle of the large expanded supercell. In the output file a category 'num' is also included; this integer number distinguish the magnetic species Co and Mn, but also each of them with respect whether they are left or right of the APB. This is to be able to set different initial direction of magnetic moment required to later on perform magnetic domain wall calculations.

```
a=3.9926
b=27.6523
c=9.76878
ny=100
for iy in range(0,ny):
    for j in range(0,96):
        if (matr[j,0]=='Co'):
            if ((matr[j, 2] + iy)/ny) >= 0.5:
                num=2
            else:
                num=0
        elif (matr[j,0]=='Mn'):
            if ((matr[j, 2] + iy)/ny) >= 0.5:
                num = 3
```

```
            else:
                num = 1
        else:
            num=4

        if ((matr[j, 2] + iy) / ny) >= 0.5:
            if (matr[j, 3] + 0.25) >= 1:
                sh = matr[j, 3] + 0.25 - 1
            else:
                sh = matr[j, 3] + 0.25
        else:
            sh = matr[j, 3]

        p1 = np.array([num, matr[j, 1], (matr[j, 2] + iy)/ny, sh])
        f = np.vstack((f,p1))
A=pandas.DataFrame(f,columns=['index','x','y','z'])
t=A.to_excel(writer,index=False,sheet_name='SuperCell')
writer.save()
```

c) A script that generates input files for the atomistic magnetic simulations

Once the large ~280 nm supercell is created with the previous script, the script below generates all the interactions and list of all atoms in a format required for the code used for magnetic simulations.

```
(''The part below reads the input large supercell.'')

data= pandas.read_excel("APB_supercell_280nm.xlsx")
matr = data.as_matrix()
dl = np.dtype((np.float64))
list_atoms=np.array([0,0,0,0,0,0,0],dtype=dl)

(''The following part generates the list of atoms in a specific form to which a magnetic moment is allocated later on in the VAMPIRE code.'')

k=0
for j in range(0,ny*96):
    if matr[j,0]>3:
        continue
    pt = np.array([k, matr[j, 1], matr[j, 2], matr[j, 3], matr[j,0], matr[j,0], matr[j,0]])
    list_atoms = np.vstack((list_atoms,pt))
    k=k+1
```

```
atoms =
pandas.DataFrame(list_atoms,columns=['index','x','y','z','number','number','number'])
atoms.to_excel(writer,index=False,sheet_name='atoms_list')
```

(‘’The list of atoms is stored in ‘list_atoms’ and then transferred to Excel file. The first column is the index for each atom, then the fractional coordinates, and the final three columns distinguish the atoms by their magnetic moment. This is important for the atomistic magnetic simulations.’’)

(‘’The following part creates equivalent neighbours to the initial large supercell.’’)

```
dt = np.dtype((np.float64))
f=np.array([0,0,0,0,0,0,0,0],dtype=dt)
for ix in range(-1,2):
   print(ix)
   for iy in range(-1,2):
      for iz in range(-1,2):
         kk=0
         for j in range(0,ny*96):
            if matr[j,0]>3:
               continue
            p1 = np.array([matr[j,0], matr[j, 1] + ix, matr[j, 2] + iy, matr[j, 3] + iz, ix, iy, iz, kk])
            f = np.vstack((f,p1))
            kk=kk+1
```

(‘’All magnetic species from this system are stored in the variable ‘f’.‘’)

(‘’The code below finds the interactions between atoms, similarly as shown above, and calculates the exchange constant for each of them.’’)

```
interlist=np.array([0,0,0,0,0,0,0])
int_index=0
for i in range (1,f.__len__()):
   print(i)
   tem=f[i,:]
   if (tem[4]*tem[4]+tem[5]*tem[5]+tem[6]*tem[6])==0:
      for j in range(1,f.__len__()):
         tem1=f[j,:]
         distance=inv_lat*(a*a*(tem[1]-tem1[1])**2+b*b*(tem[2]-
tem1[2])**2+c*c*(tem[3]-tem1[3])**2)**(0.5)
         if (distance<rc) and (distance>0.1):
            dx = tem[4] - tem1[4]
            dy = tem[5] - tem1[5]
```

```
        dz = tem[6] - tem1[6]
        ch = 0
        if (distance > 0.4) and (distance < 0.55):
           J = 0.6 * mRy
           ch = 1
        if (distance>0.42) and (distance<0.44) and ((tem[0] % 2 + tem1[0] % 2) == 1):
           J=MnCo43
        elif (distance>0.48) and (distance<0.51) and ((tem[0] % 2 + tem1[0] % 2) == 0):
           J=CoCo50
        elif (distance>0.65) and (distance<0.75) and ((tem[0] % 2 + tem1[0] % 2) == 2):
           J=MnMn70
        elif (distance>0.84) and (distance<0.9) and ((tem[0] % 2 + tem1[0] % 2) == 0):
           J=CoCo86
        else:
           if ch == 0:
              continue
        new_interaction=np.array([int_index, tem[7],tem1[7],dx,dy,dz,J])
        interlist=np.vstack((interlist,new_interaction))
        int_index=int_index+1
```

(‘’The interactions are stored in the list ‘interlist’ and using the code below an output to Excel is created.’’)

```
df = pandas.DataFrame(interlist,columns=['int_index','index_1','index_2','dx','dy','dz','J'])
df.to_excel(writer,index=False,sheet_name='exchange_int')
writer.save()
```

(‘’The interaction list contains all the interactions as rows, and the columns specify: the first one is the index of the interaction, second and third are the indexes of the two atoms of the interacting pair, the next three indexes show whether both of the atoms belong to the same supercell or, one of them is within while the other one belongs to the neighbouring cell (this is important for the calculations in VAMPIRE) and the last column gives the exchange constant.’’)

d) A section of the VAMPIRE ‘ucf’ input file provided to illustrate the required format

```
# Unit cell size:
3.9926  27.6523  9.76878
# Unit cell vectors:
1.0 0.0 0.0
0.0 1.0 0.0
0.0 0.0 1.0
```

(‘’In the next section all atoms are listed; the first row gives the total number of atoms.’’)

```
# Atoms num, id cx cy cz mat lc hc
72
0       0       0       0.583329        0       0       0
1       0       0       0.333333        1       1       1
2       0       0       0.083337        0       0       0
……..
```

(‘’Here the exchange interactions are listed; the first number gives the total number of interactions. The meaning of these columns is explained in the previous section.’’)

```
#Interactions n exctype, id i j dx dy   dz      Jij
1344 0
0       0       68      1       1       0       6.53962E-22
1       0       70      1       1       0       6.10365E-21
2       0       71      1       1       0       1.63491E-21
```

e) A section of the VAMPIRE ‘mat’ input file

```
material:num-materials=4

material[1]:material-name= Co
material[1]:atomic-spin-moment=1.0!muB
material[1]:initial-spin-direction= 0,0,1

material[2]:material-name= Mn
material[2]:atomic-spin-moment=3.0!muB
material[2]:initial-spin-direction= 0,0,1
……
```

f) An example of the VAMPIRE input file

```
dimensions:system-size-x = 15.630049 !nm
dimensions:system-size-y = 15.9705 !nm
dimensions:system-size-z = 276.524 !nm
create:periodic-boundaries-x
create:periodic-boundaries-y
material:file=APB_CMS.mat
material:unit-cell-file=APB_CMS.ucf
sim:program=time-series
```

(‘’This task is for finding an equilibrium configuration; it can be instead ‘curie-temperature’ if curie-temperature simulation is required; many other tasks are also available.’’)

```
sim:integrator=llg-heun
sim:temperature=0
sim:total-time-steps=300000
sim:load-checkpoint=restart
sim:save-checkpoint=end
output:time-steps
output:height-magnetisation-normalised
```

Abbreviations

2D	Two Dimensional
AFM	Antiferromagnetic
APB	Anti-Phase Boundary
ARCHER	name of the used national supercomputer
BF	Bright Field
BF STEM	Bright Field Scanning Transmission Electron Microscopy
BF TEM	Bright Field Transmission Electron Microscopy
BFGS	Broyden–Fletcher–Goldfarb–Shanno
CASTEP	plane wave pseudopotential code
CCD	Charge Coupled Device
CFA	Co_2FeAl
CFAS	$Co_2Fe(Al_{0.5},Si_{0.5})$
CFMS	$Co_2(Fe_{0.5},Mn_{0.5})Si$
CFS	Co_2FeSi
CIP	current-in-plane
CMS	Co_2MnSi
CPP	current-perpendicular-to-plane
CrystalKit	a software to create and visualise atomic models
DF	Dark Field
DF TEM	Dark Field Transmission Electron Microscopy
DFT	Density Functional Theory
DOS	Density Of States
DRAM	Dynamical Random Access Memory
EDXS	Energy Dispersive X-ray Spectroscopy
EELS	Electron Energy Loss Spectroscopy
EFTEM	Energy Filtered Transmission Electron Microscopy
FET	Field Effect Transistor
FIB	Focused Ion Beam
FM	Ferromagnetic
GGA	Generalised Gradient Approximation
GMR	Giant Magnetoresistance
HAADF STEM	High Angle Annular Dark Field STEM
HRTEM	High Resolution Transmission Electron Microscopy
ICSD	Inorganic Crystal Structure Database
JEMS	electron microscopy software
JEOL	Electron microscopes manufacturer
LDA	Local Density Approximation
MAADF	Middle Angle Annular Dark Field

MBE	Molecular Beam Epitaxy
MOSFET	Metal Oxide Semiconductor Field Effect Transistor
MR	Magnetoresistance
MTJ	Magnetic Tunnelling Junction
OPTADOS	software for DOS analysis
PBE	Perdew–Burke–Ernzerhof
PDOS	Partial Density Of States
PIPS	Precision Ion Polishing System
PNR	Polarised Neutron Reflectivity
QSTEM	software for simulation of microscopy images
SAED	Selected Area Electron Diffraction
SP	Spin Polarisation
STEM	Scanning Transmission Electron Microscopy
STT-MRAM	Spin-Transfer-Torque Magnetoresistive Random Access Memory
SV	Spin Valve
TEM	Transmission Electron Microscopy
TDS	Thermal Diffuse Scattering
TMR	Tunnelling Magnetoresistance
VAMPIRE	software for atomistic magnetic simulations
VESTA	software for visualisation of atomistic models

Symbols

$*$	convolution
°C	Degree Celsius
Å	Angstrom
a_i	Proportion of electrons with spins oriented along the magnetisation
B2	type of ordering in Heusler alloys
$B.Z.$	Brillouin zone
β	Spin-polarisation
c	speed of light
$c_{i,\boldsymbol{G}}$	expansion coefficients
C_s	spherical aberration coefficient
d_{xy}	Type of *d*-orbital
d_{xz}	Type of *d*-orbital
d_{yz}	Type of *d*-orbital
$d_{x^2-y^2}$	Type of *d*-orbital
$d_{3z^2-r^2}$	Type of *d*-orbital
δ	Dirac delta function
Δ	Laplace operator
e	charge of the electron
e_u	orbital
e_g	orbital
E	total energy
E_c	cut-off energy
E_f	Fermi-level
E_{form}	Formation energy
$E^{GGA}{}_{xc}$	Generalised Gradient Approximation energy functional
E_H	Hartree energy
E^{LSDA}	Local Spin Density Approximation energy functional
E_v	Valence band edge
E_{xc}	exchange-correlation energy
ε_i	single particle energies
$\varepsilon_{i,\boldsymbol{k}}^{\uparrow,\downarrow}$	Energy levels at given ***k*** vector
ε_0	dielectric constant of vacuum
$\varepsilon_{xc}^{\mathrm{unif}}$	exchange-correlation energy of a uniform electron gas
φ	critical angle
Φ_i	electron wave-functions
G_p (G_a)	Conductivity coefficient for MTJ's parallel (antiparallel) configuration
$\boldsymbol{G}$	Inverse lattice unit vectors
h	Planck's constant
H	Hamiltonian
$H_{anisothropy}$	Anisotropy part of the Hamiltonian

Symbols

$H_{exchange}$	Exchange part of the Hamiltonian
$H_{ext.\ field}$	Hamiltonian due to interaction with an external field
$\hbar$	$h/2\pi$
$J_{i,j}$	exchange interaction constants
$J_{\uparrow(\downarrow)}$	Spin-up(down) current density
J	Total current density
$\boldsymbol{k}$	wave vector
K	Kelvin
K_α	EDXS edge
l_s	Spin diffusion length
$L2_1$	type of ordering in Heusler alloys
$L_{2,3}$	EELS edge
λ	wavelength
m	mass of the electron
$\mu_{\uparrow(\downarrow)}$	Spin-up(down) electrochemical potentials
μ_B	Bohr magneton
M	Magnetic moment
$n_{\uparrow,\downarrow}$	spin up/down DOS at the Fermi-level
ω	smearing width
p	momentum
$p(x,y,z)$	propagator
Ψ	wavefunction
$\boldsymbol{r}$	position
$r_{N,F}$	Product of resistivity and spin diffusion length
ρ	electron density
$\rho^{\uparrow,\downarrow}$	spin up/down electron density
$\nabla\rho_\uparrow(\boldsymbol{r}), \nabla\rho_\downarrow(\boldsymbol{r})$	gradient of spin up and down electron densities
R_a (R_p)	Resistance of MTJ in antiparallel (parallel) configuration
Ry	Rydberg
$\boldsymbol{S}_i$	magnetic moment direction
σ	interaction parameter
$\sigma_{\uparrow(\downarrow)}$	Spin-up(down) conductivity
t_{2g}	orbital
t_{1u}	orbital
T	kinetic energy
t(**x**)	transmission function
U	Hubbard-U energy
U_0	potential in interstitial region
V	voltage
v_{eff}	effective potential
v_{ext}	external potential
V_p	electrostatic potential
$v_z(x,y)$	projected potential
V	Number of valence electrons

(x, y, z)	coordinates
Z	atomic number

References

[1] Felser, C., Fecher, G. H. & Balke, B. Spintronics: A challenge for materials science and solid-state Chemistry. *Angewandte Chemie International Edition* **46**, 668 (2007).

[2] Moore, G. E. Cramming more components onto integrated circuits, Reprinted from Electronics, volume 38, number 8, April 19, 1965, pp.114 ff. *IEEE Solid-State Circuits Society Newsletter* **11**, 33 (2006).

[3] Datta, S. & Das, B. Electronic analog of the electro-optic modulator. *Applied Physics Letters* **56**, 665 (1990).

[4] Baibich, M. N., Broto, J. M., Fert, A., Nguyen, F., Petroff, F., Eitenne, P., Creuzet, G., Friederich, A. & Chazelas, J. Giant magnetoresistance of (001)Fe/(001)Cr magnetic superlattices. *Physical Review Letters* **61**, 2472 (1988).

[5] Binasch, G., Grünberg, P., Saurenbach, F. & Zinn, W. Enhanced magnetoresistance in layered magnetic structures with antiferromagnetic interlayer exchange. *Physical Review B* **39**, 4828 (1989).

[6] Prinz, G. A. Magnetoelectronics. *Science* **282**, 1660 (1998).

[7] Ikeda, S., Hayakawa, J., Ashizawa, Y., Lee, Y. M., Miura, K., Hasegawa, H., Tsunoda, M., Matsukura, F. & Ohno, H. Tunnel magnetoresistance of 604% at 300K by suppression of Ta diffusion in CoFeB/MgO/CoFeB pseudo-spin-valves annealed at high temperature. *Applied Physics Letters* **93**, 082508 (2008).

[8] Wolf, S. A., Awschalom, D. D., Buhrman, R. A., Daughton, J. M., Molnar, S., Roukes, M. L., Chtchelkanova, A. Y. & Treger, D. M. Spintronics: A spin-based electronics vision for the future. *Science* **294**, 1488 (2001).

[9] Butler, W. H., Zhang, X. G., Schulthess, T. C. & MacLaren, J. M. Spin-dependent tunneling conductance of Fe|MgO|Fe sandwiches. *Physical Review B* **63**, 054416 (2001).

[10] Kent, A. D. & Worledge, D. C. A new spin on magnetic memories. *Nature Nanotechnology* **10**, 187 (2015).

[11] Julliere, M. Tunneling between ferromagnetic films. *Physics Letters A* **54**, 225 (1975).

[12] Atsufumi, H. & Koki, T. Future perspectives for spintronic devices. *Journal of Physics D: Applied Physics* **47**, 193001 (2014).

[13] Dowben, P. A., Ning, W. & Christian, B. When measured spin polarization is not spin polarization. *Journal of Physics: Condensed Matter* **23**, 171001 (2011).

[14] Soulen, R. J., Byers, J. M., Osofsky, M. S., Nadgorny, B., Ambrose, T., Cheng, S. F., Broussard, P. R., Tanaka, C. T., Nowak, J., Moodera, J. S., Barry, A. & Coey J. M. D. Measuring the spin polarization of a metal with a superconducting point contact. *Science* **282**, 85 (1998).

[15] Kämper, K. P., Schmitt, W., Güntherodt, G., Gambino, R. J. & Ruf, R. CrO_2 A new half-metallic ferromagnet? *Physical Review Letters* **59**, 2788 (1987).

[16] Jourdan, M., Minar, J., Braun, J., Kronenberg, A., Chadov, S., Balke, B., Gloskovskii, A., Kolbe, M., Elmers, H. J., Schonhense, G., Ebert, H., Felser, C. & Klaui, M. Direct observation of half-metallicity in the Heusler compound Co_2MnSi. *Nature Communications* **5***,* 3974 (2014).

[17] Bowen, M., Bibes, M., Barthelemy, A., Contour, J. P., Anane, A., Lemaitre, Y. & Fert, A. Nearly total spin polarization in $La_{2/3}Sr_{1/3}MnO_3$ from tunneling experiments. *Applied Physics Letters* **82***,* 233 (2003).

[18] Hamaya, K., Hashimoto, N., Oki, S., Yamada, S., Miyao, M. & Kimura, T. Estimation of the spin polarization for Heusler-compound thin films by means of nonlocal spin-valve measurements: Comparison of Co_2FeSi and Fe_3Si. *Physical Review B* **85***,* 100404 (2012).

[19] Palmstrøm, C. J. Heusler compounds and spintronics. *Progress in Crystal Growth and Characterization of Materials* **62***,* 371 (2016).

[20] Stroppa, A., Picozzi, S., Continenza, A. & Freeman, A. J. Electronic structure and ferromagnetism of Mn-doped group-IV semiconductors. *Physical Review B* **68***,* 155203 (2003).

[21] Gilks, D., McKenna, K., Nedelkoski, Z., Kuerbanjiang, B., Matsuzaki, K., Susaki, T., Lari, L., Kepaptsoglou, D., Ramasse, Q., Tear, S. & Lazarov, V. K. Polar spinel-perovskite interfaces: an atomistic study of $Fe_3O_4(111)/SrTiO_3(111)$ structure and functionality. *Scientific Reports* **6***,* 29724 (2016).

[22] Gilks, D., Nedelkoski, Z., Lari, L., Kuerbanjiang, B., Matsuzaki, K., Susaki, T., Kepaptsoglou, D., Ramasse, Q., Evans, R., McKenna, K. & Lazarov, V. K. Atomic and electronic structure of twin growth defects in magnetite. *Scientific Reports* **6***,* 20943 (2016).

[23] McKenna, K. P., Hofer, F., Gilks, D., Lazarov, V. K., Chen, C., Wang, Z. & Ikuhara, Y. Atomic-scale structure and properties of highly stable antiphase boundary defects in Fe_3O_4. *Nature Communications* **5***,* 5740 (2014).

[24] Park, J. H., Vescovo, E., Kim, H. J., Kwon, K., Ramesh, R., & Venkatesan, T. Direct evidence for a half-metallic ferromagnet. *Nature* **392***,* 794 (1998).

[25] Galanakis, I. Surface half-metallicity of CrAs in the zinc-blende structure. *Physical Review B* **66***,* 012406 (2002).

[26] Galanakis, I. & Mavropoulos, P. Zinc-blende compounds of transition elements with N, P, As, Sb, S, Se, and Te as half-metallic systems. *Physical Review B* **67***,* 104417 (2003).

[27] Katsnelson, M. I., Irkhin, V. Y., Chioncel, L., Lichtenstein, A. I. & de Groot, R. A. Half-metallic ferromagnets: From band structure to many-body effects. *Reviews of Modern Physics* **80***,* 315 (2008).

[28] Žutić, I., Fabian, J. & Das Sarma, S. Spintronics: Fundamentals and applications. *Reviews of Modern Physics* **76***,* 323 (2004).

[29] Balke, B., Wurmehl, S., Fecher, G. H., Felser, C. & Kübler, J. Rational design of new materials for spintronics: Co_2FeZ (Z =Al, Ga, Si, Ge). *Science and Technology of Advanced Materials* **9***,* 014102 (2008).

[30] de Groot, R. A., Mueller, F. M., Engen, P. G. v. & Buschow, K. H. J. New class of materials: half-metallic ferromagnets. *Physical Review Letters* **50***,* 2024 (1983).

[31] Caruso, A. N., Borca, C. N., Ristoiu, D., Nozières, J. P. & Dowben, P. A. A comparison of surface segregation for two semi-Heusler alloys: TiCoSb and NiMnSb. *Surface Science* **525***,* L109 (2003).

[32] Ristoiu, D., Nozières, J. P., Borca, C. N., Borca, B. & Dowben, P. A. Manganese surface segregation in NiMnSb. *Applied Physics Letters* **76***,* 2349 (2000).

[33] Caballero, J. A., Reilly, A. C., Hao, Y., Bass, J., Pratt, W. P., Petro, F. & Childress, J. R. Effect of deposition parameters on the CPP-GMR of NiMnSb-based spin-valve structures. *Journal of Magnetism and Magnetic Materials* **198–199***,* 55 (1999).

[34] Webster, P. J. Magnetic and chemical order in Heusler alloys containing cobalt and manganese. *Journal of Physics and Chemistry of Solids* **32***,* 1221 (1971).

[35] Ziebeck, K. R. A. & Webster, P. J. A neutron diffraction and magnetization study of Heusler alloys containing Co and Zr, Hf, V or Nb. *Journal of Physics and Chemistry of Solids* **35***,* 1 (1974).

[36] Picozzi, S., Continenza, A. & Freeman, A. J. Co_2MnX (X=Si, Ge, Sn) Heusler compounds: An ab-initio study of their structural, electronic, and magnetic properties at zero and elevated pressure. *Physical Review B* **66***,* 094421 (2002).

[37] Galanakis, I., Dederichs, P. H. & Papanikolaou, N. Slater-Pauling behavior and origin of the half-metallicity of the full-Heusler alloys. *Physical Review B* **66***,* 174429 (2002).

[38] Okamura, S., Miyazaki, A., Sugimoto, S., Tezuka, N. & Inomata, K. Large tunnel magnetoresistance at room temperature with a Co_2FeAl full-Heusler alloy electrode. *Applied Physics Letters* **86***,* 232503 (2005).

[39] Sakuraba, Y., Nakata, J., Oogane, M., Ando, Y., Kato, H., Sakuma, A., Miyazaki, T. & Kubota, H. Magnetic tunnel junctions using B2-ordered Co_2MnAl Heusler alloy epitaxial electrode. *Applied Physics Letters* **88***,* 022503 (2006).

[40] Sakuraba, Y., Hattori, M., Oogane, M., Ando, Y., Kato, H., Sakuma, A. & Miyazaki, T. H. Kubota *et al.* Giant tunneling magnetoresistance in Co_2MnSi/Al–O/Co_2MnSi magnetic tunnel junctions. *Applied Physics Letters* **88***,* 192508 (2006).

[41] Tezuka, N., Ikeda, N., Sugimoto, S. & Inomata, K. 175% tunnel magnetoresistance at room temperature and high thermal stability using $Co_2FeAl_{0.5}Si_{0.5}$ full-Heusler alloy electrodes. *Applied Physics Letters* **89***,* 252508 (2006).

[42] Nobuki, T., Naomichi, I., Satoshi, S. & Koichiro, I. Giant tunnel magnetoresistance at room temperature for junctions using full-Heusler $Co_2FeAl_{0.5}Si_{0.5}$ electrodes. *Japanese Journal of Applied Physics* **46***,* L454 (2007).

[43] Li, S., Takahashi, Y. K., Furubayashi, T. & Hono, K. Enhancement of giant magnetoresistance by L21 ordering in $Co_2Fe(Ge_{0.5}Ga_{0.5})$ Heusler alloy current-perpendicular-to-plane pseudo spin valves. *Applied Physics Letters* **103***,* 042405 (2013).

[44] Nakatani, T. M., Furubayashi, T., Kasai, S., Sukegawa, H., Takahashi, Y. K., Mitani, S. & Hono, K. Bulk and interfacial scatterings in current-perpendicular-to-plane giant

magnetoresistance with $Co_2Fe(Al_{0.5}Si_{0.5})$ Heusler alloy layers and Ag spacer. *Applied Physics Letters* **96***,* 212501 (2010).

[45] Kimura, T., Hashimoto, N., Yamada, S., Miyao, M. & Hamaya, K. Room-temperature generation of giant pure spin currents using epitaxial Co_2FeSi spin injectors. *NPG Asia Materials* **4***,* e9 (2012).

[46] Shan, R., Sukegawa, H., Wang, W. H., Kodzuka, M., Furubayashi, T., Ohkubo, T., Mitani, S., Inomata, K. & Hono, K. Demonstration of half-metallicity in Fermi-level-tuned Heusler alloy $Co_2FeAl_{0.5}Si_{0.5}$ at room temperature. *Physical Review Letters* **102***,* 246601 (2009).

[47] Hasnip, P. J., Smith, J. H. & Lazarov, V. K. Ab initio studies of disorder in the full Heusler alloy $Co_2Fe_xMn_{1-x}Si$. *Journal of Applied Physics* **113***,* 17B106 (2013).

[48] Inomata, K., Okamura, S., Miyazaki, A., Kikuchi, M., Tezuka, N., Wojcik, M. & Jedryka, E. Structural and magnetic properties and tunnel magnetoresistance for $Co_2(Cr,Fe)Al$ and Co_2FeSi full-Heusler alloys. *Journal of Physics D: Applied Physics* **39***,* 816 (2006).

[49] Hasnip, P., Loach, C. H., Smith, J. H., Probert, M. I. J., Gilks, D., Sizeland, J., Lari, L., Sagar, J., Yoshida, K., Oogane, M., Hirohata, A. & Lazarov, V. K. The effect of cobalt-sublattice disorder on spin polarisation in $Co_2Fe_xMn_{1-x}Si$ Heusler alloys. *Materials* **7***,* 1473 (2014).

[50] Nedelkoski, Z., Hasnip, P. J., Sanchez, A. M., Kuerbanjiang, B., Higgins, E., Oogane, M., Hirohata, A., Bell, G. R. & Lazarov, V. K. The effect of atomic structure on interface spin-polarization of half-metallic spin valves: Co_2MnSi/Ag epitaxial interfaces. *Applied Physics Letters* **107***,* 212404 (2015).

[51] Hasnip, P. J., Loach, C. H., Smith, J. H., Probert, M. I. J., Gilks, D., Sizeland, J., Yoshida, K., Oogane, M., Hirohata, A. & Lazarov, V. K. B2 atomic disorder in $Co_2Fe_XMn_{1-X}Si$ Heusler alloys. *Journal of the Magnetics Society of Japan* **38***,* 50 (2014).

[52] Picozzi, S., Continenza, A. & Freeman, A. J. Role of structural defects on the half-metallic character of Co_2MnGe and Co_2MnSi Heusler alloys. *Physical Review B* **69***,* 094423 (2004).

[53] Picozzi, S. & Freeman, A. J. Polarization reduction in half-metallic Heusler alloys: the effect of point defects and interfaces with semiconductors. *Journal of Physics: Condensed Matter* **19***,* 315215 (2007).

[54] Li, G.-f., Honda, Y., Liu, H., Matsuda, K., Arita, M., Uemura, T., Yamamoto, M., Miura, Y., Shirai, M., Saito, T., Shi, F. & Voyles, P. M. Effect of nonstoichiometry on the half-metallic character of Co_2MnSi investigated through saturation magnetization and tunneling magnetoresistance ratio. *Physical Review B* **89***,* 014428 (2014).

[55] Kozina, X., Karel, J., Ouardi, S., Chadov, S., Fecher, G. H., Felser, C., Stryganyuk, G., Balke, B., Ishikawa, T., Uemura, T., Yamamoto, M., Ikenaga, E., Ueda, S. & Kobayashi, K. Probing the electronic states of high-TMR off-stoichiometric

Co_2MnSi thin films by hard x-ray photoelectron spectroscopy. *Physical Review B* **89***,* 125116 (2014).

[56] Lari, L., Yoshida, K., Galindo, P. L., Sato, J., Sizeland, J., Gilks, D., Uddin, G. M., Nedelkoski, Z., Hasnip, P. J., Hirohata, A., Oogane, M., Ando, Y. & Lazarov, V. K. Correlations between atomic structure and giant magnetoresistance ratio in Co_2(Fe,Mn)Si spin valves. *Journal of Physics D: Applied Physics* **47***,* 322003 (2014).

[57] Hägele, D., Oestreich, M., Rühle, W. W., Nestle, N. & Eberl, K. Spin transport in GaAs. *Applied Physics Letters* **73***,* 1580 (1998).

[58] Huang, B., Monsma, D. J. & Appelbaum, I. Coherent Spin Transport through a 350 Micron Thick Silicon Wafer. *Physical Review Letters* **99***,* 177209 (2007).

[59] Schmidt, G., Ferrand, D., Molenkamp, L. W., Filip, A. T. & van Wees, B. J. Fundamental obstacle for electrical spin injection from a ferromagnetic metal into a diffusive semiconductor. *Physical Review B* **62***,* R4790 (2000).

[60] Fert, A. & Jaffrès, H. Conditions for efficient spin injection from a ferromagnetic metal into a semiconductor. *Physical Review B* **64***,* 184420 (2001).

[61] Rashba, E. I. Theory of electrical spin injection: Tunnel contacts as a solution of the conductivity mismatch problem. *Physical Review B* **62***,* R16267 (2000).

[62] Jansen, R. Silicon spintronics. *Nature Materials* **11***,* 400 (2012).

[63] van 't Erve, O. M. J., Hanbicki, A. T., Holub, M., Li, C. H., Awo-Affouda, C., Thompson, P. E. & Jonker, B. T. Electrical injection and detection of spin-polarized carriers in silicon in a lateral transport geometry. *Applied Physics Letters* **91***,* 212109 (2007).

[64] Sasaki, T., Oikawa, T., Suzuki, T., Shiraishi, M., Suzuki, Y. & Tagami, K. Evidence of electrical spin injection into silicon using MgO tunnel barrier. *IEEE Trans Magn* **46***,* 1436 (2010).

[65] Dash, S. P., Sharma, S., Patel, R. S., de Jong, M. P. & Jansen, R. Electrical creation of spin polarization in silicon at room temperature. *Nature* **462***,* 491 (2009).

[66] Farshchi, R. & Ramsteiner, M. Spin injection from Heusler alloys into semiconductors: A materials perspective. *Journal of Applied Physics* **113***,* 191101 (2013).

[67] van 't Erve, O. M. J., Kioseoglou, G., Hanbicki, A. T., Li, C. H., Jonker, B. T., Mallory, R., Yasar, M. & Petrou, A. comparison of Fe/Schottky and Fe/Al_2O_3 tunnel barrier contacts for electrical spin injection into GaAs. *Applied Physics Letters* **84***,* 4334 (2004).

[68] Ohno, Y., Young, D. K., Beschoten, B., Matsukura, F., Ohno, H. & Awschalom, D. D. Electrical spin injection in a ferromagnetic semiconductor heterostructure. *Nature* **402***,* 790 (1999).

[69] Fiederling, R., Keim, M., Reuscher, G., Ossau, W., Schmidt, G., Waag, A. & Molenkamp, L. W. Injection and detection of a spin-polarized current in a light-emitting diode. *Nature* **402***,* 787 (1999).

[70] Wurmehl, S., Fecher, G. H., Kandpal, H. K., Ksenofontov, V., Felser, C. & Lin, H. Investigation of Co_2FeSi: The Heusler compound with highest Curie temperature and magnetic moment. *Applied Physics Letters* **88**, 032503 (2006).

[71] Hashimoto, M., Herfort, J., Trampert, A., Schönherr, H. P. & Ploog, K. H. Growth temperature dependent interfacial reaction of Heusler-alloy Co_2FeSi/GaAs(001) hybrid structures. *Journal of Physics D: Applied Physics* **40**, 1631 (2007).

[72] Yamada, S., Hamaya, K., Yamamoto, K., Murakami, T., Mibu, K., & Miyao, *M.* Significant growth-temperature dependence of ferromagnetic properties for Co_2FeSi/Si(111) prepared by low-temperature molecular beam epitaxy. *Applied Physics Letters* **96**, 082511 (2010).

[73] Singh, L. J., Barber, Z. H., Kohn, A., Petford-Long, A. K., Miyoshi, Y., Bugoslavsky, Y. & Cohen, L. F. Interface effects in highly oriented films of the Heusler alloy Co_2MnSi on GaAs(001). *Journal of Applied Physics* **99**, 013904 (2006).

[74] Kohn, A., Lazarov, V. K., Singh, L. J., Barber, Z. H. & Petford-Long, A. K. The structure of sputter-deposited Co_2MnSi thin films deposited on GaAs(001). *Journal of Applied Physics* **101**, 023915 (2007).

[75] Damsgaard, C. D., Hickey, M. C., Holmes, S. N., Feidenhans'l, R., Mariager, S. O., Jacobsen, C. S. & Hansen, J. B. Interfacial, electrical, and spin-injection properties of epitaxial Co_2MnGa grown on GaAs(100). *Journal of Applied Physics* **105**, 124502 (2009).

[76] Dong, X. Y., Adelmann, C., Xie, J. Q., Palmstrøm, C. J., Lou, X., Strand, J., Crowell, P. A., Barnes, J.-P. & Petford-Long, A. K. Spin injection from the Heusler alloy Co_2MnGe into $Al_{0.1}Ga_{0.9}As$⁄GaAs heterostructures. *Applied Physics Letters* **86**, 102107 (2005).

[77] Bruski, P., Manzke, Y., Farshchi, R., Brandt, O., Herfort, J. & Ramsteiner, M. All-electrical spin injection and detection in the Co_2FeSi/GaAs hybrid system in the local and non-local configuration. *Applied Physics Letters* **103**, 052406 (2013).

[78] Ramsteiner, M., Brandt, O., Flissikowski, T., Grahn, H. T., Hashimoto, M., Herfort, J. & Kostial, H. Co_2FeSi/GaAs/(Al,Ga)As spin light-emitting diodes: Competition between spin injection and ultrafast spin alignment. *Physical Review B* **78**, 121303 (2008).

[79] Chadov, S., Graf, T., Chadova, K., Dai, X., Casper, F., Fecher, G. H. & Felser, C. Efficient spin injector scheme based on Heusler materials. *Physical Review Letters* **107**, 047202 (2011).

[80] Ko, V., Han, G., Qiu, J. & Feng, Y. P. The band structure-matched and highly spin-polarized Co_2CrZ/Cu_2CrAl Heusler alloys interface. *Applied Physics Letters* **95**, 202502 (2009).

[81] Picozzi, S., Continenza, A. & Freeman, A. J. Spin injection at Heusler/semiconductor interfaces: First-principles determination of potential discontinuity and half-metallicity. *Journal of Applied Physics* **94**, 4723 (2003).

[82] Iosif, G. Towards half-metallic interfaces: Co_2CrAl/InP contacts. *Journal of Physics: Condensed Matter* **16**, 8007 (2004).

[83] Feng, Y., Wu, B., Yuan, H. & Chen, H. Structural, electronic and magnetic properties of Co_2MnSi/Ag(1 0 0) interface. *Journal of Alloys and Compounds* **623**, 29 (2015).

[84] Khosravizadeh, S., Hashemifar, S. J. & Akbarzadeh, H. First-principles study of the Co_2FeSi(001) surface and Co_2FeSi/GaAs(001) interface. *Physical Review B* **79**, 235203 (2009).

[85] Nagao, K., Miura, Y. & Shirai, M. Half-metallicity at the (110) interface between a full Heusler alloy and GaAs. *Physical Review B* **73**, 104447 (2006).

[86] Chen, L.-Y., Wang, S.-F., Zhang, Y., Zhang, J.-M. & Xu, K.-W. Ab initio calculation of Co_2MnSi/semiconductor (SC, = GaAs, Ge) heterostructures. *Thin Solid Films* **519**, 4400 (2011).

[87] Venkateswaran, S. P., Nuhfer, N. T. & De Graef, M. Anti-phase boundaries and magnetic domain structures in Ni_2MnGa-type Heusler alloys. *Acta Materialia* **55**, 2621 (2007).

[88] Margulies, D. T., Parker, F. T., Rudee, M. L., Spada, F. E., Chapman, J. N., Aitchison, P. R. & Berkowitz, A. E. Origin of the anomalous magnetic behaviour in single crystal Fe_3O_4 films. *Physical Review Letters* **79**, 5162 (1997).

[89] Eerenstein, W., Palstra, T. T. M., Saxena, S. S. & Hibma, T. Spin-polarized transport across sharp antiferromagnetic boundaries. *Physical Review Letters* **88**, 247204 (2002).

[90] Eerenstein, W., Palstra, T. T. M. & Hibma, T. Spin-valve behaviour of anti-ferromagnetic boundaries in ultrathin magnetite films. *Thin Solid Films* **400**, 90 (2001).

[91] McKenna, K. P., Hofer, F., Gilks, D., Lazarov, V. K., Chen, C., Wang, Z. & Ikuhara, Y. Atomic-scale structure and properties of highly stable antiphase boundary defects in Fe_3O_4. *Nat Commun* **5**, 5740 (2014).

[92] Arthur, J. R. Molecular beam epitaxy. *Surface Science* **500**, 189 (2002).

[93] Window, B. Recent advances in sputter deposition. *Surface and Coatings Technology* **71**, 93 (1995).

[94] Lari, L., Lea, S., Feeser, C., Wessels, B. W. & Lazarov, V. K. Ferromagnetic InMnSb multi-phase films study by aberration-corrected (scanning) transmission electron microscopy. *Journal of Applied Physics* **111**, 07C311 (2012).

[95] Williams, D. B. & Carter, B. C., Transmission electron microscopy, Springer (2009).

[96] Pennycook, S. J. & Nellist, P. D., Scanning Transmission Electron Microscopy: Imaging and analysis, Springer (2011).

[97] Fultz, B. & Howe, J., Transmission electron microscopy and diffractometry of materials, Springer (2013).

[98] Pennycook, S. J. & Jesson, D. E. High-resolution Z-contrast imaging of crystals. *Ultramicroscopy* **37**, 14 (1991).

[99] Ishikawa, R., Okunishi, E., Sawada, H., Kondo, Y., Hosokawa, F. & Abe, E. Direct imaging of hydrogen-atom columns in a crystal by annular bright-field electron microscopy. *Nature Materials* **10**, 278 (2011).

[100] Okunishi, E., Ishikawa, I., Sawada, H., Hosokawa, F., Hori, M. & Kondo, Y. Visualization of light elements at ultrahigh resolution by STEM annular bright field microscopy. *Microscopy and Microanalysis* **15***,* 164 (2009).

[101] Krivanek, O. L., Corbin, G. J., Dellby, N., Elston, B. F., Keyse, R. J., Murfitt, M. F., Own, C. S., Szilagyi, Z. S. & Woodruff, J. W. An electron microscope for the aberration-corrected era. *Ultramicroscopy* **108***,* 179 (2008).

[102] van Benthem, K. & Pennycook, S. J. Imaging and spectroscopy of defects in semiconductors using aberration-corrected STEM. *Applied Physics A* **96***,* 161 (2009).

[103] Muller, D. A., Kourkoutis, L. F., Murfitt, M., Song, J. H., Hwang, H. Y., Silcox, J., Dellby, N. & Krivanek, O. L. Atomic-scale chemical imaging of composition and bonding by aberration-corrected microscopy. *Science* **319***,* 1073 (2008).

[104] Klenov, D. O. & Zide, J. M. O. Structure of the InAlAs/InP interface by atomically resolved energy dispersive spectroscopy. *Applied Physics Letters* **99***,* 141904 (2011).

[105] Mitchell, D. *Dave Mitchell's DigitalMicrograph™ Scripting Website*. Available from: http://www.dmscripting.com/recent_updates.html.

[106] Schaffer, B., Grogger, W. & Kothleitner, G. Automated spatial drift correction for EFTEM image series. *Ultramicroscopy* **102***,* 27 (2004).

[107] Schneider, C. A., Rasband, W. S. & Eliceiri, K. W. NIH Image to ImageJ: 25 years of image analysis. *Nature Methods* **9***,* 671 (2012).

[108] Momma, K. & Izumi, F. VESTA 3 for three-dimensional visualization of crystal, volumetric and morphology data.

[109] *Software - JEMS* Available from: http://www.jems-saas.ch/Home/jemsWebSite/jems.html.

[110] *CrystalKit*. Available from: http://www.totalresolution.com/CrystalKit.html.

[111] *Database ICSD*. Available from: http://icsd.cds.rsc.org/search/basic.xhtml;jsessionid=5C12531922DD285E3F7C5AC3A031BD05?cdsrdr=3.

[112] Kuerbanjiang, B., Nedelkoski, Z., Kepaptsoglou, D., Ghasemi, A., Glover, S. E., Yamada, S., Saerbeck, T., Ramasse, Q. M., Hasnip, P. J., Hase, T. P. A., Bell, G. R., Hamaya, K., Hirohata, A. & Lazarov, V. K. The role of chemical structure on the magnetic and electronic properties of $Co_2FeAl_{0.5}Si_{0.5}$/Si(111) interface. *Applied Physics Letters* **108***,* 172412 (2016).

[113] Kirkland, E. J., Advanced computing in electron microscopy, Springer (2010).

[114] Koch, C. T., Determination of core structure periodicity and point defect density along dislocations, Arizona State University (2002).

[115] Forbes, B. D., D'Alfonso, A. J., Findlay, S. D., VanDyck, D., LeBeau, J. M., Stemmer, S. & Allen, L. J. Thermal diffuse scattering in transmission electron microscopy. *Ultramicroscopy* **111***,* 1670 (2011).

[116] Bocher, L., Gloter, A., Crassous, A., Garcia, V., March, K., Zobelli, A., Valencia, S., Enouz-Vedrenne, S., Moya, X., Marthur, N., Deranlot, C., Fusil, S., Bouzehouane, K.,

Bibes, M., Barthélémy, A., Colliex, C. & Stéphan, O. Atomic and electronic structure of the $BaTiO_3$/Fe interface in multiferroic tunnel junctions. *Nano Letters* **12**, 376 (2012).

[117] Qiao, Q., Klie, R. F., Öğüt, S. & Idrobo, J. C. Atomic and electronic structures of $SrTiO_3$/GaAs heterointerfaces: An 80-kV atomic-resolution electron energy-loss spectroscopy study. *Physical Review B* **85**, 165406 (2012).

[118] Clark, S. J., Segall, M. D., Pickard, C. J., Hasnip, P. J., Probert, M. I. J., Refson, K. & Payne, M. C. First principles methods using CASTEP. *Zeitschrift für Kristallographie* **220**, 567 (2005).

[119] Hohenberg, P. & Kohn, W. Inhomogeneous Electron Gas. *Physical Review* **136**, B864 (1964).

[120] Martin, R., Electronic Structure: Basic theory and practical methods. 2008, Cambridge University Press.

[121] Kohn, W. & Sham, L. J. Self-Consistent Equations Including Exchange and Correlation Effects. *Physical Review* **140**, A1133 (1965).

[122] Gunnarsson, O. & Lundqvist, B. I. Exchange and correlation in atoms, molecules, and solids by the spin-density-functional formalism. *Physical Review B* **13**, 4274 (1976).

[123] Perdew, J. P., Burke, K. & Ernzerhof, M. Generalized gradient approximation Made Simple. *Physical Review Letters* **77**, 3865 (1996).

[124] Perdew, J. P. & Wang, Y. Accurate and simple analytic representation of the electron-gas correlation energy. *Physical Review B* **45**, 13244 (1992).

[125] Kohanoff, J., Electronic structure calculations for solids and molecules: theory and computational methods, Cambridge University Press (2006).

[126] Payne, M. C., Teter, M. P., Allan, D. C., Arias, T. A. & Joannopoulos, J. D. Iterative minimization techniques for ab-initio total-energy calculations: molecular dynamics and conjugate gradients. *Reviews of Modern Physics* **64**, 1045 (1992).

[127] Denteneer, P. J. H. & Haeringen, W. v. The pseudopotential-density-functional method in momentum space: details and test cases. *Journal of Physics C: Solid State Physics* **18**, 4127 (1985).

[128] Ihm, J., Zunger, A. & Cohen, M. L. Momentum-space formalism for the total energy of solids. *Journal of Physics C: Solid State Physics* **12**, 4409 (1979).

[129] Pickett, W. E. Pseudopotential methods in condensed matter applications. *Computer Physics Reports* **9**, 115 (1989).

[130] Bachelet, G. B., Hamann, D. R. & Schlüter, M. Pseudopotentials that work: From H to Pu. *Physical Review B* **26**, 4199 (1982).

[131] Baldereschi, A. Mean-Value Point in the Brillouin Zone. *Physical Review B* **7**, 5212 (1973).

[132] Chadi, D. J. & Cohen, M. L. Electronic structure of $Hg_{1-x}Cd_xTe$ alloys and charge-density calculations using representative k-points. *Physical Review B* **7**, 692 (1973).

[133] Monkhorst, H. J. & Pack, J. D. Special points for Brillouin-zone integrations. *Physical Review B* **13**, 5188 (1976).

[134] Morris, A. J., Nicholls, R. J., Pickard, C. J. & Yates, J. R. *OPTADOS user guide*. 2015; Available from: http://www.tcm.phy.cam.ac.uk/~ajm255/optados/files/user_guide_1.2.pdf.

[135] Morris, A. J., Nicholls, R. J., Pickard, C. J. & Yates, J. R. OptaDOS: A tool for obtaining density of states, core-level and optical spectra from electronic structure codes. *Computer Physics Communications* **185***,* 1477 (2014).

[136] Sanchez-Portal, D., Artacho, E. & Soler, J. M. Projection of plane-wave calculations into atomic orbitals. *Solid State Commun* **95***,* 685 (1995).

[137] Vladimir, I. A., Aryasetiawan, F. & Lichtenstein, A. I. First-principles calculations of the electronic structure and spectra of strongly correlated systems: the LDA + U method. *Journal of Physics: Condensed Matter* **9***,* 767 (1997).

[138] Hubbard, J. Electron correlations in narrow energy bands. *Proceedings of the Royal Society of London Series A Mathematical and Physical Sciences* **276***,* 238 (1963).

[139] Anisimov, V. I., Zaanen, J. & Andersen, O. K. Band theory and Mott insulators: Hubbard U instead of Stoner I. *Physical Review B* **44***,* 943 (1991).

[140] Chadov, S., Fecher, G. H., Felser, C., Min´ar, J., Braun, J. & Ebert, H. Electron correlations in $Co_2Mn_{1-x}Fe_xSi$ Heusler compounds. *Journal of Physics D: Applied Physics* **42***,* 084002 (2009).

[141] *CASTEP*. Available from: http://www.castep.org.

[142] Evans, R. F. L., Fan, W. J., Chureemart, P., Ostler, T. A., Ellis, M. O. A. & Chantrell, R. W. Atomistic spin model simulations of magnetic nanomaterials. *Journal of Physics: Condensed Matter* **26***,* 103202 (2014).

[143] Uhl, M. & Siberchicot, B. A first-principles study of exchange integrals in magnetite. *Journal of Physics: Condensed Matter* **7***,* 4227 (1995).

[144] Ležaić, M., Mavropoulos, P., Bihlmayer, G. & Blügel, S. Exchange interactions and local-moment fluctuation corrections in ferromagnets at finite temperatures based on noncollinear density-functional calculations. *Physical Review B* **88***,* 134403 (2013).

[145] Tsunegi, S., Sakuraba, Y., Oogane, M., Takanashi, K. & Ando, Y. Large tunnel magnetoresistance in magnetic tunnel junctions using a Co_2MnSi Heusler alloy electrode and a MgO barrier. *Applied Physics Letters* **93***,* 112506 (2008).

[146] Hirohata, A., Sagar, J., Lari, L., Fleet, L. & Lazarov, V. Heusler-alloy films for spintronic devices. *Applied Physics A* **111***,* 423 (2013).

[147] Ishikawa, T., Marukame, T., Kijima, H., Matsuda, K. I., Uemura, T., Arita, M. & Yamamoto, M. Spin-dependent tunneling characteristics of fully epitaxial magnetic tunneling junctions with a full-Heusler alloy Co_2MnSi thin film and a MgO tunnel barrier. *Applied Physics Letters* **89***,* 192505 (2006).

[148] Furubayashi, T., Kodama, K., Sukegawa, H., Takahashi, Y. K., Inomata, K. & Hono, K. Current-perpendicular-to-plane giant magnetoresistance in spin-valve structures using epitaxial $Co_2FeAl_{0.5}Si_{0.5}$/Ag/$Co_2FeAl_{0.5}Si_{0.5}$ trilayers. *Applied Physics Letters* **93***,* 122507 (2008).

[149] Taku, I., Sakuraba, Y.,Bosu, S., Saito, K., Mitani, S. & Takanashi, K. Large interface spin-asymmetry and magnetoresistance in fully epitaxial Co_2MnSi/Ag/Co_2MnSi current-perpendicular-to-plane magnetoresistive devices. *Applied Physics Express* **2***,* 063003 (2009).

[150] Sakuraba, Y., Iwase, T., Saito, K., Mitani, S. & Takanashi, K. Enhancement of spin-asymmetry by *$L2_1$*-ordering in Co_2MnSi/Cr/Co_2MnSi current-perpendicular-to-plane magnetoresistance devices. *Applied Physics Letters* **94***,* 012511 (2009).

[151] Miura, Y., Uchida, H., Oba, Y., Abe, K. & Shirai, M. Half-metallic interface and coherent tunneling in Co_2YZ/MgO/Co_2YZ (YZ=MnSi, CrAl) magnetic tunnel junctions: A first-principles study. *Physical Review B* **78***,* 064416 (2008).

[152] Nedelkoski, Z., Kepaptsoglou, D., Ghasemi, A., Kuerbanjiang, B., Hasnip, P. J., Yamada, S., Hamaya, K., Ramasse, Q. M., Hirohata, A. & Lazarov, V. K. Controlling the half-metallicity of Heusler/Si(1 1 1) interfaces by a monolayer of Si–Co–Si. *Journal of Physics: Condensed Matter* **28***,* 395003 (2016).

[153] Tanikawa, K., Oki, S., Yamada, S., Kawano, M., Miyao, M. & Hamaya, K. High-quality $Co_2FeSi_{0.5}Al_{0.5}$/Si heterostructures for spin injection in silicon spintronic devices. *Thin Solid Films* **557***,* 390 (2014).

[154] Oki, S., Yamada, S., Murakami, T., Miyao, M. & Hamaya, K. Influence of Al co-deposition on the crystal growth of Co-based Heusler-compound thin films on Si(111). *Thin Solid Films* **520***,* 3419 (2012).

[155] Falke, M., Falke, U., Bleloch, A., Teichert, S., Beddies, G. & Hinneberg, H. J. Real structure of the $CoSi_2$/Si(001) interface studied by dedicated aberration-corrected scanning transmission electron microscopy. *Applied Physics Letters* **86***,* 203103 (2005).

[156] Al-Allak, H. M. & Clark, S. J. Valence-band offset of the lattice-matched beta-$FeSi_2$(100)/Si(001) heterostructure. *Physical Review B* **63***,* 033311 (2001).

[157] Nedelkoski, Z., Kuerbanjiang, B., Glover, S. E., Sanchez, A. M., Kepaptsoglou, D., Ghasemi, A., Burrows, C. W., Yamada, S., Hamaya, K., Ramasse, Q. M., Hasnip, P. J., Hase, T., Bell, G. R., Hirohata, A. & Lazarov, V. K. Realisation of magnetically and atomically abrupt half-metal/semiconductor interface: $Co_2FeSi_{0.5}Al_{0.5}$/Ge(111). *Scientific Reports* **6***,* 37282 (2016).

[158] Nedelkoski, Z., Sanchez, A. M., Ghasemi, A., Hamaya, K., Evans, R. F. L., Bell, G. R., Hirohata, A. & Lazarov, V. K. The antiphase boundary in half-metallic Heusler alloy $Co_2Fe(Al,Si)$: atomic structure, spin polarization reversal, and domain wall effects. *Applied Physics Letters* **109***,* 222405 (2016).

[159] Simon, T., Oksana, G., Jaroslav, H. & Burkard, H. Magnetic anisotropy, exchange and damping in cobalt-based full-Heusler compounds: an experimental review. *Journal of Physics D: Applied Physics* **43***,* 193001 (2010).

[160] Zander, M., Herfort, J., Kumakura, K., Schönherr, H. P. & Trampert, A. Epitaxial Heusler alloy Co_2FeSi films on Si(1 1 1) substrates grown by molecular beam epitaxy. *Journal of Physics D: Applied Physics* **43***,* 305004 (2010).